

TWO HII/HI COMPLEXES IN THE OUTER GALAXY

By

WILLIAM FRANK WALL

B.Sc., The University of Toronto, 1983

A THESIS SUBMITTED IN PARTIAL FULFILLMENT OF
THE REQUIREMENTS FOR THE DEGREE OF
MASTER OF SCIENCE

in

THE FACULTY OF GRADUATE STUDIES

Department of Physics

We accept this thesis as conforming
to the required standard

THE UNIVERSITY OF BRITISH COLUMBIA

July 1986

©William Frank Wall

In presenting this thesis in partial fulfilment of the requirements for an advanced degree at the University of British Columbia, I agree that the Library shall make it freely available for reference and study. I further agree that permission for extensive copying of this thesis for scholarly purposes may be granted by the head of my department or by his or her representatives. It is understood that copying or publication of this thesis for financial gain shall not be allowed without my written permission.

Department of PHYSICS

The University of British Columbia
1956 Main Mall
Vancouver, Canada
V6T 1Y3

Date July 17/86

ABSTRACT

The HII regions S211 and S212 have been observed at 1420 MHz, in both line and continuum, using the synthesis telescope at the Dominion Radio Astrophysical Observatory. S211 and S212 and their associated atomic hydrogen were studied as part of an ongoing investigation of HII/HI complexes within molecular clouds.

S211 and S212 both require a flux of ionizing photons consistent with the ultraviolet emission from an O6V star. S211 was barely resolved (1.6 beam widths) and was thus modelled with a constant density model with density 85 cm^{-3} . S212 was modelled with linear density gradients and a central density of 50 cm^{-3} . S212 is probably density bounded towards the east and south. There is evidence for S212 and indirect evidence for S211 to suggest that both HII regions contain unresolved clumps of enhanced density. This would imply young ages ($< 10^5$ yrs) for both HII regions.

S211 was found to have $4000 M_{\odot}$ of associated HI, roughly hemispherical in shape and extending 20 pc from the major ionizing star of S211. S212 possesses $1200 M_{\odot}$ of atomic hydrogen which reaches an extent of 20 pc from its major ionizing star. Neither HI region would easily conform to a steady state photodissociation model assuming uniform hydrogen density. This is undoubtedly due to the young age of the HII regions as well as to a gradient in the gas density.

CONTENTS

ABSTRACT	ii
LIST OF TABLES	v
LIST OF FIGURES	vi
LIST OF ABBREVIATIONS	viii
ACKNOWLEDGEMENTS	x
1 INTRODUCTION	1
2 OBSERVATIONS AND REDUCTIONS	6
2.1 THE OBSERVATIONS	6
2.2 HI REDUCTIONS	10
2.2.1 Making the Interferometer Maps	10
2.2.2 Adding the Low Order Spacings	14
2.3 CONTINUUM MAP REDUCTIONS	18
3 CONTINUUM EMISSION OF S211, S212	23
3.1 THEORY	23
3.2 DISTANCES	26
3.3 MODELLING	27
3.4 IMPLICATIONS OF THE MODELS	40
4 HI EMISSION	48
4.1 THEORY	48
4.2 S211 ATOMIC HYDROGEN EMISSION	52
4.2.1 Previous Models for the S211 Complex	62
4.3 S212 ATOMIC HYDROGEN EMISSION	68
5 A COHERENT PICTURE	72
5.1 THE S211 COMPLEX	75
5.2 THE S212 COMPLEX	84
6 CONCLUSIONS AND DISCUSSION	92
REFERENCES	97

APPENDIX A – CC SURVEY CONTINUUM MAP	100
APPENDIX B – CC SURVEY HI MAPS	101
APPENDIX C – HIIBLOB3 DOCUMENTATION	114
APPENDIX D – CONVOLUTION COMPENSATION FUNCTION	124
APPENDIX E – S211 HI MAPS AND SPECTRA	126
APPENDIX F – S212 HI MAPS AND SPECTRA	147

LIST OF TABLES

TABLE 1.1	Positions of S211 and S212	4
TABLE 2.1	DRAO Synthesis Telescope Parameters	9
TABLE 3.1	S211 Model Parameters	37
TABLE 3.2	S212 Model Parameters	37
TABLE 3.3	Estimates of Age and Expansion Velocity for S211	45
TABLE 3.4	Estimates of Age and Expansion Velocity for S212	46
TABLE 4.1	Derived Masses of the S211 HI Cloud	59
TABLE 4.2	Derived Masses of the S212 HI Cloud	69
TABLE 6.1	Comparison of HII/HI Parameters	94

LIST OF FIGURES

FIGURE 1.1a	Reproduction of the Palomar Observatory Sky Survey Print (Red)	2
FIGURE 1.1b	Reproduction of the Palomar Observatory Sky Survey Print (Blue)	3
FIGURE 2.1	CC Survey Low Order Spacings Grid	8
FIGURE 2.2a	Example of “Tube”	12
FIGURE 2.2b	Example of “Tube” Removed	13
FIGURE 2.3	Baseline Offset Map	17
FIGURE 2.4	Low Order Spacings Continuum Map	20
FIGURE 3.1	Schematic Representation of HIIBLOB3	28
FIGURE 3.2a	S211 Emission Measure Profile	31
FIGURE 3.2b	S212 Emission Measure Profile	32
FIGURE 3.3a	S211 Theoretical Emission Measure Profile	35
FIGURE 3.3b	S212 Theoretical Emission Measure Profile	36
FIGURE 3.4	Positions in S212 where Optical Line Ratios were Measured	41
FIGURE 4.1	Schematic Representation of Equation 4.1	49
FIGURE 4.2	Cloud 1 Column Densities	55
FIGURE 4.3	Cloud 1 in Absorption	55
FIGURE 4.4	Ring 1 Spectrum	57
FIGURE 4.5	Baseline Spectrum for S211	60
FIGURE 4.6	Cloud 2 Column Densities	61
FIGURE 4.7	Absorption Model 1	64
FIGURE 4.8	Schematic Representation of Absorption Model 2	65
FIGURE 4.9	Stellar Wind Model for S211	67
FIGURE 4.10	S212 HI Column Densities	70
FIGURE 5.1	Total HI Mass vs. Spectral Class	74

FIGURE 5.2	Schematic Representation of the S211 Complex	76
FIGURE 5.3	Systematic HI Velocity Variation for the S211 Complex	78
FIGURE 5.4	Theoretical Column Density Profiles (S211)	80
FIGURE 5.5	Theoretical HI Density Profiles (S211)	83
FIGURE 5.6	Theoretical Temperature Profiles (S211)	83
FIGURE 5.7	Schematic Representation of the S212 Complex	87
FIGURE 5.8	Theoretical Column Density Profile (S212)	89
FIGURE 5.9	Theoretical HI Density Profile (S212)	90
FIGURE 5.10	Theoretical Temperature Profile (S212)	90

LIST OF ABBREVIATIONS

- CC – survey designation used at DRAO for field observed
containing S211 and S212 (see Section 2.1)
- CSS map – Compressed Spectrum Subtracted map
- 128 SS maps averaged in groups of 3 consecutive
channels yielding 43 CSS maps
 - example of LMC map
- DRAO – Dominion Radio Astrophysical Observatory
- EW – East-West
- FFT – Fast Fourier Transform
- FS map – “Full” Spacings map
- sum of 128 LOS LMC maps and 128 interferometer LMC
maps thereby yielding 128 LMC maps containing all
spacings from 0m to 605m.
- FWHM – Full Width at Half Maximum
- HPBW – Half Power Beam Width
- LMC map – Line Minus Continuum map
- different LMC maps include – interferometer maps
 - LOS maps
 - FS maps
 - SS maps
 - CSS maps
 - SSG maps
- LOS map – Low Order Spacings map

– can be either a continuum LOS map or an LMC LOS map

lsr – local standard of rest

NS – North-South

SS map – Spectrum Subtracted map

- these are the 128 FS maps with a spectrum subtracted
where the spectrum represents large scale emission
- example of LMC map

SSG map – Spectrum Subtracted Galactic map

- 128 SS maps averaged in groups of 12 consecutive
channels rotated to galactic coordinates and
smoothed to 3' resolution yielding 11 SSG maps.
- example of LMC map

WW – Weaver and Williams, 1974

ACKNOWLEDGEMENTS

This thesis is the result of consultations with, and contributions by, a large number of people to whom I would like to express my gratitude.

I am grateful to my supervisors Bill McCutcheon, Peter Dewdney and Chris Purton, whose contributions and comments made this thesis possible. I am especially indebted to Bill McCutcheon whose guidance, generosity and cheerful disposition made the rocky times easier. Peter Dewdney and Chris Purton are greatly appreciated for their advice, their patience and their general willingness to help.

Special thanks to Rob Roger who took the time to read the first draft of this thesis and made several valuable comments. I am particularly indebted to Geoff Croes who wrote, and modified on my behalf, the plotting software that made the figures possible. I will always fondly remember the D.R.A.O. team for providing a warm and friendly atmosphere in which to conduct research; I leave knowing more than when I came.

I am grateful to K.T. Kim and Dale A. Frail for their assistance with the data reduction and providing thought provoking, and sometimes offbeat, discussions.

Thanks to Ernie Seaquist for getting the ball rolling and to a special friend who inspired its final stages.

The financial support of the Natural Sciences and Engineering Research Council is gratefully acknowledged.

1 INTRODUCTION.

S211 and S212 (NGC1624) are two relatively unstudied HII regions in the outer part of the galaxy ($l = 154^{\circ}65$ and $l = 155^{\circ}35$ respectively). No modelling has been done previously on the nebulae themselves. Most of the work on these objects has been in relation to extending the galactic rotation curve beyond the solar circle (Fich and Blitz, 1984; Chini and Wink, 1984; Moffat et. al., 1979) where they were included in studies of a large number of objects. S212 was studied in some detail by Talent and Dufour (1979) in order to reassess galactic abundance gradients. They measured some forbidden line strengths and electron densities and temperatures. Chini & Wink (1984) have observed the $H_{112\alpha}$ recombination line obtaining a velocity with respect to the local standard of rest and an estimate of electron temperatures. They also found the spectral and luminosity classes of the exciting stars to be O9Ib, O9V, B0V for S211 and O6I, B1III for S212. Moffat et. al. (1979) found the exciting stars of S212 to be O5.5 and B0V. They were unable to obtain a luminosity classification for the O star but ZAMS fitting by Fitzgerald (1985, priv. comm.) suggests that the star may not be class I as believed by Chini & Wink. This is discussed again in Chapter 3.

The enlargements of the Palomar prints (Fig. 1.1) show S212 towards the lower left and S211 towards the upper right. On the E print (photographed in red) S212 is more prominent than S211; the former having a diameter of about $4'$ and the latter about $1'.5$. A dust lane appears to be cutting across the southern side of S211, but this "bite" is an actual feature of S211 as seen on a 6 cm map by M. Fich (unpublished) from the VLA. On the O print (in blue light) the nebulosity of S212 is faint and internal stars are revealed. The nebulosity of S211 is not visible in this print. The O print also shows that this area has patches of high extinction.

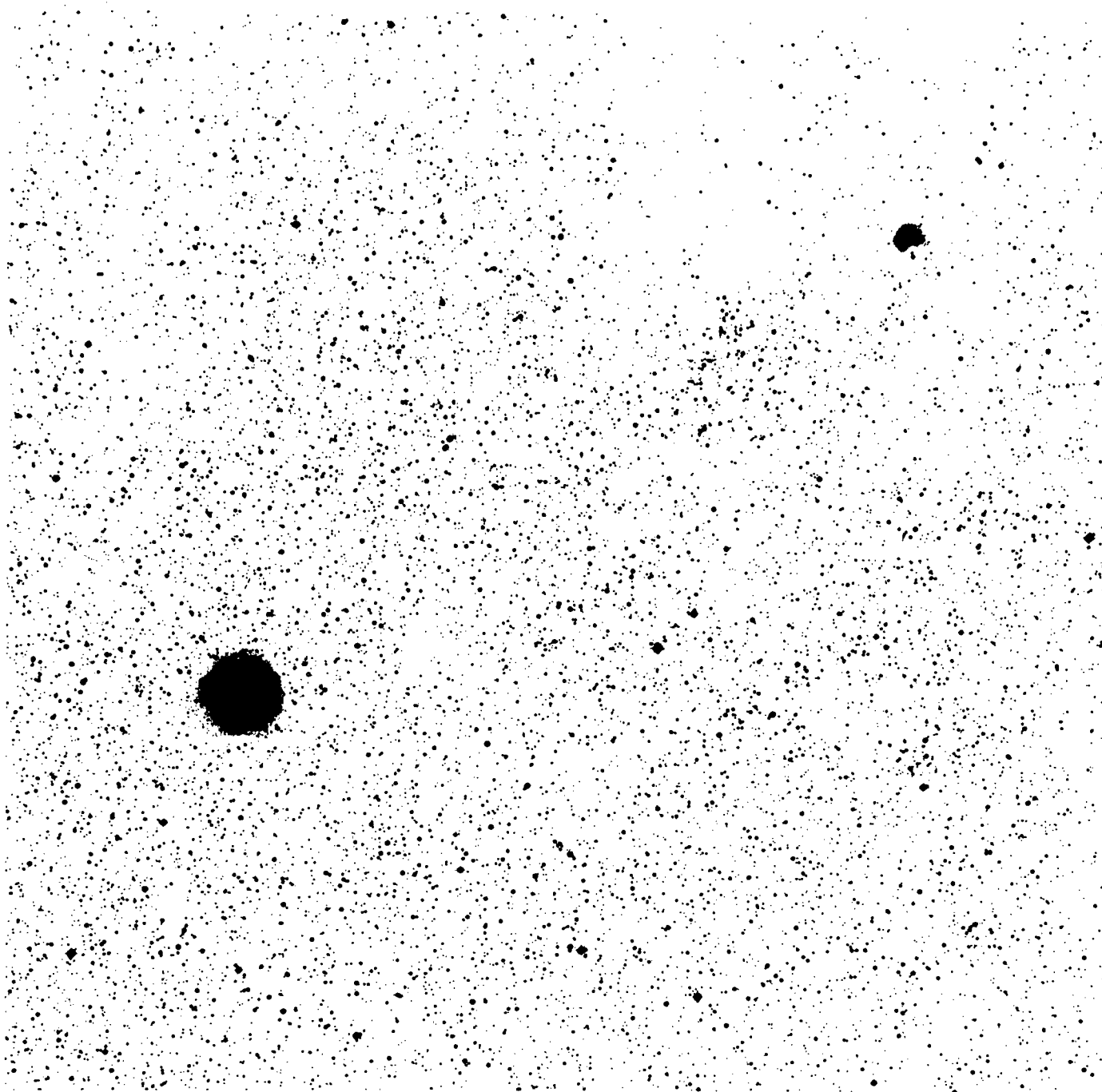


FIG. 1.1a: Reproduction of the Palomar Observatory Sky Survey print of Sharpless Regions S212 (lower left) and S211 (upper right) in red light. Notice the "bite" out of the southern limb of S211. Scale: 3mm/arcminute

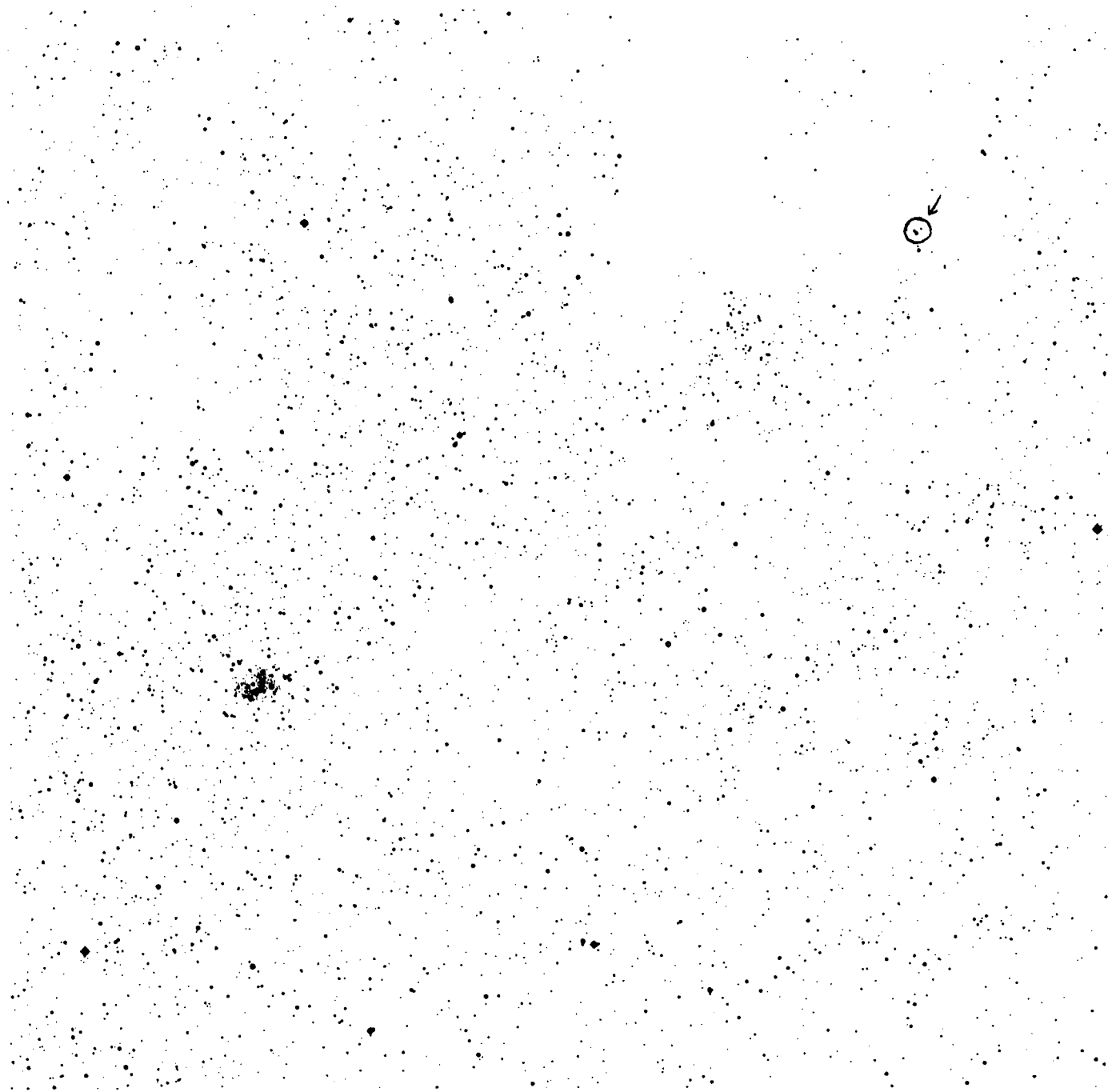


FIG. 1.1b: Reproduction of the Palomar Observatory Sky Survey print of Sharpless Regions S212 (lower left) and S211 (not visible) in blue light. The position of S211 is indicated. The exciting stars are visible in both nebulae.
Scale: 3mm/arcminute

TABLE 1.1: POSITIONS (Sharpless)

OBJECT	$\alpha(1950)$	$\delta(1950)$	l	b
S211	4h 33m 5.80s	50° 47' 21''6	154°65	2°46
S212	4h 36m 42.52s	50° 21' 54''9	155°35	2°60

Table 1.1 shows the positions of S211 and S212. Notice that the objects have a galactic latitude of only about 2°5 suggesting that the 21 cm neutral hydrogen emission of the sources S211 and S212 would be confused in distributed emission from the galactic plane. In studying the maps of 21 cm emission it is therefore necessary to somehow distinguish between galactic plane HI emission and HI emission associated with the HII regions S211/S212.

Maps of neutral hydrogen emission have been produced from a survey using the synthesis radio telescope at the Dominion Radio Astrophysical Observatory (DRAO) near Penticton, B.C. This instrument can achieve resolutions of $1'.0 \times 1'.0 \text{ cosec } \delta$ ($\alpha \times \delta$) and $0.33 \text{ km} \cdot \text{s}^{-1}$ at a wavelength of 21 cm. See Table 2.1 for telescope parameters.

Both S211 and S212 are probably associated with the molecular clouds, i.e. clouds of H_2 , that lie in their respective directions (McCutcheon, 1985 priv. comm.). Carbon monoxide is a tracer for H_2 since molecular hydrogen does not emit at radio wavelengths; the presence of H_2 is inferred from the rotational transition $J = 1 \rightarrow 0$ of CO which has been collisionally excited by the H_2 . Molecular clouds have masses of 10^2 to 10^5 solar masses and are believed to be the birthplaces of stars. Those stars that are born as O or early B stars form surrounding HII regions. Stellar photons just longwards of the Lyman limit ($912 \text{ \AA} < \lambda < 1120 \text{ \AA}$) penetrate beyond the HII region boundary and dissociate the molecular hydrogen into HI. Thus HII regions and their associated HI complexes are usually found in molecular clouds. The individual components of this three phase system, their interactions, and evolution are subjects of continuing investigation. The purpose of the survey

was to investigate these subjects for the specific cases of S211 and S212 and, through modelling, determine parameters of the HII and HI regions. The circular symmetry of S212, seen in optical photographs, suggested that it would be a relatively simple specimen to study. S211 was included in the survey due to its proximity to S212 and also due to its relatively simple appearance.

2 OBSERVATIONS AND REDUCTIONS

2.1 THE OBSERVATIONS

The observations were made with the DRAO synthesis telescope which consists of four 8.6 m paraboloids on an east-west baseline. Two of these are mounted on a 300 m track allowing full uv coverage with spacings from 13 m to 605 m. Each of the two stationary dishes are correlated with each of the two translational dishes giving 4 spacings for each 12 hour observing run. The 8.6 m dishes allow a large field of view – $2^{\circ}.1$ one-third-power-beamwidth at 1420 MHz. Further details of the synthesis telescope are given in Table 2.1 (page 9). (Note: The 408 MHz system was not in operation at the time of these observations.) The DRAO synthesis telescope is ideal for studying HII regions and their associated molecular clouds because it combines a large field of view, that can include both S211 and S212, with resolution that allows easy comparison to millimetre wave observations of CO.

The observations, dubbed the CC Survey, took place from Oct. 8, 1982 to Nov. 27, 1982 with an extra observing run on Sept. 20, 1983 to obtain the shortest spacing. The field centre of the CC Survey was $\alpha(1950) = 4\text{h } 35\text{m}$, $\delta(1950) = 50^{\circ} 35'$. At this declination one has a resolution of $1'.0 \times 1'.3$ ($\alpha \times \delta$). The spectrometer bandwidth chosen was 0.25 MHz centred on $V_{\text{lsr}} = -35.0 \text{ km s}^{-1}$. The spectral resolution was $0.66 \text{ km} \cdot \text{s}^{-1}$ and for 128 channels the velocity difference between channels is $0.41 \text{ km} \cdot \text{s}^{-1}$. The out-of-band continuum was measured in two 7.5 MHz sub-bands on either side of a 5 MHz “notch” centred on 1420 MHz. Calibrations were done before and after each 12 hour observing run. The calibrator sources were 3C380 and 3C147 with adopted fluxes 14.80 Jy and 22.13 Jy respectively (Baars et. al., 1977). In addition calibrations, locally called “cross-talks”, were performed on Oct. 7, Nov. 3, Nov. 10, and Nov. 18 in 1982, and Sept. 21, 1983 to determine the amplitude and phase within the spectrometer band. This was achieved

by observing outside the hydrogen line frequencies while pointing the dishes in different directions to produce uncorrelated noise and introducing small amounts of the noise from one signal path to the other. The two noise signals are then cross-correlated both in the continuum band and in the spectrometer band. The spectrometer output is then normalized to the continuum output.

To obtain spacings 0 to 13 m the 25.6 m dish at DRAO observed the CC field on Jan. 27-28, 1985. This dish has a half-power beam width (HPBW) of 36' at 1420 MHz. The observations were made in a 16×16 grid forming a 4° square centred on $\alpha(1950) = 4\text{h } 35\text{m}$, $\delta(1950) = 50^\circ 35'$. The 256 spectra thus obtained had bandwidths of 0.25 MHz. The corners of the 4 degree survey field along with the middles of the edges and the geometric centre form a 3×3 pattern (see Fig. 2.1) where 1 MHz spectra were measured. These were necessary in order to determine a baseline for the 0.25 MHz spectra since the 0.25 MHz bands are too narrow to include all the galactic HI emission plus a suitable length of baseline. All spectra were calibrated against the standard region S7 whose spectrum has a peak brightness temperature of 100 ± 7 K (Williams, 1973). Frequency switching was employed to remove gain fluctuations.

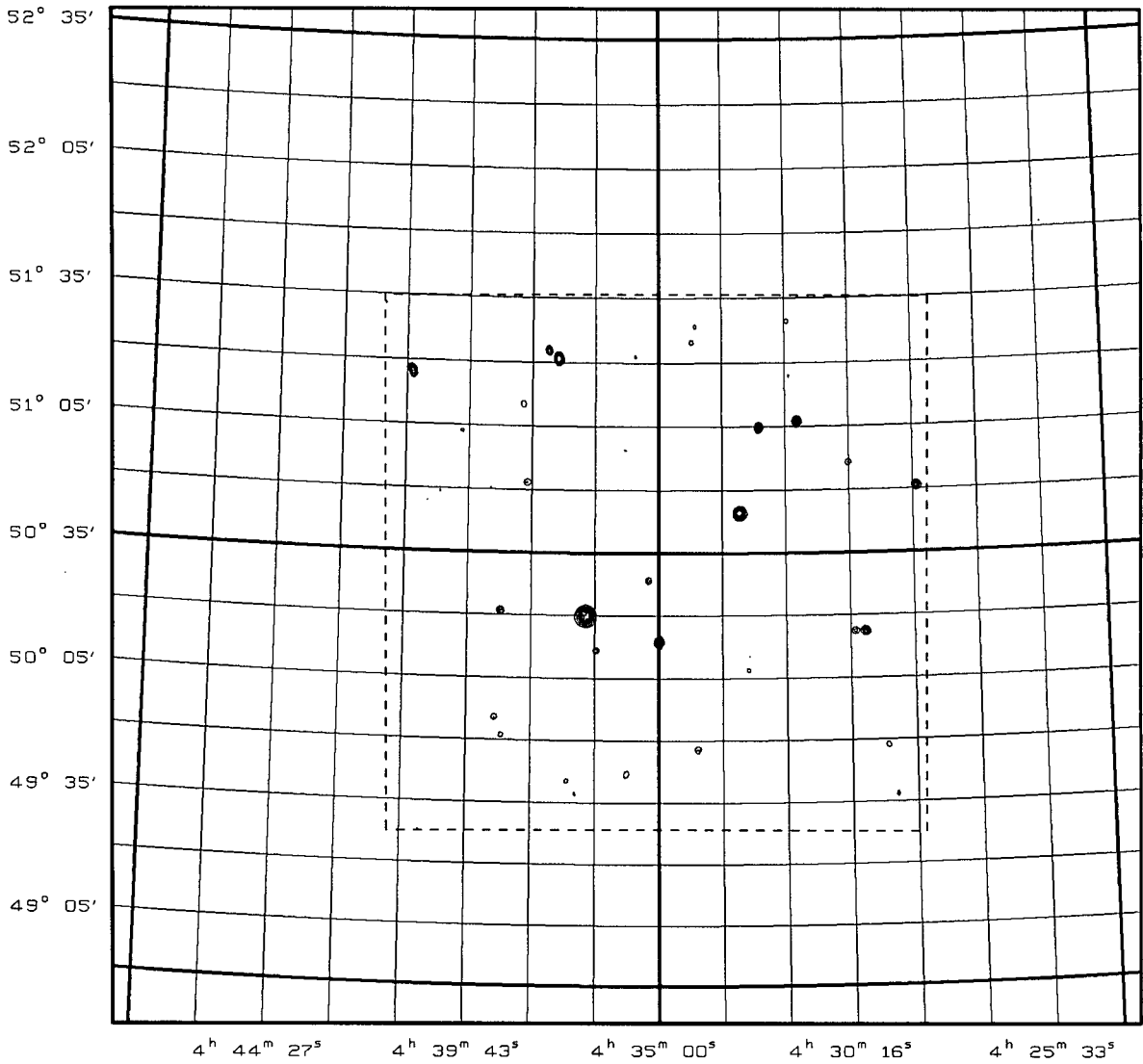


FIG. 2.1: CC Survey Low Order Spacings Coordinate Grid
 Each point on the grid represents a location where the 25.6m dish observed with 0.25MHz bandwidth. The dark lines form the grid where additional 1MHz samples were taken. The 2° interferometer continuum map is shown to provide a sense of position and scale.

TABLE 2.1: THE DRAO SYNTHESIS TELESCOPE

T. Landecker

FUNDAMENTAL INSTRUMENT PARAMETERS

DESCRIPTION: – 4 antennas on a 600 m E-W baseline

– 2 movable on a track and 2 fixed

OPERATING FREQUENCY: – 1420 MHz and 408 MHz continuum

– HI spectral line

RESOLUTION: – $1'.0 \times 1'.0 \operatorname{cosec} \delta$ at 1420 MHz– $3'.5 \times 3'.5 \operatorname{cosec} \delta$ at 408 MHz

SENSITIVITY IN CONTINUUM: – 0.8 mJy/beam rms noise } (1420 MHz)
 (at field centre) (or) $0.14 \sin \delta$ K
 – 3.3 mJy/beam rms } (408 MHz)
 (or) $0.55 \sin \delta$ K

FIELD OF VIEW: – $2^\circ.1$ at 1420 MHz– $7^\circ.4$ at 408 MHz

SPATIAL FREQUENCY COVERAGE: – continuous from 13 m to 605 m
 in 35 days observing

SPECTRAL LINE SYSTEM: – 128 channel maps

– spectral resolution (W):

max $0.33 \operatorname{km} \cdot \operatorname{s}^{-1}$ min $10.6 \operatorname{km} \cdot \operatorname{s}^{-1}$ – Sensitivity: $12.8 \left(\frac{W}{\operatorname{km} \cdot \operatorname{s}^{-1}} \right)^{-\frac{1}{2}} \sin \delta$ K

POLARIZATION CAPABILITIES: – being developed

MAP DATA COLLECTED (each field): ~ 65000 spectra

~ 10^7 data points

2.2 HI REDUCTIONS

2.2.1 Making The Interferometer Maps –

The interferometer maps were produced in a three stage process (see Irwin, 1978) – PHASE0, PHASE1, PHASE2. In PHASE0 all the required information for the reductions is presented in a tabular form. Here, the astronomer has the option of suppressing some of the contaminated data. In PHASE1 the calibrations are applied to the data to put them in units of flux density. For each spectrometer channel the data, or visibilities, are arranged in a two dimensional array where each row represents an elliptical track in the uv plane. In PHASE2 the visibilities are gridded in rectangular form. A two-dimensional fast Fourier transform (FFT) is applied to each channel producing 128 line maps and one continuum map. The line maps are $2^\circ \times 2^\circ$ containing 256×256 pixels. The continuum map is $4^\circ \times 4^\circ$ containing 512×512 pixels. The central $2^\circ \times 2^\circ$ of the continuum map was subtracted from the line maps to obtain the line minus continuum maps. The LMC maps thus form a three dimensional data structure where two dimensions are spatial and one is velocity (or frequency). A “slice” of this structure parallel to the $\alpha\delta$ plane gives an α - δ map at a particular velocity; a slice parallel to the δv plane gives a δ -v map at a particular right ascension; a slice parallel to the αv plane gives a v- α map at a particular declination. A single row of numbers parallel to the v axis at a particular α , δ represents the HI spectrum at the point α , δ .

In this particular survey it was twice necessary to scale up the line maps before subtracting the continuum map. This procedure was peculiar to this survey and its details are not necessary for a general understanding of the data reductions that occurred; the rest of Section 2.2.1 is devoted to describing these two scalings. The necessity for the first scaling was apparent from inspection of the HI spectra centred on six of the continuum sources in the field: S211, S212, RAFGL5124, 11P13 (DRAO Survey, Higgs, 1986), 4C+51.14, 4C+50.13 – all labelled in Appendix A.

Depending on which source, the last 32 to 64 channels of each spectrum were taken to represent the intensity level of the corresponding continuum source since HI emission was assumed to be weak in this frequency range. This level was found to be lower than that of the corresponding continuum source. A box was placed around the position of each continuum source. An average of the spectra contained within each box, weighted by the out-of-band continuum level at the corresponding position was compared with a weighted average of the continuum itself. The resulting ratio of 1.72 ± 0.17 was used to scale up the line maps. The continuum map was subtracted from each of the line maps to produce line minus continuum maps (LMC maps).

Examination of the LMC maps revealed “holes” in the HI emission at positions of the continuum sources. These holes extended through all channels of the LMC maps. The different channel maps together compose a three dimensional data structure which allows the holes to be viewed as “tubes” running through the maps. A longitudinal section of such a tube is shown in Fig. 2.2a which is a declination-velocity map around the source 4C+50.13. The tubes were caused by oversubtraction of the out-of-band continuum. In other words it was again necessary to scale up the line maps and again subtract the continuum. To compute the amount of oversubtraction the intensity decrease in each tube was found with respect to the intensity just outside the tube. This was averaged over different frequency ranges for each tube and expressed as a fraction of the out-of-band continuum level at the corresponding position. The values for different tubes were averaged to yield a ratio of 2.17 ± 0.41 by which to scale up the line maps. Application of this ratio and subtraction of the continuum map produced the final version of the LMC maps. Fig. 2.2b shows the same declination-velocity map as in 2.2a with the tube removed.

A natural question is why the line maps were scaled up rather than scaling the continuum map down. The continuum map has been calibrated directly against sources of known flux density whereas the line maps were calibrated indirectly in the cross-talks. Another question is, Why was the first scaling of the line maps

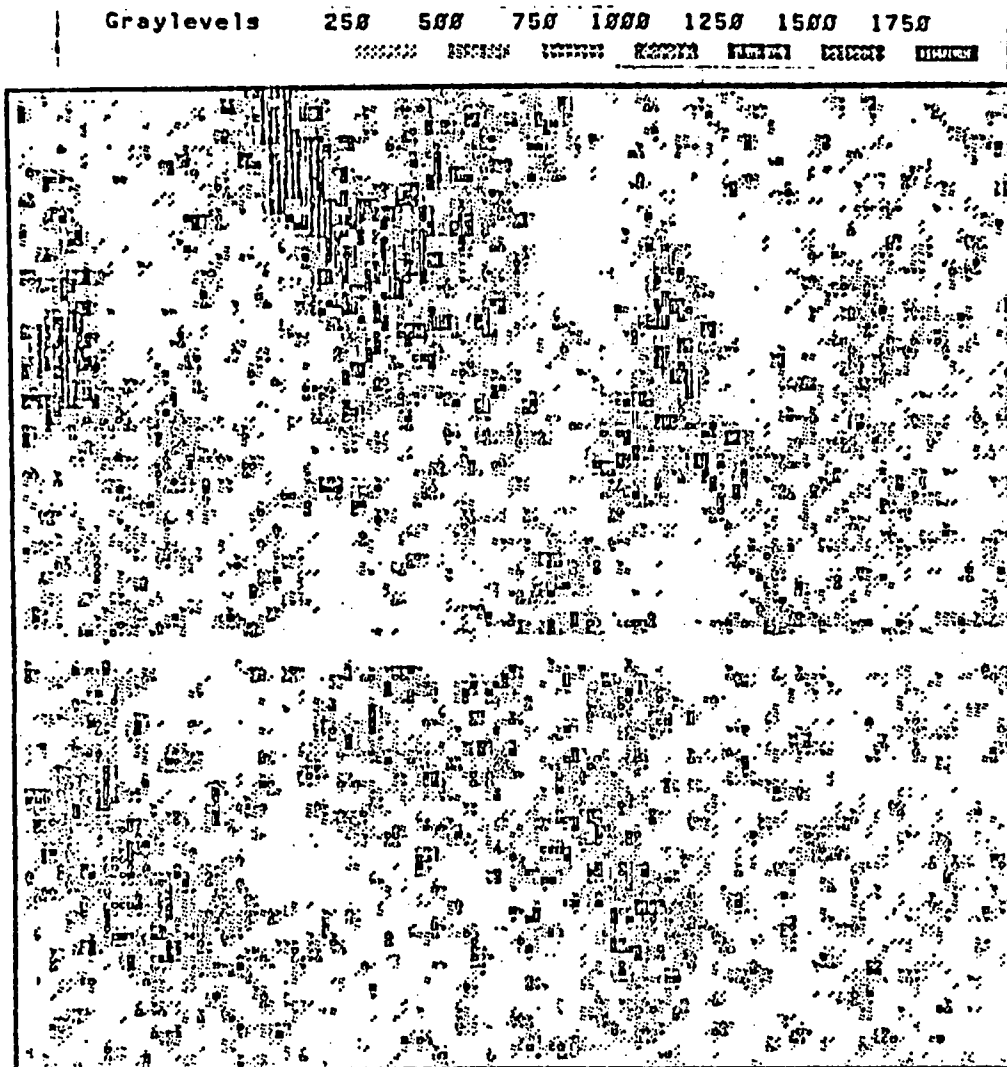


FIG. 2.2a: The "tube" discussed in Section 2.2.1 is clearly displayed above in this declination versus velocity grayscale plot. The grayscale levels are in units of $(\text{mJy}/\text{beam area})/2.17$

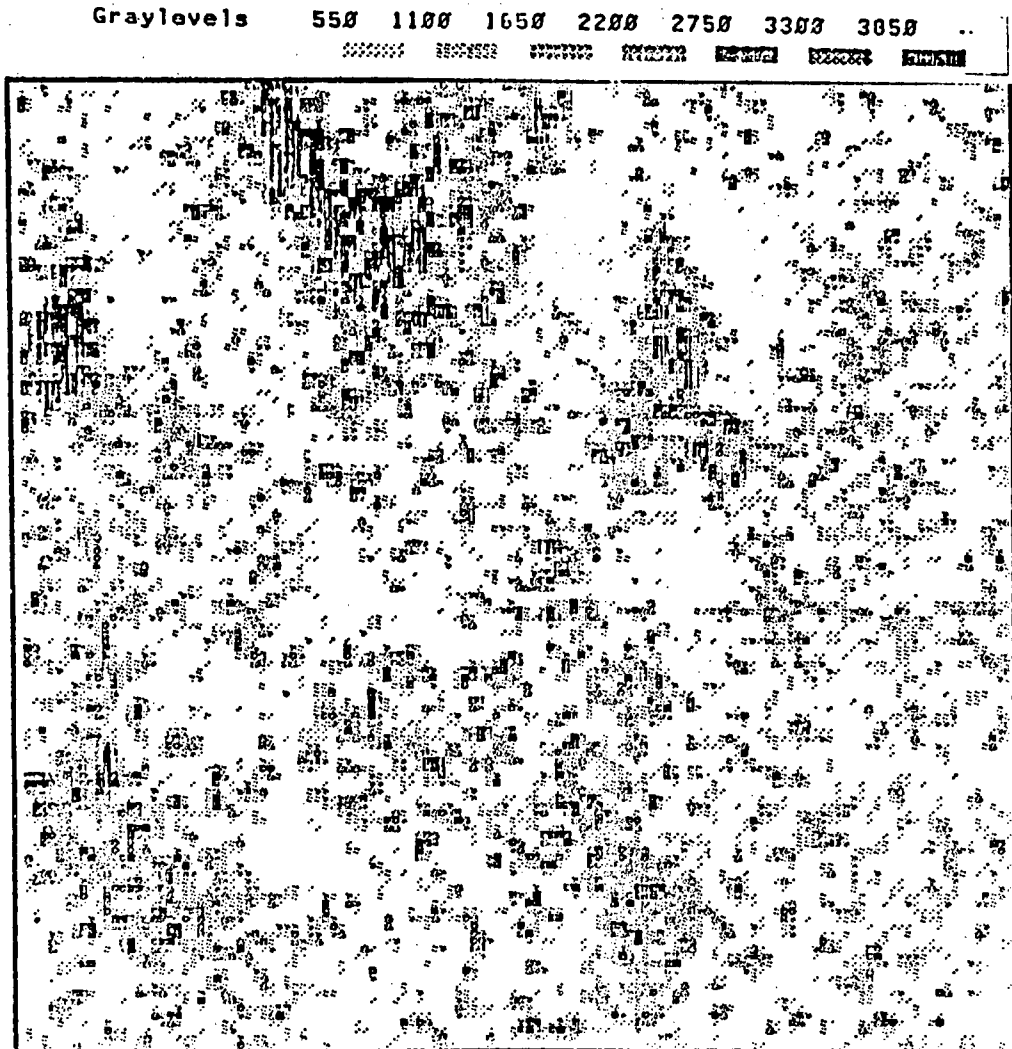


FIG. 2.2b: The same declination versus velocity grayscale plot as in Fig. 2.2a but with the proper calibration of the line maps as is evidenced by the absence of the tube. Grayscale levels are in units of mJy/beam area.

inadequate? A probable explanation is that the last channels of the spectra, used in estimating the continuum level, contained HI emission. This means that the continuum level would be overestimated and, when compared with the out-of-band continuum level; the scaling ratio would be underestimated.

A more pertinent question is why such scaling was necessary at all. Current surveys at DRAO perform cross-talks daily. However, for the CC Survey only 5 days of cross-talks were done over 35 days of observations; this could be an insufficient number to eliminate gain and phase fluctuations in the telescope's electronics.

2.2.2 Adding The Low Order Spacings –

Up to this point the LMC maps were missing spacings 0 m to 13 m. The lack of broad spatial emission caused a bowl-like depression in the central region of each map. Before addition to the interferometer maps the low order spacings (LOS) maps from the 25.6 m dish were processed in the following way:

- 1) The 16×16 LOS maps were interpolated to 128×128 maps.
- 2) The new LOS maps were Fourier transformed to the uv plane and all spacings beyond 12.86 m were zeroed. This removes the unnecessary high spatial frequencies and their associated noise.
- 3) A correction was made for the beam of the 25.6 m dish by dividing the uv plane maps through by a model of the aperture illumination function – a Gaussian of half-width at half-maximum of 9.02 m. This gives all spatial frequencies out to 12.86 m equal weight.
- 4) The modified uv plane maps were Fourier transformed back to the image plane and interpolated again from 128×128 to 512×512 .
- 5) All but the central $2^\circ \times 2^\circ$ was discarded yielding one hundred twenty-eight 256×256 LOS maps.

In summary steps 1) to 5) basically do three things:

a) Interpolate the LOS maps so that their pixel size matches that of the interferometer maps ($30'' \times 30''$).

b) Filter out noisy high spatial frequencies that will be replaced by the interferometer's spatial frequency measurements.

and most importantly

c) Step 3 matches the interferometer maps to the LOS maps in the uv plane.

Similarly the interferometer maps were processed before adding to the LOS maps.

1) The interferometer maps were zeroed beyond $68'$ from the centre of the maps. This was necessary because step 2), below, raises the noise at the edges and corners of the maps.

2) The interferometer maps were then corrected for the primary beam – the beam of the individual 8.6 m dishes. This was done by dividing by a cosine to the sixth power function representing the beam. Primary beam correction is necessary because emission away from the phase centre is artificially reduced by attenuation of the primary beam pattern. Correcting for this allows the interferometer maps to match the LOS maps in the uv plane.

3) The maps were Fourier transformed and zeroed inside a spacing of 12.86 m to make them compatible with the filtered LOS maps.

4) The uv plane maps were Fourier transformed back to the image plane.

5) A conversion factor of $(2k/\lambda^2) \int P d\Omega = 7.694$ was divided into the maps to convert them from units of 0.1 mJy/beam to units of 0.1 K.

The full spacings (FS) maps were then produced by adding the processed interferometer LMC maps to the processed LOS maps (converted to units of 0.1 K).

Before addition to the interferometer maps, problems were discovered with the LOS maps that were peculiar to this survey. This paragraph and the following paragraph describe corrections made to the LOS maps that are not crucial to one's understanding of the low order spacings reductions. The LOS maps were converted to galactic latitude-velocity (bv) maps at galactic longitudes (l) $154^{\circ}5$, $155^{\circ}0$, $155^{\circ}5$. These were compared with the Weaver & Williams (WW, 1974) bv maps; the agreement was poor. In order to compute the correction required for the LOS maps the WW bv maps were subtracted from the LOS bv maps and the residuals were averaged along the velocity direction. This gave baseline offsets – difference between CC LOS baseline and WW baseline – as a function of galactic latitude, b , for the three longitudes (l) $154^{\circ}5$, $155^{\circ}0$, $155^{\circ}5$. The WW baseline was taken as the “true” zero point for the corrections that followed. A baseline offset map was made by assuming a north-south (constant α) variation of baseline offsets given by the residuals computed above and by assuming a ramp-like rise towards the east. The slope of the east-west ramp was determined from the differences of the residuals divided by their spatial separation. The east-west ramp was then multiplied by the north-south variation, determined from the residuals, to produce the baseline offset map shown in Fig. 2.3. This was subtracted from the LOS maps. These were used to create new bv maps which were again compared with WW. The agreement was quite satisfactory this time.

The ramp model for the east-west baseline offset was not fully satisfactory because it allowed the baseline offset map to rise as high as 14 K towards the north-east corner. This was brought down to a more believable 10 K by multiplying an eastern strip of the file 25' wide by a linear taper, tapering west to east. Comparison with WW suggested that the offsets should be less than about 8 K. Hence the values of the LOS maps are not trustworthy (± 6 K) toward the edges, especially the north-east corner. Fortunately the objects of interest – S211, S212 – are far ($> 1^{\circ}$) from this trouble spot. The motivation for the ramp model, besides from inspection of

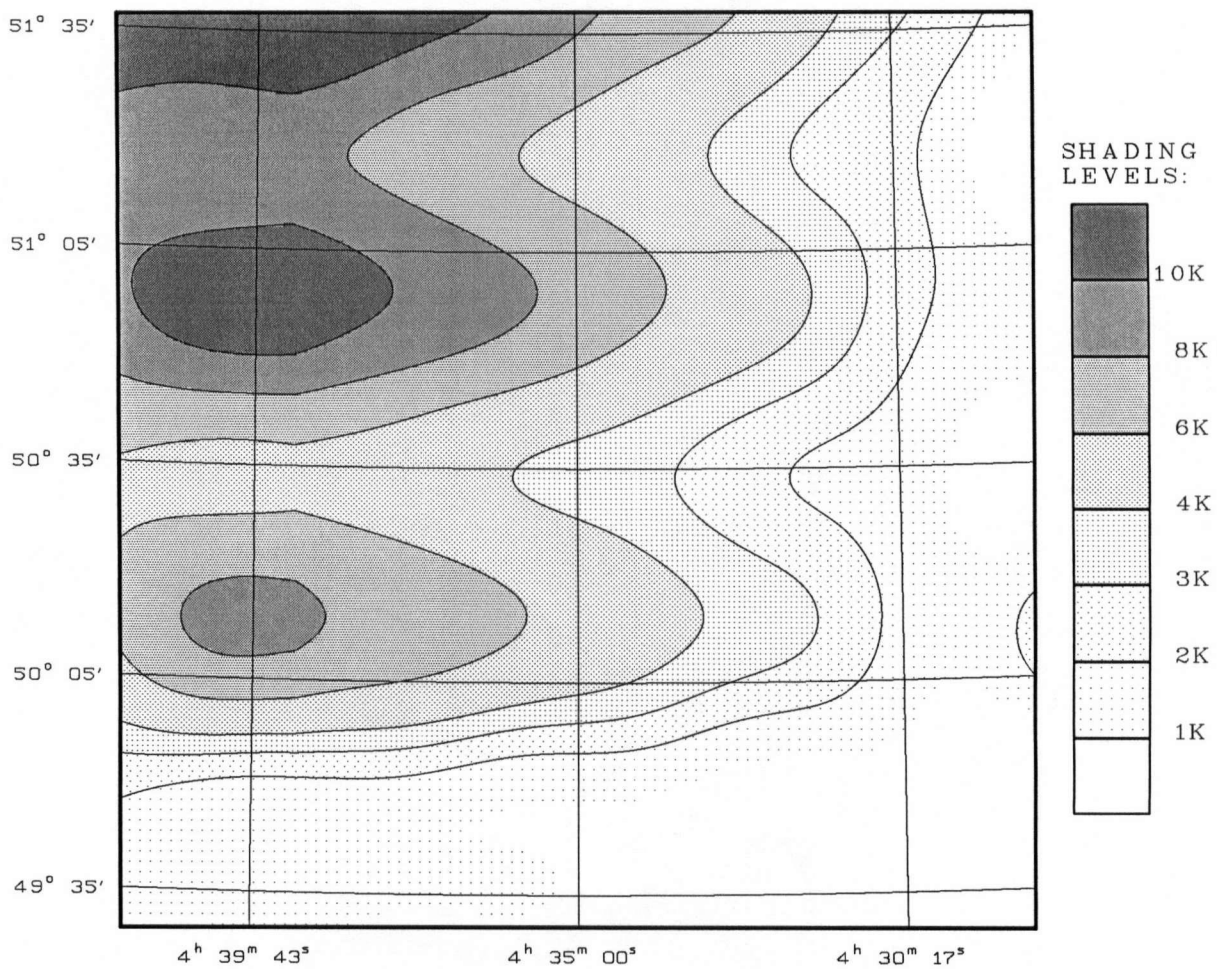


FIG. 2.3: Baseline Offset Map - The above map represents the difference between the low order spacings baseline for the CC Survey and the Weaver and Williams baseline. Notice the large values (>10K) near the north-east (upper left) corner.

the residuals, comes from assuming that the telescope’s gain varied systematically as it scanned from east to west. It is not clear why such a variation should have occurred. It is possible that the spillover, which varies with hour angle, produced this variation.

The final FS maps contain large scale structure that is not associated with S211 and S212. The obvious way to remove the unwanted large scale HI is to filter out the unwanted short spacings. But this would again result in the bowl depression in the maps. A better alternative, the one chosen, is to subtract a constant from each map where the constant for each map is the minimum value in the corresponding LOS map. This is effectively subtracting a spectrum from the maps. The resulting spectrum subtracted (SS) maps, to a first approximation, are free of large scale HI emission. The effects of this subtraction are examined in detail in Chapter 4.

The SS maps were averaged in groups of 3 consecutive channels. The 128 maps were thus “compressed” into 43 maps. The compressed SS (CSS) maps are shown in Appendix B.

2.3 CONTINUUM MAP REDUCTIONS

The relatively low noise in the continuum map (0.16 K rms) allows the appearance of beam artifacts around strong sources. The observed sky brightness is the true sky brightness convolved with the beam pattern of the telescope. If this beam has undesirable characteristics, i.e. diffraction grating rings termed “sidelobes”, it is necessary to deconvolve the map from this “dirty” beam and convolve again with a beam with no sidelobes – a “clean” beam. This process is called “cleaning a map”. Because the CC Survey was complete with all spacings from about 13 m to 605 m any beam artifacts would be weak and would only show up around strong sources in a low noise map. This is one reason why the continuum map was cleaned and why it was not necessary to clean the LMC maps (rms noise > 12 K).

Another reason is that strong continuum sources were subtracted in order to make the LMC maps. The clean beam chosen was an elliptical Gaussian with HPBW's of $0'.99 \times 1'.24$ ($\alpha \times \delta$).

Incidentally, strong continuum sources near, but outside, the 2° field can also produce artifacts inside the 2° field. This is why the original continuum map is a 4° square even though only the inner 2° is used in further analysis; it is necessary to clean the full $4^\circ \times 4^\circ$ to ensure that the important central $2^\circ \times 2^\circ$ is clean. Because the LMC maps are not cleaned it is not necessary to produce $4^\circ \times 4^\circ$ line maps.

Low order spacings added to the continuum map were taken from the Effelsberg 1420 MHz Survey (Kallas and Reich, 1980) which covered galactic latitudes $|b| < 4^\circ$ and longitudes $93^\circ \leq l \leq 162^\circ$. The $4^\circ \times 4^\circ$ square corresponding to the field of the CC continuum map extends beyond the Effelsberg survey northern limit. Consequently the north-east corner of the LOS continuum map, shown in Fig. 2.4, is unsampled. Fortunately only a small section of north-east corner of the important central $2^\circ \times 2^\circ$ is affected. Inspection of the Kennedy, 1975 survey indicates that there is little variation in intensity in this region. Hence an average along the north-eastern edge of the LOS map was placed in the unsampled area.

It was necessary to use the full $4^\circ \times 4^\circ$ CC continuum map because, in the filtering described below, the FFT was employed which introduces edge artifacts; the central $2^\circ \times 2^\circ$ remains unaffected. (The LMC maps, however, have low signal to noise so that edge effects are not important; only 2° maps were necessary for the filtering described in Section 2.2.2.)

The LOS map was processed in the following way:

- 1) It was Fourier transformed to the uv plane and divided by the aperture illumination function of the Effelsberg antenna (Gaussian of full-width at half maximum equal to 32.06 m) to equalize weights of the different spatial frequencies.

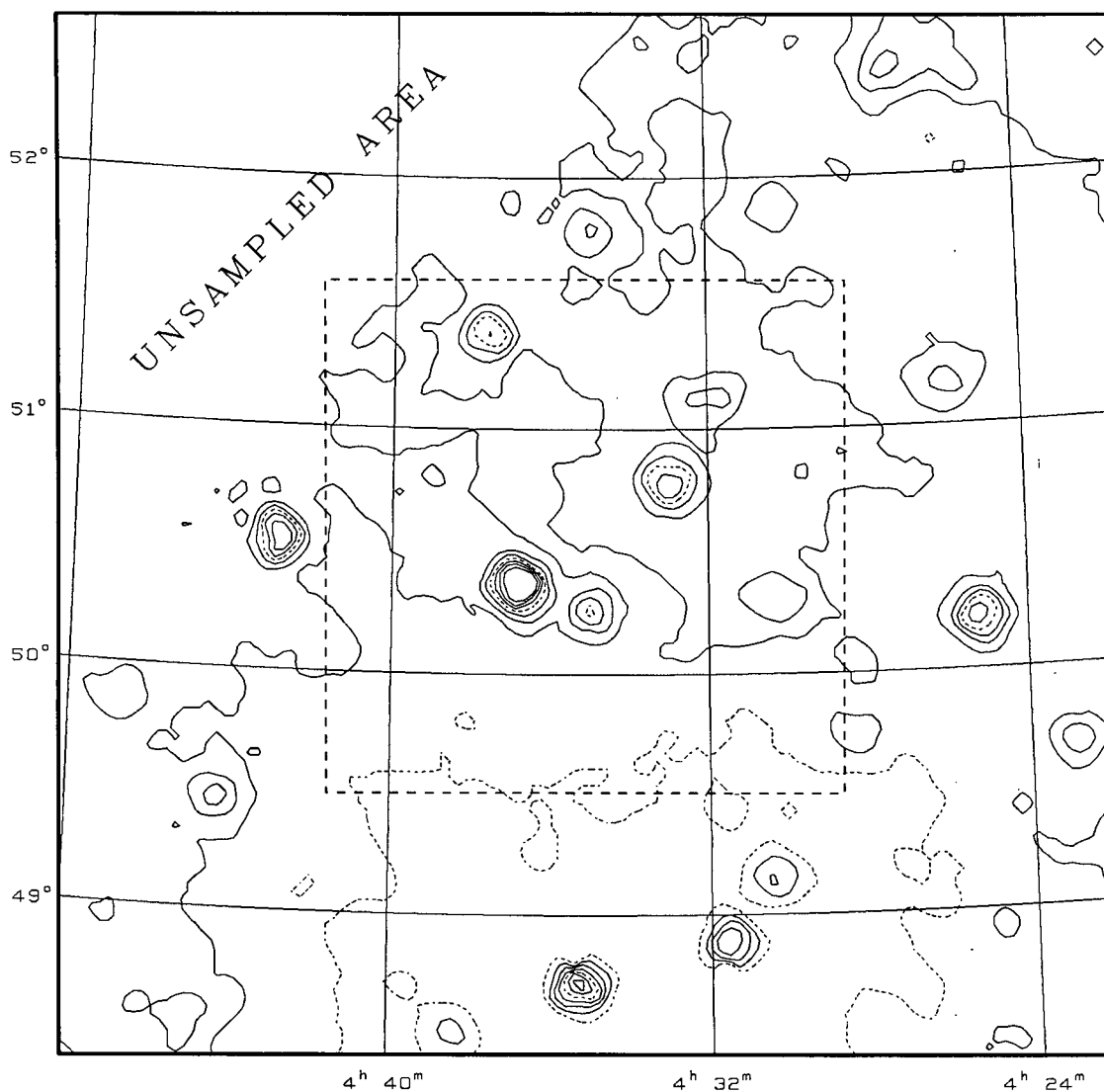


FIG. 2.4: Low Order Spacings Continuum Map - The above map is from the Effelsburg Survey (Kallas and Reich, 1980). The north-east corner is outside the Effelsburg Survey area. The CC Survey map area is indicated by the square in dashed lines. Contours are in brightness temperature steps of 2.5K, starting at 2.5K and ending at 20.0K.

- 2) All spacings beyond 21.4 m were zeroed and spacings of 8.6 m to 21.4 m were tapered from full weighting at 8.6 m to zero weighting at 21.4 m.
- 3) The filtered map was Fourier transformed back to the image plane.

Similarly the interferometer continuum map was filtered thus:

- 1) Divided by primary beam pattern and Fourier transformed map to uv plane.
- 2) All spacings inside 8.6 m were set to zero and spacings 8.6 m to 21.4 m were tapered from zero weighting at 8.6 m to full weighting at 21.4 m. This tapering, called “feathering”, was necessary for the continuum map because artifacts would result if a sharp cutoff were used. (Feathering was not necessary for the LMC maps again due to their low signal-to-noise.)
- 3) The filtered map was Fourier transformed back to the image plane.

The two maps were then added together, rotated by $16''.11$ and expanded by $6''.0$ per degree from the phase centre. The final FS continuum map is shown in Appendix A.

The rotation was necessary because the interference fringes did not correspond to the north pole of 1950.0. Even though the CC field was precessed to 1950.0 coordinates an additional rotation was required to compensate for the “misalignment” of the fringes. The expansion was applied because the apparent distance of an object from the survey phase centre can be different from its actual distance. This occurs if the mean frequency (where $\nu_{mean} = \int_{-\infty}^{+\infty} \nu b(\nu) d\nu$ where $b(\nu)$ is the normalized bandshape) of the observing band does not occur at the middle of the band. Both the rotation and expansion had a minimal effect on the map. Hence applying such a treatment to low signal-to-noise data, i.e. the FS LMC maps, is unnecessary. Also, the LMC maps have no point sources to make the correction worthwhile.

Fluxes of 51 different continuum sources were measured using the routine FLUXFIT. A box is placed around each of the sources and a baselevel in the form

of a twisted plane (function of the form $z = ax + by + cxy + d$) is fitted to the corners or to the edges. The baselevel is subtracted and, depending on the source angular size, one or more Gaussians are fitted to the data in the box. Two fluxes are provided: an integrated flux and a total flux contained within the fitted Gaussians. The former is the total flux above the baselevel, and within the box, whereas the latter is the total flux that would occur if the sources perfectly matched the fitted Gaussians.

Particular attention was paid to S211 and S212 whose fluxes were measured many times each; trying different box sizes and, in the case of S212, fitting two Gaussians as well as one. The noise level was estimated from rms fluctuations about the fitted baselevel along the edges of the box. The noise level should be about 0.8 mJy/beam for a DRAO synthesis telescope continuum map (see Table 2.1) and this is close to the noise level in an empty part of the map found to be 1.2 mJy/beam. Some boxes had rms levels much higher than this indicating that the box was either too small, so that it was cutting through the source itself, or too large, thereby overlapping other sources. Hence two criteria were used in determining whether to accept the flux measurements associated with a given box:

- a) The estimated box noise level must be less than about two or three times the expected value of 0.8 mJy/beam.
- b) The integrated flux must be within 2 or 3% of the total flux in Gaussians.

The following fluxes were adopted for S211 and S212:

$$0.79 \pm 0.04 \text{ Jy for S211}$$

$$1.60 \pm 0.12 \text{ Jy for S212}$$

Each of the above fluxes is a mean of the total flux in Gaussians associated with those boxes (six for S211 and five for S212) that obeyed criteria a) and b). The errors are due to a combination of calibration uncertainties ($\pm 5\%$) and errors computed in the Gaussian fitting process ($\pm 1\%$ to 6%). These are larger than the standard deviations of the averaged fluxes.

3 CONTINUUM EMISSION OF S211, S212

3.1 THEORY

The continuum emission of the HII regions is thermal bremsstrahlung radiation. This is the radiation of free electrons as they are accelerated by positive ions. The energy of each emitted photon is dependent on the impact parameter and original velocity of the electron. Since the electrons possess a continuous velocity distribution the spectrum produced by this process is also continuous. The velocity distribution is Maxwellian, hence the process is a thermal mechanism. The emissivity (in units of $erg \cdot s^{-1} \cdot cm^{-3} \cdot ster^{-1} \cdot Hz^{-1}$) is given by (Spitzer, 1978)

$$j_\nu = \frac{8}{3} \sqrt{\frac{2\pi}{3}} \left(\frac{Z_i^2 e^6}{m_e^{3/2} c^3 (kT_e)^{1/2}} \right) g_{ff} n_e n_i \exp\left(-\frac{h\nu}{kT_e}\right) \quad 3.1$$

where m_e , e are the mass and charge of the electron in cgs units, $Z_i e$ the charge on the positive ions, T_e the kinetic temperature of the electrons, and where n_e , n_i are the number densities of electrons and ions respectively. The g_{ff} is called the gaunt factor. It is unitless and is given by

$$g_{ff} = \frac{\sqrt{3}}{\pi} \left[\ln \left(\frac{(2kT_e)^{3/2}}{\pi e^2 \nu m_e^{1/2}} \right) - \frac{5\gamma}{2} \right] \quad 3.2$$

where γ is Euler's constant and is equal to 0.577. The gaunt factor is the quantum mechanical correction which is necessary because it is more appropriate to consider the electron as being a wave packet scattering from a central potential than as a particle being deflected by its interaction with another particle (Oster, 1961). Applying Kirchoff's law to 3.1) and integrating along the line of sight gives, after fitting powers to g_{ff} 's weak T_e and ν dependence (Osterbrock, 1974), the unitless quantity known as optical depth, i.e.

$$\tau_\nu = 8.24 \times 10^{-2} T_e^{-1.35} E \nu^{-2.1} \quad 3.3$$

where ν is in GHz and E is the emission measure (electron density squared integrated along the line of sight) in $cm^{-6} \cdot pc$. The intensity of radiation (units= $erg \cdot s^{-1} \cdot cm^{-2} \cdot ster^{-2} \cdot Hz^{-1}$) is given by the equation of radiative transfer;

$$I_{\nu}(\tau_{\nu}) = I_{\nu}(\tau_{\nu} = 0) \exp(-\tau_{\nu}) + B_{\nu}(T_e)(1 - \exp(-\tau_{\nu})) \quad 3.4)$$

where $I(\tau_{\nu} = 0)$ is the the intensity of some background source and where $B_{\nu}(T)$ is the Planck function. In the absence of a background source and in the optically thin approximation, i.e. $\tau_{\nu} \ll 1$, equation 3.4) becomes

$$I_{\nu}(\tau_{\nu}) = B_{\nu}(T_e) \tau_{\nu} \quad 3.5).$$

As will be seen later, the optically thin approximation holds for both S211 and S212 at 1420 MHz. Integrating equation 3.5) over the solid angle subtended by the source and assuming constant T_e throughout gives the flux density (units= Jy)

$$S_{\nu} = B_{\nu}(T_e) \int_{\text{source}} d\Omega \tau_{\nu} \quad 3.6).$$

Substituting 3.3) for τ_{ν} and abbreviating the factors multiplying E by α gives

$$S_{\nu} = (\alpha B_{\nu}/D^2) \int_{\text{source}} D^2 d\Omega E$$

where D = distance to the source. The integral represents the volume emission measure so that

$$S_{\nu} = \left(\frac{\alpha B_{\nu}}{D^2} \right) E_{\text{vol}} \quad 3.7).$$

The above will be used to test models of S211 and S212.

Now define a quantity called brightness temperature, T_b , given by

$$I_{\nu} = \frac{2kT_b}{\lambda^2} \quad 3.8).$$

In the Rayleigh-Jeans limit ($h\nu/kT_e \ll 1$)

$$B_\nu = \frac{2kT_e}{\lambda^2} \quad (3.9).$$

Thus 3.8) and 3.9) change 3.5) to

$$T_b = T_e \tau_\nu \quad (3.10)$$

or

$$T_b = 8.24 \times 10^{-2} \nu^{-2.1} T_e^{-0.35} E \quad (3.11).$$

Hence emission measure is proportional to brightness temperature in the optically thin case.

The emission measure profile for an HII region is dependent on its number density of electrons and on its radius. These in turn depend on the total Lyman continuum photon flow, $N_u(0)$ (units= *photons* · *s*⁻¹), from the central star(s). Specifically, Spitzer (1978) gives

$$\frac{dN_u(r)}{dr} = -4\pi r^2 n_e^2 \alpha_B \quad (3.12)$$

where $N_u(r)$ is the Lyman continuum photon flow through a sphere of radius r centred on the star and where α_B is the case B recombination coefficient for hydrogen. The radius, r_s , of the HII region is then given by integrating 3.12) from $r=0$ to $r=r_s$ and setting $N_u(r_s)$ equal to zero;

i.e.
$$N_u(0) = \frac{4\pi r_s^3}{3} n_e^2 \alpha_B \quad (3.13).$$

Equations 3.12) and 3.13) depict an idealized HII region consisting only of pure, totally ionized hydrogen of uniform density. One complication in the above picture is the presence of dust in HII regions. This produces a situation that cannot be solved analytically. The problem can be simplified however if one assumes that the

opacity of the dust, K_d , is constant throughout the Lyman continuum. In this case 3.12) becomes

$$\text{i.e.} \quad \frac{dN_u(r)}{dr} = -4\pi r^2 n_e^2 \alpha_B - K_d N_u(r) \quad 3.14)$$

Equation 3.14) cannot be solved analytically for the radius r_s , especially if n_e varies with r , but it can be solved numerically. This is discussed in Section 3.3.

3.2 DISTANCES

Before modelling could proceed it was necessary to adopt realistic values for the distances of S211 and S212. The distance of S212 was given as 4.4 kpc by Talent & Dufour (1979). This seems to have been determined from the Schmidt Model of galactic rotation ($R_\odot = 10$ kpc, $V_\odot = 250$ km · s⁻¹) using the radial velocity, -36.4 km · s⁻¹, obtained from Georgelin & Georgelin (1970). Talent & Dufour's distance was not used for this work because it was not based on more reliable methods of spectral analysis of the exciting stars. Chini & Wink (1984), on the other hand, derived distances for S212 and S211 using the method of spectroscopic parallax. They determined the ionizing stars of S212 to be O6I and B1III with a distance of 10.3 kpc. Moffat et. al. (1979) determined the corresponding stars to be an O5.5 or O6 (no luminosity class obtained) and a B0V. Fitzgerald (1985, priv. comm.) did zero age main sequence (ZAMS) fitting of the 14 stars of S212 observed by Moffat, Fitzgerald and Jackson (1979). He derived a distance of 4.7 to 5.9 kpc and consequently asserts that the O6 star cannot be a supergiant (i.e. luminosity class I). A distance of 6 kpc was adopted for S212 because this is more consistent with those distance moduli given in Moffat et. al. Six kpc is also the distance chosen by Moffat et. al. who used ZAMS fitting as well. In the absence of other information, Chini's & Wink's distance, 7.8 kpc, was adopted for S211.

Since the distance of S212 could be as little as 4.7 kpc an error of 20% was assigned to the distance. The different distance moduli for the stars of S211 (Chini

& Wink, 1984) suggest distances from 7.2 kpc up to 8.2 kpc. Hence one could assign an error of about 10% to the distance of S211, but it is probably not unrealistic to suppose that other sources of error exist and so an error of 20% will also be used for the distance of S211.

3.3 MODELLING

S211 and S212 are not strongly resolved sources. S211 has a FWHM of 1'8 or 1.6 beam widths and for S212 these are 3'0 or 2.6 beam widths. Consequently only simple models were fitted to each. S211 has a uniform density model and S212 was modelled with linear density gradients (see Table 3.1 and Table 3.2, page 37).

The program HIIBLOB3, documented in Appendix C, generated the models. HIIBLOB3 works in the $z = 0$, $x \geq 0$ half-plane with the exciting star at $x = 0$, $y = 0$ and the observer at $y = +\infty$. The user specifies the number of Lyman continuum photons per second, the number density of electrons at the origin, the density gradient in the x direction, the dust opacity (i.e. K_d in equation 3.14) and the integration step size. The program numerically integrates 3.14) in steps along rays radiating from the origin ($\theta = \text{constant}$). Each time a step is taken the new density, due to the gradient, is computed and two decrements are made to the photon flux: one for the bound-free absorption due to HI and one for absorption by dust. The dust opacity used in all modelling was $3 \times 10^{-21} \text{ pc}^{-1}$. This is based on a ratio $\langle N(\text{HI})/E(B - V) \rangle = 5 \times 10^{21} \text{ cm}^{-2} \cdot \text{mag}^{-1}$ (Savage and Mathis, 1979) and an extinction of $A_{912\text{\AA}} = 15 \times E(B - V)$. The integration continues until no photons are left. The radius at which this occurs is stored as a function of θ . Since 3.12) applies to spherically symmetric HII regions the radius above is the radius, r_s , of a spherically symmetric HII region with the same radial density gradient as the density gradient existing on the ray $\theta = \text{constant}$. The integration procedure is repeated for values of θ from $-\pi/2$ to $\pi/2$; each giving a different r_s ; each corresponding to a spherically symmetric HII region with a radial density gradient equal to the

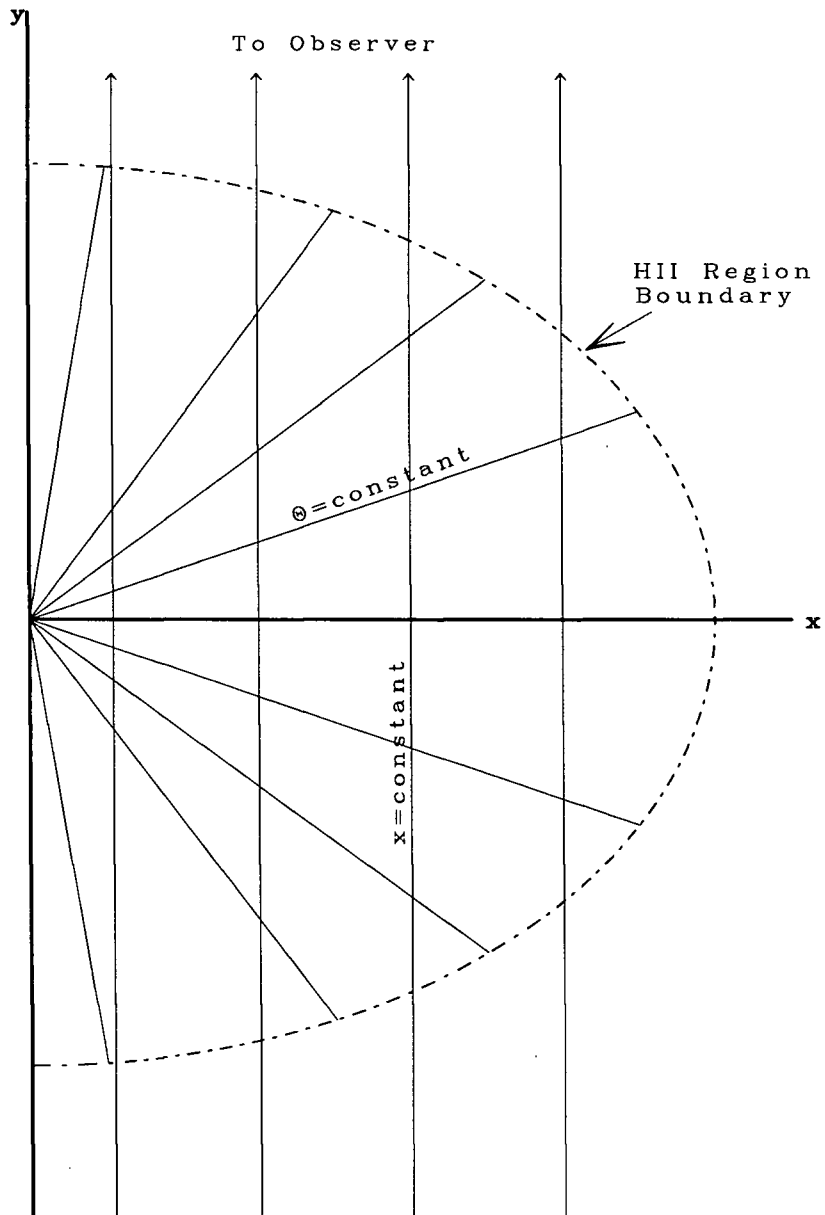


FIG. 3.1: Schematic Representation of HIIBLOB3
 The program HIIBLOB3 integrates out from the origin along rays of constant θ in order to establish the HII region boundary in the $x > 0$ half-plane. HIIBLOB3 then finds the emission measure along lines of constant x .

gradient found along the corresponding θ -ray. In this way the boundary of the HII region is established as illustrated in Fig. 3.1. It should be noted that using an equation based on spherical symmetry to model an aspherical region undoubtedly introduces some errors into the position of the HII-HI boundary. Nevertheless, this method still serves as a good first approximation in determining the boundary.

Now that the ionization boundary is established the emission measure is computed as a function of x . The length of the segment of a line of constant x , that lies within the HII boundary, is determined for discrete values of x from $x = 0$ to the maximum x of the nebula. Each length is multiplied by the square of the density which is constant along the line since it depends only on x . The resulting emission measure profile represents an intensity distribution from the centre of an HII region along a single direction.

In order to represent a “full slice”, from $-r_s$ to $+r_s$, through the HII region the program is run twice, only altering the density gradient for the second run (if necessary). The order of one of the outputs is reversed and concatenated to the other output. The “full slice” is convolved with a Gaussian representing the synthesized beam of the interferometer. The final convolved emission measure profile is ready for comparison with the data.

One important point that must be addressed is the one dimensional nature of the convolution. A more accurate treatment of the problem would be to generate a two dimensional emission measure map, convolve with an elliptical Gaussian beam and then take the desired slice. The procedure followed with HIIBLOB3 resembles first taking a slice of the unconvolved emission measure map and then convolving with a slice of the beam. The two approaches are *not* equivalent. In the former treatment any given slice of the unconvolved map is affected, during the convolution, by values away from that slice. Since the effort in creating a program that could generate such a two dimensional map is disproportionate to the spatial information

available on S211 and S212 the one dimensional convolution must suffice.

It is possible however to multiply the convolved profile by a kind of compensating function which is meant to correct for the absence of convolution in the other dimension. To do this it is necessary to make assumptions about the intensity distribution of the unconvolved source. Assume that, to first approximation, the source has a Gaussian distribution. The compensating function (see Appendix D) for an east-west slice is then θ_y/θ_b where θ_y is the 1/e half-width of the unconvolved source in the north-south direction,

$$\theta_b^2 = \theta_y^2 + b^2 \quad 3.15)$$

and b is the 1/e half-width of the synthesized beam in the north-south direction. Similarly the compensating function for a north-south slice is θ_x/θ_a where θ_x is the east-west analog of θ_y . θ_a is defined by

$$\theta_a^2 = \theta_x^2 + a^2 \quad 3.16)$$

with a as the east-west analog of b . Hence for a Gaussian source the compensating function is merely a constant factor. In the absence of other information it is simplest to assume that the unconvolved source is Gaussian in order that one may apply the compensating functions given above.

Because S211 is barely resolved the parameters of any model that would attempt to explain differences between slices in different directions would be highly uncertain. Thus the map of S211 was averaged in 360° rings and emission measure was plotted as a function of radius. This represents a kind of average slice; i.e. an average of slices in all directions (Fig. 3.2a). North-south and east-west slices were taken of S212 since it is more resolved (Fig. 3.2b).

The conversion of the brightness temperature profiles to emission measure profiles was done according to 3.11). The electron temperatures, T_e , chosen for the

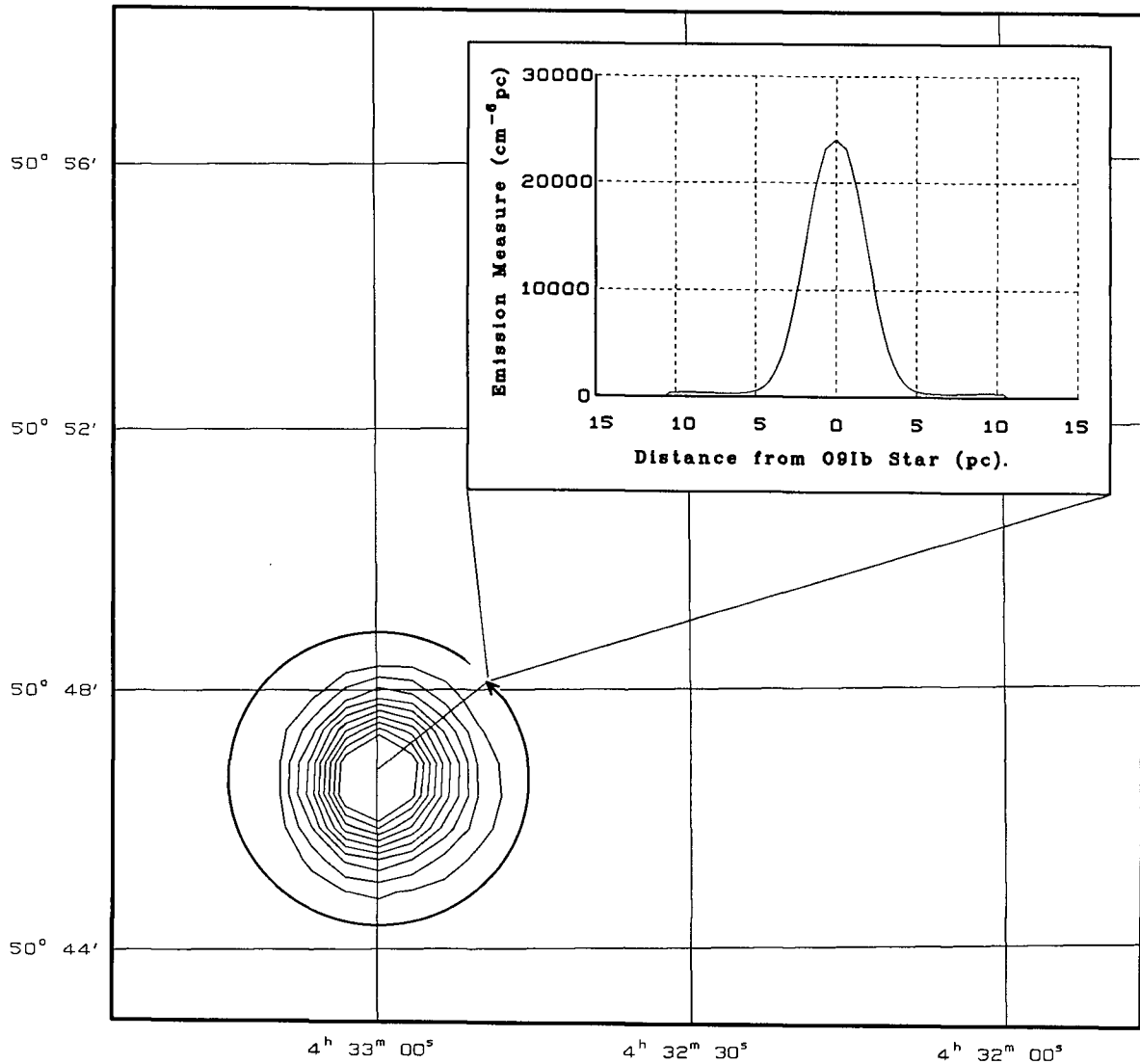


FIG. 3.2a: S211 Emission Measure Profile - The map of S211 was averaged over 360° to get the emission measure profile shown at upper right.

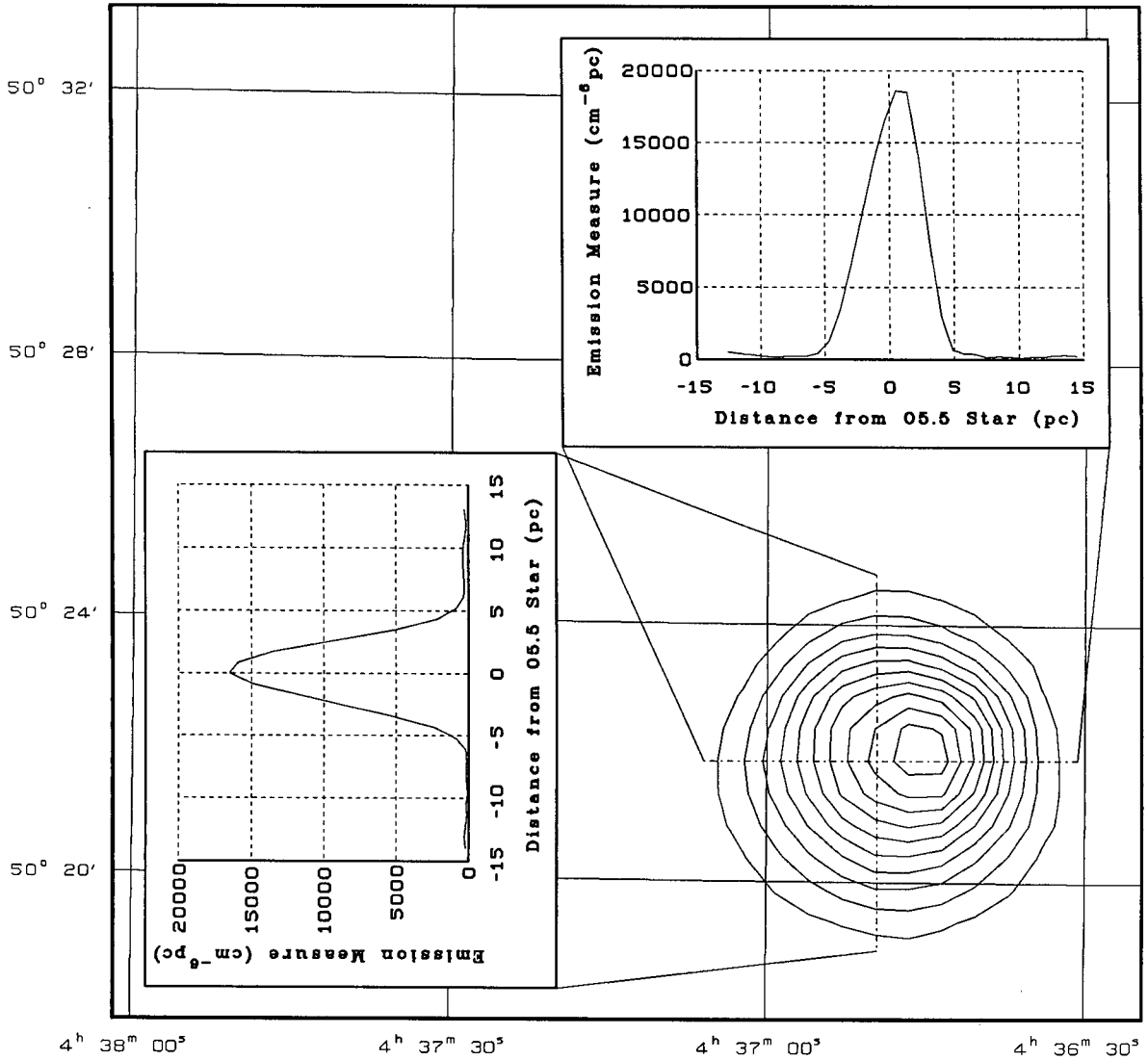


FIG. 3.2b: S212 Emission Measure Profiles - The map of S212 was "sliced" in the north-south and east-west directions giving the emission measure profiles in the lower left and upper right corners respectively.

conversion factors were 7000 K for S211 and 8000 K for S212. These are based on Chini's & Wink's (1985, priv. comm.) observations of the H112 α recombination line; i.e.

$$6850 \pm 950 \text{ K for S211}$$

$$8180 \pm 420 \text{ K for S212.}$$

Talent & Dufour (1979) obtained $T_e = 10800 \pm 1400 \text{ K}$ for S212. Chini's & Wink's temperature was chosen because Talent's & Dufour's method selects for high density regions within S212. This is discussed further in Section 3.4. It should be noted from 3.11) that the relationship between the brightness temperature, T_b , and the emission measure, E , is obviously insensitive as to whether the T_e chosen is 8000 K or 11000 K. For S211 the conversion factor is $1.78 \times 10^{-3} \text{ cm}^6 \cdot \text{pc}^{-1} \cdot \text{K}$ and for S212 this is $1.70 \times 10^{-3} \text{ cm}^6 \cdot \text{pc}^{-1} \cdot \text{K}$.

It should be noted that the peak brightness temperature observed for S211 is 42 K and for S212 the peak is 28 K. When comparing these with $T_e = 7000 \text{ K}$ and 8000 K it is easy to see that S211 and S212 are indeed optically thin at 1420 MHz. The use of equations 3.5) through 3.11) in association with S211 and S212 is then justified.

The beam has 1/e half-widths of

$$\left. \begin{array}{l} a = 0'60 \\ b = 0'78 \end{array} \right\} \text{ or } \left. \begin{array}{l} a = 1.36 \text{ pc} \\ b = 1.77 \text{ pc} \end{array} \right\} \text{ at } 7.8 \text{ kpc} \quad \left. \begin{array}{l} a = 1.05 \text{ pc} \\ b = 1.35 \text{ pc} \end{array} \right\} \text{ at } 6 \text{ kpc}$$

Measuring the direction averaged profile of S211 implies

$$\theta_x / \theta_a = 0.78$$

The profiles of S212 imply compensating functions of

$$\begin{aligned} \theta_y/\theta_b &= 0.91 && \text{for east-west convolution and} \\ \theta_x/\theta_a &= 0.94 && \text{for north-south convolution.} \end{aligned}$$

The above compensating functions were used to derive the model curves shown in Fig. 3.3a and Fig. 3.3b with parameters given in Tables 3.1 and 3.2. The average radius, r_{AV} , was computed by taking it to be the radius of a semicircle of area equal to the sum of the areas associated with the line segments ($x = \text{constant}$) used in HIIBLOB3 where each “line segment area” is defined as the product of the length of the segment and the distance separating two adjacent segments. The average density, n_{eAV} , was derived from the sum of the column densities found in HIIBLOB3 divided by the sum of the lengths of the line segments. The masses were derived from

$$M_{\text{HII}} = \frac{2\pi}{3} (n_{eAV1} r_{AV1}^3 + n_{eAV2} r_{AV2}^3) m_{\text{H}} \left(\frac{M_{\odot}}{1.989 \times 10^{33} \text{ g}} \right) \quad 3.17$$

where subscripts 1 and 2 refer to the two sides of each model profile and $m_{\text{H}} = 1.66 \times 10^{-24} \text{ g}$ is the mass of the hydrogen atom. The flux density was determined from 3.7) where the volume emission measure was given by

$$E_{\text{vol}} = \frac{2\pi}{3} (n_{eAV1}^2 r_{AV1}^3 + n_{eAV2}^2 r_{AV2}^3) \quad 3.18$$

and

$$\begin{aligned} B_{\nu}(T_e) &= \frac{2kT_e}{\lambda^2} = 4.38 \times 10^8 \text{ Jy} \cdot \text{ster}^{-1} && \text{for S211} \\ &= 5.01 \times 10^8 \text{ Jy} \cdot \text{ster}^{-1} && \text{for S212.} \end{aligned} \quad 3.19$$

The model flux densities agree well with the measured flux densities of S211 and S212, 0.79 Jy for S211 and 1.60 Jy for S212.

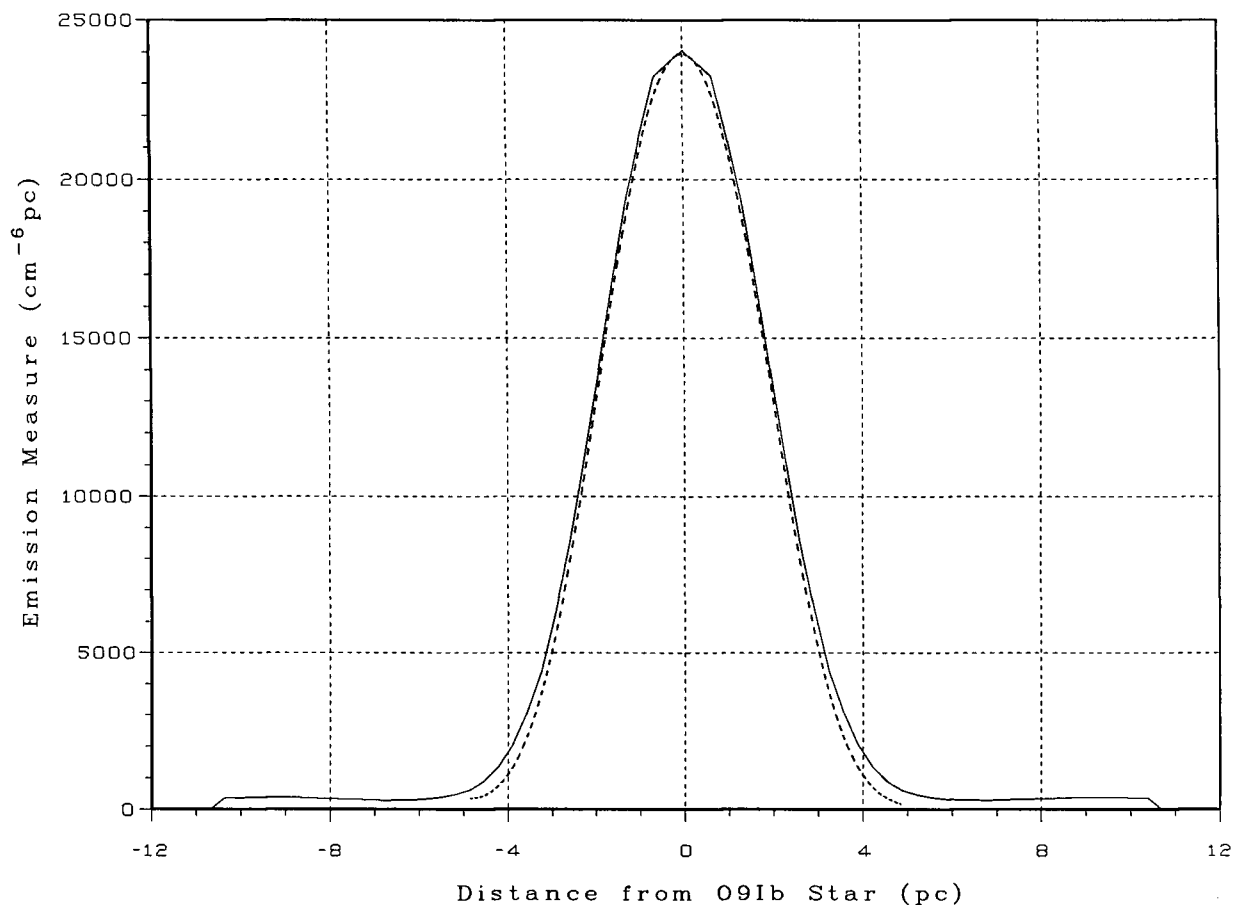


FIG. 3.3a: S211 Emission Measure Profile (solid line) is compared with the theoretical profile (dashed line) generated by HIIBLOB3. Assuming a constant electron temperature throughout S211 the uncertainty in the observed emission measure is about 5% due to a 14% uncertainty in the electron temperature (Chini and Wink, 1985 priv. comm.). The uncertainty remains above $\pm 100 \text{ cm}^{-6} \text{ pc}$ due to noise in the original continuum map.

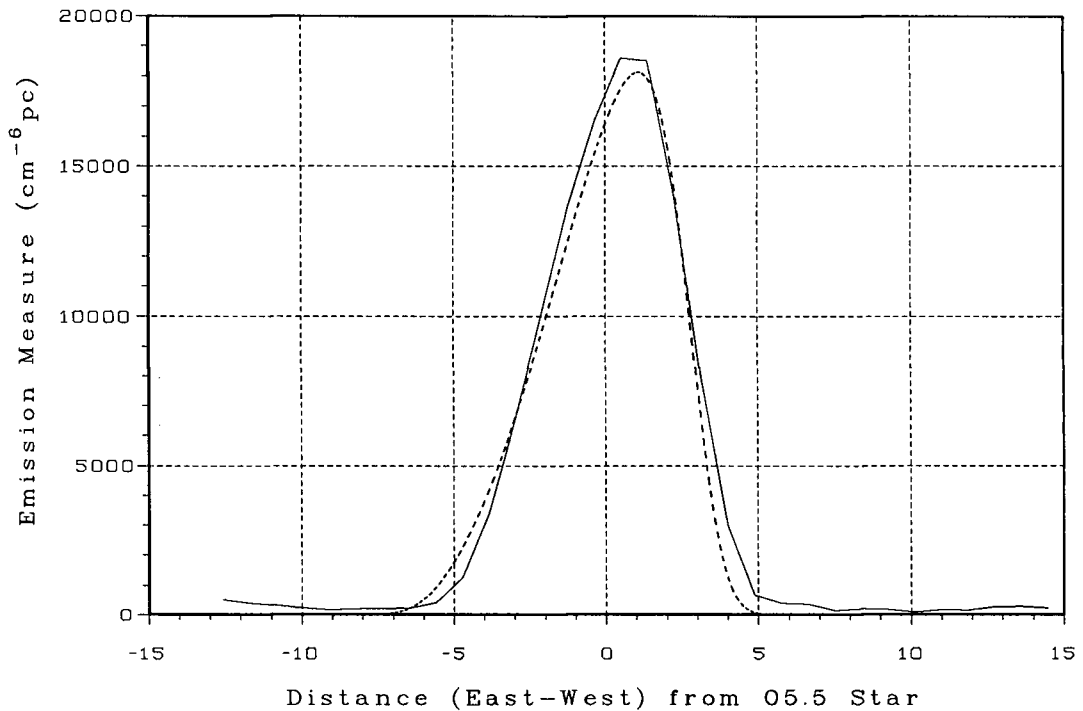
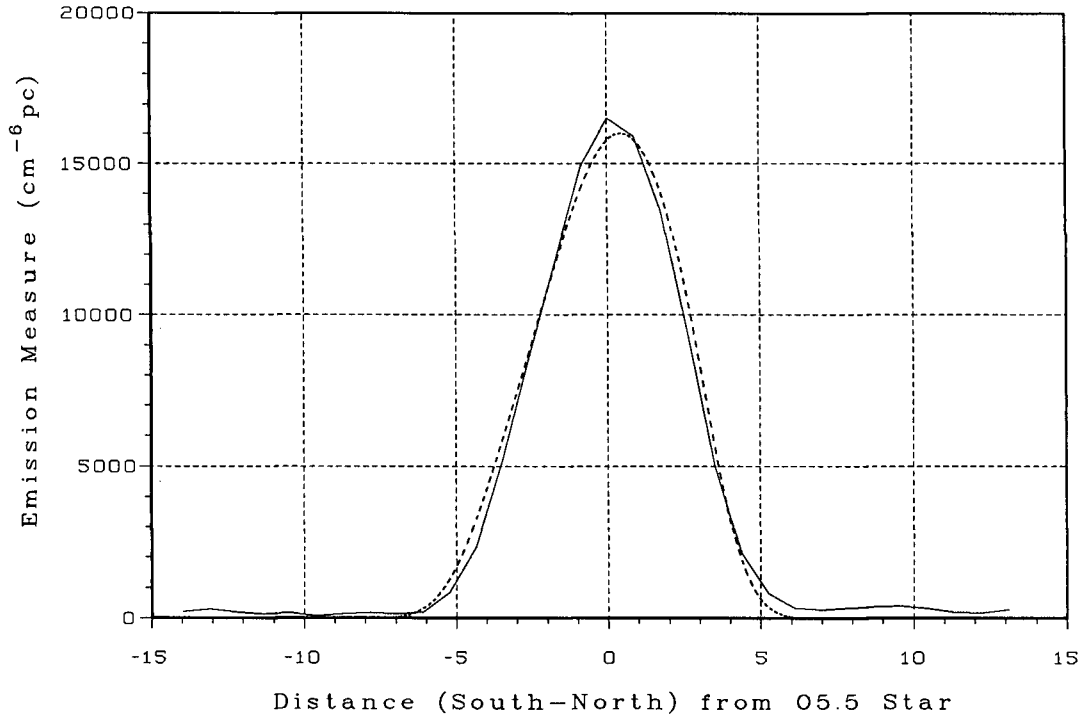


FIG. 3.3b: S212 Emission Measure Profiles (solid lines) are compared with the theoretical profiles (dashed lines) generated by HIIBLOB3. The north-south profile is at the top and the east-west profile is just below that. The emission measure uncertainty is the same as in Fig. 3.3a.

TABLE 3.1: S211 MODEL PARAMETERS
($T_e = 7000$ K)

	Model from the Average slice
Flux of Ionizing Photons	$1.8 \times 10^{49} \text{ s}^{-1}$
Central Density	85 cm^{-3}
Average Radius	2.4 pc
Projected Radius	2.4 pc
Mass	$126 M_\odot$
including He	$200 M_\odot$
Flux Density	0.80 Jy

TABLE 3.2: S212 MODEL PARAMETERS
($T_e = 8000$ K)

	Model from	
	NS slice	EW slice
Flux of Ionizing Photons	$1.9 \times 10^{49} \text{ s}^{-1}$	$1.9 \times 10^{49} \text{ s}^{-1}$
Central Density	50 cm^{-3}	50 cm^{-3}
Gradient	$0 \text{ cm}^{-3} \cdot \text{pc}^{-1}$ (North) $-5 \text{ cm}^{-3} \cdot \text{pc}^{-1}$ (South)	$-6 \text{ cm}^{-3} \cdot \text{pc}^{-1}$ (East) $+6 \text{ cm}^{-3} \cdot \text{pc}^{-1}$ (West)
Average Radius	3.7 pc (North) 4.5 pc (South)	4.9 pc (East) 3.3 pc (West)
Projected Radius	3.7 pc (North) 5.0 pc (South)	6.1 pc (East) 3.1 pc (West)
Mass	$306 M_\odot$	$311 M_\odot$
including He	$450 M_\odot$	$450 M_\odot$
Flux Density	1.61 Jy	1.60 Jy

The deviation of the fits from the data (see Figures 3.3a and 3.3b) is due to the oversimplified density variation chosen for the model. The density in a real HII region does not vary in a simple linear fashion, although this is probably not a bad first approximation. Another probable source of deviation is the approach to the one dimensional convolution. The compensating functions assumed that the unconvolved sources were Gaussian. But, in order to have complete consistency with the models chosen, the compensating functions should have been found for a source of linear density variation. This was not done for two reasons:

- 1) Lack of spatial resolution obtained for the sources made it justifiable to use a simple compensating function rather than applying the effort required in deriving the more appropriate compensating function because
- 2) it cannot be done analytically.

It is desirable to have an estimate of the uncertainties of the parameters of the models. The uncertainty in the distance is undoubtedly the largest source of error. Thus it is necessary to see how the parameters vary with distance, D . The emission measure, E , is independent of distance and is related to the distance through the nebula $d(x, y)$ at any point x, y by

$$d(x, y) = E(x, y)n_e^{-2}(x, y) \quad 3.20).$$

If we assume some simple three dimensional geometry of the nebula then $d \propto D$ and 3.20) becomes

$$n_e \propto D^{-\frac{1}{2}} \quad 3.21).$$

To obtain such a relationship for $N_u(0)$ assume a simple constant density HII region; i.e. use 3.13) and use $r_s \propto D$ to obtain

$$N_u \propto D^2 \quad 3.22).$$

The variation of density gradient is given by

$$\frac{dn_e}{dx} \propto D^{\frac{3}{2}} \quad 3.23)$$

where x is the x of HIIBLOB3 (i.e. projected distance from the centre) and is proportional to D . For the dependence of M_{HII} on D use 3.17) and $r_{\text{AV}} \propto D$ to obtain

$$M_{\text{HII}} \propto D^{\frac{5}{2}} \quad 3.24).$$

The flux densities of the models is independent of D as is apparent from the development of 3.7). Relationships 3.21), 3.22), 3.23), 3.24) are of the form

$$f(D) = k_0 D^n$$

where k_0 is some proportionality constant. The relative uncertainty is given by

$$\frac{\Delta f}{f} = |n| \frac{\Delta D}{D} \quad 3.25).$$

Since $\frac{\Delta D}{D}$ was estimated to be 20% in Section 3.2 the following relative uncertainties result:

$$\begin{aligned} \frac{\Delta n_e}{n_e} &= 10\% & \frac{\Delta N_u(0)}{N_u(0)} &= 40\% \\ \frac{\Delta\left(\frac{dn_e}{dx}\right)}{\left(\frac{dn_e}{dx}\right)} &= 30\% & \frac{\Delta r_{\text{AV}}}{r_{\text{AV}}} &= 20\% \\ \frac{\Delta M_{\text{HII}}}{M_{\text{HII}}} &= 50\% . \end{aligned}$$

The error in the density gradient given above is probably optimistic for values less than $10 \text{ cm}^{-3} \cdot \text{pc}^{-1}$. Uncertainties associated with the non-uniqueness of the model chosen indicate that this error should be at least $\pm 3 \text{ cm}^{-3} \cdot \text{pc}^{-1}$. If there is a systematic temperature variation through either HII region then the conversion

factor from brightness temperature to emission measure is a function of x . In this eventuality the uncertainty in the density gradient is much greater than the above analysis implies.

3.4 IMPLICATIONS OF THE MODELS

Talent & Dufour (1979) measured the electron densities of S212 from the $I(^2D_{3/2} \rightarrow ^4S_{3/2})/I(^2D_{5/2} \rightarrow ^4S_{3/2})$ ratio of SII. They obtain values of 1900 cm^{-3} at the centre of S212 (position 1 in Fig. 3.4) and 300 cm^{-3} on the eastern side (position 2 in Fig. 3.4). This is in stark contrast to the corresponding values of 50 cm^{-3} and 15 cm^{-3} from the radio model. The discrepancy is probably due to the high degree of clumping in S212. Line ratios give root mean square densities which are sensitive to high density regions along the line of sight. The degree of clumping can be estimated by assuming that the density between clumps is negligible (Spitzer, 1978); i.e.

$$F = \frac{\langle n_e \rangle^2}{\langle n_e^2 \rangle} \quad 3.26).$$

F is the fraction of the volume occupied by clumps within the radio beam and $\langle \rangle$ denotes an average along the line sight. The mean square density, $\langle n_e^2 \rangle$, is given by the line ratio and the mean density, $\langle n_e \rangle$, is from the radio model. These give $F = 1/1600$ at the centre and $F = 1/300$ at the eastern edge; the degree of clumping is more pronounced in the centre than at the eastern edge.

The electron temperature of Talent & Dufour is due to the same selection effect as for the electron density. The temperature derived by Chini & Wink from $H112\alpha$ is probably a better indicator of the global properties of S212.

Talent & Dufour also find that S212 has a non-trivial abundance of singly ionized helium, $n(\text{HeII})/n(\text{H}) = 0.09$. The emissivity of HeII is the same as that of HII according to 3.1). It then follows that equations 3.1) to 3.11) are still valid. The model parameters, with the exception of M_{HII} and $N_{\text{u}}(0)$, are still valid. The

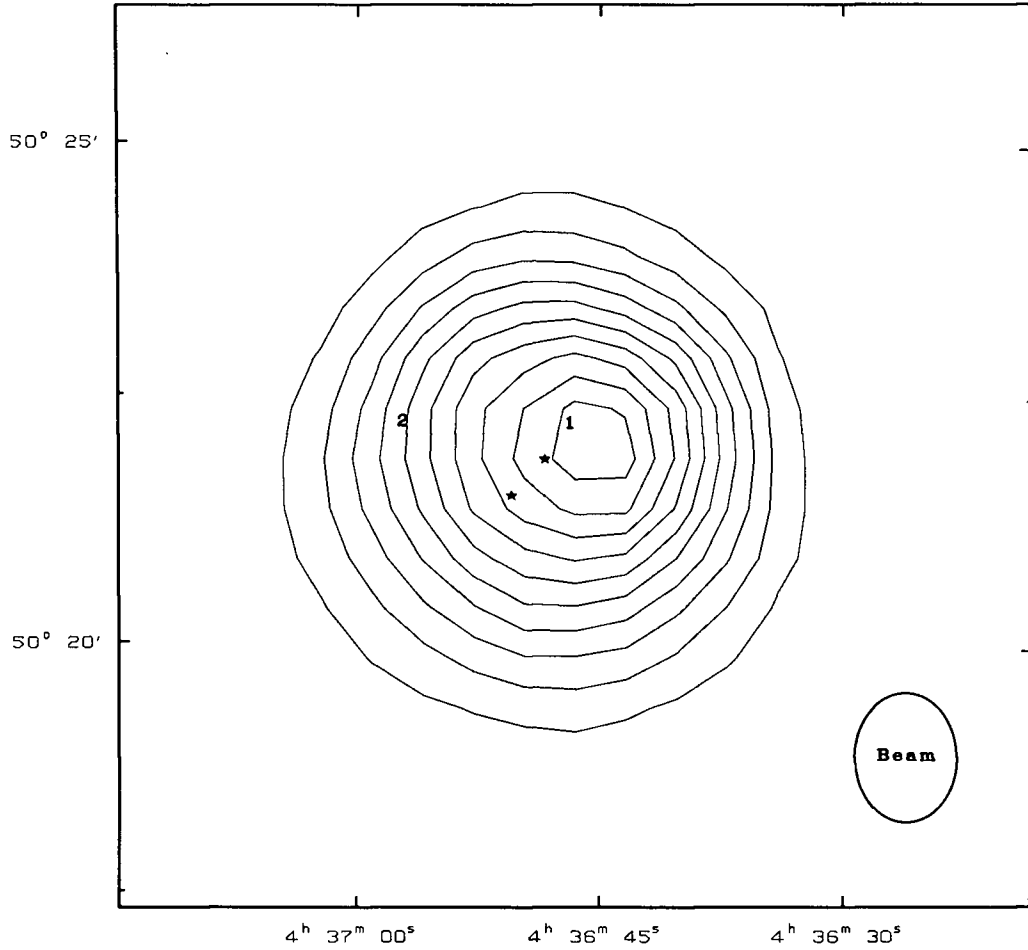


FIG. 3.4: Positions in S212 where Optical Line Ratios were Measured. The above contour map shows the positions where Talent and Dufour measured their electron densities (positions 1 and 2) and temperature (position 1 only). The positions of the exciting stars are indicated by asterisks (BOV left and O5.5 right). The radio beam to half power is shown in the lower right.

correction to M_{HII} takes account of the fact that some of the electron density is due to helium. This can be written as

$$\begin{aligned} n_e &= n_e(\text{HII}) + n_e(\text{HeII}) \\ &= 1.09n_e(\text{HII}) \end{aligned} \quad 3.27)$$

where n_e is the n_{eAV} that appears in 3.17). The n_{eAV} should be represented by $n_e(\text{HII})$. The correction factor to M_{HII} is then $1/1.09$ or 0.92 giving $M_{\text{HII}} = 290 M_{\odot}$ for S212. The total mass of the nebula, including helium (neutral He as well as ionized He), is given by

$$\begin{aligned} M_{S212} &= \frac{n(\text{H}) + 4n(\text{He})}{n(\text{H})} M_{\text{HII}}(\text{corrected}) \\ &= \left(1 + 4 \frac{n(\text{He})}{n(\text{H})} \right) M_{\text{HII}}(\text{corrected}) \end{aligned} \quad 3.28).$$

Talent & Dufour find $n(\text{He})/n(\text{H}) = 0.14$ giving $M_{S212} = 450 M_{\odot}$. No such information is available for S211 but assuming similar corrections would give

$$M_{\text{HII}}(\text{corrected}) \simeq M_{\text{HII}}(\text{uncorrected}).$$

This is because the exciting stars are an O9 and B0. According to Osterbrock (1974) the Stroemgren radius of helium would then be 0.2 to 0.4 times that of the hydrogen Stroemgren radius. When $n(\text{HeII})/n(\text{H}) \simeq 0.1$, within the HeII-HeI boundary, is averaged over the entire volume of S211 the correction factor is within 1% of unity. Equation 3.28) is still applicable so that $M_{S211} = 200 M_{\odot}$.

The correction to $N_{\text{u}}(0)$ is not so straight forward. If $n_e < 10^3 \text{ cm}^{-3}$ there is no need to correct $N_{\text{u}}(0)$ (Spitzer, 1978). The energy of photons that ionize HeI ($> 24.6 \text{ eV}$) is regained in the form of lower energy photons when HeII recombines and cascades down to the ground state. The lower energy photons are still energetic

enough to ionize hydrogen. In short, photons that ionize HeI are still “recovered” to ionize HI; no correction to $N_u(0)$ is necessary. Talent’s & Dufour’s work, however, shows that S212 contains clumps of $n_e > 10^3 \text{ cm}^{-3}$. In this eventuality the HeII that just recombined would be collisionally de-excited, not allowing the energy to ionize HI. The photons $> 24.6 \text{ eV}$ would be effectively lost to the process of ionizing hydrogen. The model $N_u(0)$ would be underestimated. To correct for this it would be necessary to know how many clumps, the sizes of clumps, their spatial distribution, etc. According to Osterbrock (1974), the critical density at which collisional de-excitations become as important as radiative de-excitations is about 4000 cm^{-3} – more than twice the highest density observed by Talent & Dufour. Even if the density were much higher than this critical density only about one-third of those photons absorbed by helium are lost to collisional de-excitation; of those photons capable of ionizing helium only about one-half are absorbed by helium rather than hydrogen (assuming $n(\text{He})/n(\text{H}) = 0.10$ to 0.15 and assuming the ratio of absorption cross-sections of 8 to 1 for helium to hydrogen at the helium ionizing frequencies); and of all the Lyman continuum photons only about one-fifth are capable of ionizing helium for an O6 star. These rough estimates when multiplied together imply that less than 5% of the Lyman continuum photons are lost to collisional de-excitation even when the density exceeds the critical density. Hence the correction to $N_u(0)$ is not important for S212. Clumping information for S211 is not available, but it is probably safe to assume that any clumps it contains are not as dense as those in S212. The model $N_u(0)$ should suffice.

It is interesting to note that collisional de-excitation in the clumps of S212 would heat the clumps to temperatures higher than that of the “inter-clump” medium. This may explain the discrepancy between the electron temperatures of Chini & Wink and those of Talent & Dufour.

The flux of ionizing photons required by the model of S211 is consistent with that produced by three stars of types O9I, O9V, B0V (Panagia, 1973). This agrees

reasonably well with Chini's & Wink's classification of the ionizing stars of S211. The flux of ionizing photons for the model of S212 is consistent with that of an O6V which agrees with the assertion of Fitzgerald (1985, priv. comm.).

The density of S211 is high, 85 cm^{-3} , in relation to the HI density suggesting that it is a young HII region. The most likely density of HI outside the ionization boundary is 100 cm^{-3} and the maximum likely density is 200 cm^{-3} (see Section 5.1). There exists a pressure difference across the ionization boundary that results in a shock front in the neutral material that moves outwards at a velocity V_s , relative to the central star(s), given by (Spitzer, 1978)

$$V_s^2 = C_{\text{II}}^2 \frac{\rho_{\text{II}}}{\rho_{\text{I}}} \left(1 - \frac{\rho_{\text{II}}}{4\rho_{\text{I}}} \right)^{-1} \quad 3.29)$$

where ρ_{II} , ρ_{I} are the mass densities in the ionized and atomic regions respectively. C_{II} is the isothermal sound speed in the ionized region given by

$$C_{\text{II}}^2 = \frac{kT_e}{\mu m_{\text{H}}} \quad 3.30)$$

where μ is the mean mass per particle in units of m_{H} . For $T_e = 7000 \text{ K}$ we have $C_{\text{II}} = 10.8 \text{ km} \cdot \text{s}^{-1}$. If we again assume that $n_{\text{HI}} = 100 \text{ cm}^{-3}$ just outside the HII region then $V_s = 11.2 \text{ km} \cdot \text{s}^{-1}$. And if we use $n_{\text{HI}} = 200 \text{ cm}^{-3}$ we have $V_s = 7.4 \text{ km} \cdot \text{s}^{-1}$. The rate of expansion of an HII region can be used to estimate its age by using (Spitzer, 1978)

$$\frac{\rho_{\text{I}}}{\rho_{\text{II}}} = \left[1 + \frac{7}{4} \left(\frac{C_{\text{II}} t}{r_{\text{i0}}} \right) \right]^{\frac{6}{7}} \quad 3.31)$$

where r_{i0} is the radius before expansion and can be found from

$$\frac{\rho_{\text{II}}}{\rho_{\text{I}}} = \left(\frac{r_{\text{i0}}}{r_{\text{i}}} \right)^{\frac{3}{2}} \quad 3.32)$$

where r_i is the same as the r_s used previously. For $n_{\text{HI}} = 100 \text{ cm}^{-3}$ the initial radius of S211 was 2.2 pc and for $n_{\text{HI}} = 200 \text{ cm}^{-3}$ this was 1.4 pc. Combining 3.31) and 3.32) gives

$$t = \frac{4}{7} \left[\left(\frac{\rho_{\text{I}}}{\rho_{\text{II}}} \right)^{\frac{1}{2}} - \left(\frac{\rho_{\text{II}}}{\rho_{\text{I}}} \right)^{\frac{2}{3}} \right] \left(\frac{r_i}{C_{\text{II}}} \right) \quad 3.33)$$

For S211 $r_i = 2.4 \text{ pc}$ and $\rho_{\text{II}}/\rho_{\text{I}} = 0.43$ to 0.85 giving $t = 2.4 \times 10^4$ to 1.2×10^5 years.

There is a possibility that S211 is density bounded on the back side (see Section 5.1); i.e. there is no HI beyond the ionization boundary thereby allowing the HII to “break-out” in a champagne-like flow (Tenorio-Tagle, 1979). In the case of an HII region bounded on one side the t derived from 3.33) is changed by a factor $(\frac{2}{3})^{\frac{1}{2}}$ (Elmegreen and Lada, 1978). This would give ages of 1.8×10^4 years and 9.8×10^4 years.

Also, if S211 is bounded on one side, the velocity of expansion into the cloud that bounds it is given by (Elmegreen and Lada, 1978)

$$V_s = \left(\frac{3}{2} \right)^{\frac{1}{2}} C_{\text{II}} \left(\frac{\rho_{\text{II}}}{\rho_{\text{I}}} \right)^{\frac{1}{2}} \quad 3.34)$$

which is $12.1 \text{ km} \cdot \text{s}^{-1}$ for $n_{\text{HI}} = 100 \text{ cm}^{-3}$ and $8.6 \text{ km} \cdot \text{s}^{-1}$ for $n_{\text{HI}} = 200 \text{ cm}^{-3}$. These estimated velocities, and the age estimates are tabulated in Table 3.3.

TABLE 3.3: ESTIMATES OF AGE AND EXPANSION VELOCITY FOR S211

	$n_{\text{HI}} = 100 \text{ cm}^{-3}$	$n_{\text{HI}} = 200 \text{ cm}^{-3}$
Age	$2.4 \times 10^4 \text{ yrs}$	$1.2 \times 10^5 \text{ yrs}$
(Density bounded case)	$1.8 \times 10^4 \text{ yrs}$	$9.8 \times 10^4 \text{ yrs}$
Expansion Velocity	$11 \text{ km} \cdot \text{s}^{-1}$	$7.4 \text{ km} \cdot \text{s}^{-1}$
(Density bounded case)	$12^* \text{ km} \cdot \text{s}^{-1}$	$8.6^* \text{ km} \cdot \text{s}^{-1}$

* Into side bounded by HI.

The density of S212 on the other hand implies that it is more evolved. The isothermal sound velocity is $11.5 \text{ km} \cdot \text{s}^{-1}$. S212 is density bounded on more than one side (i.e. more than a full hemisphere, see Section 5.2). Equation 3.33) modified by $(\frac{2}{3})^{\frac{1}{2}}$ may not be applicable because it would underestimate the rate of expansion and hence overestimate the age. At least 3.33) can provide an upper limit for the age of S212. The density of HI just beyond the ionization front lies in the range 100 cm^{-3} to 500 cm^{-3} (see Section 5.2). These densities give ages of 1.0×10^5 years to 3.8×10^5 years. If we now take an average radius, r_i , of 4.1 pc then the initial radius of S212, using 3.32), was 2.5 pc ($n_{\text{HI}} = 100 \text{ cm}^{-3}$) or 0.9 pc ($n_{\text{HI}} = 500 \text{ cm}^{-3}$). We can also estimate the age by assuming the material in the break-out on the east side is flowing at $30 \text{ km} \cdot \text{s}^{-1}$ (Bodenheimer, et. al., 1979) from the initial radius to the present maximum radius of 6.1 pc on the east side. This gives an age of 1.2×10^5 years ($n_{\text{HI}} = 100 \text{ cm}^{-3}$) or 1.6×10^5 years ($n_{\text{HI}} = 500 \text{ cm}^{-3}$) which compare well with the previous values.

An estimate of the expansion velocity of S212 into the HI would be given by 3.34); $10 \text{ km} \cdot \text{s}^{-1}$ for $n_{\text{HI}} = 100 \text{ cm}^{-3}$ and $4.5 \text{ km} \cdot \text{s}^{-1}$ for $n_{\text{HI}} = 500 \text{ cm}^{-3}$. See Table 3.4 for expansion velocity estimates as well as the age estimates.

TABLE 3.4: ESTIMATES OF AGE AND EXPANSION VELOCITY FOR S212

	$n_{\text{HI}} = 100 \text{ cm}^{-3}$	$n_{\text{HI}} = 500 \text{ cm}^{-3}$
Age	$1.0 \times 10^5 \text{ yrs}$	$3.8 \times 10^5 \text{ yrs}$
Expansion Velocity (into HI)	$10 \text{ km} \cdot \text{s}^{-1}$	$4.5 \text{ km} \cdot \text{s}^{-1}$

Ages of $\sim 10^5$ yrs or less for both S211 and S212 imply that these HII regions are still rather unevolved. The age estimates are dependent upon the HI density which, as mentioned in Chapter 5, is quite uncertain. But even if n_{HI} is as high as 10^3 cm^{-3} S211 and S212 would still be only 4×10^5 and 6×10^5 yrs old respectively. The HII regions are still probably much younger than this because more evolved

HII regions tend to develop complicated geometries because of instabilities (e.g. Rayleigh-Taylor) that develop during the expansion whereas S211 and S212 are still relatively spherical. Also younger HII regions are more likely to contain clumps since density contrasts, within the ionized hydrogen, tend to even out with time; S212 is heavily clumped indeed ($1/F = 1600$). At the time of this writing, optical line ratios were not available for S211 so that it was not possible to estimate the degree of clumping, if any, in S211. However, the CO observations (McCutcheon, 1985) show evidence of clumping in the H_2 associated with S211 similar to the case of H_2 associated with S212.

If we accept that S212 is indeed about 10^5 yrs old then we have further evidence that the spectral classification for S212's exciting stars by Moffat et. al. (1979) is more reliable than that of Chini & Wink (1984) because the former determined that the stars were young ZAMS or V stars whereas the latter derived luminosity classes of I and III for the exciting stars. Chini & Wink also classified the major ionizing star of S211 to be O9Ib which implies a degree of evolution in conflict with the age determined for the HII region. If, however, we consider the major ionizing star to be O6V then this conflict no longer exists and the Lyman continuum photon flux is unchanged (Panagia, 1973).

Reclassifying the ionizing stars of S211 may imply some change in luminosity and hence in distance. Considering the similarities of S211 to S212 (age, clumpiness) it may be that they both lie at about the same distance, 6 kpc, and formed out of the same giant complex. But until other distance estimates are available the distance of S211 will still be considered as 7.8 kpc.

4 HI EMISSION

4.1 THEORY

The line radiation of neutral hydrogen results from the hyperfine transition in the ground state of the hydrogen atom. The excitation or spin temperature is, in most cases ($n_{\text{HI}} \geq 1.0 \text{ cm}^{-3}$), the same as the kinetic temperature of the gas. Using this fact and the emissivity of the process yields the column density (Spitzer, 1978)

$$N(\text{HI}) = \frac{8\pi\nu^2 k T_s}{3hc^3 A_{10}} \int_{\text{line}} \tau(v) dv \quad 4.1)$$

where ν is 1.42 GHz, $A_{10} = 2.869 \times 10^{-15} \text{ s}^{-1}$ is the spontaneous transition probability, T_s is the spin temperature and $\tau(v)$ is the optical depth as a function of the radial velocity. Expressing v in $\text{km} \cdot \text{s}^{-1}$ gives

$$N(\text{HI}) = 1.823 \times 10^{18} T_s \int_{\text{line}} \tau(v) dv \quad \text{cm}^{-2}.$$

Before analyzing the HI data it was necessary to somehow remove the large scale HI emission. The method chosen, in this study, as discussed in Chapter 2, was to subtract the minimum value of each LOS map from the corresponding FS map yielding the SS maps. (The compressed SS maps are shown in Appendix B.) To examine this in more detail consider Fig. 4.1. (The rest of this paragraph and the following paragraph, which examine the consequences of this subtraction in detail, may be omitted by the reader without great loss of coherence.) The brightness temperature measured, T_b , would be related to the large scale emission brightness temperature, T_{bL} , and the brightness temperature observable in the absence of the large scale emission, T_{bc} , by the equation of radiative transfer, i.e.

$$T_b = T_{bL} + T_{bc} \exp(-\tau_{\nu L}) \quad 4.2)$$

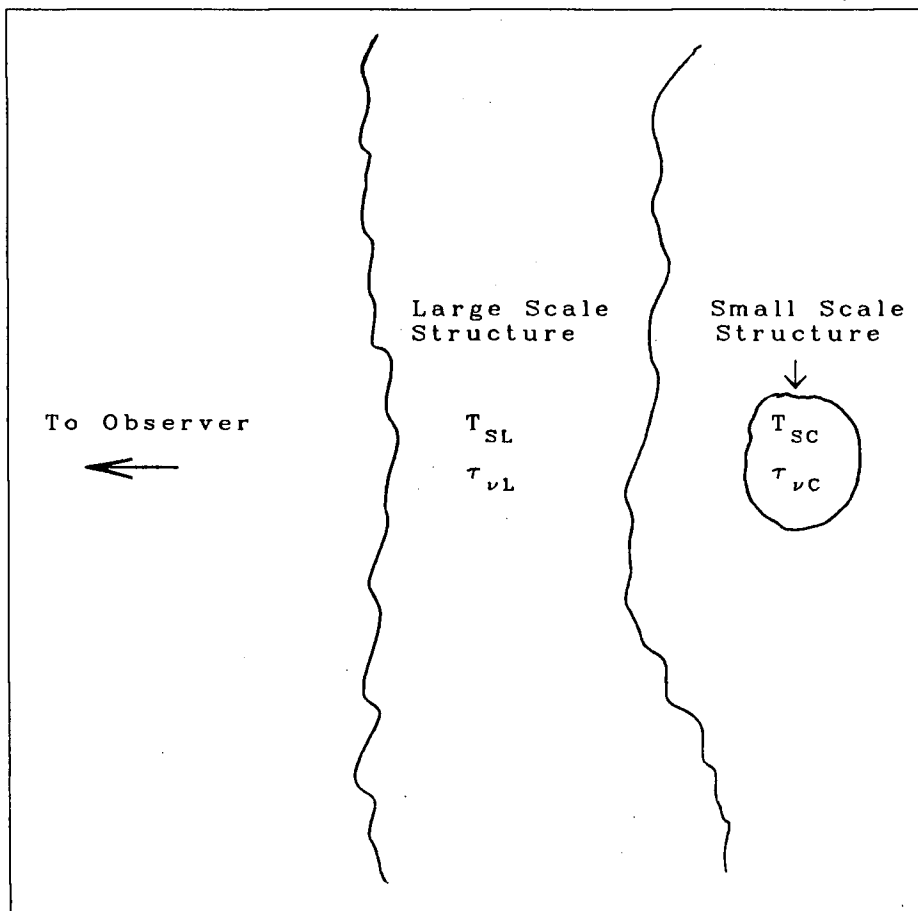


FIG. 4.1: Schematic Representation of Equation 4.2
The large scale structure has spin temperature T_{SL} and optical depth $\tau_{\nu L}$. The small scale structure (eg. S212 HI cloud(s)) has spin temperature T_{SC} and optical depth $\tau_{\nu C}$.

where we have assumed, for the moment, that the large scale structure is foreground material. The units of the FS maps, ΔT_b , are given by

$$\Delta T_b = \Delta T_{bL} + \Delta T_{bi} \quad (4.3)$$

where Δ denotes a line minus continuum temperature. The T_{bi} is the interferometer brightness temperature and T_{bL} is the low order spacings brightness temperature which is taken to be the same as the large scale HI brightness temperature. It follows that

$$\Delta T_{bL} = T_{bL} - T_{Lcont} \quad (4.4)$$

and

$$\Delta T_{bi} = T_{bi} - T_{icont}$$

where T_{Lcont} and T_{icont} are the brightness temperatures in the out-of-band continuum of the low order spacings and interferometer maps respectively. Substitute equations 4.4) into 4.3) to obtain

$$\begin{aligned} \Delta T_b &= T_{bL} - T_{Lcont} + T_{bi} - T_{icont} \\ &= T_b - T_{Lcont} - T_{icont} \end{aligned} \quad (4.5)$$

where $T_b = T_{bL} + T_{bi}$ has been used. The SS maps are defined by

$$\begin{aligned} \Delta T_{bSS} &= \Delta T_b - \Delta T_{bL} \\ &= T_b - T_{bL} - T_{icont} \quad \text{using 4.4) and 4.5)} \\ &= T_{bc} \exp(-\tau_{\nu L}) - T_{cont} \quad \text{using 4.2) and dropping subscript i;} \end{aligned}$$

$$\text{i.e.} \quad \Delta T_{bc} = (\Delta T_{bSS} + T_{cont}) \exp(+\tau_{\nu L}) - T_{cont} \quad (4.6).$$

The relationship between T_{bL} and the spin temperature, T_{sL} , is given by

$$T_{bL} = T_{sL} (1 - \exp(-\tau_{\nu L}))$$

so that

$$\exp(\tau_{\nu L}) = \frac{T_{sL}}{T_{sL} - T_{bL}} \quad (4.7).$$

Substituting 4.7) into 4.6) gives

$$\Delta T_{bc} = a_1 \Delta T_{bss} + a_2 \quad 4.8)$$

where

$$a_1 = \frac{T_{sl}}{T_{sl} - T_{bl}}$$

and

$$a_2 = \frac{T_{cont} \cdot T_{sl}}{T_{sl} - T_{bl}} .$$

The correction to the SS maps is the application of a multiplicative and an additive constant. The large scale emission is mostly due to the intercloud medium, suggesting that its spin temperature is between 600 K and 8000 K (Davies and Cummings, 1975). The maximum values of a_1 and a_2 are given by taking the minimum T_{sl} , 600 K, the maximum T_{bl} from the maps, 92 K, and the maximum T_{cont} from the continuum map, 42 K. These give $a_1 = 1.18$ and $a_2 = 7.6$ K which are extreme overestimates. More realistic values are $T_{bl} = 20$ K and $T_{cont} = 0.5$ K. These would give $a_1 \simeq 1.03$ and $a_2 \simeq 0.02$ K so that

$$\Delta T_{bc} \simeq \Delta T_{bss} \quad 4.9).$$

In short, the SS maps are essentially devoid of foreground large scale structure.

If the above analysis is repeated, assuming the large scale emission is due to background material, then we have

$$\Delta T_{bss} = \Delta T_{bc} - T_{bl} \left(\frac{T_{bc}}{T_{sc}} \right) \quad 4.10).$$

If the small scale clouds are not optically thin then the parenthesized quantity will not be negligible when compared with unity. Spectra extracted from the SS maps would then show absorption dips at the positions of the clouds. But these features would not be absorption of the clouds' emission by colder foreground clouds; they would be absorption by the clouds of the background large scale emission. Anything

that appears to be an absorption feature must then be viewed with caution: is it absorption of the cloud emission by other foreground clouds (not seen in emission) or is it absorption by the clouds of the large scale structure? The latter case is an artifact of the spectrum subtraction used to make the SS maps.

Another problem in analyzing the HI data is distinguishing between the HI clouds associated with S211 and S212 and the HI emission of the galactic plane. Even though the CC Survey centre is at $b = 2^{\circ}5$, maps of the Leiden-Green Bank survey of the atomic hydrogen in the galactic disk (Burton et. al., 1985) show that the galactic disk HI emission extends beyond $b = 2^{\circ}5$ at $l = 155^{\circ}$ over most of the CC Survey velocity range. In fact the half-maximum intensity level extends beyond $b = \pm 5^{\circ}$. To examine this problem the SS maps were averaged in groups of 12 consecutive channels, smoothed to $3'$ resolution and rotated to galactic coordinates. The resultant spectrum subtracted galactic (SSG) maps are also shown in Appendix B. Map 1 (-8.8 to $-13.7 \text{ km} \cdot \text{s}^{-1}$) shows a 1° long spur of HI between $b = 2^{\circ}25$ and $b = 2^{\circ}50$. This is highly suggestive of galactic plane HI emission. Extensive HI emission, though not spur-like, shows up again in maps 4 through 6 (-23.7 to $-38.6 \text{ km} \cdot \text{s}^{-1}$). HI appears in these maps to be more clumped than in the case of map 1. The clumping makes difficult the distinction between S211/S212 HI and galactic disk HI. Hence column densities and masses determined for the S211/S212 HI clouds were possibly overestimated.

4.2 S211 ATOMIC HYDROGEN EMISSION

Maps showing HI in the vicinity of S211 are shown in Appendix E. The maps are integrated in eleven velocity ranges throughout the bandwidth of the CC Survey (-8.8 to $-61.7 \text{ km} \cdot \text{s}^{-1}$). Maps 4 (-22.4 to $-27.4 \text{ km} \cdot \text{s}^{-1}$) and 7 (-34.8 to $-43.5 \text{ km} \cdot \text{s}^{-1}$) each show a roughly circular patch of HI emission about $6'$ to $10'$ in radius with brightness temperatures exceeding 70 K. Map 7 also shows a tail-like structure on the south side projecting about $6'$ towards the south. Map 6 (-31.1

to $-36.1 \text{ km} \cdot \text{s}^{-1}$) shows a “gap” ($T_b < 30 \text{ K}$) in HI emission at, and surrounding, the position of S211. The circular patch of HI emission shown in maps 4 and 7 was believed to be associated with S211 for the following reasons:

- 1) HI emission in both maps lies in the same direction as S211 with S211 roughly in the centre.
- 2) The emission area in each map is of comparable size to S211.
- 3) A decrease in HI intensity at the position of S211 is present in both maps suggesting that there may be some influence of the HII region on the neutral hydrogen.
- 4) The central velocity of map 4 ($-25 \text{ km} \cdot \text{s}^{-1}$) and map 7 ($-39 \text{ km} \cdot \text{s}^{-1}$) are both within $10 \text{ km} \cdot \text{s}^{-1}$ of the HII region velocity ($-34.8 \text{ km} \cdot \text{s}^{-1}$, Chini & Wink).

However, considering both the map 4 and map 7 emission features to be associated with S211 leads to significant problems; it is difficult to explain the lack of HI emission between the two maps, at the velocity range of map 6 (i.e. the gap), as well as the large velocity separation between the two features ($14 \text{ km} \cdot \text{s}^{-1}$). It is then simplest to assume that one of the features is not at all associated with S211. In other words, the two emission features are entirely different HI clouds where the one in map 4 shall be dubbed “Cloud 1” and the one in map 7 shall be called “Cloud 2”. Which cloud is associated with S211? According to the Blitz model of galactic rotation ($R_\odot = 10 \text{ kpc}$, $V_\odot = 250 \text{ km} \cdot \text{s}^{-1}$) the S211 complex, at a distance of 7.8 kpc , should be moving at $-39 \text{ km} \cdot \text{s}^{-1}$. This is the radial velocity of Cloud 2. Also, Cloud 2 is moving close to the CO velocity ($-38 \text{ km} \cdot \text{s}^{-1}$) measured in the direction of S211 by McCutcheon. It would then seem that Cloud 2 is associated with S211 whereas Cloud 1 is not associated.

This means that there are a couple of coincidences to explain. The first is that if Cloud 1 and Cloud 2 are not part of the same complex how is it that Cloud 1

is roughly the same angular size and position as Cloud 2? Examination of map 4 of the SSG maps in Appendix B shows Cloud 1 is part of a larger complex of HI emission that consists of many clumps of angular size similar to that of Cloud 2. It is then not unlikely for such a clump to lie in front of Cloud 2.

The second coincidence is that the intensity dip in the centre of Cloud 1 is at the position of S211. This normally suggests a lack of atomic hydrogen due to the presence of the ionized hydrogen. Another possibility, however, is that Cloud 1 has an optical depth great enough to significantly absorb the continuum emission of S211. This requires a spin temperature low enough (a higher optical depth requires a smaller spin temperature for a given observed brightness temperature) for the optical depth to remain large within $1'$ of the centre of Cloud 1. This can be best illustrated by Fig. 4.2 which shows column density versus projected radius for two possible spin temperatures of Cloud 1. The column density profiles were computed using equations 4.12 (page 56) and 4.14 (replacing T_{s2} by T_{s1} in equation 4.14 on page 58) and the ring spectra (see next paragraph) found in Appendix E (pages 144 to 146). The 140 K profile rises as one moves towards the centre and then drops again within $1'$ of the centre, reflecting a lack of HI in this central area. In contrast, the 105 K profile increases monotonically all the way to the centre, implying that the intensity dip is due only to absorption. Since 105 K is not an unlikely spin temperature for a galactic HI cloud it is quite probable that the intensity dip in Cloud 1 is indeed due only to continuum absorption. The alternative is to have Cloud 1 as part of the S211 complex and this leads to numerous difficulties that are described in Section 4.2.1. The absorption profile of Cloud 1 is shown in Fig. 4.3 where a spectrum of Cloud 1 just away from S211 (i.e. ring 3 spectrum) has been subtracted from a spectrum directly towards the centre of S211 (i.e. ring 1 spectrum).

To infer characteristics of S211's HI cloud, i.e. Cloud 2, the HI spectra in the area of S211 are spatially averaged (i.e. spectra from neighbouring pixels, each

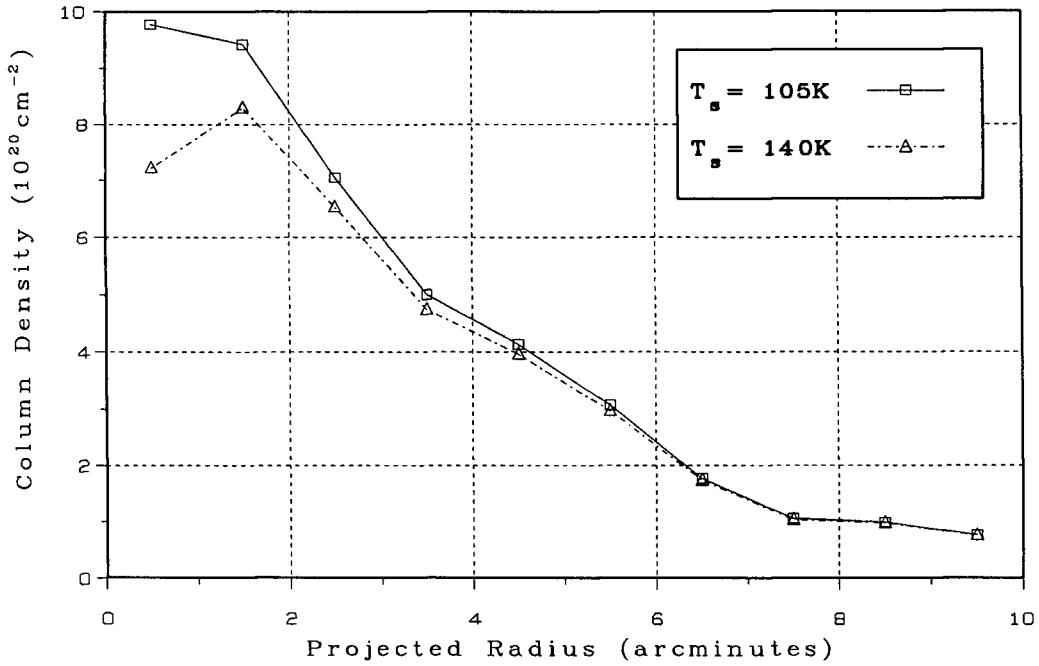


FIG. 4.2: Cloud 1 Column Densities - HI column density is plotted against projected radius (no distance assumed) for a low spin temperature (eg. 105K). This demonstrates that Cloud 1's central intensity dip, seen in map 4 of Appendix E, is not necessarily due to a lack of HI. The column density profile for $T_s = 140K$ is shown for comparison.

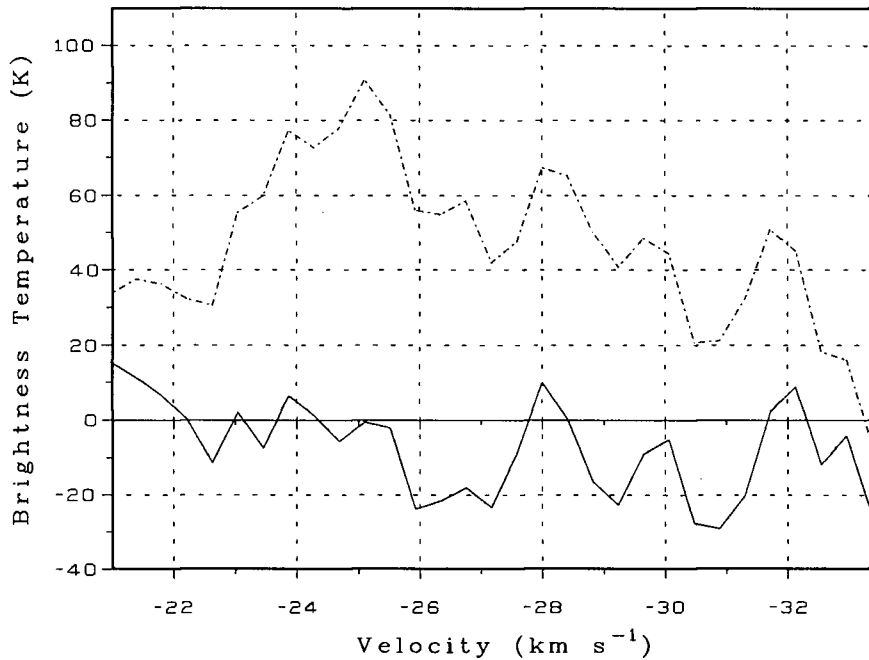


FIG. 4.3: Cloud 1 in Absorption - The spectral profile of Cloud 1 in absorption as seen against the continuum source S211 is represented above by a solid line. The emission profile of Cloud 1 (dashed line) is shown for comparison. The complexity of both profiles is undoubtedly due to interference by galactic plane HI emission.

$0'.5 \times 0'.5$, are averaged) to reduce the noise. Two sets of these spectra are shown in Appendix E. The first set of spectra are averaged in 3 pixel by 3 pixel blocks running from south to north through the centre of S211 and also from east to west through the centre of S211 (pages 141 to 143). The rms noise in the block spectra is about 5 K to 7 K. The second set (pages 144 to 146) are averaged in rings, $1'$ thick, centred on S211. The noise in the ring spectra starts at about 5 K to 7 K rms and drops in succeeding spectra in proportion to the square root of the ring radius. The ring 1 spectrum is shown in Fig. 4.4. The spectrum of Cloud 1 is found in the velocity range -22 to $-27 \text{ km} \cdot \text{s}^{-1}$ and the Cloud 2 spectrum is found at -37 to $-43 \text{ km} \cdot \text{s}^{-1}$. A strong absorption-like dip is visible between the velocity ranges of the two clouds at $-34 \text{ km} \cdot \text{s}^{-1}$.

In order to estimate a likely spin temperature for Cloud 2 the ring spectra were each fitted with a Gaussian and a sloped baseline. The sloped baseline was a first approximation to the spectrum of extraneous HI in the field. The CC field is immersed in galactic disk HI emission so that it is reasonable to expect considerable HI emission from other sources. The exact shape of the baseline is not important at this point since the Gaussians are merely used to estimate an upper limit to the spin temperature from (Allen, 1973)

$$T_s \leq 21.7(\Delta v)^2 \quad 4.11)$$

where Δv is the full width at half maximum (FWHM) of the Gaussian. The equality obtains when there is no turbulence; the spectral profile is only thermally broadened. The Δv for Cloud 2 varies with angular distance from S211. This is due to varying amounts of turbulence within the cloud and due to errors in the fit. The three smallest $(\Delta v)^2$ are averaged to obtain

$$T_s(\text{max}) = 320 \pm 100 \text{ K} .$$

The errors were derived from the uncertainty in Δv .

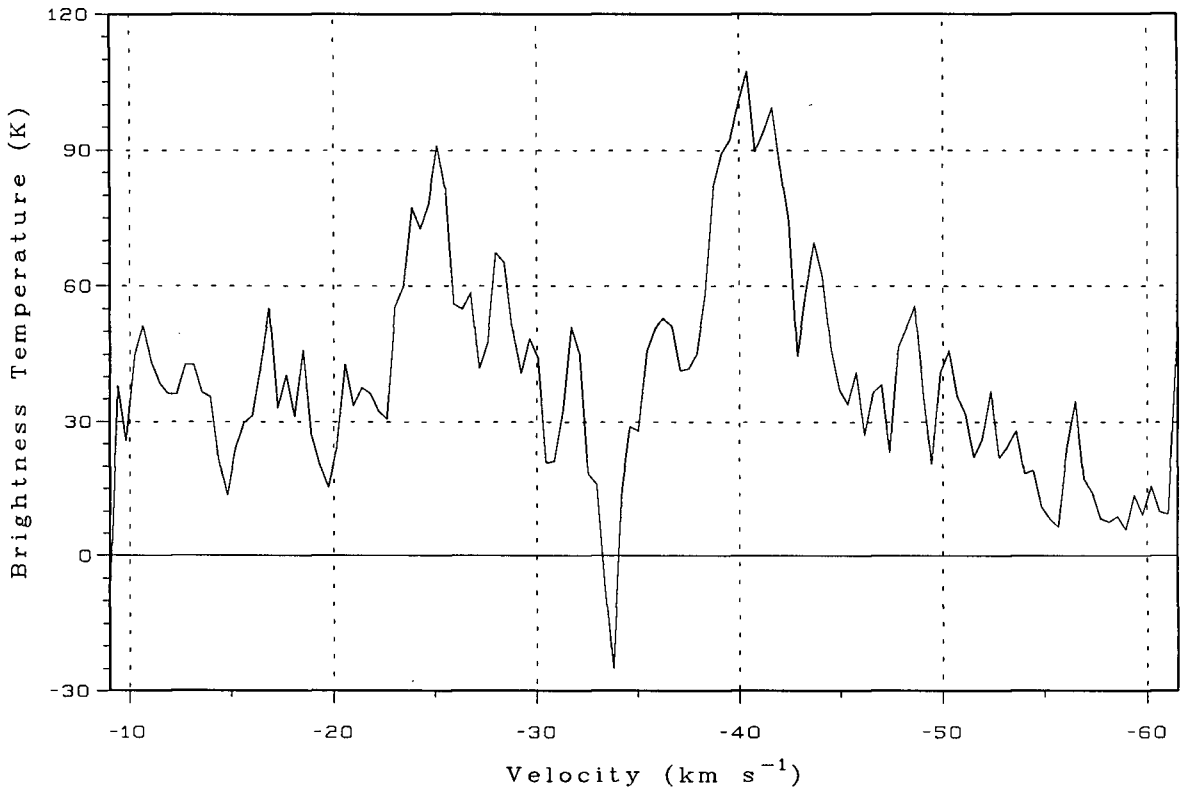


FIG. 4.4: Ring 1 Spectrum - An HI spectrum in the direction of S211 shows Cloud 1 and Cloud 2 at -22 to -27 km s^{-1} and -37 to -43 km s^{-1} respectively. The strong dip at -34 km s^{-1} is probably due to continuum absorption by some foreground cloud. This spectrum is identical to NS11 and EW11 of the block spectra.

The column density within the j^{th} ring was estimated from

$$N_j(\text{HI}) = 1.823 \times 10^{18} \Delta v_c T_s \sum_k \tau_j(v_k) \quad \text{cm}^{-2} \quad 4.12$$

where Δv_c is the channel velocity width of $0.41 \text{ km} \cdot \text{s}^{-1}$ and $\tau_j(v_k)$ is the optical depth in the j^{th} ring at the velocity in the k^{th} channel. The summation is over the velocity of Cloud 2, $-37 \text{ km} \cdot \text{s}^{-1}$ to $-43 \text{ km} \cdot \text{s}^{-1}$. The brightness temperature of Cloud 2 is given by

$$T_{\text{bH}} = T_{\text{s2}}(1 - \exp(-\tau_{\nu 2})) + T_{\text{cont}}\exp(-\tau_{\nu 2}) \quad 4.13$$

with T_{s2} , $\tau_{\nu 2}$ the spin temperature and optical depth of Cloud 2. It has been assumed in 4.13) that S211's HI cloud lies in front of S211 itself. Reasons for this are discussed in Section 5.1. Subtracting T_{cont} from both sides, solving for $\tau_{\nu 2}$ and expressing in discrete form gives

$$\tau_j(v_k) = \ln \left(\frac{T_{\text{s2}} - T_{\text{cont}}(j)}{T_{\text{s2}} - T_{\text{cont}}(j) - \Delta T_{\text{bH}}(j, k)} \right) \quad 4.14$$

where $T_{\text{cont}}(j)$ represents the continuum map averaged in rings centred on S211 and T_{s2} was treated as a free parameter. $\Delta T_{\text{bH}}(j, k)$ is related to the ring spectra brightness temperatures, $\Delta T_{\text{b}}(j, k)$, by

$$\Delta T_{\text{bH}}(j, k) = \Delta T_{\text{b}}(j, k) - T_{\text{bb}}(k) \quad 4.15$$

where $T_{\text{bb}}(k)$ is the brightness temperature spectrum that was chosen as the baseline spectrum. Strictly speaking, T_{bb} should be included in the equation of radiative transfer, 4.13), but since it was not known how the baseline spectrum is distributed between foreground and background material it seemed that the straight subtraction of 4.15) was the best compromise.

It was then necessary to make a good choice for the baseline spectrum, $T_{\text{bb}}(k)$. The ring spectra from 10' to 16' were inspected and it was found that they are

remarkably similar to one another. If these spectra are relatively unchanging going out from the tenth ring (at 9' to 10'), then, in the absence of Cloud 2, they would probably be unchanging going inwards from the tenth ring to the centre. Hence an average of these spectra was used for T_{bb} . The baseline is shown in Fig. 4.5. A natural question at this point is, "How do we know that the S211 HI cloud terminates at 10'?" In other words, the baseline might actually be a spectrum of Cloud 2 beyond 10'. Inspection of CSS maps 22 to 29 in Appendix B appears to show that HI emission this far from the position of S211 is largely separate from Cloud 2. In addition the integrated maps in Appendix E strongly suggest a limit of about 10' for the two clouds. Finally, the molecular cloud in which S211 is situated (see Chapter 5) is too small to account for HI emission beyond 10'. Observations of CO (McCutcheon, 1985 priv. comm.) show that the molecular cloud is contained within about 3' to 4' of S211 in all directions except the southeast.

Equations 4.12), 4.14) and 4.15) combined give the column density profiles shown in Fig. 4.6. Since the spin temperature was not known, two different values for T_{s_2} were used in 4.14) – 320 K, 140 K – while the upper bound dictated by 4.11) and the lower bound dictated by the observed brightness temperature were kept in mind. The mass in solar masses was determined from

$$M = \sum_j N_j(\text{HI})(A_j)m_{\text{H}} \left(\frac{M_{\odot}}{1.989 \times 10^{33} \text{ g}} \right) \quad 4.16),$$

A_j is the area of the j^{th} ring assuming $D = 7.8 \text{ kpc}$. The possible masses of the S211 HI cloud are presented in Table 4.1 and scale as D^2 .

TABLE 4.1: DERIVED MASSES OF THE S211 HI CLOUD

T_{s}	Mass
320 K	3700 M_{\odot}
140 K	4100 M_{\odot}

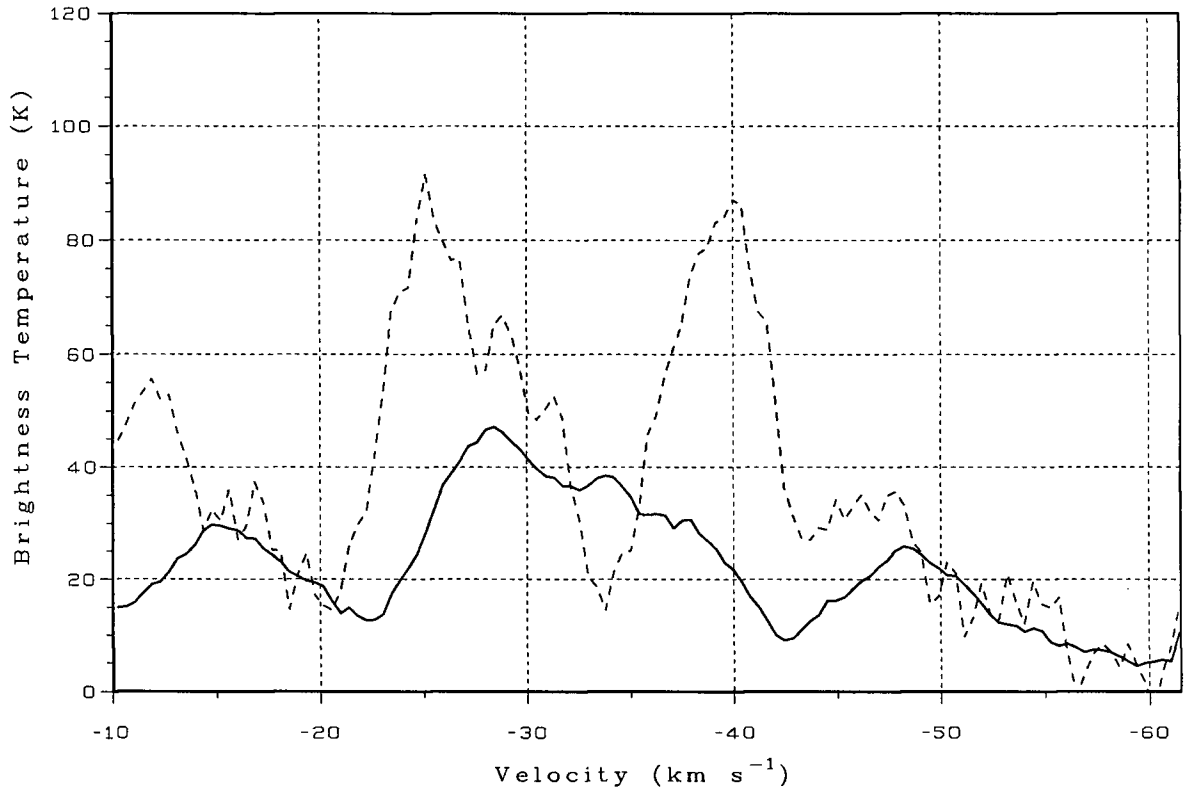


FIG. 4.5: Baseline Spectrum for S211 - The dark line represents the spectrum, in the direction of S211, that is used as a baseline for the ring spectra in Appendix E. One of the ring spectra is shown in dashed lines for comparison.

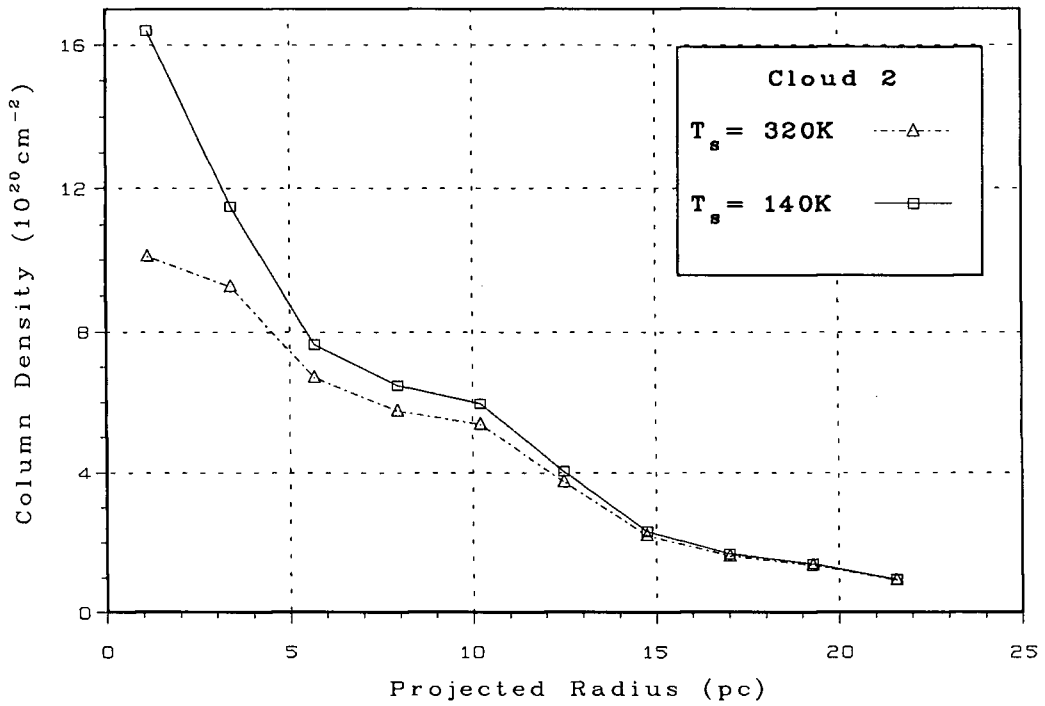


FIG. 4.6: Cloud 2 Column Densities - HI column density of S211's HI cloud, Cloud 2, versus projected radius (at $D=7.8\text{kpc}$) is shown for two possible spin temperatures.

Finally, the negative dip at $-34 \text{ km} \cdot \text{s}^{-1}$ is most likely due to absorption by a foreground cloud. The feature is not a noise spike since it is about 5 sigma below the mean. It is also not likely an artifact since it is much stronger at the position of the continuum source, S211, than elsewhere. This suggests that the dip is due to continuum absorption by some foreground cloud. The Blitz model of galactic rotation ($V_{\odot} = 250 \text{ km} \cdot \text{s}^{-1}$, $R_{\odot} = 10 \text{ kpc}$) suggests the absorbing cloud is at a distance of 6.6 kpc. The position of the absorbing cloud in relation to Clouds 1 and 2 is represented schematically in Fig. 5.2.

4.2.1 Previous Models for the S211 Complex –

This section describes in more detail the necessity of excluding Cloud 1 – the emission feature in map 4 of Appendix E – from the S211 complex. The previous unsuccessful models assumed that both the map 4 and the map 7 emission features were associated with S211. This placed the gap within the velocity range of the S211 atomic hydrogen emission and hence the gap's existence became harder to explain. The gap appears in the v - α , δ - v maps of Appendix E (pages 139 and 140) as a blank strip about $4 \text{ km} \cdot \text{s}^{-1}$ wide running along a line of constant velocity, i.e. $-33 \text{ km} \cdot \text{s}^{-1}$. The gap is not unusual in that it is an area in v - α , δ - v maps with $T_b < 30 \text{ K}$. What is unusual, however, is that it is straight and narrow and flanked by emission peaks of $T_b \geq 70 \text{ K}$ for $6'$ to $10'$ in all directions.

How did one then interpret the gap? Examination of the block spectra (pages 141 to 143) showed negative dips in those spectra well away ($16'$) from S211; i.e. continuum absorption could not explain their presence. These dips, in whole or in part, are artifacts of the spectrum subtraction used to make the SS maps. Could the gap be the result of these artifacts? This is quite unlikely because the HI associated with HII regions is usually optically thin so that there would be too little absorption of the large scale structure by the S211 HI to account for the gap (see

equation 4.10). This left two pictures in which to interpret the gap: it is the result of absorption by some foreground cloud or it is due to lack of HI emission.

In the first picture the emission features of maps 4 and 7 were considered to be the broad (i.e. large velocity width) emission of a single cloud that had been largely absorbed in the velocity range covered by map 6 (the gap). This is similar to the case of the HI associated with LkH α 101 (Dewdney and Roger, 1982). Three different absorption models were tried where each required two components of absorption because the ring spectra showed that the gap between the two large peaks appeared to be a broad absorption component together with a narrow component. The absorption dip in the ring 1 spectrum at $-34 \text{ km} \cdot \text{s}^{-1}$ is a prime example of the narrow absorption component whereas the broad “valley” between the two peaks is a good example of the broad absorption component. Model 1 in the absorption picture assumed two absorbing clouds in front of the S211 complex. Unfortunately this model required $2.0 \times 10^4 M_{\odot}$ of absorbing material. Model 2 in the absorption picture assumed that the S211 HI cloud has a temperature gradient and is optically thick so that the colder outer layers absorb the central frequencies of the emission from the hotter inner layers. This model was represented by a series of isothermal shells of HI surrounding S211 where the innermost and outermost layers had spin temperatures of 1000 K and 20 K respectively. Model 2 could indeed reproduce the observed spectra but required $1.43 \times 10^5 M_{\odot}$ of atomic hydrogen. If one uses the HII region density, 85 cm^{-3} , as a lower limit for the HI density then Fig. 5.1, based on the photodissociation model of Dewdney and Roger (1982, unpublished), suggests that the maximum mass of atomic hydrogen associated with S211 (assuming spectral O6, see Chapter 5) should be only about $10^4 M_{\odot}$. Thus Absorption Model 2 requires an order of magnitude more than could be dissociated by S211’s ionizing stars. Model 3 was developed to bring down the mass required by Model 2. Model 3 was similar to Model 2 except that the shells were expanding. This model failed because it predicted that the velocity separation between the two emission features would

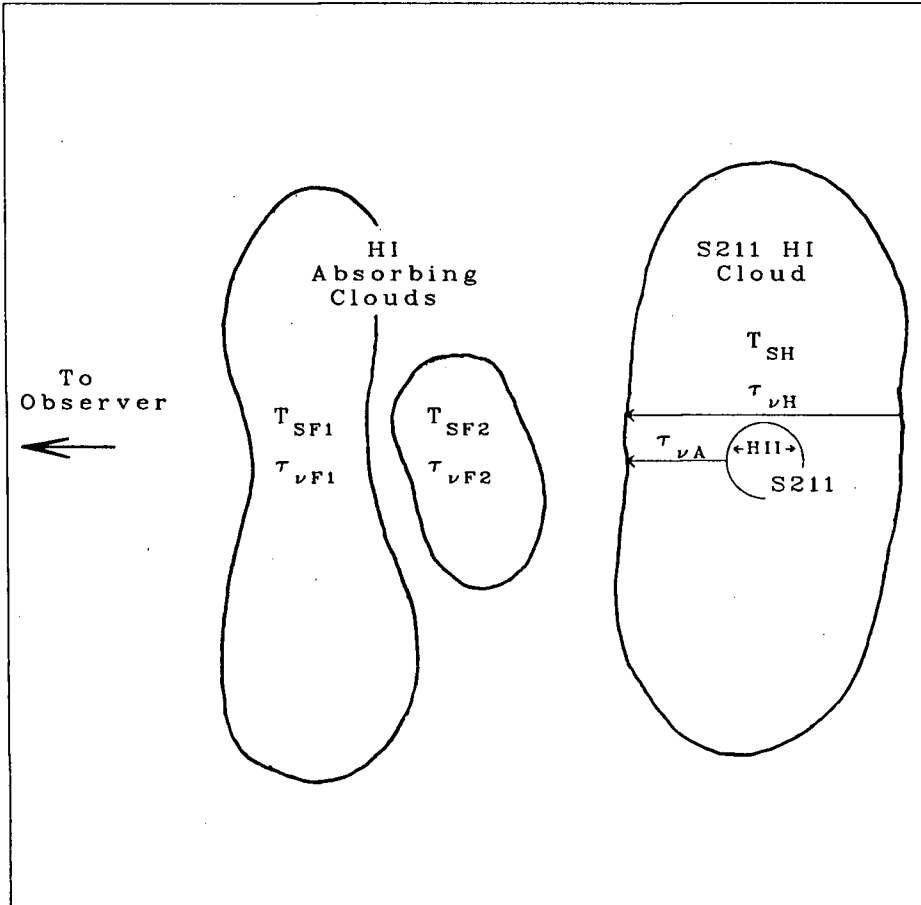


FIG. 4.7: Absorption Model 1 - Two absorbing clouds, spin temperatures T_{SF1} and T_{SF2} and optical depths $\tau_{\nu F1}$ and $\tau_{\nu F2}$, between the observer and the S211 complex are used as a possible explanation for the observed spectra. The optical depth from S211, $\tau_{\nu A}$, was taken to be half of the total optical depth, $\tau_{\nu H}$, through the HI cloud of S211.

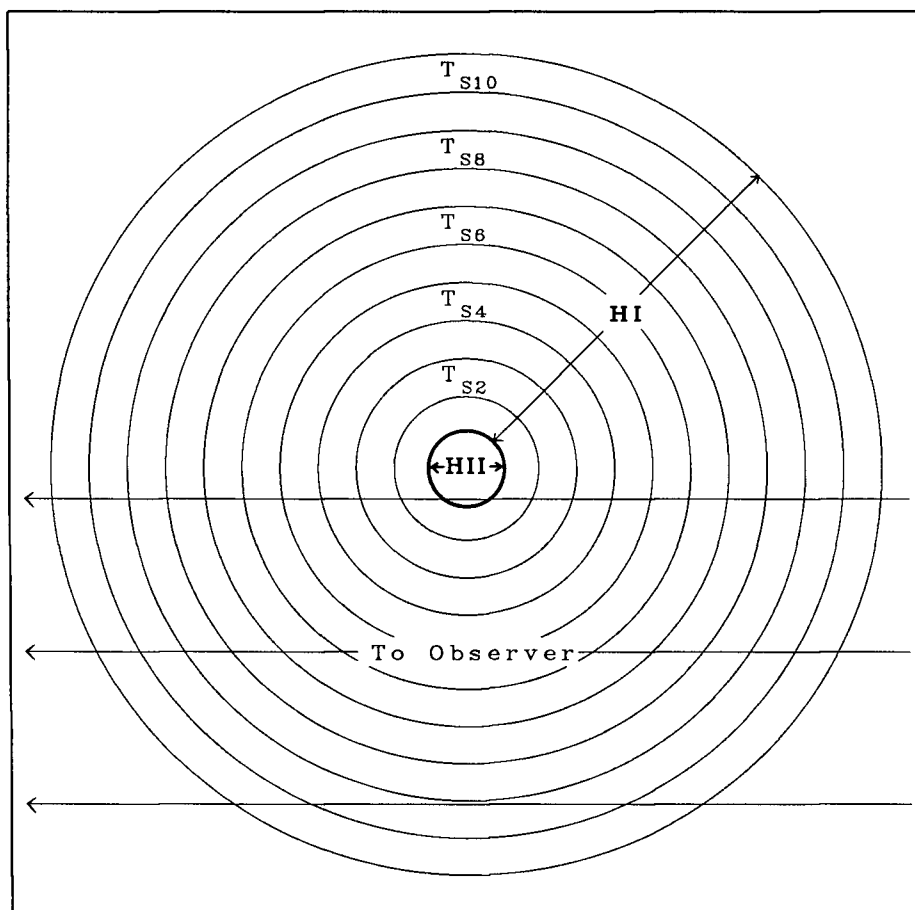


FIG. 4.8: Schematic Representation of Absorption Model 2 S211 (denoted by "HII" above) is considered to be surrounded by concentric isothermal shells of atomic hydrogen (HI). This model is meant to represent an optically thick HI cloud with a temperature gradient such that the outer layers absorb the central frequencies of the emission from the inner layers. (Shell thicknesses not drawn to scale.) As can be seen above, different lines of sight intersect different shells thereby yielding different spectral profiles.

decrease as one looked away from the centre of S211; this would show up as curved emission features in the v - α , δ - v maps. But this is obviously not what is observed. Schematic representations of absorption Models 1 and 2 are shown in Figures 4.7 and 4.8 respectively. Models 1 and 2 also had the problem that the broad emission must have had a velocity width (FWHM) of $12 \text{ km} \cdot \text{s}^{-1}$. This required either an extremely high cloud temperature (i.e. $T_s = 3000 \text{ K}$) or an extremely turbulent cloud.

In the second picture the map 4 emission feature is a separate emission component from that of map 7. Thus we are dealing with a two cloud picture in which Cloud 1 is visible in map 4 and Cloud 2 is in map 7. Because of the reasons given at the beginning of Section 4.2 it seemed that both clouds were part of the S211 complex. In the two cloud model Cloud 2 was in front of Cloud 1 with S211 between them; the two clouds were then expanding away from each other. While this model gave reasonable masses for the two clouds ($2900 M_\odot$ for Cloud 1 and $4100 M_\odot$ for Cloud 2) it left the difficulty of explaining how the two clouds developed such a large relative velocity ($14 \text{ km} \cdot \text{s}^{-1}$). An acceleration mechanism had to be chosen that would also explain why this relative velocity is constant to within $3 \text{ km} \cdot \text{s}^{-1}$ over the faces of the two clouds. One source of acceleration is the HII region thermal expansion. While this would provide the necessary velocity, the HII region is less than $1'5$ in radius and cannot supply acceleration beyond this radius. This is smaller than the $10'$ radius of Clouds 1 and 2. Also it seems unlikely that a $200 M_\odot$ HII region would accelerate $7000 M_\odot$ of atomic hydrogen. Another source of acceleration considered was expansion of a thermal pressure bubble resulting from the O stars' stellar winds striking the surrounding material. In this scenario Clouds 1 and 2 would have been the shell material, or its remains, accelerated by the hot gas and S211 was actually a reverse shock front smoothed by the radio beam in a much larger, more diffuse, HII region. This is represented in Fig. 4.9 reproduced from Kwok and Volk (1985). This model can reproduce the required velocity and cloud

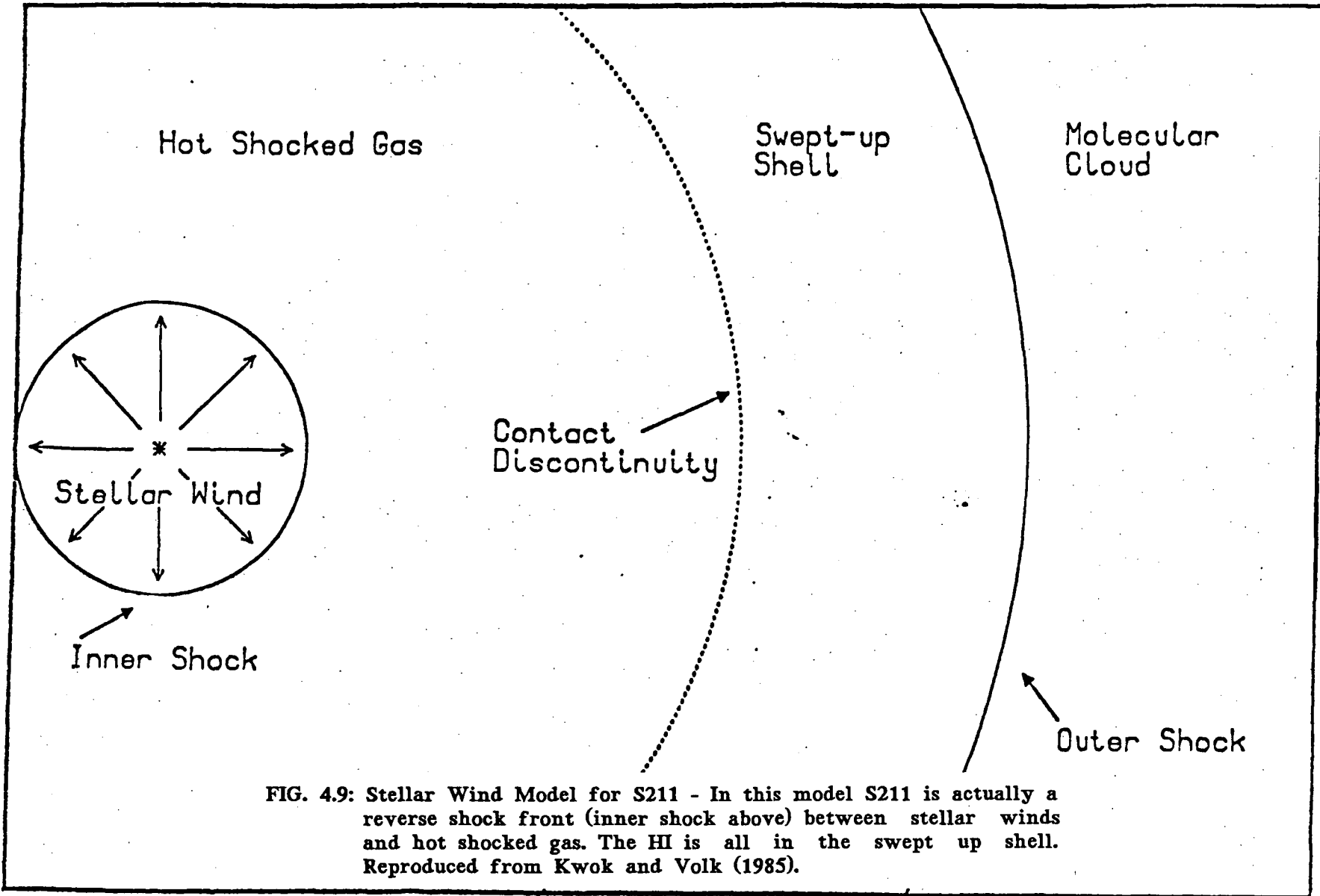


FIG. 4.9: Stellar Wind Model for S211 - In this model S211 is actually a reverse shock front (inner shock above) between stellar winds and hot shocked gas. The HI is all in the swept up shell. Reproduced from Kwok and Volk (1985).

dimensions but it required too high a temperature, 10^6 to 10^7 K, for the hot gas in the reverse shock front. The recombination line observations (Chini & Wink, 1985 priv. comm.) showed that the material visible in the radio continuum map is only at a temperature of 7000 K.

Considering the difficulties involved with the models discussed in this section it became advantageous to “remove” the map 4 emission feature from the S211 cloud complex.

4.3 S212 ATOMIC HYDROGEN EMISSION

Maps showing HI emission near the position of S212 are shown in Appendix F. HI apparently connected with S212, shows up in maps 4 (-22.4 to -24.9 $\text{km} \cdot \text{s}^{-1}$) and 6 (-29.9 to -37.3 $\text{km} \cdot \text{s}^{-1}$). The emission in map 4 looks as though it is part of a long spur projecting northward from a larger complex to the south. In addition, the material is moving at more than 10 $\text{km} \cdot \text{s}^{-1}$ with respect to the molecular material (McCutcheon, 1985 priv. comm.). On the other hand, the material in map 6 appears to be radiating from S212 itself toward the west and south; and it moves within 2 $\text{km} \cdot \text{s}^{-1}$ of the molecular material. Therefore only the material in map 6 is believed to be associated with S212.

To determine column densities and masses, spectra were averaged in rings centered on S212. These were not full rings, but rings divided into four sections: a quarter ring towards each of north, east, south, west. This is illustrated in Appendix F, pages 159 and 162. The rings are $1'$ thick and the corresponding spectra are shown in Appendix F. The western and southern spectra show a strong peak at about -32 $\text{km} \cdot \text{s}^{-1}$ which exists out to $11'$ and $5'$ respectively. The northern and eastern spectra show the peak out to $7'$ and $4'$ respectively.

The actual spatial extent of the material producing the peak is uncertain due to the complicated nature of the spectra. The spectra vary greatly from ring to ring

due to ever abundant foreground and background galactic disk HI. In other words, the baseline to be subtracted is quite changeable from ring to ring. Inspection of the spectra reveals that this baseline, under the S212 peak, gets higher away from S212 and the peak gets lower; the distinction between peak and baseline becomes confused. This is unlike the case of S211 which had an unchanging baseline. This also means that estimates of the column densities and mass are highly uncertain.

The baseline chosen for each spectrum is also shown in Appendix F. These were fitted by a polynomial fitting routine. There was a certain degree of freedom in choosing each baseline in that the user could specify which sections of the spectrum, containing non-baseline features, were to be omitted from the fitting procedure. In short, the baselines are subject, in part, to individual judgement. The baselines chosen probably provide lower limits on the column densities. It is conceivable that the lowest believable baseline could increase the derived column densities by a factor of at most two. Equations 4.12) and 4.14) were again used to derive the column densities shown in Fig. 4.10. (T_{cont} was omitted since the HI is believed to lie behind S212. See Section 5.2.) A Gaussian fitting routine was applied to the peak in each spectrum. This gave velocity widths used to estimate a maximum spin temperature. As was done for S211 the $(\Delta v)^2$ for the three narrowest peaks were averaged and 4.11) was used to obtain

$$T_s(\text{max}) = 370 \text{ K} \quad \text{for cloud west}$$

$$T_s(\text{max}) = 210 \text{ K} \quad \text{for cloud south.}$$

Three spin temperatures were used in 4.14) to obtain the derived column densities and masses: 250 K, 150 K, 70 K. Table 4.2 shows the corresponding masses.

The velocity range for the summation in equation 4.14) for the northern and western spectra (-30 to $-37 \text{ km} \cdot \text{s}^{-1}$) was different from that of the eastern and southern spectra (-28 to $-34 \text{ km} \cdot \text{s}^{-1}$). This is because the S212 HI peak was at a different velocity for the eastern and southern parts of the cloud ($-31.3 \text{ km} \cdot \text{s}^{-1}$

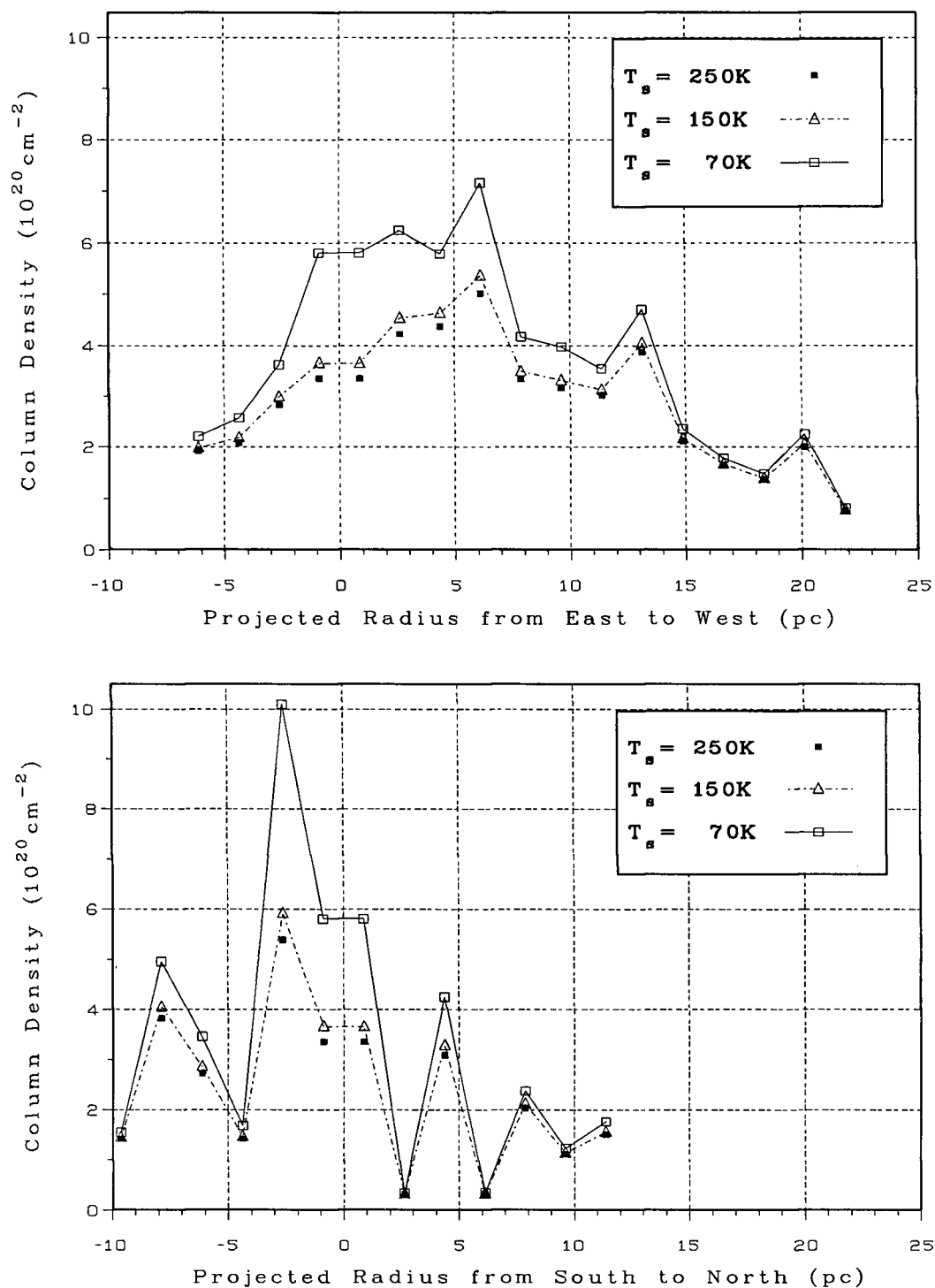


FIG. 4.10: S212 HI Column Densities - HI column densities are plotted vs. projected distance (at $D=6\text{kpc}$) from east to west (at top) and from south to north (just above); the zero denotes the position of the O5.5 star. The column densities were computed from spectra averaged in quarter rings centred on the O5.5 star and oriented towards east, west, south and north (see Appendix F for illustration of quarter ring orientations). The strong fluctuating nature of the profiles, especially for the south to north, may be due to clumpiness of the HI.

for both) than for the western and northern parts of the cloud ($-33.8 \text{ km} \cdot \text{s}^{-1}$ and -32.5 to $-34.6 \text{ km} \cdot \text{s}^{-1}$ respectively). Ring 1 has the same spectrum for all four directions so there was some question as to which velocity range to use for the ring 1 spectrum. The ring 1 material, the eastern and southern material are all believed to lie just beyond S212 itself (see Section 5.2). Therefore the ring 1 column density was derived from the velocity range applied to the eastern and southern spectra.

TABLE 4.2: DERIVED MASSES OF THE S212 HI CLOUD

T_s	Mass
250 K	1130 M_\odot
150 K	1180 M_\odot
70 K	1390 M_\odot

The northern spectra seem to show that the S212 HI peak vanishes in rings 2 and 4. Fig. 4.10 shows that the corresponding column densities are low (around $3 \times 10^{19} \text{ cm}^{-2}$) whereas neighbouring points have high column densities (around $3 \times 10^{20} \text{ cm}^{-2}$). The reason for this double discontinuity not clear; HI not associated with S212 is confusing the picture or the HI cloud is quite clumpy. This latter explanation is supported by CO observations which suggest that the molecular material is clumpy (McCutcheon, 1985 priv. comm.).

A final point to be addressed is the break that appears in the western part of the cloud about $4'$ to $6'$ from the centre. Could it be that the emission beyond this distance is not associated with S212? Examination of the spectra suggests that the peak either drops low after ring 6 or vanishes entirely into the baseline. This question will be discussed further in Section 5.2.

5 A COHERENT PICTURE

In Chapter 1 it was mentioned that S211 and S212 are probably associated with the molecular clouds observed in their directions because HII regions are often found in molecular clouds. This argument is strengthened by the fact that the H112 α recombination line velocities (Chini & Wink, 1984) of S211 and S212 are within 10 km \cdot s $^{-1}$ of their CO velocities (McCutcheon, 1985 priv. comm.). The HI detected around both S211 and S212 is then due to photodissociation of these clouds. Under steady state conditions the amount of HI at a given radius is found by equating the dissociation rate to the rate of reformation on dust grains. According to Hill and Hollenbach, 1978

$$R'n_g n_{\text{HI}} = n_{\text{HI}} I_0 \left(\frac{r_0}{r} \right)^2 \beta N_{\text{H}_2}^{-\frac{1}{2}} \exp(-K'N_g) \quad (5.1)$$

where R' is the reformation rate coefficient, n_g and n_{HI} are the number densities of dust grains, hydrogen atoms respectively. N_{H_2} , N_g are the column densities of hydrogen molecules and dust grains out to distance r . I_0 is the dissociation rate at distance r_0 and K' is the dust absorption coefficient (as opposed to K_d , the dust opacity). The factor $\beta N_{\text{H}_2}^{-\frac{1}{2}}$ accounts for the self-shielding of Lyman band absorption in the square root portion of the curve of growth. If we now let $n_t = n_{\text{HI}} + 2n_{\text{H}_2}$ be the total gas density, where n_{H_2} is the number density of hydrogen molecules, and let N_t be the total gas column density and assume a constant ratio between n_g and n_t then we obtain

$$n_{\text{H}_2} = \frac{Rn_t^2}{2Rn_t + I_0 \left(\frac{r_0}{r} \right)^2 \beta N_{\text{H}_2}^{-\frac{1}{2}} \exp(-KN_t)} \quad (5.2)$$

after absorbing the n_g/n_t ratio into the R' and K' and dropping the primes. Equation 5.2) must be integrated in a reiterative manner since the left side depends on a factor on the right side (i.e. N_{H_2}). Examples of solutions are shown in Sections 5.1 and 5.2 in Figures 5.4, 5.5 and Figures 5.8, 5.9. These were solved by using the

photodissociation model of Dewdney and Roger (1982, unpublished). This is a steady state photodissociation model that assumes a spherically symmetric hydrogen cloud of uniform density n_t with an O or B star at the centre. The program that computes the model parameters first calculates the radius of the HII region surrounding the star and then proceeds to determine the atomic hydrogen density as a function of radius. This is done by calculating the ultraviolet spectrum at a particular radius for the given stellar effective temperature by taking into account $1/r^2$ diminution, scattering by dust, and absorption by the intervening hydrogen; and thus equation 5.2 is solved for n_{H_2} which in turn gives n_{HI} . The ultraviolet spectrum is computed for that gas temperature at which the computed heating and cooling rates are equal; the temperature is adjusted step by step until the heating and cooling rates match. The radial column density (i.e. from the central star) of molecular hydrogen is increased according to the solution of equation 5.2) and the above process is repeated at the next increment in the radius. This continues until the HI density falls to some limiting fraction (usually 1%) of the total gas density n_t . At this point the program terminates by giving the mass of atomic hydrogen in the cloud. Fig. 5.1 shows the mass of dissociated HI versus ZAMS spectral class for different values of n_t .

The photodissociation program not only gives an HI density profile but also a gas temperature profile which can be taken as a spin temperature profile (see Fig. 5.6 and 5.10). In Sections 4.2 and 4.3 it was assumed that the HI associated with S211 and S212 had a constant spin temperature throughout. There is no real difficulty here provided that the atomic hydrogen is optically thin ($T_b \ll T_s$). In this case equation 4.12) is independent of T_s . For a rough test of this condition both Figures 5.6 and 5.10 show brightness temperature profiles. These show that indeed the brightness temperature is considerably less than the spin temperature. However, one must view these comparisons with caution for two reasons:

- 1) The spin temperature curve is temperature plotted against the distance

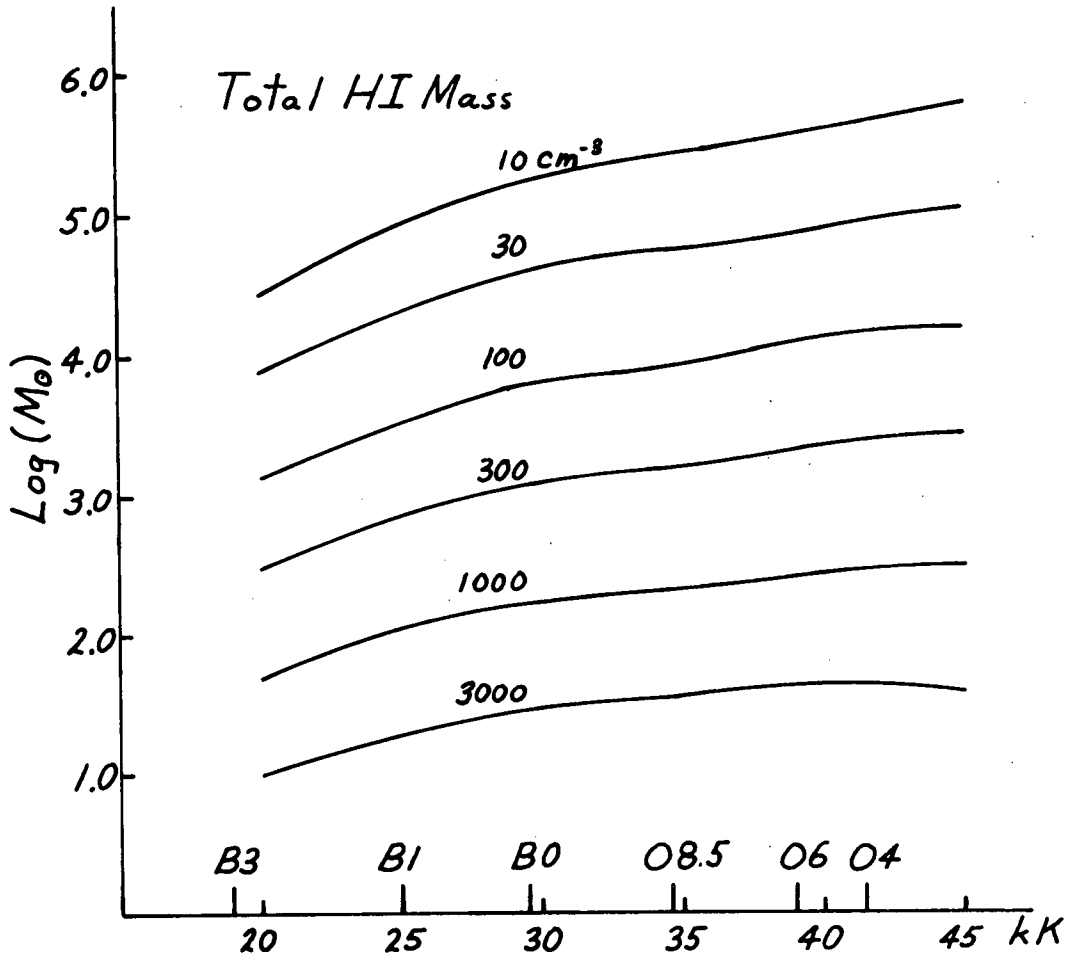


FIG. 5.1: Total HI Mass vs. Spectral Class - The amount of dissociated hydrogen for a given ZAMS spectral type is plotted for different densities of hydrogen atoms. This is reproduced from the unpublished work of Dewdney and Roger (1982).

from the star whereas the brightness temperature profile is temperature versus projected radius. Nevertheless, the comparison may still be useful as a rough indicator of the optical depth of the gas.

2) The spin temperature curves are based on a model in a steady state condition and do not fit the observations (see Figures 5.4 and 5.8). This means that the comparison may not be valid. However, non-steady state photodissociation models have higher spin temperatures thereby enhancing the optically thin condition.

In short it is probably a reasonably good approximation to assume that the HI associated with both S211 and S212 is optically thin.

The column density profiles in Figures 5.4 and 5.8 were derived from the HI density profiles and by assuming a hemispherical geometry for the HI cloud in each case. This is a reasonable geometry for S211 (see Section 5.1) but may not be reasonable for S212 (see Section 5.2). S212's HI cloud may behave like a hemisphere from the centre of S212 towards the west (i.e. quarter sphere) in that the line of sight thickness of the associated HI will vary with projected radius, to the west, in the same way it would for a hemisphere.

The applicability of the steady state photodissociation model to the cases of the S211 and S212 complexes is discussed in Sections 5.1 and 5.2.

5.1 THE S211 COMPLEX

Before applying photodissociation theory to the S211 complex it was necessary to decide on a configuration for the HI surrounding S211. Considering that the velocity of S211 with respect to Cloud 2 is +3 to +6 km·s⁻¹ it was considered likely that S211 is on the back edge of Cloud 2 and is expanding away from its parent cloud. The S211 complex is shown schematically in Fig. 5.2. Expansion of the HI cloud is expected because of heating processes powered by the exciting stars. If Cloud 2

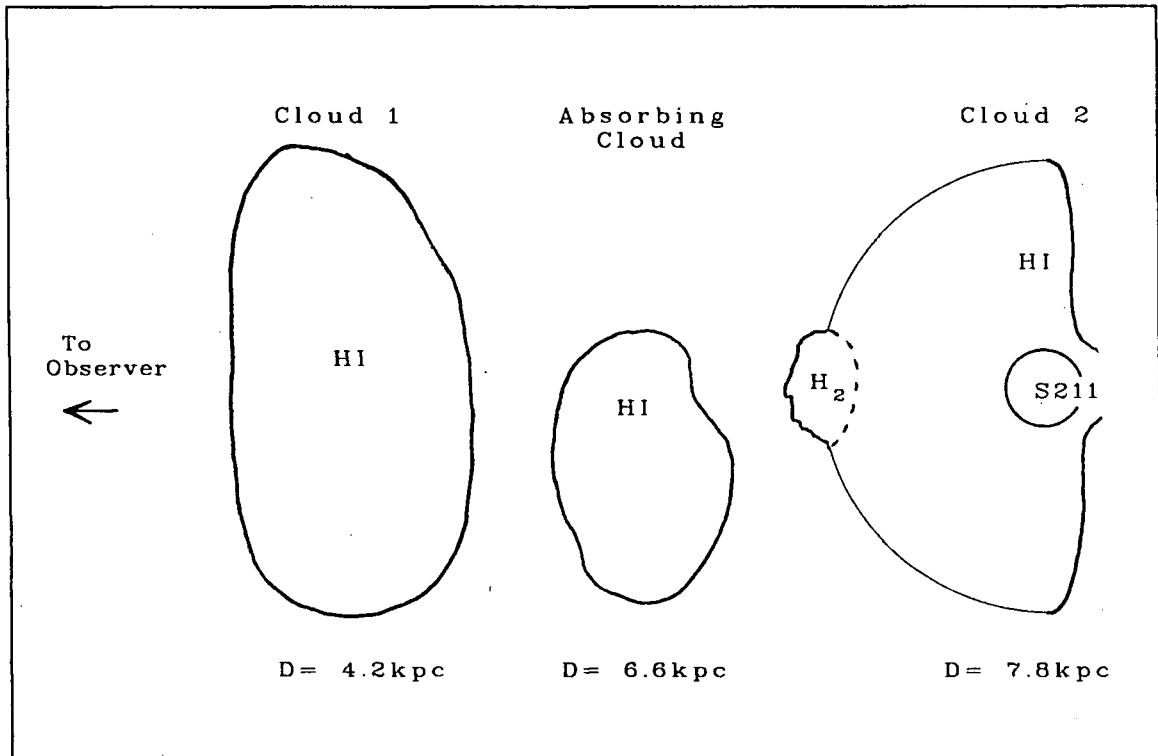


FIG. 5.2: Schematic Representation of the S211 Complex and Foreground Material - S211 may be on the far side of a roughly hemispherical Cloud 2. Cloud 1 and the absorbing cloud lie in the foreground at distances estimated from the Blitz Model of galactic rotation ($V_0 = 250 \text{ km s}^{-1}$, $R_0 = 10 \text{ kpc}$).

does indeed possess the hemispherical geometry depicted in Fig. 5.2 then one would expect the absolute magnitude of the HI velocity to be highest at the centre of Cloud 2 and decrease away from the centre; i.e. the component of expansion along the line of sight decreases. This trend is demonstrated in Fig. 5.3 which shows the HI velocity with respect to the CO velocity plotted against projected radius. These velocities are peak velocities of Gaussians fitted to the ring spectra, after the baseline had been removed (see Section 4.2). It is apparent that the HI has acquired some velocity with respect to undisturbed molecular material. The CO velocity does not show the same trend that is apparent in the HI. In fact, the CO velocity tends to become more negative by $\sim 1.5 \text{ km} \cdot \text{s}^{-1}$ from the centre out to about $3'$ from the centre. A rough average of $-38(\pm 0.8) \text{ km} \cdot \text{s}^{-1}$ was used as the zero point for the velocities in Fig. 5.3. This plot also shows the velocity profile expected for a hemispherical cloud 18 pc in radius expanding at $3 \text{ km} \cdot \text{s}^{-1}$.

Fig. 5.2 suggests that a large amount of material lies between S211 and the observer. McCutcheon has estimated that the column density of H_2 in the direction of S211 to be $1.4 \times 10^{21} \text{ cm}^{-2}$. Fig. 4.6 shows that the central column density of Cloud 2 is $1.6 \times 10^{21} \text{ cm}^{-2}$ and Fig. 4.2 shows the central column density for Cloud 1 to be $1.0 \times 10^{21} \text{ cm}^{-2}$. The column density of the absorbing cloud was found to be only about $1 \times 10^{20} \text{ cm}^{-2}$. The total column density of hydrogen due to Cloud 2, Cloud 1 and the absorbing cloud is then $N(\text{HI} + \text{H}_2) \simeq 4 \times 10^{21} \text{ cm}^{-2}$. The total $B - V$ colour index due to the HI and H_2 clouds is then $E(B - V) = 0.7$ magnitudes based on a value of $\langle N(\text{HI} + \text{H}_2) / E(B - V) \rangle = 5.8 \times 10^{21} \text{ cm}^{-2} \cdot \text{mag}^{-1}$ from Savage & Mathis, 1979. Chini & Wink have measured $E(B - V) = 1.6$ to 1.7 for the exciting stars. Therefore the above mentioned clouds can indeed contribute to the observed extinction, implying that the configuration depicted in Fig. 5.2 is not unreasonable.

In order to apply equation 5.2) to the S211 molecular cloud it was necessary to choose a density, n_t , for the molecular cloud. This corresponds to the peak density of HI near the ionization boundary. The standard approach for estimating n_t is to

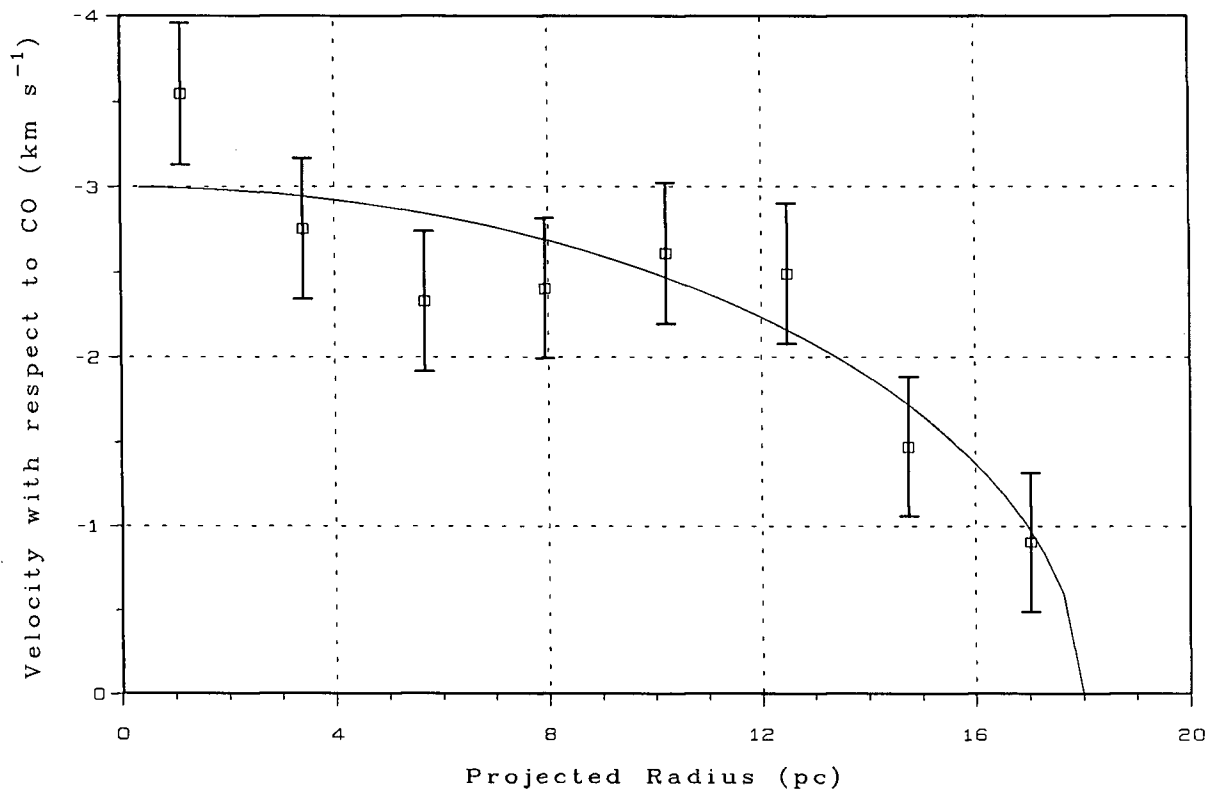


FIG. 5.3: Systematic HI Velocity Variation for S211 Complex. The velocity of Cloud 2 with respect to the CO velocity measured by McCutcheon, 1985 (-38 km s^{-1}) is plotted against projected radius (at $D = 7.8 \text{ kpc}$). The vertical error bars assume the HI velocity is uncertain by one channel velocity width (i.e. $\pm 0.4 \text{ km s}^{-1}$). The solid line represents the velocity profile expected from a hemispherical cloud of radius 18 pc expanding at 3 km s^{-1} .

take the peak HI column density and divide by the projected size of the HI cloud. This approach has difficulties with S211 because it yields a density lower than the HII region density, i.e. 70 cm^{-3} . This is also the case for the HII and HI surrounding LkH α 101 (Dewdney and Roger, 1982). One can account for the HII density being higher than the HI density by reasoning that the HII region formed in a denser part of the cloud complex, it is particularly young and had not had the time to expand to the point where its density was lower than that of the surrounding HI. It could also be that the HI density has been underestimated. This could be due to a density gradient in the HI so that the projected size is overestimated. Also, galactic plane emission contaminating the field may contribute to the projected size.

It was assumed that the HI density had been underestimated and a new HI density was estimated. (In either case it was necessary to use a higher value for the HI density in order to estimate the ages given in Section 3.4). The next best way of estimating the density was to use the HII region density as a lower limit and the density derived from Fig. 5.1 as an upper limit. The three stars exciting S211 produce the same Lyman continuum photon flux as an O6 ZAMS star. Even though it is not the Lyman continuum photon flux that is responsible for the dissociation (these photons are used up in the HII region), it was probably not a bad first approximation in taking the ZAMS spectral class corresponding to this value when using Fig. 5.1. The mass of the S211 HI cloud is $4000 M_{\odot}$ which implies a maximum HI density of around 200 cm^{-3} (assuming the equivalent of an O6 star). The HII region density is 85 cm^{-3} so that the density of the surrounding atomic gas is between about 90 cm^{-3} and 200 cm^{-3} . S211, according to Fig. 5.2, is dissociating a hemisphere of molecular material. That means it is capable of dissociating $8000 M_{\odot}$ of H_2 into HI. Figure 5.1 then implies a density of about 100 cm^{-3} . This was the density adopted for the S211 complex keeping in mind that it is uncertain from about 90 cm^{-3} to about 200 cm^{-3} . Assuming a hemispherical geometry gives the column density profiles shown Figure 5.4. These were done for two total gas

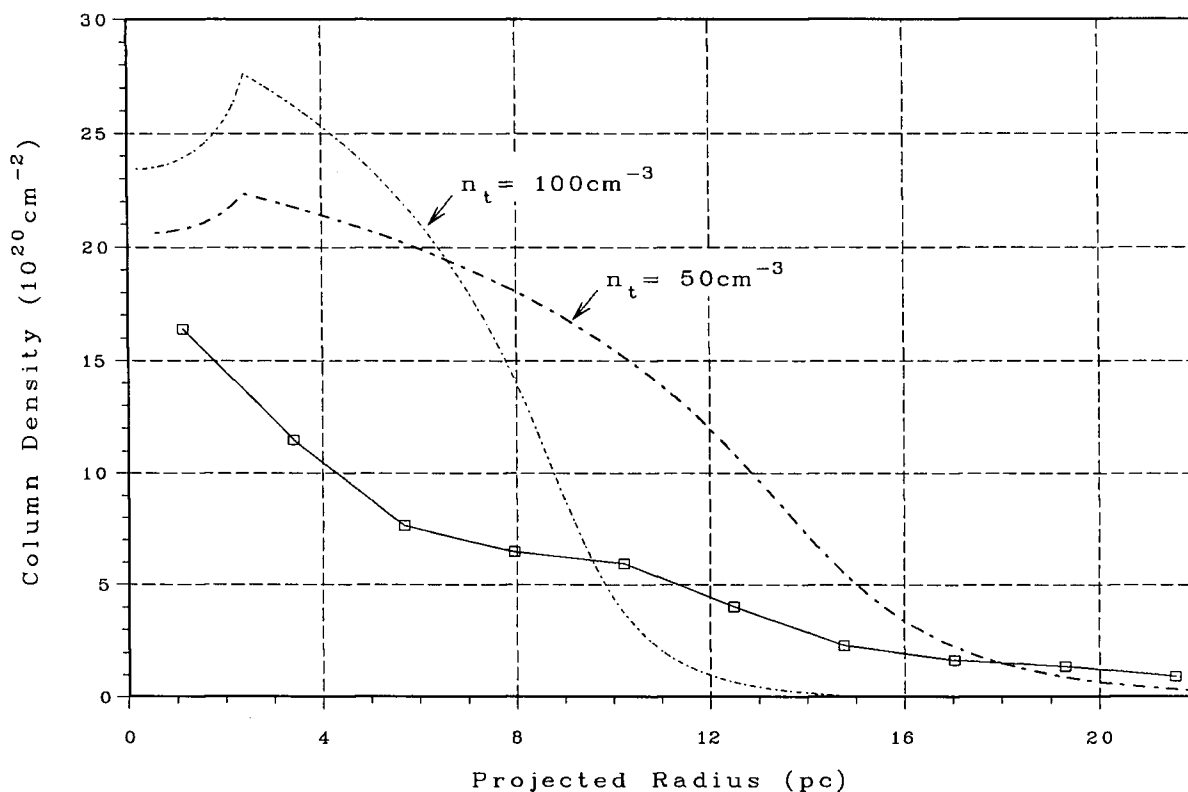


FIG. 5.4: Theoretical Column Density Profiles (S211) - HI column density is plotted against projected radius (at $D= 7.8\text{kpc}$) for the Dewdney and Roger (1982) photodissociation model (dashed lines) and for S211's observed HI (solid line). The observational curve for the S211 HI cloud assumes $T_s= 140\text{K}$. The model curves were plotted for two different values of the total gas density ($n_t= n_{\text{HI}} + 2n_{\text{H}_2}$). S211's ionizing stars are likely too young for the photodissociation to have reached a steady state condition, which would account for the discrepancy between model and observation. The rise in the model curves out to 2.5pc is due to the geometric effect of assuming a spherical HII region contained within the HI.

densities, $n_t = 100 \text{ cm}^{-3}$ and $n_t = 50 \text{ cm}^{-3}$ and an effective stellar temperature of 40000 K. Neither theoretical curve agrees with the observed column density profile also shown in Figure 5.4. There are two possible reasons for this disagreement. Firstly, the shape of the HI cloud may deviate from that of a hemisphere. But in order for the observed and theoretical curves to match, the theoretical curves must be brought down by a factor of as much as 3 in some places. This requires a shape markedly differently from that of a hemisphere which contradicts the evidence, discussed earlier in this section, advocating such a geometry.

The second more likely reason for the discrepancy is that S211 and its ionizing stars are too young to have reached a steady state with the reformation process. Dewdney (1986, priv. comm.) estimates a time of at least 10^6 to 10^7 years is required to achieve steady state. S211 is probably less than about 10^5 years old. In other words, as S211's stars dissociate more and more H_2 the observed HI column density curve should rise until it meets one of the theoretical curves in about 10^6 to 10^7 years from now, provided that the supply of H_2 is not exhausted and assuming no significant stellar evolution. The $n_t = 100 \text{ cm}^{-3}$ curve terminates too quickly, at 15 pc, whereas the observed profile extends out to about 22 pc. This means that the actual S211 HI cloud column density profile could never evolve to match the $n_t = 100 \text{ cm}^{-3}$ curve beyond 15 pc since this theoretical curve terminates there. The $n_t = 50 \text{ cm}^{-3}$ curve, however, does not cut off before 23 pc and is thus more likely to match the actual column density profile.

The column density curves imply a total gas density of around 50 cm^{-3} which is less than the HII region density. Since the HII region density must be less than that of the material out of which it formed, the value 50 cm^{-3} can be taken as an average of the total gas density, n_t , over the entire cloud volume. The S211 complex is better modelled by a cloud with a density gradient in the total gas density. This leads to the question of the applicability of Fig. 5.1 in estimating the HI density, just outside the HII-HI boundary, in the first place; the photodissociation model

of Dewdney and Roger assumes a steady state and a constant density – neither of which seems to apply to the S211 complex. Assuming a steady state model for a non-steady state cloud means that Fig. 5.1 overestimates n_t (i.e. average n_t for a non-zero gradient). Assuming a uniform density model for a cloud with a density gradient means that Fig. 5.1 underestimates the total gas density just outside the ionization boundary (same as the HI density at this position) provided that a steady state exists. But a steady state does not exist so that the density estimates obtained from Fig. 5.1 could be higher or lower than n_{HI} just outside the HII region; the value of n_{HI} outside HII-HI boundary does not then necessarily fall in the range 90 cm^{-3} to 200 cm^{-3} estimated earlier. Fortunately the exact value of n_{HI} at the ionization boundary is only really important in determining the age of the HII region (and boundary conditions such as shock expansion velocity) and the age is not all that sensitive to this value. (See Section 3.4 for details.)

The Dewdney and Roger photodissociation model can still be used to confirm estimates of the average n_t through the use of column density comparisons such as the one in Fig. 5.4; i.e. dimensional arguments give $n_t = 70 \text{ cm}^{-3}$ and Fig. 5.4 suggests $n_t \simeq 50 \text{ cm}^{-3}$. A much better fit could be made to the observed column density curve but would require assuming a much lower gas density, i.e. 10 to 20 cm^{-3} . This is unreasonably small compared with the density obtained from dimensional arguments and the theoretical curve would have a long tail beyond the 20 pc extent of S211's HI cloud.

Figure 5.5 shows the density profiles that were integrated to yield the theoretical column density profiles shown in Figure 5.4. Considering that a photodissociation model with a density gradient would have been more appropriate, neither of these two curves apply to S211's associated HI. A more appropriate curve would not show the flat plateaus shown in Fig. 5.5; it would show a decreasing curve in place of those plateaus.

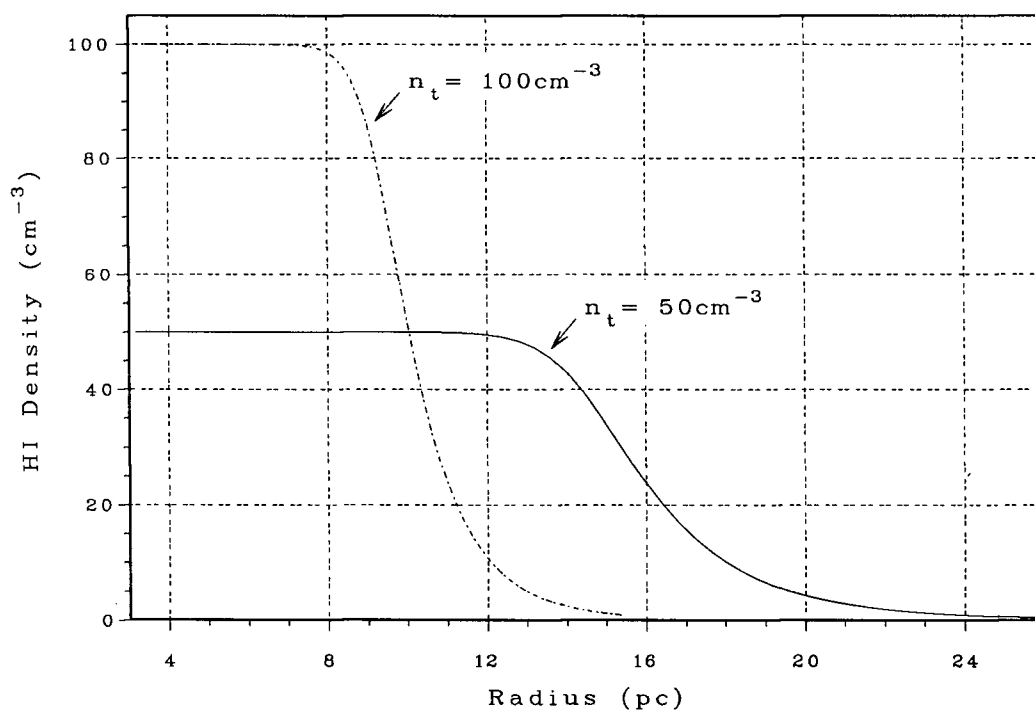


FIG. 5.5: Theoretical HI Density Profiles (S211) - HI density is plotted against distance from the central star(s) for two different values of the total (HI and H₂) gas density according to the photodissociation model of Dewdney and Roger (1982).

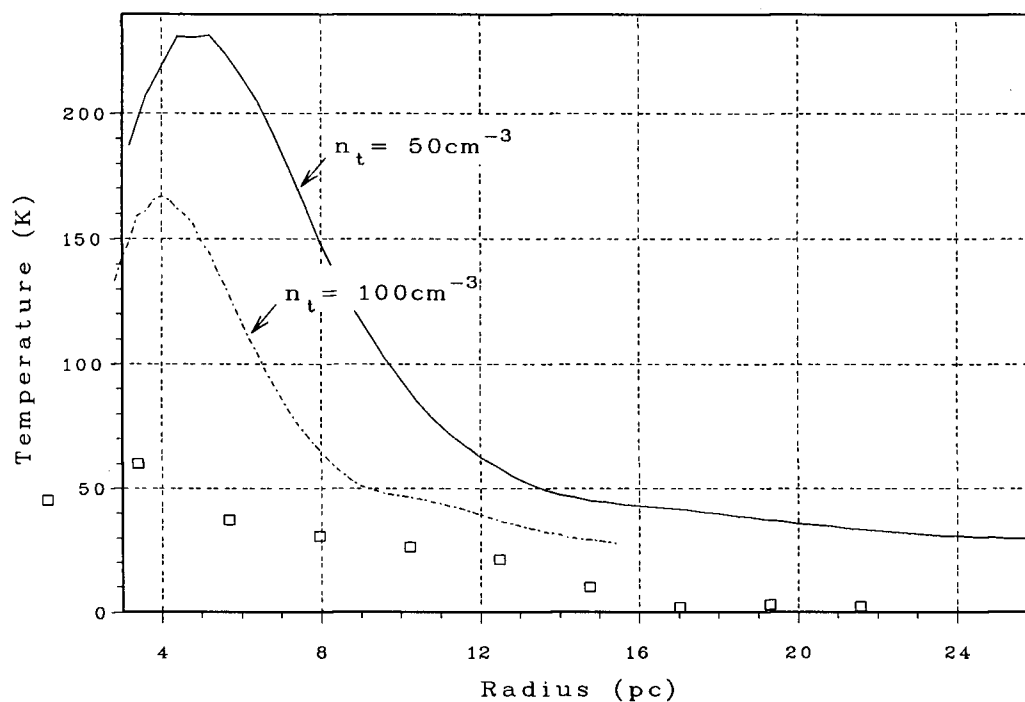


FIG. 5.6: Theoretical Temperature Profiles (S211) - Spin temperature versus distance from the central star(s) is shown for two possible values of the total gas density according to the photodissociation model of Dewdney and Roger (1982). The initial rise of the curves is due to decreasing charge on dust grains which enhances photoelectric heating of the surrounding gas. Brightness temperature of the S211 HI cloud versus projected radius is shown (squares) for comparison.

Figure 5.6 shows the theoretical spin temperature profiles as compared with the observed brightness temperature profile. The brightness profile was produced by averaging each ring spectrum over the velocity range of map 7 of Appendix E (i.e. -34.8 to $-43.5 \text{ km} \cdot \text{s}^{-1}$) and subtracting the baseline spectrum averaged over the same velocity range. The comparison of the theoretical and observational curves shows that, to first approximation, the HI surrounding S211 is optically thin.

In short, it would seem that application of photodissociation theory to the S211 complex requires a non-steady state model with a density gradient. Map 7 of Appendix E shows that S211's HI is extended more towards the south than in any other direction. This may be modelled by assuming a steeper decline in the total gas density towards the south than elsewhere.

5.2 THE S212 COMPLEX

In map 6 of Appendix F the HI associated with S212 is moving at -31 to $-35 \text{ km} \cdot \text{s}^{-1}$. S212 itself is moving at $-41.8 \text{ km} \cdot \text{s}^{-1}$ (H112 α recombination line, Chini & Wink, 1984). The difference of 9 to 11 $\text{km} \cdot \text{s}^{-1}$ compares well with the $V_s = 10 \text{ km} \cdot \text{s}^{-1}$ derived in Section 3.4. This suggests that S212 is either in front of the HI visible in map 6 or S212 is at the same distance as the HI in map 6. The HI lying directly towards S212 must be behind since S212 is moving towards the observer faster than the HI. For the material lying to the north, east, south, and west the density gradients of S212 (see Tables 3.1 and 3.2) provide the answers. To the west the density rises implying that the ionized hydrogen is contained by material to the west. Hence the western HI is at the distance of S212 - i.e. beside S212. To the south the density falls implying that the HII is not contained so that the southern material lies just beyond S212. To the north the density remains constant implying that the HI to the north is beside S212. To the east the density decline is at its steepest ($-6 \text{ cm}^{-3} \cdot \text{pc}^{-1}$) suggesting that the little material that exists to the east is in the background.

The supposition that the eastern and southern HI lie at the same distance as each other, and that the same applies to the northern and western HI, has some support from the velocity information: the southern and eastern HI share a peak velocity of about $-31.3 \text{ km} \cdot \text{s}^{-1}$ and the northern and western HI have a peak velocity of about $-32.5 \text{ km} \cdot \text{s}^{-1}$ to $-34.6 \text{ km} \cdot \text{s}^{-1}$ (see Section 4.3). It would then seem reasonable that the HI to the east and to the south also share a similar position with respect to S212. The same argument applies to the northern and western HI.

It is difficult to say whether or not S212 is density bounded towards the observer. In map 7 (-37.3 to $-47.2 \text{ km} \cdot \text{s}^{-1}$) of Appendix F we see HI at S212's position that could be material pushed by S212's expansion. In the declination-velocity (δ - v) and velocity-right ascension (v - α) maps (pages 157 and 158) in Appendix F this hypothetical "swept-up" HI is $4'$ in extent and is found at $-42 \text{ km} \cdot \text{s}^{-1}$ to $-47 \text{ km} \cdot \text{s}^{-1}$. If it is part of the S212 complex then it has a mass of $50 M_{\odot}$ ($T_s = 250 \text{ K}$) or $60 M_{\odot}$ ($T_s = 150 \text{ K}$). Also notice in the δ - v and v - α maps that there is little HI emission at roughly $-41 \text{ km} \cdot \text{s}^{-1}$ at the position of S212. This suggests that most of the HI at this velocity has been ionized. On the other hand, not all the HI in map 7 is around S212. It is possible that it is a chance superposition of HI emission and HII emission. In this case S212 would be density bounded toward the observer.

As mentioned in Section 4.3 the western part of the HI cloud exhibits a "break" at about $4'$ to $6'$ from S212. The HI more than $6'$ from S212 may not be associated. The CO emission to the west and at this angular separation from the centre is weak ($T_A^*(^{12}\text{CO}) < 3.0 \text{ K}$ and $T_A^*(^{13}\text{CO}) < 0.3 \text{ K}$ where T_A^* is the mm-wave analog of T_b). One can either infer that the stars of S212 have dissociated all the molecular material to the west or that the HI more than $6'$ to the west was never part of the S212 complex in the first place. If the latter case applies then the mass of the S212 HI is overestimated by $\sim 500 M_{\odot}$. The most likely explanation for the break in the intensity is that galactic plane HI emission increases beyond $6'$ to the west just as

the S212 HI is decreasing; i.e. the HI at this angular distance from the centre is a mixture of S212 HI and galactic plane HI.

There is strong CO emission to the east of S212 and yet there is little HI to the east of S212. This means that either the molecular material is extremely resistant to dissociation, i.e. $n_t > 10^3 \text{ cm}^{-3}$, or it is not associated with the S212 complex.

The S212 complex is represented in Fig. 5.7. The extinction one can infer from Fig. 5.7 would be small; Chini & Wink (1984) and Moffat et. al. (1979) measure $E(B - V)$ to be 0.84 to 0.91 for S212's stars. Notice that S212's $B - V$ colour excess is less than that of S211; this is partly because S212 is believed to be on the front of its molecular cloud whereas S211 is believed to be behind its molecular cloud. This would explain why S211 is not visible in the O print from the Palomar Sky Survey even though S212 is still visible.

Because of the extreme baseline difficulties it is difficult to determine if systematic motions are present in the S212 HI. However the spectra of the northern part of the cloud show clearly that the velocity changes systematically from $-32.5 \text{ km} \cdot \text{s}^{-1}$ at ring 3 to $-34.6 \text{ km} \cdot \text{s}^{-1}$ at ring 7. The same trend seems to be present in the CO velocity. It is then probable that the behaviour of the northern HI is due to the properties of the original molecular cloud. This is already believed to explain the double discontinuity phenomenon discussed in Section 4.3.

The density of the S212 complex had to be estimated in the same way as done for S211 (the standard approach gives 30 cm^{-3}); the mass of HI implies a certain density for a given spectral type of dissociating stars, i.e. refer to Fig. 5.1. If we assume that S212 has $1000 M_\odot$ of atomic hydrogen in a westward facing cone of apex angle 90° then one-sixth of a full sphere is dissociated. This means the stars of S212 are capable of dissociating $6000 M_\odot$ of hydrogen. Fig. 5.1 then implies a density of 100 cm^{-3} assuming the equivalent of an O6 star. If the outer region of

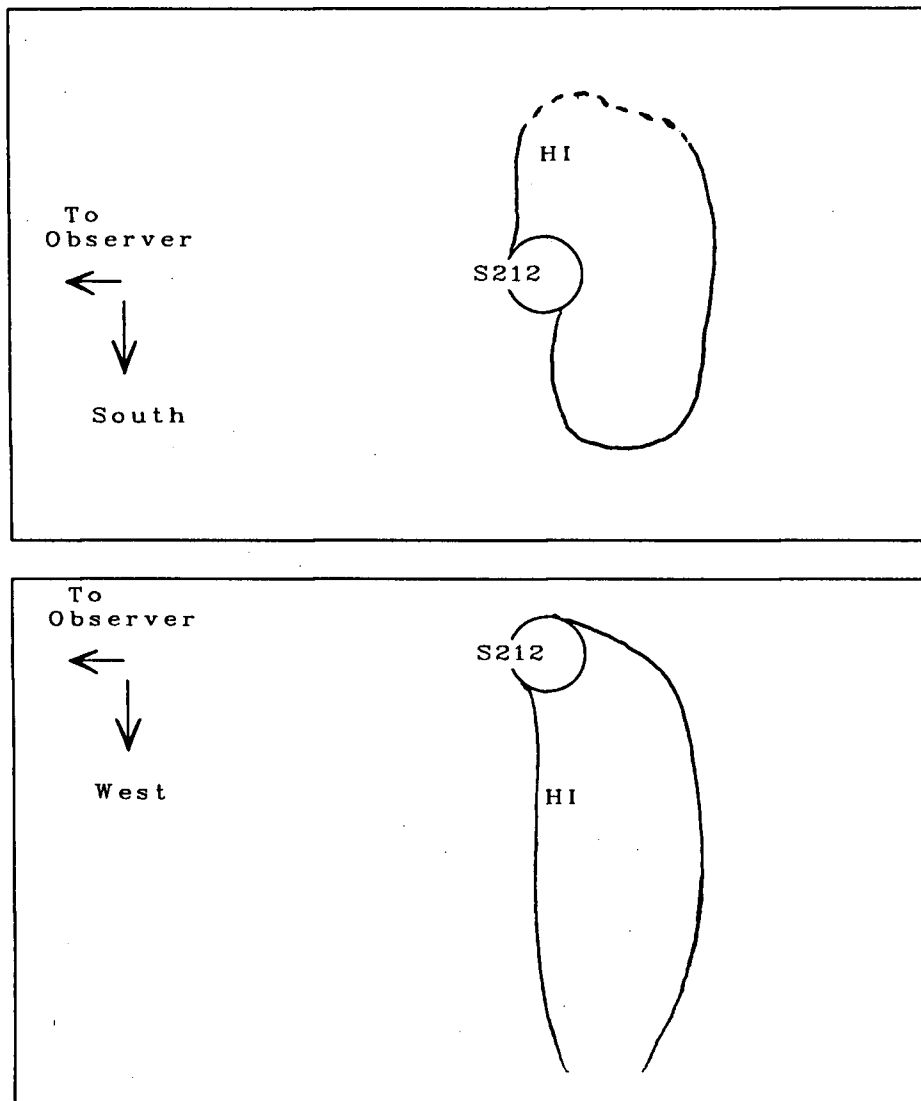


FIG. 5.7: Schematic Representation of S212 Complex - The top diagram shows the S212 complex in the plane formed by the line of sight and the north-south axis. The diagram below is the east-west analog of the top diagram. Notice that S212 is represented as being density bounded towards the east, south and the observer.

the western part of the cloud ($> 6'$) is not part of the S212 complex then it may be that the S212 stars are only capable of dissociating $1000 M_{\odot}$. This would give a density of 500 cm^{-3} . Hence the S212 complex has density of about 100 cm^{-3} but could be as low as 70 cm^{-3} (peak HII region density) and as high as 500 cm^{-3} .

Figure 5.8 shows the column density profile for the HI west of S212 as compared with a theoretical column density profile ($n_t = 100 \text{ cm}^{-3}$, $T_{\text{eff}} = 45000 \text{ K}$). Comparison between theory and observation to the north, south and east would be more dubious due to the more erratic variations of the observed column density curves in these directions. As in the case for S211's HI there is a large discrepancy between the observational and theoretical column density curves. S212 is also a young HII region but the uncertainty in the geometry of the associated HI is probably just as important in explaining this discrepancy; there is no evidence, as there is for S211, that the HI associated with S212 should behave as a hemisphere. It did not seem necessary to plot theoretical curves for values of n_t lower than 100 cm^{-3} considering the uncertainties in the shape of S212's HI cloud and considering the fact that the actual extent of the HI is unknown due to baseline uncertainties. The density of 100 to 500 cm^{-3} from Fig. 5.1 may be an overestimate for the average n_t (averaged over the whole cloud) and an incorrect estimate for n_{HI} just outside the ionization boundary. Again the effect of this on age estimation is discussed in Section 3.4.

Figures 5.9 and 5.10 show the theoretical density and spin temperature profiles respectively for $n_t = 100 \text{ cm}^{-3}$. Since a non-steady state photodissociation model would be applicable to S212's HI the temperature profile illustrated in Figure 5.10 is a lower limit to the actual temperature profile. Hence the comparison of this curve with the observed brightness temperature profile, also shown in Figure 5.10, suggests that the HI associated with S212 may be optically thin. The brightness temperature profile was produced by averaging the west quarter-ring spectra, with polynomial baselines subtracted, over the velocity range of map 6 of Appendix F (i.e. -29.9 to $-37.3 \text{ km} \cdot \text{s}^{-1}$).

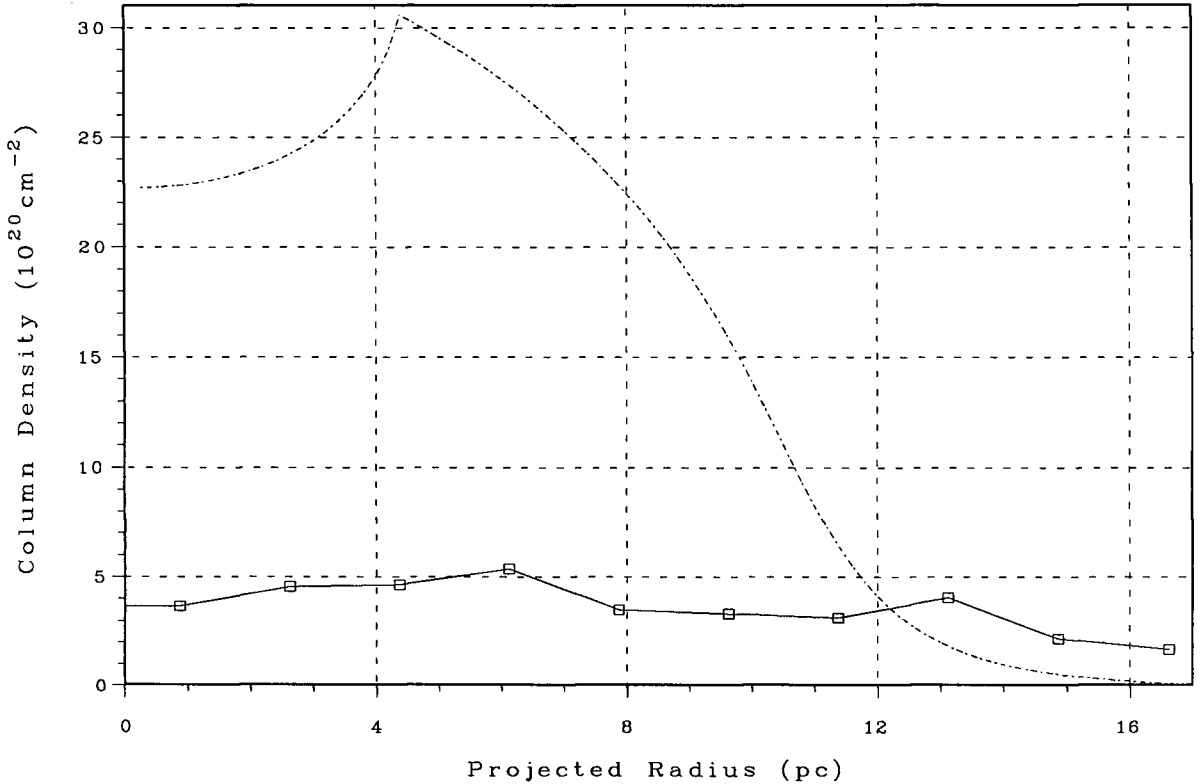


FIG. 5.8: Theoretical Column Density Profile (S212) - HI column density is plotted against projected radius (at $D= 6\text{kpc}$) for the Dewdney and Roger (1982) photodissociation model (dashed line) and for S212's observed HI (solid line). The observational curve represents the column densities of the HI to the west of S212, averaged between position angles 225° and 315° , and assumes $T_s = 150\text{K}$; column density profiles for HI in other directions vary more erratically. The model curve was plotted for a total gas density ($n_t = n_{\text{HI}} + 2n_{\text{H}_2}$) of 100cm^{-3} . Uncertainties in the geometry and the young age of S212's ionizing stars could account for the large discrepancy between model and observation. A curve assuming a lower total density would probably reduce this discrepancy but the projected extent of the HI to west of S212 is uncertain.

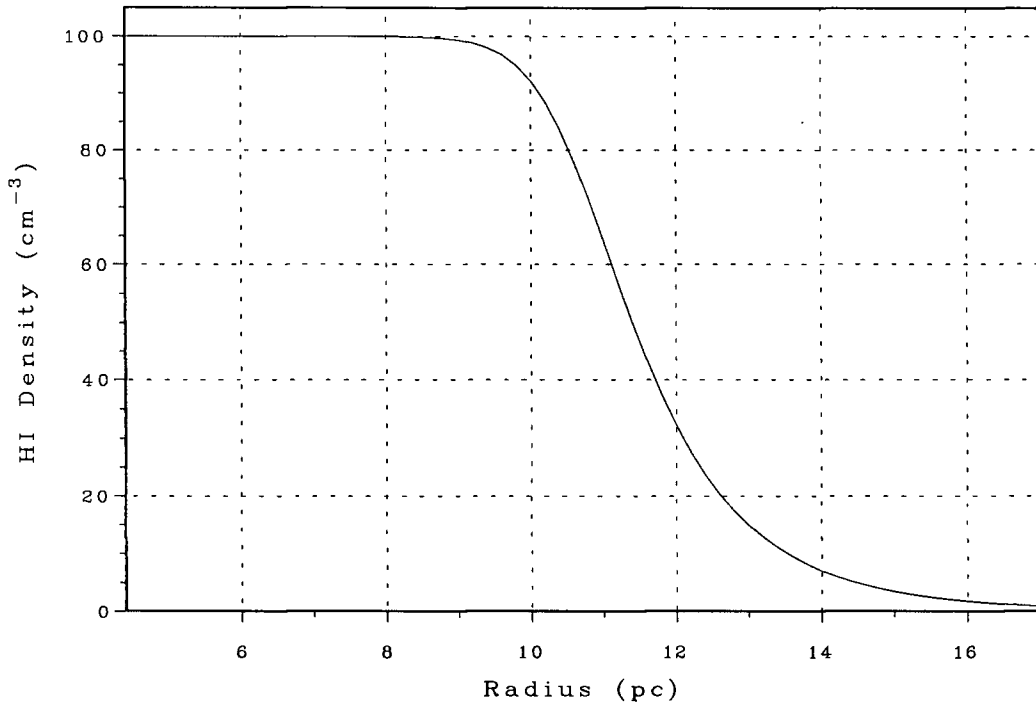


FIG. 5.9: Theoretical HI Density Profile (S212) - HI density is plotted against distance from the central star(s) for a total (HI and H₂) gas density of 100cm⁻³ according to the photodissociation model of Dewdney and Roger (1982).

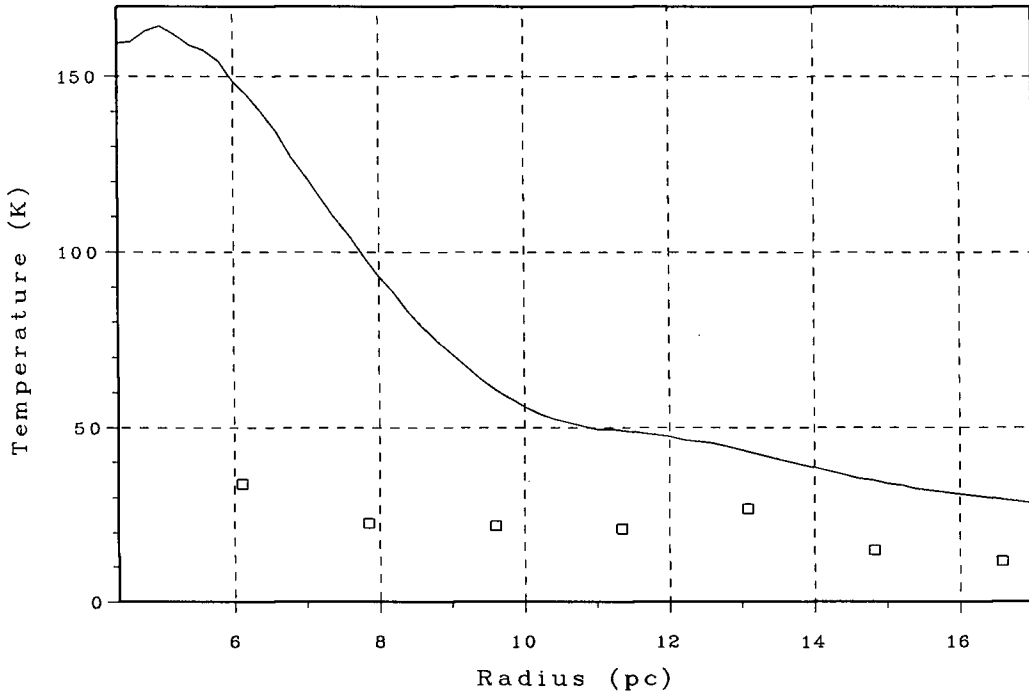


FIG. 5.10: Theoretical Temperature Profile (S212) - Spin temperature versus distance from the central star(s) is shown for a total gas density of 100cm⁻³ according to the photodissociation model of Dewdney and Roger (1982). Brightness temperature of the HI to the west of S211, averaged over position angles 225° to 315°, versus projected radius is shown (squares) for comparison.

It would seem that application of photodissociation theory to the HI surrounding S212 is complicated by the complexities of the HI geometry, clumping of the HI, and S212's young age. The extent of the HI differs in various directions, which is probably due to the fact that the HII region formed near the edge of its parent cloud, thereby giving a smaller extent to the east than elsewhere.

6 CONCLUSIONS AND DISCUSSION

It has been found that both HII regions, S211 and S212, have the mass and extent consistent with the UV emission expected from an O6V star. Both HII regions have densities that are higher than the HI densities averaged over the volume of their respective HI clouds. There is evidence for density gradients in the HII and the HI for both the S211 and S212 complexes although S211 itself was modelled as a constant density HII region due to its smaller angular size (1.7 beam widths). Both cloud complexes show evidence for clumping of the H_2 (McCutcheon, 1985 priv. comm.) and the S212 complex shows evidence for clumping of the HI (i.e. Fig. 4.10) and of the HII (see Section 3.4). The clumping and density gradients mean that the HI properties of neither complex fit the steady state photodissociation model of Dewdney and Roger (1982) which assumes a constant total gas density ($n_t = n_{HI} + 2n_{H_2}$) throughout the cloud. In addition to this neither HII region is believed to be much older than about 10^5 yrs and could be as young as 10^4 yrs; steady state photodissociation models would not apply to such young objects. The belief in such young ages is supported by the presence of clumps, the high HI density to HII density ratios and the simple geometry of the HII regions as seen in optical photographs.

Other detailed studies of HII/HI/ H_2 complexes include those by Roger and Irwin, 1982 (IC5146 and associated HI/ H_2), Roger and Pedlar, 1981 (NGC281 and associated HI/ H_2), and Dewdney and Roger, 1982 (complex enveloping the emission line star LkH α 101). Some parameters of these HII regions and their associated HI are listed in Table 6.1. The S211 and S212 complexes were more difficult to study in that they were much further away than any of the objects studied by the authors above; S211 and S212 are at distances of 6.0 and 7.8 kpc respectively as opposed to 2.3 kpc for NGC281, 0.96 kpc for IC5146 and 0.8 kpc for LkH α 101. S211 is about 2.4pc in radius and contains about $130 M_{\odot}$ of ionized hydrogen. S211 may be density

bounded along the line of sight as is the HII region IC5146 (Roger and Irwin, 1982). But S211 has an order of magnitude more ionized hydrogen than IC5146 because the Lyman continuum photon flux is about 10^2 times lower for IC5146. IC5146 was best modelled with a Gaussian density profile. The density profile of S211 may also be Gaussian depending on whether or not S211 is density bounded along the line of sight. S211 was barely resolved by the CC Survey so that it was not easy to distinguish between the constant density model and the Gaussian density model. S212 extends as little as 3.3 pc, to the east, from the major ionizing star and as much as 6.1 pc, to the west, and contains about $300 M_{\odot}$ of HII. This is about 30 times more HII than in IC5146 but is also about 7 times less HII than is found in NGC281 (Roger and Pedlar, 1981). Like S212 the HII region NGC281 is density bounded, possibly on more than one side. It was basically modelled as having a Gaussian density profile with a $1/e$ radius of 8.8 pc and a peak density of 22 cm^{-3} . S212 could have been modelled in the same way but it was simpler to model the asymmetrical emission measure profiles (north-south and east-west) as being due to linear density gradients. S212 was also only slightly resolved (2.6 beam widths) by the CC Survey observations so that the distinction between the two density models is not clear.

The maximum extent of the HI for both complexes is about 20 pc. With the exception of the long tail to the south, the HI surrounding S211 is roughly circularly symmetrical and has a mass of $4000 M_{\odot}$. On the other hand, the HI associated with IC5146 extends only about 6 pc from the exciting star and has a mass of only about $400 M_{\odot}$ (Roger and Irwin, 1982). The HI associated with S212 extends about 20 pc only to the west and extends much less than this in other directions, e.g. 6 pc to the east. S212 has only about $1200 M_{\odot}$ of associated HI whereas NGC281 possesses about 3 times this amount of HI. NGC281 is similar to S212 in that it lies on one side of its HI in the "plane of the sky" and consists of more than one cloud. The HI to the north and to the south of S212 shows column density variations that suggest that the HI in these directions may be separated into distinct clouds.

TABLE 6.1: COMPARISON OF HII/HI PARAMETERS

	S211	S212	IC5146	NGC281	Lk α 101
Distance (kpc)	6.0	7.8	0.96	2.3	0.8
Ionizing Photon Flux (10^{47}s^{-1})	180	190	1.7	80	0.18
HII Region Radius* (pc)	2.4	4.1	1.7	8.8	0.05
HII Mass (M_{\odot})	130	300	9.8	2100	85
Average HII Density (cm^{-3})	85	50	26	22*	850
Flux Density [†] (Jy)	0.79	1.60	1.95	21.3	0.18
	± 0.04	± 0.12	± 0.10	± 1.5	± 0.02
HI Extent [‡] (pc)	20	20	6	15	3
HI Mass (M_{\odot})	4000	1200	400	3500	85
Average HI Density (cm^{-3})	70	30	350	20	200

*Averaged over position angle

[†]At 1.42 GHz

[‡]From ionizing star

*Peak Density

Another interesting aspect of S212 is the evidence of clumping in the HII. Densities derived from optical line ratios (Talent & Dufour, 1979) as compared with densities derived from radio continuum observations have shown that the fraction of the HII region volume occupied by clumps or blobs varies ranges from about $F = 1/1600$ to $F = 1/300$ (Section 3.4). These numbers suggest a very high degree of clumping; the same ratio for the Orion nebula is $1/30$ (Osterbrock and Flather, 1959). This means that the mass of S212 is concentrated into relatively few clumps as compared with the Orion nebula. It is interesting to speculate on the mass of the clumps. Assuming that they subtend less than a second of arc at a distance of 6 kpc their mass could reach about $0.05 M_{\odot}$ – close to the typical mass

for a red dwarf. These clumps probably originated in the parent cloud from which S212 formed. This view is weakly supported by the clumpy nature of the molecular material observed in the CO emission (McCutcheon, 1985 priv. comm.). Since the clumps are still present in S212 it argues for a young age for the HII region ($< 10^5$ yrs). Optical recombination line densities were not available for S211 at the time of this writing but it too has clumpy molecular material (CO observations of McCutcheon, 1985) which implies that S211 may also be highly clumped. It is quite possible that both HII regions are only about 10^4 yrs old.

The HII density to HI density ratios also argues for young ages for both HII regions. These ratios are greater than one for both S211 and S212 and this is also the case for the hydrogen surrounding LkH α 101. Dewdney and Roger conclude that this unusual density ratio is due to the young age of the HII region ($\leq 10^4$ yrs).

Further work on the S211 and S212 complexes should include additional stellar observations in order to determine the distances with greater certainty; it seems unusual that the two complexes, which have many similarities, are separated by 2 kpc of distance. It would be helpful to have complete CO maps at $1'$ resolution of the CC Survey field to compare with the HI maps. It may also be interesting to obtain more quantitative data on clumping in the two complexes by performing autocorrelation analysis on line maps (HI and CO) and continuum maps of the areas around each HII region, preferably of higher resolution than those maps already available. Far infrared observations of S211 and S212 at better than $30''$ resolution in order to search for dust and gas remaining from formation of the exciting stars along with clumping statistics may provide more accurate estimates of their ages. Theoretical research into the dynamics of the HI regions surrounding HII regions is necessary to fully account for the $3 \text{ km} \cdot \text{s}^{-1}$ expansion of the HI associated with S211. An inexplicable $6 \text{ km} \cdot \text{s}^{-1}$ expansion was also observed by Roger and Pedlar (1981) for the HI southeast of NGC281. Finally, both the S211 and S212 complexes require

a photodissociation model that takes into account their non-steady state conditions in HI formation and their gas density variations. Continued research on the HII/HI/H₂ complexes belonging to S211 and S212 may provide valuable insights into the properties of molecular clouds including star formation.

REFERENCES

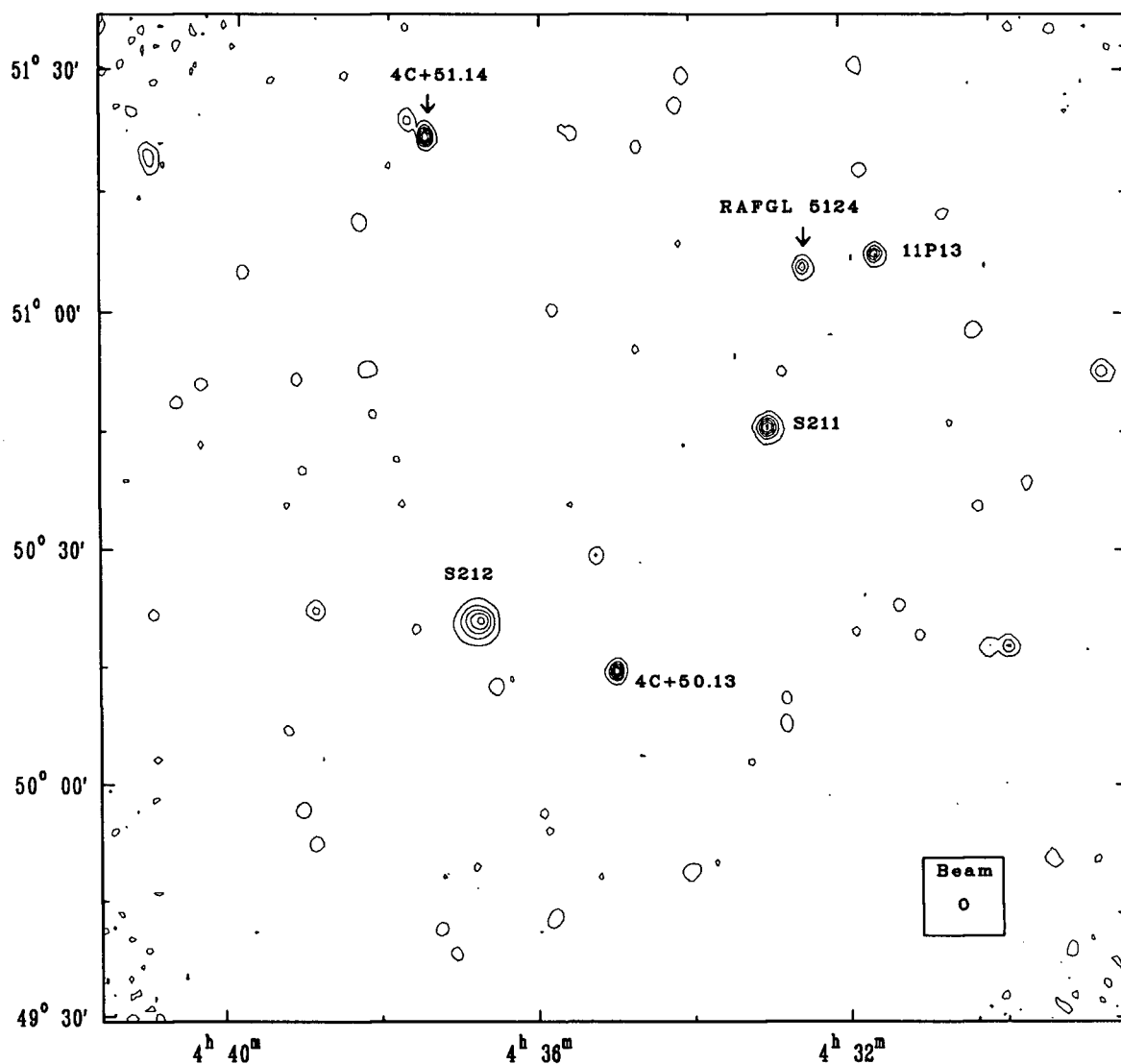
- Allen, C.W. 1973, *Astrophysical Quantities*, 3rd ed. The Athlone Press, University of London, London, England.
- Baars, J.W.M., Genzel, R., Pauliny-Toth, I.I.K. and Witzel, A. 1977, *Astron. Astrophys.* **61**, 99
- Berkhuijsen, E.M. 1972, *Astron. Astrophys. Suppl.* **5**, 263
- Burton, W.B., te Lintel Hekkert, P. 1985, *Astron. Astrophys. Suppl.* **62**, 645
- Bodenheimer, P., Tenorio-Tagle, G., Yorke, H.W. 1979, *Ap. J.* **233**, 85
- Chini, R., Wink, J.E. 1984, *Astron. Astrophys.* **139**, L5
- Christiansen, W.N., Högbom, J.A. 1985, *Radiotelescopes*, 2nd ed. Cambridge University Press, London
- Croes, G.A. 1978, *A Manual for Force, a Fortran Dialect*, unpublished
- Davies, R.D., Cummings, E.R. 1975, *M.N.R.A.S.* **170**, 95
- Dewdney, P.E., Roger, R.S., 1982, *Ap. J.* **255**, 564
- Dewdney, P.E., Roger, R.S. 1985, submitted to *Astrophysical Journal*
- Dewdney, P.E., Roger, R.S. 1982, *Equilibrium Models in Photodissociation Regions*, unpublished
- Dewdney, P.E., Roger, R.S., Robert, N. 1985, in M. Peimbert and J. Jugaki (eds.), *Star Forming Regions*, D. Reidel, Boston, U.S.A., p.83
- Elmegreen, B.G., Lada, C.J. 1978, *Ap. J.* **219**, 467
- Felli, M., Churchwell, E. 1972, *Astron. Astrophys. Suppl.* **5**, 69
- Fich, M. 1985, unpublished
- Fich, M., Blitz, L. 1984, *Ap. J.* **279**, 125
- Georgelin, Y.P., Georgelin, Y.M. 1970, *Astron. Astrophys.* **6**, 349
- Higgs, L.A. 1986, *J. Roy. Astron. Soc. Can.* **80**, 1
- Hill, J.K., Hollenbach, D.J. 1978, *Ap. J.* **225**, 390
- IRAS Explanatory Suppl.*, 1984, eds. Beichmann, C.A., Neugebauer, G. Habing, H.J., Clegg, P.E., Chester, T.J., JISWG, Pasadena, U.S.A.

- IRAS Point Source Catalog*, 1984, eds. Beichmann, C.A., Neugebauer, G. Habing, H.J., Clegg, P.E., Chester, T.J., JISWG, Pasadena, U.S.A.
- Irwin, J.A. 1978, *M.Sc. Thesis*, University of Victoria
- Joncas, G., Dewdney, P.E., Higgs L.A., Roy, J.R. 1985, *Ap. J.* **298**, 596
- Jura, M. 1974, *Ap. J.* **191**, 375
- Kahn, F.D. 1983, in D.R. Flower (ed.), *Planetary Nebulae*, D. Reidel, Boston, U.S.A., p.305
- Kallas E., Reich W. 1980, *Astron. Astrophys. Suppl.* **42**, 227
- Kennedy, J.E.D. 1975, *Ph.D. Thesis*, University of Western Ontario
- Kwok, S., Volk, K. 1985, *Ap. J.* **299**, 191
- Mayer, P., Macak, P. 1973, *Bull. Astr. Inst. Czech.* **24**, 50
- McCutcheon, W.H. 1985, unpublished
- Moffat, A.F.J., Fitzgerald, M.P. Jackson, P.D. 1979, *Astron. Astrophys. Suppl.* **38**, 197
- Oort, J.H., Spitzer, L. 1955 *Ap. J.* **121**, 6
- Oster, L. 1961, *Ap. J.* **134**, 1010
- Osterbrock, D.E. 1974, *Astrophysics of Gaseous Nebulae*, W.H. Freeman and Co., San Fransisco, U.S.A.
- Osterbrock, D., Flather, E. 1959, *Ap. J.* **129**, 26
- Panagia, N. 1973, *A.J.* **78**, 929
- Reifenstein, E.C., Wilson, T.L., Burke, B.F., Mezger, P.G., Altenhoff, W.J. 1969, *Astron. Astrophys.* **4**, 357
- Roger, R.S. 1983, *Proc. Astron. Soc. Australia* **5**, 158
- Roger, R.S., Dewdney, P.E. 1985, in M. Peimbert and J. Jugaki (eds.), *Star Forming Regions*, D. Reidel, Boston, U.S.A., p.102
- Roger, R.S., Irwin, J.A. 1982, *Ap. J.* **256**, 127
- Roger, R.S., Pedlar, A. 1981, *Astron. Astrophys.* **94**, 238
- Savage, B.D., Mathis, J.S. 1979, *Ann. Rev. Astron. Astrophys.* **17**, 87

- Schmidt-Kaler Th. 1965, in H.H. Voigt (ed.), *Physical Parameters and Two-Parameter Diagrams of the Stars*, Springer-Verlag, Berlin, p.284
- Schull, J.M. 1982, in R.S. Roger and P.E. Dewdney (eds.), *Regions of Recent Star Formation*, D. Reidel, Boston, U.S.A., p.91
- Sharpless, S. 1959, *Ap. J. Suppl.* **4**, 257
- Spitzer, L. 1976, *Q.J.R. Astr. Soc.* **17**, 97
- Spitzer, L. 1978, *Physical Processes in the Interstellar Medium*, Wiley and Sons, New York, U.S.A.
- Talent, D.L., Dufour, R.J. 1979, *Ap. J.* **233**, 888
- Tenorio-Tagle, G. 1979, *Astron. Astrophys.* **71**, 59
- Weaver, H., Williams, W. 1973, *Astron. Astrophys. Suppl.* **8**, 1
- Weaver, H., Williams, W. 1974, *Astron. Astrophys. Suppl.* **17**, 1
- Williams, D.R.W. 1973, *Astron. Astrophys. Suppl.* **8**, 505

APPENDIX A: CC SURVEY CONTINUUM MAP

Below is the continuum map of the CC Survey containing the low order spacings of the Effelsberg Survey (Kallas and Reich, 1980). Those sources used for recalibration of the hydrogen line maps are labelled (see Section 2.2). The map has been corrected for the primary beam of the 8.6m dishes resulting in a noise level in the corners that is 5 times that in the map centre (0.16K rms).



Contours: (1.5, 7.5, 15.0, 22.5, 30.0, 40.0) K Brightness Temperature

APPENDIX B: CC SURVEY HI MAPS

Two types of HI maps are shown in Appendix B: the compressed spectrum subtracted (CSS) maps (B2 to B9) and the spectrum subtracted galactic (SSG) maps (B10 to B13). As mentioned in Section 2.2.2 the CSS maps are 3 channel averages of the SS maps, except for map 43 which is a 2 channel average. This means that the velocity width of maps 1 to 42 is 1.24 km s^{-1} where the central velocity of map number MN is given by

$$V_{\text{lsr}} = -1.24MN - 8.17 \quad \text{km s}^{-1} \quad \text{B.1)}$$

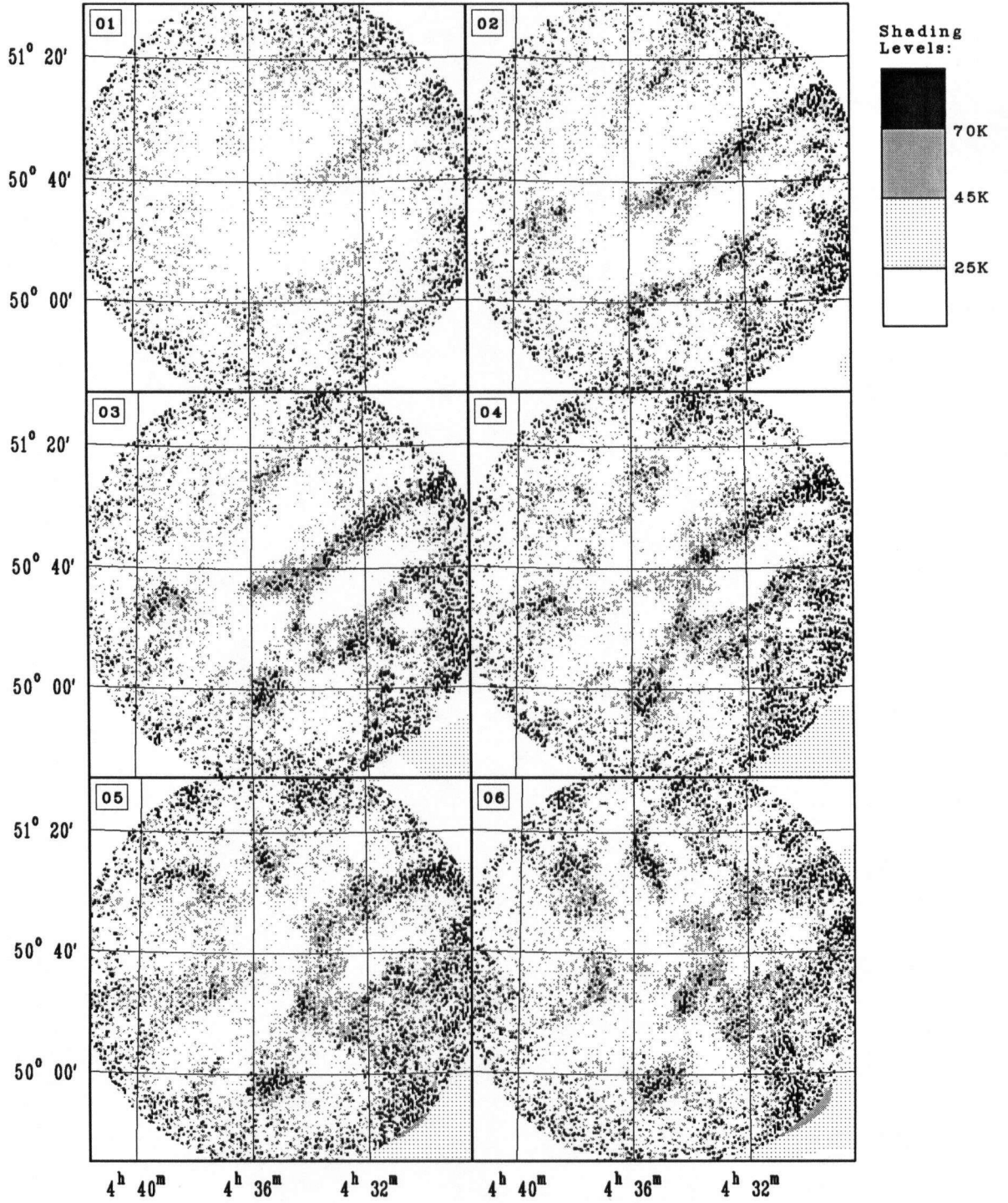
except for map 43 whose velocity range is -60.8 to -61.7 km s^{-1} . All the maps are corrected for the primary beam of the 8.6m dishes. This means that the noise in the corners would rise to extreme levels (30 to 70K rms). Consequently all values beyond 68' from the map centre were set to zero in the original interferometer LMC maps. (But this was not done in the LOS LMC maps so that some smooth shading may be visible beyond the 68' radius.) The noise in maps 1 to 42 is expected to be 7K rms (9K rms for map 43) in the map centre to 24K rms (30K for map 43) at the 68' radius. The continuum map is shown on page 109 for comparison.

The SSG maps are first described in Section 4.1. Maps 1 to 10 are 12 channel averages of the SS maps, smoothed to 3' resolution and rotated to galactic coordinates. Map 11 is an 8 channel average. The velocity width of maps 1 to 10 is 4.96 km s^{-1} where the central velocity is given by

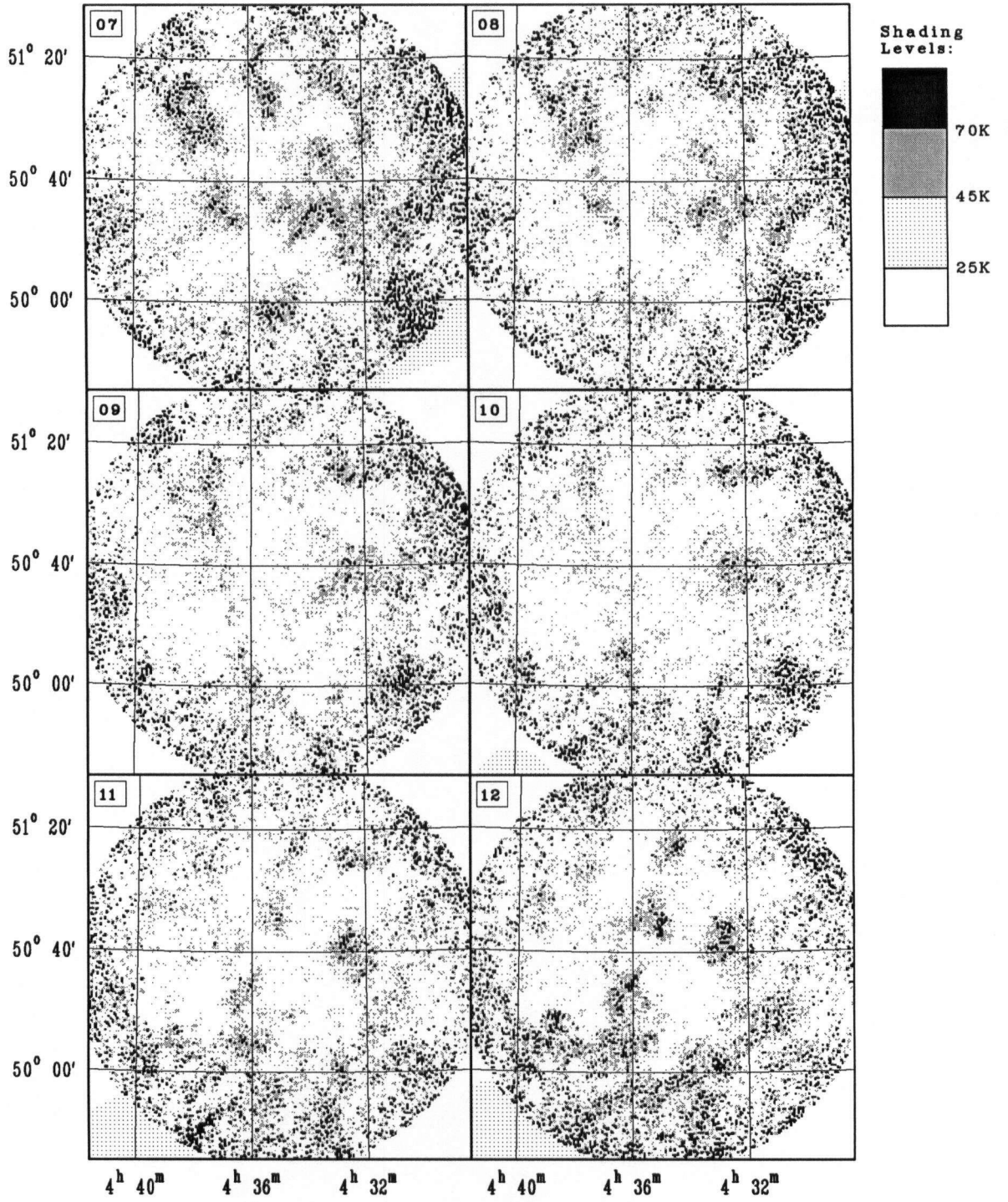
$$V_{\text{lsr}} = -4.96MN - 6.31 \quad \text{km s}^{-1} \quad \text{B.2)}$$

except for map 11 whose velocity range is -58.4 to -61.7 km s^{-1} . The noise expected at the map centre is 0.12K rms for maps 1 to 10 (0.15K rms for map 11) and about 0.4K rms at the left and right edges (0.5K rms for map 11). The maps have been restricted in galactic latitude from about $l = 2^{\circ}1$ to about $l = 2^{\circ}8$ for easy comparison with the positions of S211 and S212. The continuum map, rotated to galactic coordinates, is shown on page 113

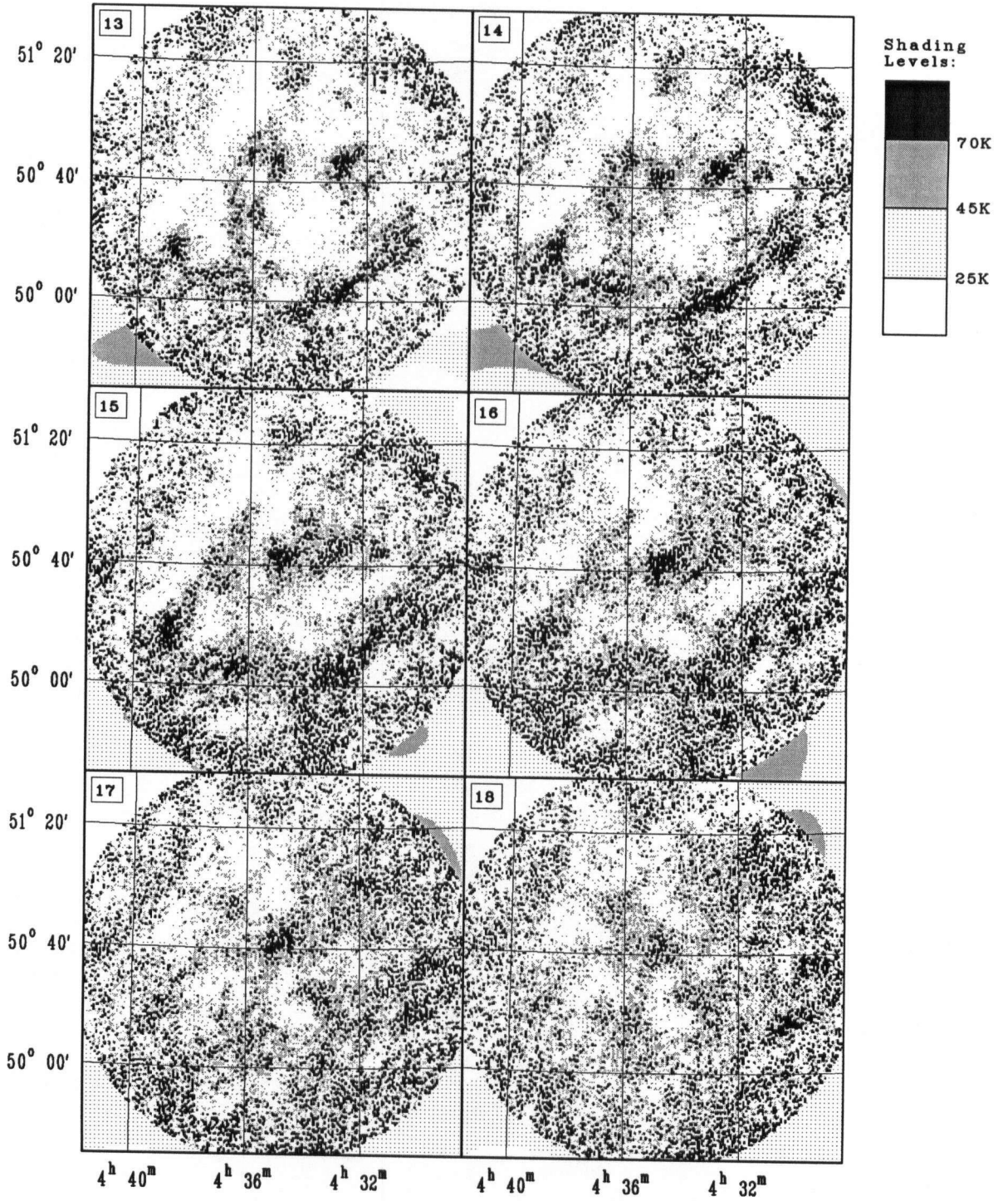
Compressed Spectrum Subtracted (CSS) Maps



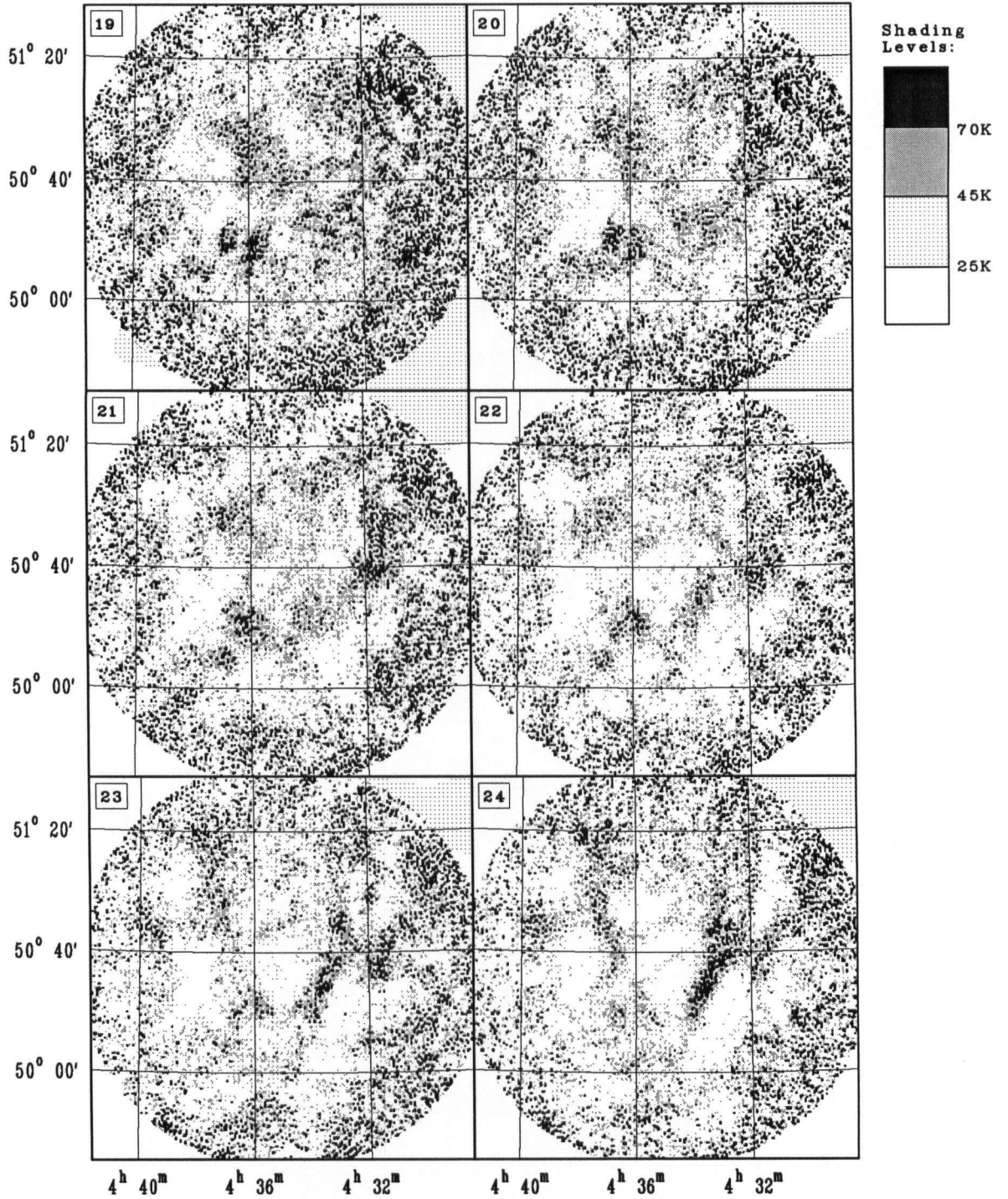
Compressed Spectrum Subtracted (CSS) Maps



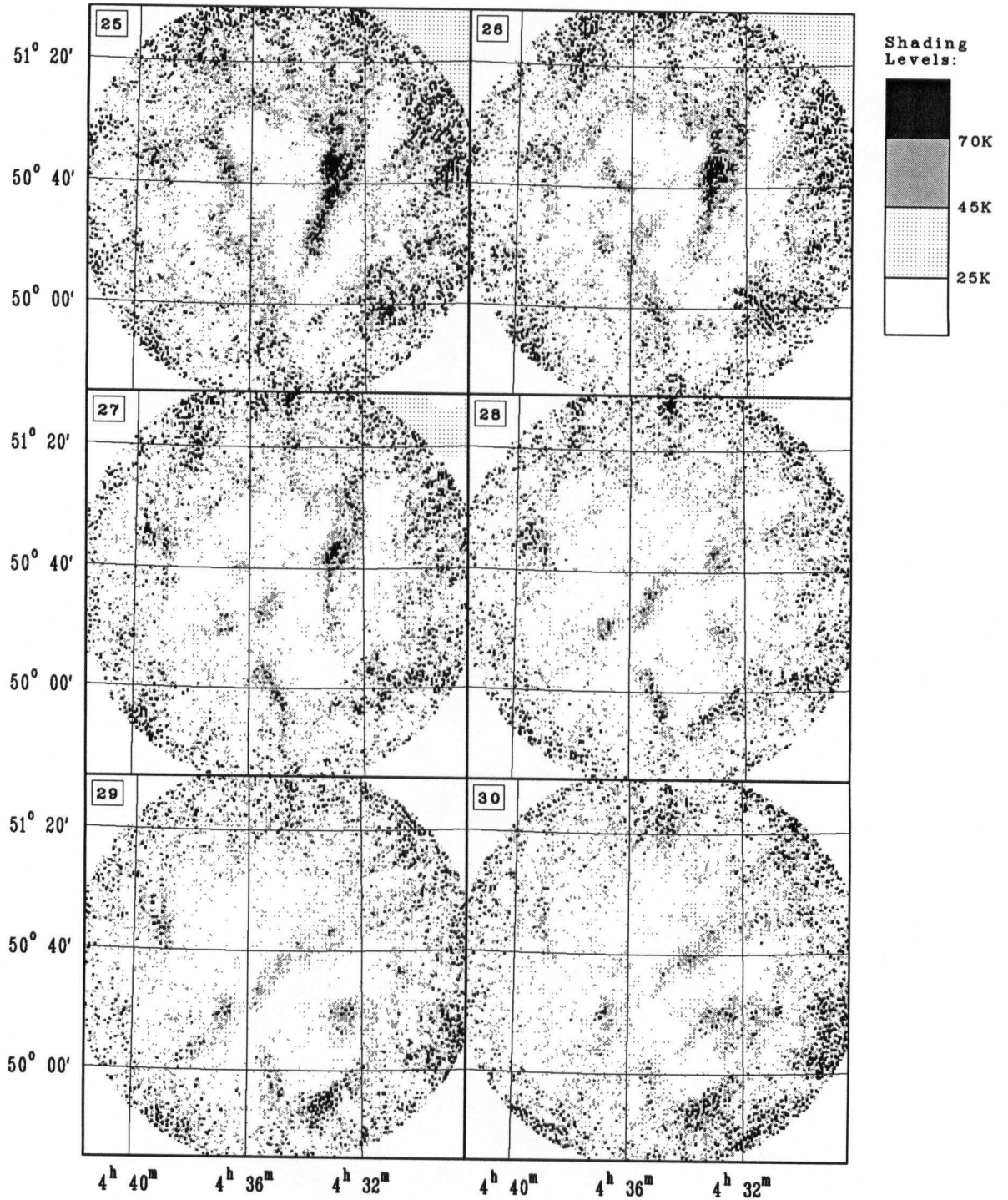
Compressed Spectrum Subtracted (CSS) Maps



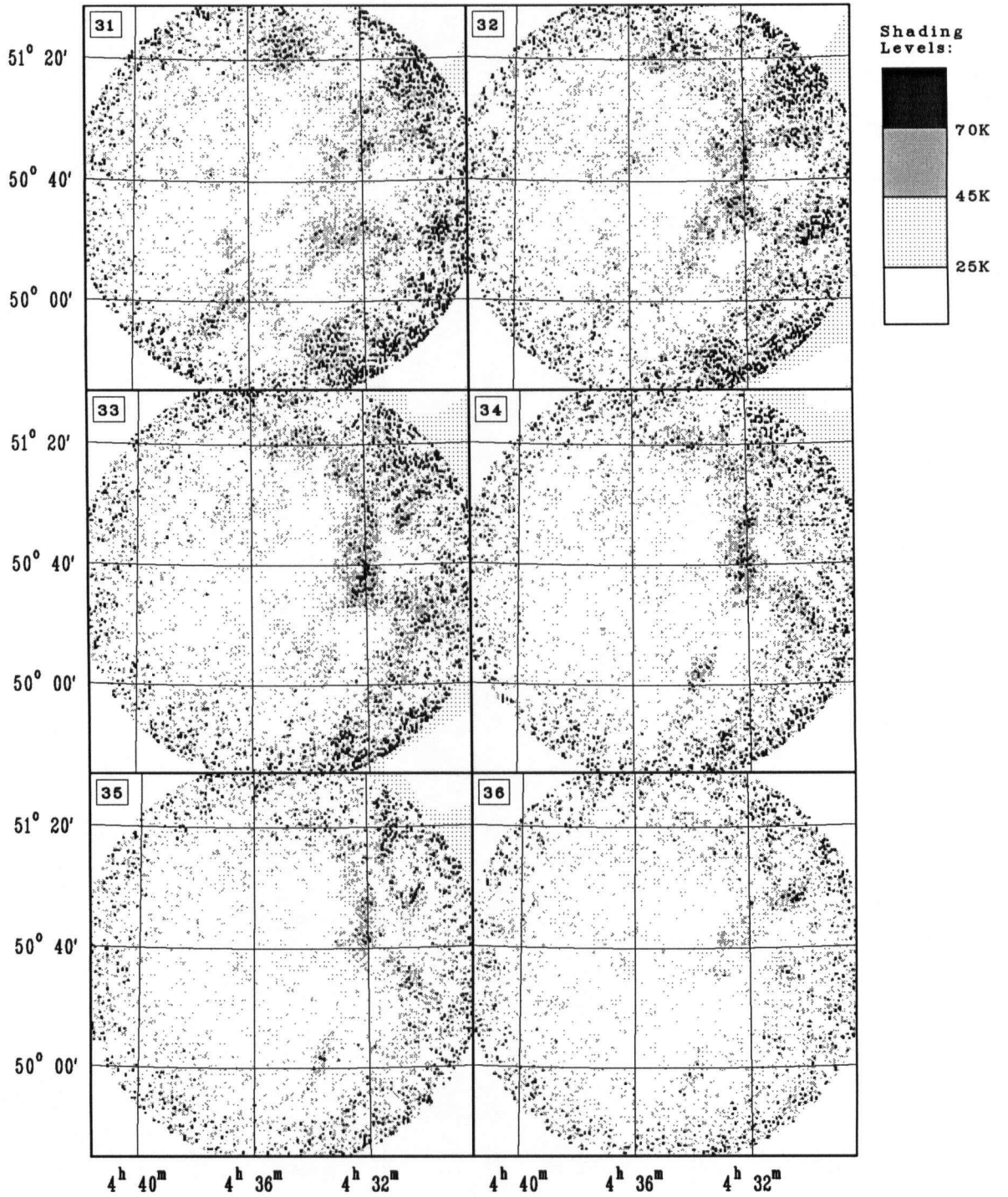
Compressed Spectrum Subtracted (CSS) Maps



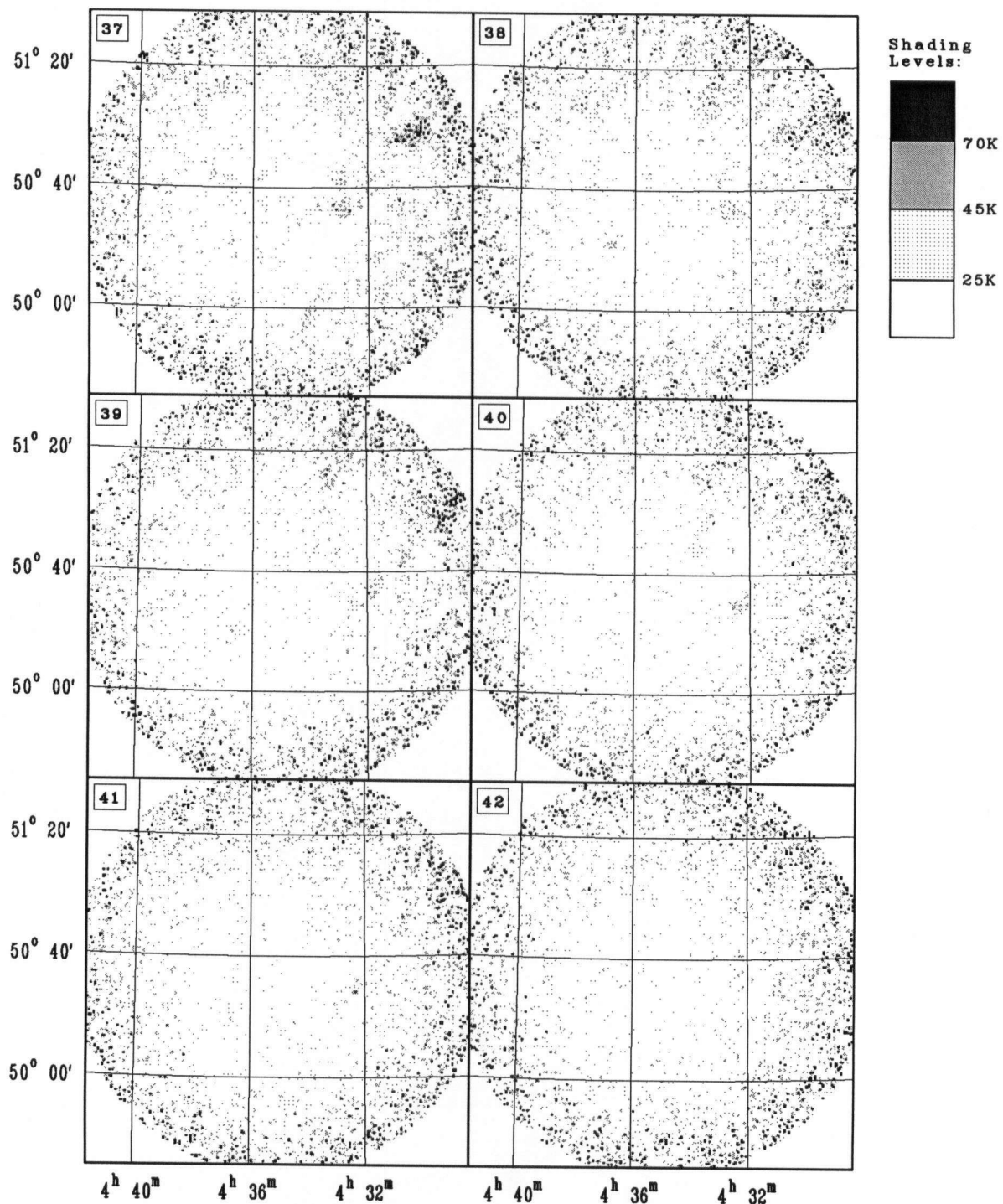
Compressed Spectrum Subtracted (CSS) Maps



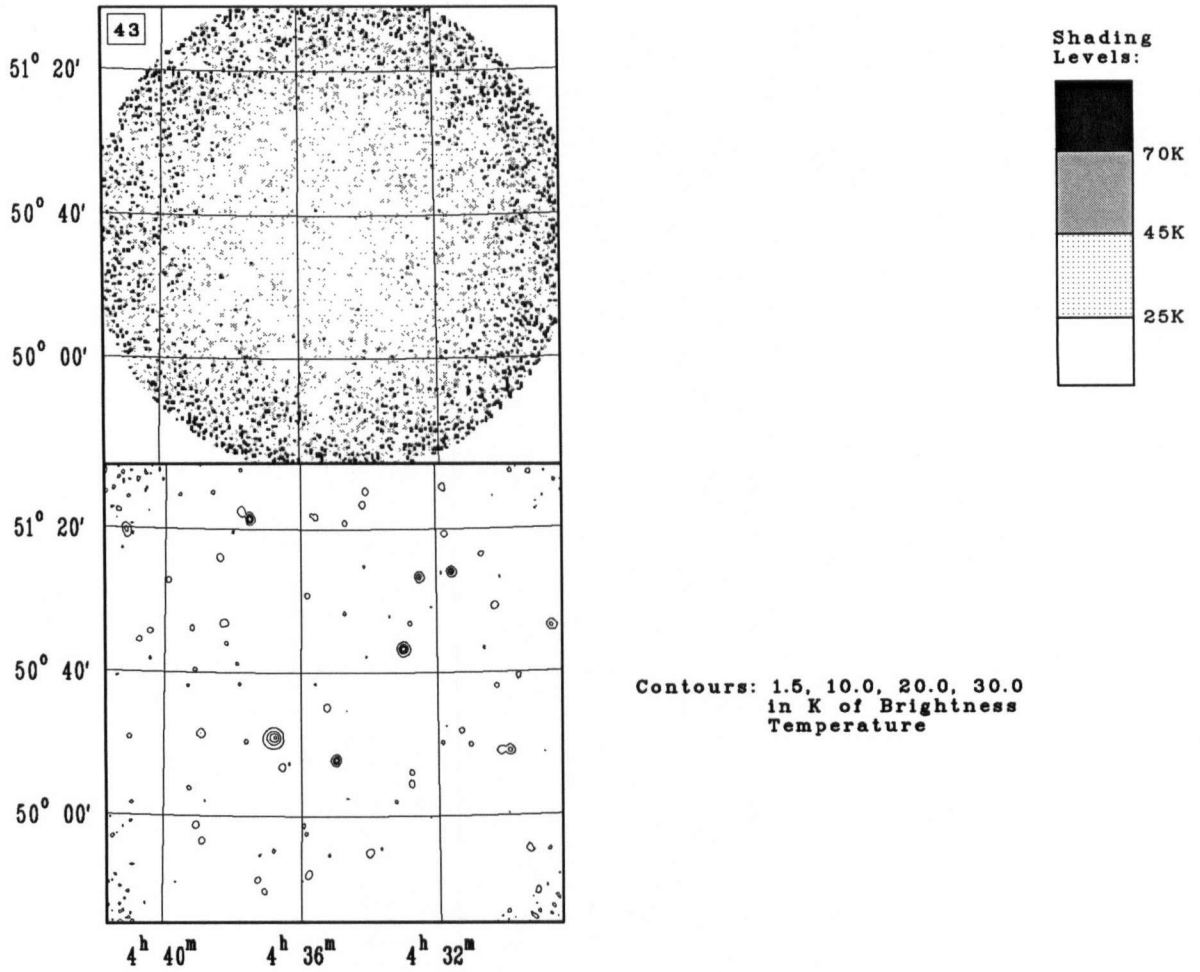
Compressed Spectrum Subtracted (CSS) Maps



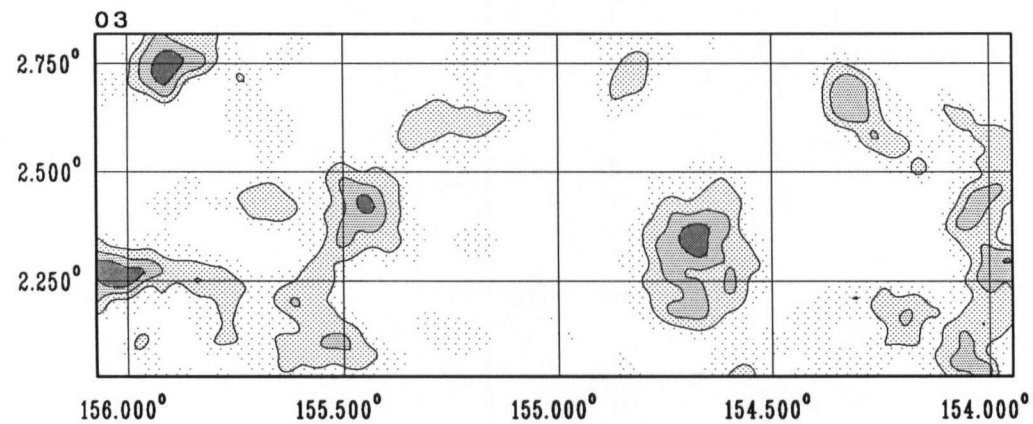
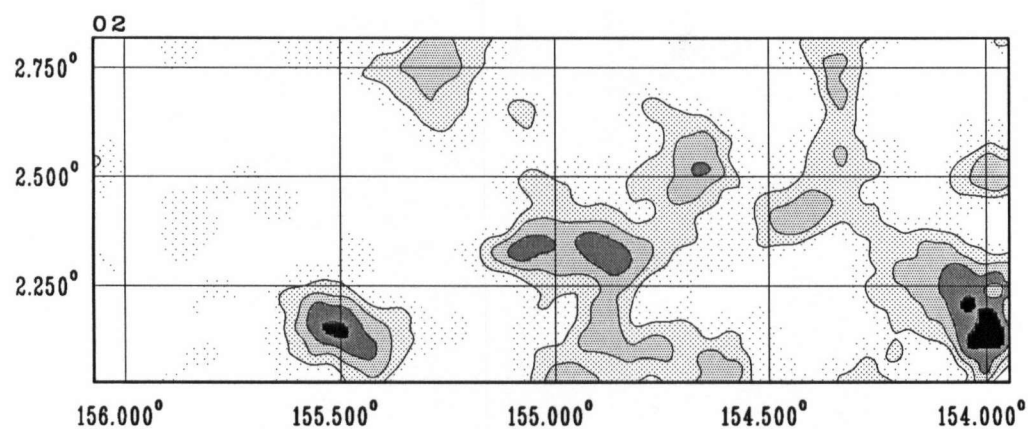
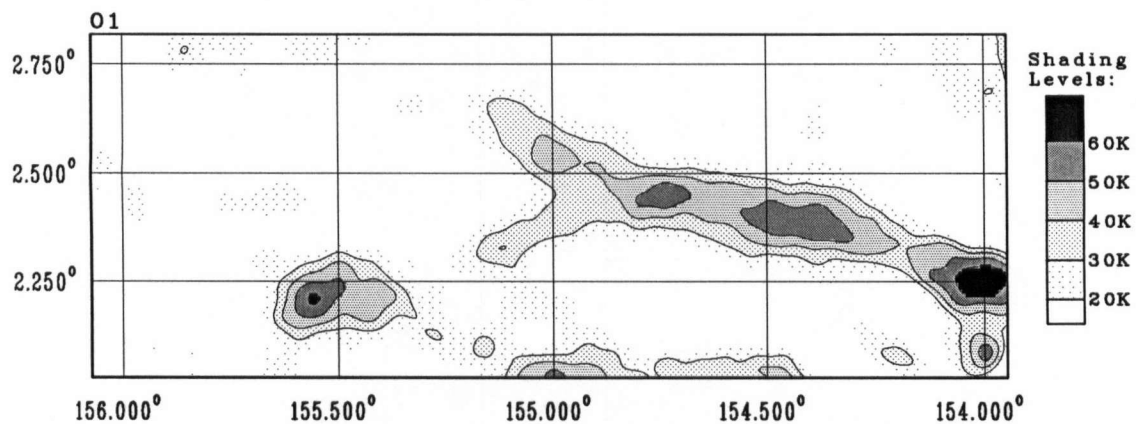
Compressed Spectrum Subtracted (CSS) Maps



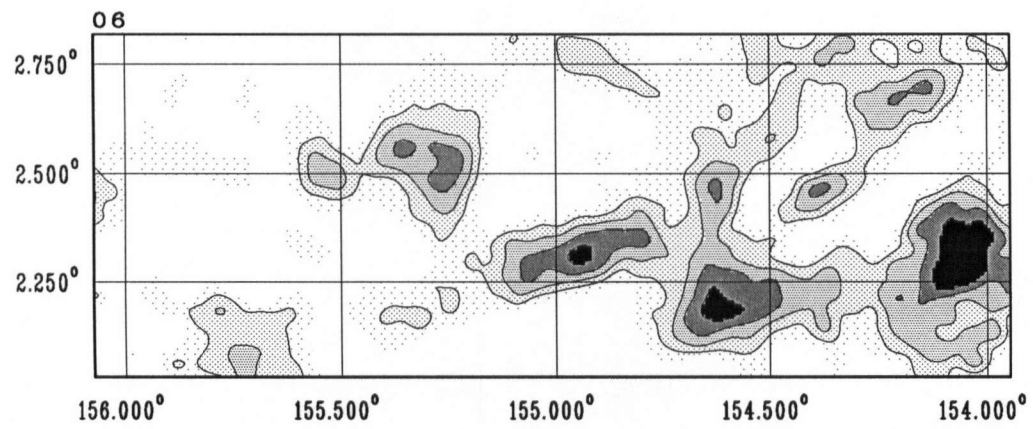
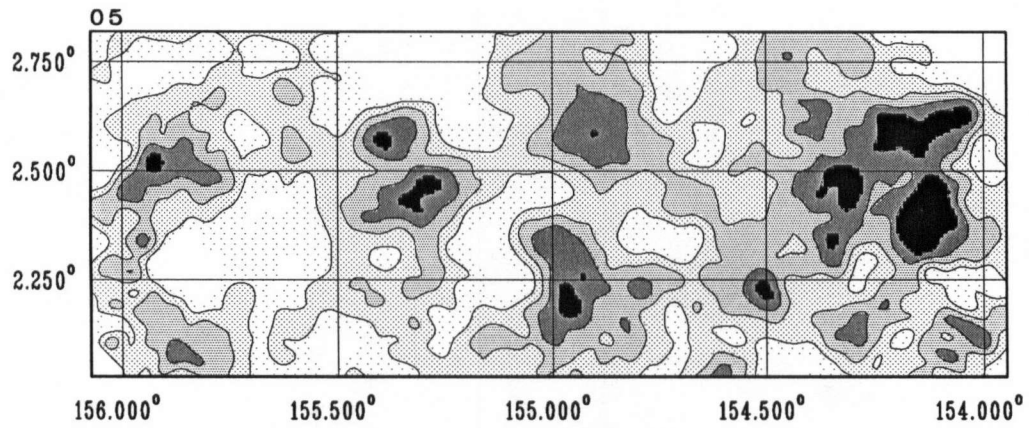
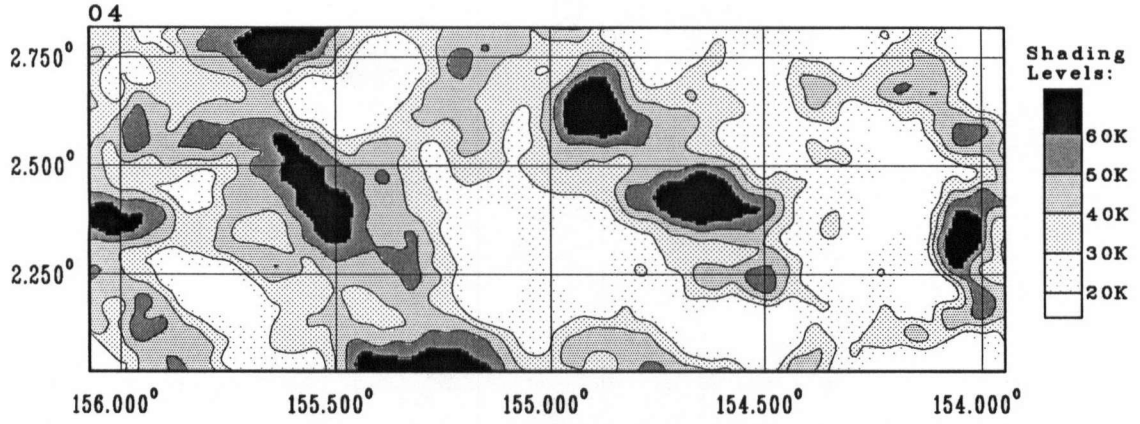
Compressed Spectrum Subtracted (CSS) Maps



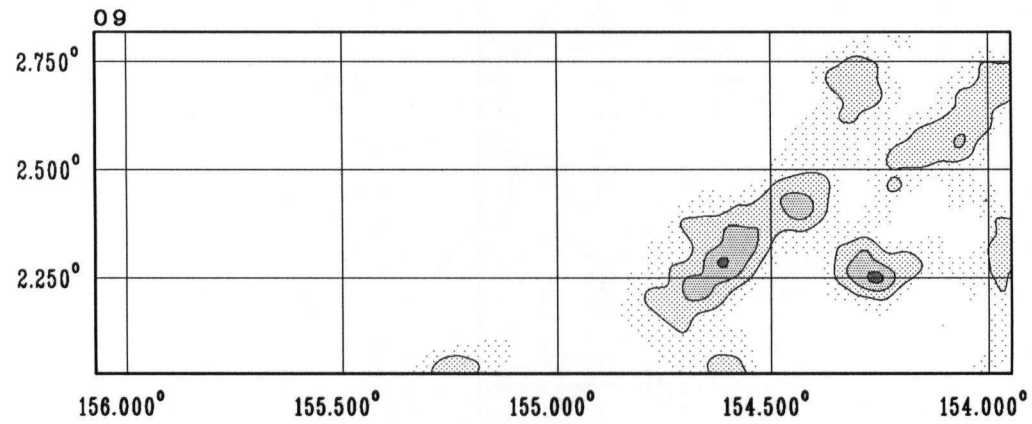
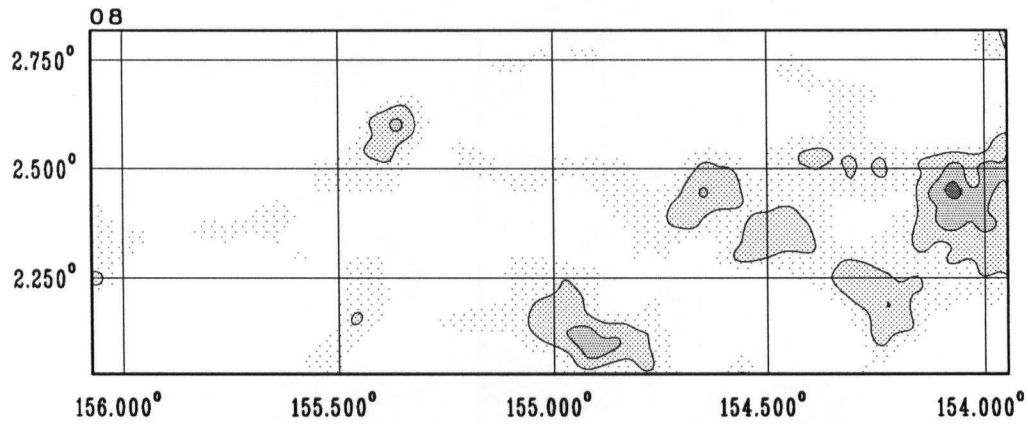
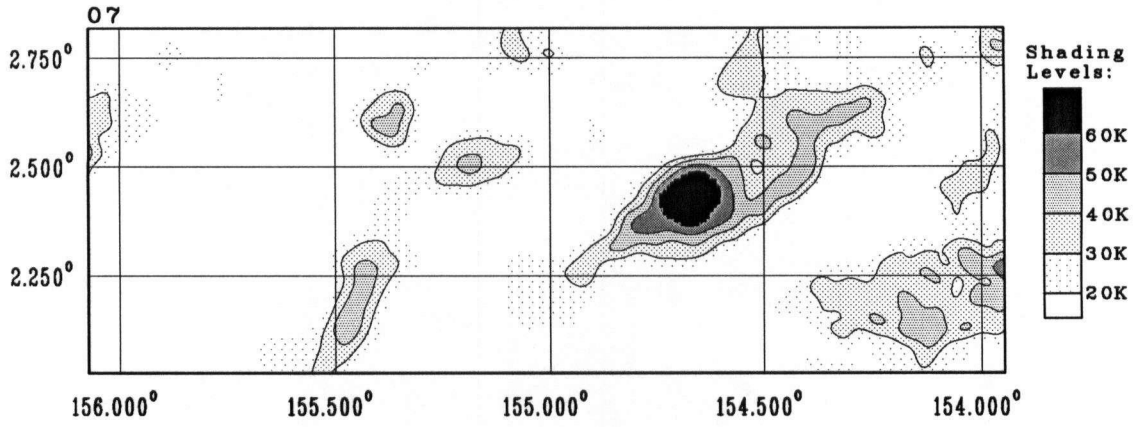
Spectrum Subtracted Galactic (SSG) Maps



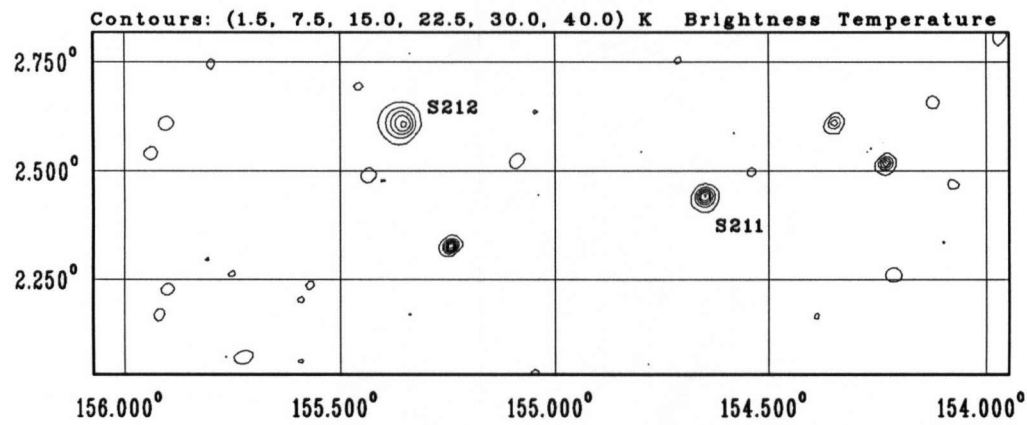
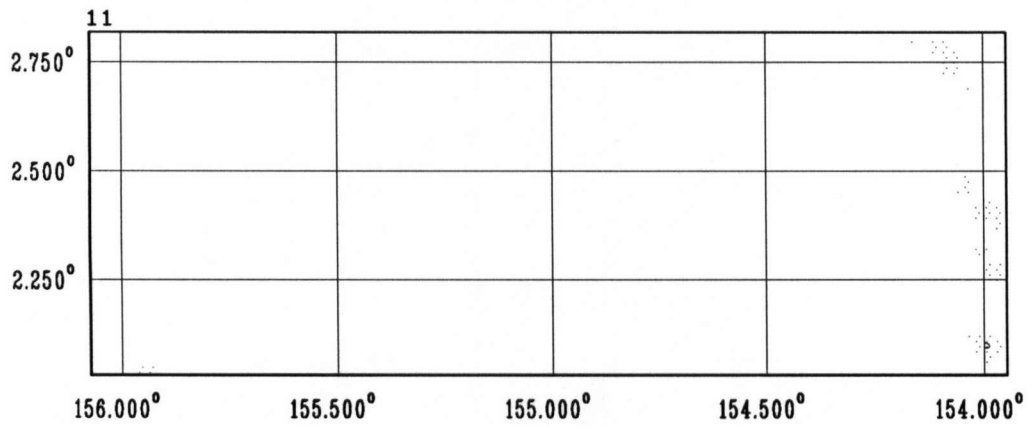
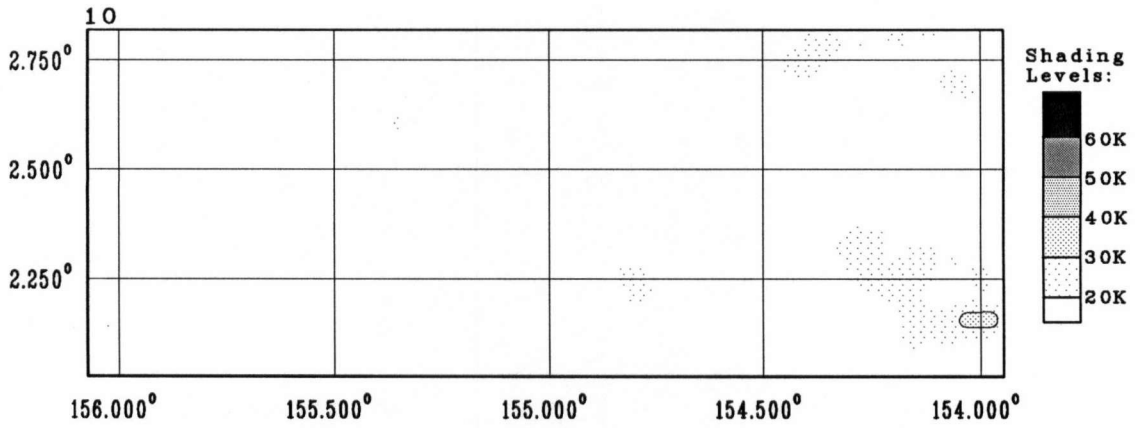
Spectrum Subtracted Galactic (SSG) Maps



Spectrum Subtracted Galactic (SSG) Maps



Spectrum Subtracted Galactic (SSG) Maps



APPENDIX C: HIIBLOB3 DOCUMENTATION

The program HIIBLOB3 (see Section 3.3) and its subroutines are listed in this appendix. This includes the files

HIIBLOB3.FRC	(pp 115 to 119)	(main program)
BLOBVAR.INC	(p119)	(declares common block)
LSEG.INC	(p119)	(declares common block)
BLOCATE.FRC	(p120)	(subroutine)
LINSEG.FRC	(p120)	(subroutine)
BLINE.FRC	(p121)	(subroutine)
DEPTH.FRC	(p121)	(subroutine)
BLOPLAC.FRC	(p122)	(subroutine)
TAPLAC.FRC	(p123)	(subroutine)

The files are in the computer language FORCE, developed at DRAO, and is similar to FORTRAN 77. The subroutines ASKINT, ASKVAL, and RAN are not important in understanding the details of HIIBLOB3 and are thus not documented here. ASKINT and ASKVAL prompt the user for required input (integer and real respectively). RAN is a random number generator.

The program was originally intended to simulate an HII region containing randomly located regions of enhanced density - i.e. "blobs". However, since neither S211 nor S212 was highly resolved by the CC Survey it was decided that blobs would not be included in any simulation of S211 or S212.

PROGRAM HIIBLOB3

```

# This program, based on HIIBLOB2 by P.E. Dewdney and R.S. Roger, computes
# the emission measure of a model HII region consisting of spherical blobs
# placed in a "soup" of ionized hydrogen. The program incorporates dust and
# an electron density gradient for the soup in the x direction.
# The dust coefficient is based on  $\langle N(\text{HI})/E(B-V) \rangle = 5.0E+21 \text{cm}^{-2} \text{mag}^{-1}$ 
# (from Savage & Mathis 1979, Ann. Rev. A & A 17,87) and an extinction of
#  $15^\circ E(B-V)$  was used at 912 Angstroms. The formula for photon loss due to
# ionization is from Spitzer 1978, Physical Processes in the Interstellar
# Medium (JOHN WILEY & SONS) p.109.
# A series of blobs is placed randomly in the half-plane  $x > 0$ . Two processes
# then take place to determine the emission measure:
# 1) A numerical integration along a ray from the origin determines the
# point along the ray at which the Lyman continuum photon flux reaches
# zero. This is repeated for rays of differing THETA: THETA ranging
# from  $-\pi/2$  to  $\pi/2$ .
# 2) The emission measure is computed along lines of constant x (the
# observer being at  $y = +\text{or} - \text{infinity}$ ) within the boundaries determined
# in STEP 1.

INCLUDE 'DISK:[DRAO]STNDRD.DEF'
INCLUDE 'BLOBVAR.INC'
INCLUDE 'LSEG.INC'

DEFINE (pctocm18,3.083)
DEFINE (plotunit,20)
DEFINE (outfile,10)

IFUNC ASKINT
RFUNC ASKVAL
REAL EMISS(2500),XPLOT(5000),COLDEN(2500),PHI,DENS(2)
REAL DNGRA(2),THETA,DENGRA,RIN,ROUT,PHOTON,TOTPHO,RAD,DELRAD,DEN
REAL TAUDUS,DUSTK,DELTHE,XBOUN,DELX,TOTLEN,AVDEN,LENBLO,DELR
REAL RADAV,PVOL,NHIIBL,EMMAX,RMAX,RMIN
INTEGER DI,NRAD,NLIN
DATA ALPHA2/3.08E-13/
# ALPHA2 is the case B recombination coefficient for HII.

# Feed in the required data.

TOTPHO = ASKVAL('\Total number of ionization photons from star~
(.01 10**48):\',0.01)
BLORAD = ASKVAL('\Blob radius (0.003 pc):\',0.003)
NBLOBS = ASKINT('\Number of blobs (200):\',200)
DENBLO = 0.
IF NBLOBS > 0
DENBLO = ASKVAL('\Blob density (1500. cm**-3):\',1500.)
CIF
DNSOUP = ASKVAL('\Central Interblob density (300. cm**-3):\',300.)
DENGRA = ASKVAL('\Interblob gradient (0. cm**-3 pc**-1):\',0.)
DUSTK = ASKVAL('\Dust absorption coefficient (3. 10**-21):\',3.)
DELRAD = BLORAD * ASKVAL('\Radial increment as fraction of blob~
radius(0.4):\',0.4)
NINCRE = ASKINT('\Maximum number of radial increments (200):\',200)
IDUMA = ASKINT('\First random number seed (0):\',0)
IDUMB = ASKINT('\Second random number seed (0):\',0)

IDUM1 = IDUMA
IDUM2 = IDUMB
XMAX = NINCRE * DELRAD
# Maximum radius for the numerical integrations. (i.e. grid size)
YMAX = XMAX
DELTHE = DELRAD / XMAX

# Choose the position of the blob centres (XTAB(I),YTAB(I)) and the
# radius of each blob's cross-section (BRADI(I)) with the xy plane.
# Also compute the distance of the blob centres from the origin
# (DISTO(I)) and the angles made at the origin between the blob
# centres and the positive x axis (POSVEC(I)). Also calculate maximum
# and minimum angles made at the origin by the circle representing
# each blob with the positive x axis (ANGOFI(I,2) and ANGOFI(I,1)
# respectively).

IF NBLOBS > 0
LOOP DO I = 1,NBLOBS
XTAB(I) = XMAX * RAN( IDUM1,IDUM2 )
YTAB(I) = 2. * YMAX * ( RAN( IDUM1-13,IDUM2+13 ) - 0.5)
BRADI(I) = SQRT( BLORAD*BLORAD - (BLORAD **
RAN(IDUM1,IDUM2)) **2 )
DISTO(I) = SQRT( XTAB(I)**2 + YTAB(I)**2)
POSVEC(I) = ASIN(YTAB(I)/DISTO(I))
# If blob surrounds origin then the maximum
# and minimum angles are set to + and - pi.
IF BRADI(I) > DISTO(I)
ANGOFI(I,1) = -pi/2
ANGOFI(I,2) = pi/2
ELSE
PHI = ASIN(BRADI(I)/DISTO(I))
# Angle subtended at origin by blob radius.

```

HIIBLOB3 (contd.)

```

      ANGOFI(1,1)= POSVEC(1) - PHI
      ANGOFI(1,2)= POSVEC(1) + PHI
    CIF
  CLOOP
  CIF
#
# Start the loop that constructs the HII region boundary. The PLACE
# array contains the blob indices in order of their distance from
# the origin as measured along the ray. DISTH(PLACE(1),1 & 2) give
# the origin distances of the near and far points of intersection
# between the blob and ray.
#
  NRAD = 1
#   No. of rays drawn from centre.
  THETA = -pi / 2.
#   Angle of ray with positive x axis.
  RMAX = 1.E-30
  RMIN = 1.E+30
  DENS(1)= DNSOUP
#   Electron density in interblob medium.
  DENS(2)= DENBLO
#   Electron density in blob.
  DNGRA(2)= 0.0
#   Density gradient in blob.
  LOOP WHILE THETA <= pi / 2.
    PLACE(1)= 1
    DISTH(PLACE(1),1)= XMAX
#
#   Determine the density gradient along the ray.
#
    DNGRA(1)= DENGRA * COS(THETA)
#
#   If there are blobs then call the subroutine that determines which
#   blobs are on the ray and which in turn calls the subroutine that
#   "PLACES" the blobs in order of their distance from the origin.
#   Succeeding this initialize some variables to be used in the inner
#   loop. This loop performs the integration out to the HII boundary.
#
    IF (NBLOBS>0) CALL BLOCATE(THETA)
    RIN= 0.0
#   RIN and ROUT are the integration boundaries for a single
#   density region i.e. blob or soup.
    ROUT= DISTH(PLACE(1),1)
    DI= 1
#   Density index =1 for soup and = 2 for blob
#
#   If ROUT is initialized to zero then there is a blob on the origin
#   and ROUT should be reinitialized to the far intersection pt. distance
#   (i.e. DISTH(PLACE(1),2)). The density index, DI, should have a new
#   initial value of 2 since the integration is starting out inside a
#   blob.
#
    IF ROUT==0
      ROUT= DISTH(PLACE(1),2)
      DI= 2
    CIF
    PHOTON= TOTPHO
    J= 1
    LOOP WHILE RIN<XMAX
      RAD= RIN + DELRAD # DELRAD is the integration step size.
#       RAD is the integration variable.
      DELR= DELRAD # This is the effective integration used because
#       it is sometimes necessary to have a step smaller than DELRAD.
      LOOP WHILE RAD<=ROUT & PHOTON>0
        DEN= DENS(DI) + RAD*DNGRA(DI)
#       DEN represents the electron density at RAD.
        XLOOP WHEN DEN<=0.0 # Boundary also reached when DEN=0
        TAUDUS= DUSTK*DEN*DELR*pctocm18*1.E-3
#       TAUDUS represents the optical depth due to dust corresponding
#       to step size DELR.
        PHOTON= PHOTON*EXP(-TAUDUS)
#       No. of Lyman continuum photons after extinction due to dust.
        PHOTON= PHOTON - (4*pi*RAD*RAD*DEN*DEN*ALPHA2*DELR)*~
#       (pctocm18**3)*1.E6
#       # No. of Lyman continuum photons after ionization of HI.
        RAD= RAD+DELRAD
        IF (RAD>ROUT) & (RAD< ROUT+DELRAD) # If RAD is at the edge of
          DELR= ROUT - (RAD - DELRAD) # a blob-soup interface then
          RAD= ROUT # there exists a gap between RAD (before incremented
          CIF # i.e. RAD- DELRAD) and ROUT. So it is necessary to reduce
          # the step size of the integration to less than DELRAD.
        CLOOP

```

HIIBLOB3 (contd.)

```

XLOOP WHEN DEN<=0
XLOOP WHEN PHOTON<=0
#   When Lyman continuum photons and/or ions are gone
#   the boundary of the HII region has been reached.
#
#   After exiting the integration loop (inside "inner loop" mentioned
#   above); change the density index by using the thoroughly clever
#   formula below that changes 1 to 2 and 2 to 1; advance the PLACE
#   index J only if going from blob to soup (i.e. DI=2 and is to be
#   changed to 1) by using another thoroughly clever formula; update
#   ROUT and RIN.
#
#   J= J + (DI - 1)
#   Thoroughly clever formula!
#   DI= (3-(-1)**DI)/2
#   Another thoroughly clever formula!!
#   RIN= ROUT
#
#   The new RIN becomes the old ROUT and the new ROUT becomes the
#   next intersection pt. between blob and ray. If, however, the
#   last blob has been passed then ROUT must be set to the outer limit
#   XMAX. This is determined by whether or not J is greater than
#   NBRAY which is the number of blobs on the ray.
#
#   IF J>NBRAY
#       ROUT= XMAX
#   ELSE
#       ROUT= DISTH(PLACE(J),DI)
#   CIF
# CLOOP
#
#   If there are still Lyman continuum photons after emerging from the
#   inner loop then the HII region boundary has not been reached along
#   this ray and the program should be stopped.
#
#   IF (PHOTON>0.0) & (DEN>0.0)
#       WRITE(terminal,945)
#       FORMAT(1X,'XMAX exceeded')
#       STOP
#   CIF
#
#   If no photons then record the x,y,r of the boundary and update
#   RMAX,RMIN and increment NRAD,THETA.
#
#   RADARR(NRAD)=RAD-DELRAD-DELR
#   XARR(NRAD)= RADARR(NRAD) * COS(THETA)
#   YARR(NRAD)= RADARR(NRAD) * SIN(THETA)
#   RMAX= AMAX1(RMAX,RADARR(NRAD))
#   RMIN= AMIN1(RMIN,RADARR(NRAD))
#   NRAD= NRAD+1
#   IF DEN<=0.0
#       WRITE(terminal,395)THETA*180/pi
#       FORMAT(X,'Density bounded in the direction THETA(degrees)= ',F5.1)
#   ELSE
#       WRITE(terminal,400)THETA*180/pi
#       FORMAT(1X,'Theta(degrees): ',F5.1)
#   CIF
#   THETA= THETA + DELTHE
#   IF (THETA>pi/2) & (THETA<(pi/2)+DELTHE) # Ensures that the HII
#       THETA= pi/2 # boundary is "marked" at THETA= pi/2.
#   CIF
# CLOOP
# NRAD= NRAD-1
# XARR(NRAD+1)= -0.1 # This pt. is added to the array to allow
# YARR(NRAD+1)= YARR(NRAD) # the subroutine LINSEG to work for X= 0.0
#
#   Now that the the HII boundary has been constructed we begin the happy
#   task of computing the emission measure profile. To this end find the
#   maximum extent of the HII in the x direction. Then initialize variables
#   for the loop that places successive vertical lines in the x>0
#   half-plane. It is along these lines that the column densities and
#   emission measures are computed.
#
#   LOOP DO I=1,NRAD
#       WRITE(9,15)I,XARR(I),YARR(I),RADARR(I)
#       FORMAT(X,'I= ',14.3X,'X= ',G12.6,3X,'Y= ',G12.6,3X,'R= ',G12.6)
#   CLOOP
#   XBOUN= 1.E-30
#   XBOUN is maximum extent of HII in x direction.
#   LOOP DO I=1,NRAD
#       XBOUN= AMAX1(XBOUN,XARR(I))
#   CLOOP

```

HIIBLOB3 (contd.)

```

NLIN=0
# No. of lines (x=const.) drawn through HII region
UB= NRAD+1
LB= 1
# UB & LB are indices (of XARR,YARR) representing points of upper
# and lower bounds on line segments (indices before when going
# counterclockwise). "Line segments" refers to those sections of
# the line actually inside the HII region.

X= 0.0
DELX= 0.5 * DELRAD
LOOP WHILE X<XBOUN
  NLIN= NLIN+1
  CALL LINSEG
# LINSEG finds those "line segments".
# IF (NBLOBS>0) CALL BLINE(X)
# BLINE is similar to BLOCATE except that it finds the blobs on
# along a vertical line (x=const.) as opposed to doing so on a ray.
CALL DEPTH(NLIN)
# Computes the lengths of the line in each density region.
# This is done such that LGTH(NLIN,1)= the length through
# the soup and LGTH(NLIN,2)= the length running through blobs.
COLDEN(NLIN)= (DNSOUP + X*DENGRA) * LGTH(NLIN,1) +~
  DENBLO*LGTH(NLIN,2)
EMISS(NLIN)= LGTH(NLIN,1) * (DNSOUP + X*DENGRA)**2 +~
  LGTH(NLIN,2)*DENBLO**2
# COLDEN is obviously column density and, yes that's right,
# EMISS is the emission measure.
X= X + DELX
CLOOP

# Compute some global properties of this plasma that we have wrought.
# I.e. average radius (RADAV), average density (AVDEN), the number of
# blobs (NHIIBL) in the total three dimensional HII region.

TOTLEN= 0.0
AVDEN= 0.0
LENBLO= 0.0
# TOTLEN is the sum of lengths of all line segments and
# LENBLO is the sum of lengths of those sections of the
# segments inside blobs.
LOOP DO I=1,NLIN
  TOTLEN= TOTLEN + LGTH(I,1) + LGTH(I,2)
  LENBLO= LENBLO + LGTH(I,2)
  AVDEN= AVDEN + COLDEN(I)
  COLDEN(I)= COLDEN(I)*pctocm18 # Convert to units of 10**18 cm**-2
CLOOP
AVDEN= AVDEN/TOTLEN

# The quantity 2*TOTLEN*DELX is roughly equivalent to the
# cross-sectional area of the HII region; hence RADAV is the
# radius of a circle of equivalent area. The ratio of
# LENBLO*DELX*DELZ (where DELZ is an assigned infinitesimal
# thickness of the xy plane) and TOTLEN*DELX*DELZ is the
# fraction of the volume, in HII, occupied by the blobs, PVOL.
# Multiplying this by the ratio of the HII region volume to
# individual blob volume gives NHIIBL.

RADAV= SQRT( 2 * TOTLEN * DELX/pi)
PVOL= LENBLO/TOTLEN
NHIIBL= PVOL * (RADAV/BLORAD)**3

# Find the maximum emission measure and produce an array containing
# all x values for the vertical lines used. Following this, output
# the data to files FOR010.DAT and EM3.DAT.

EMMAX= 1.E-30
LOOP DO I=1,2*NLIN
  XPLOT(I) = (I-1) * DELX
CLOOP
LOOP DO I=1,NLIN
  EMMAX = AMAX1(EMISS(I),EMMAX)
CLOOP

WRITE(outfile,100) TOTPHO,BLORAD,NBLOBS,DENBLO,DNSOUP,DENGRA,DUSTK,~
  DELRAD,NINCRE,IDUMA,IDUMB
100 FORMAT(/30X,' HIIBLOB OUTPUT'//1X,'Total no of ionizing photons: ',G11.4~
  /1X,'Blob radius: ',G11.4/1X,'Number of blobs: ',I6/1X,'Blob density: ',G11.4~
  /1X,'Interblob density: ',G11.4/1X,'Density gradient: ',G11.4~
  /1X,'Dust absorption coeff. ',G11.4~
  /1X,'Radial increment: ',G11.4/1X,'Maximum no of radial increments: ',I6~
  /1X,'First random no seed: ',I6/1X,'Second random no seed: ',I6)

```

HIIBLOB3 (contd.)

```

110  WRITE(outfile,110)EMMAX,AVDEN,RADAV,NHIIBL,PVOL,XBOUN,NLIN
      FORMAT(///1X,'Maximum emission measure: ',G11.4/1X,'Average density: ',G11.4~
/1X,'Average radius: ',G11.4/1X,/1X,'Number of blobs in HII region: ',G10.3~
/1X,'Fraction of HII region occupied by blobs: ',G11.4,~
/1X,'Maximum projected extent: ',G11.4,~
/1X,'Number of emission measure samples: ',I4)

115  WRITE(outfile,115)
      FORMAT(/8X,'RADIUS',9X,'EMIS MEAS',4X,'COL DEN E18'/)

120  WRITE(outfile,120)(XPLOT(I),EMISS(I),COLDEN(I),I=1,NLIN)
      FORMAT(3(5X,G11.4))

      IERR = N_OPNDF(20,"EM3.DAT",new,2*NLIN)
      WRITE(20'1)(EMISS(I),I=1,NLIN)
      WRITE(20'2)(XPLOT(I),I=1,2*NLIN)

333  WRITE(terminal,333)RMIN,RMAX,AVDEN,XBOUN,NLIN
      FORMAT(1X,'Minimum radius: ',G11.4,' Maximum radius: ',G11.4~
/1X,' Average density: ',G11.4,~
/1X,' Maximum projected extent: ',G11.4,~
/1X,' Number of emission measure samples: ',I4)

      STOP
      END

```

BLOBVAR.INC

```

#  Declares the common block to be used in HIIBLOB3,BLOCATE,BLINE,
#  BLOPLAC,TAPLAC,DEPTH.

COMMON/BLOB/ DISTO(1000),POSVEC(1000),BRADI(1000),DISTH(1000,2),~
              PLACE(500),NBRAY,ANGOFI(1000,2),NBLOBS,XMAX,XTAB(1000),~
              YTAB(1000)
REAL DISTO,POSVEC,BRADI,DISTH,ANGOFI,XMAX
INTEGER PLACE,NBRAY,NBLOBS

```

LSEG.INC

```

#  Declares common block to be used in HIIBLOB3,DEPTH,TAPLAC,LINSEG.

COMMON/LIN/X,XARR(4000),YARR(4000),RADARR(4000),LGTH(4000,2),~
              UB,LB,HIBOUN(1000),LOBOUN(1000),NBOUN
REAL X,XARR,YARR,HIBOUN,LOBOUN,LGTH
INTEGER NBOUN,UB,LB

```

```

SUBROUTINE BLOCATE(THETA)
# Finds which blobs lie on a ray from the origin and uses BLOPLAC
# to rank the blobs according to distance from the origin.
INCLUDE 'DISK:[DRAO]STNDRD.DEF'
INCLUDE 'BLOBVAR.INC'

REAL DELD,THETA

NBRAY= 0 #No. of blobs on ray.
LOOP DO I=1,NBLOBS
  IF (THETA>ANGOFI(1,1)) & (THETA<ANGOFI(1,2)) #Is blob on ray?
    DELD= SQRT(BRADI(1)**2 - (DISTO(1)*SIN(THETA-POSVEC(1)))**2)
    IF BRADI(1)>DISTO(1) # If the blob contains the origin then
      DISTH(1,1)= 0.0 # distance to first intersection pt. is 0.
      DISTH(1,2)= DELD + DISTO(1) * COS(THETA - POSVEC(1))
      # DISTH(1,1 & 2) are the near and far intersection points
      # between ray and blob circle.
    ELSE
      DISTH(1,1)= DISTO(1) * COS(THETA-POSVEC(1)) - DELD
      DISTH(1,2)= DISTH(1,1) + 2*DELD
    CIF
    IF (DISTH(1,1)>XMAX) DISTH(1,1)=XMAX
    IF (DISTH(1,2)>XMAX) DISTH(1,2)=XMAX # If the blob circle goes
    # beyond XMAX set DISTH(1,1 & 2) equal to XMAX.
    NBRAY= NBRAY+1
    PLACE(NBRAY)= I
    IF (NBRAY>1) CALL BLOPLAC # If more than one blob has been
    # found on the ray so far then call the subroutine that ranks
    # the blobs according to distance from the origin.
  CIF
CLOOP
RETURN
END

SUBROUTINE LINSEG
# Determines which segments of a line x=const. are inside a region
# bounded by points XARR,YARR.
INCLUDE 'DISK:[DRAO]STNDRD.DEF'
INCLUDE 'LSEG.INC'

INTEGER I,DIR,J,IBEF(1000,2),IAFT(1000,2)
REAL TMP,FRAC

NBOUN= 0 # No. of pairs (upper,lower) of boundaries.
I= LB-1
DIR= -1 # 1 if searching for upper boundary and -1 if searching for lower.
IN= 2 # 1 if searching for upper boundary and 2 if searching for lower.

# Start the loop that searches for the indices of those XARR,YARR
# closest to X=const.
LOOP WHILE I <= UB
  I= I+1
  IF DIR*XARR(I) < DIR*X
    NBOUN= NBOUN + IN - 1 # After finding a lower boundary increase
    # the no. of boundary pairs (or no. of line segments) by one.
    IBEF(NBOUN,IN)= I-1 # Index of XARR representing pt. closest to X
    # and before X in the counterclockwise sense.
    IAFT(NBOUN,IN)= I # Same as above except after X counterclockwise.
    DIR= -DIR # Change type of boundary being sought. Note that these
    IN= 1 + (1 - DIR)/2 # are another pair of "witty" formulae.
  CIF
CLOOP

# Interpolate linearly to find the y values of the two endpoints on
# on each line segment.
LOOP DO J=1,NBOUN
  LOOP DO IN=1,2
    FRAC= (X-XARR(IBEF(J,IN))) / (XARR(IAFT(J,IN))-XARR(IBEF(J,IN)))
    TMP= FRAC*(YARR(IAFT(J,IN))-YARR(IBEF(J,IN))) + YARR(IBEF(J,IN))
    IF (IN==1) HIBOUN(J)= TMP
    IF (IN==2) LOBOUN(J)= TMP
  CLOOP
CLOOP

# Update UB,LB to narrow down the search next time.
LB= IBEF(1,2)
UB= IBEF(NBOUN,1)

RETURN
END

```

```

SUBROUTINE BLINE(X)
#
# Similar to BLOCATE but finds blobs on line X=const. as opposed
# to ray from origin.
INCLUDE 'DISK:[DRAO]STNDRD.DEF'
INCLUDE 'BLOBVAR.INC'

REAL DELD,X

NBRAY= 0
LOOP DO I= 1,NBLOBS
  IF (X > XTAB(I)-BRADI(I)) & (X < XTAB(I)+BRADI(I)) # Does line
    # intersect blob at all?
    DELD= SQRT( BRADI(I)**2 - (X-XTAB(I))**2 )
    DISTH(I,1)= YTAB(I) - DELD
    DISTH(I,2)= YTAB(I) + DELD
    NBRAY= NBRAY+1
    PLACE(NBRAY)= I
    IF (NBRAY>1) CALL BLOPLAC # If more than one blob has been
    # found on the line so far then call the subroutine that
    # ranks the blobs according to y value of the lower
    # intersection point.
  CIF
CLOOP
RETURN
END

SUBROUTINE DEPTH(NLIN)
#
# Computes length of line of type X= const. within each density
# region such that LGTH(NLIN,1) is the length going through soup
# and LGTH(NLIN,2) is the length going through blob material.
INCLUDE 'DISK:[DRAO]STNDRD.DEF'
INCLUDE 'BLOBVAR.INC'
INCLUDE 'LSEG.INC'

REAL TABS(25)
INTEGER NLIN,DI,NTABS,I,JL,JU,K

JU= 1 # Initialize the variables for the loop that runs through
LGTH(NLIN,1)= 0.0 # the segments associated with the given line.
LGTH(NLIN,2)= 0.0
LOOP DO K=1,NBOUN
  JL= JU # JL is a PLACE index that serves as a starting place
  # in the search for the first soup-blob interface in the
  # given line segment. JU is such an index for the last
  # such interface in the segment and becomes JL for the
  # next segment.
  TABS(1)= LOBOUN(K) # Two of the TABS must be the endpoints of
  TABS(2)= HIBOUN(K) # the segment itself. The TABS are the
  # positions of the interfaces. NTABS is the number of TABS.
  NTABS= 2 # Obviously must start at 2.
  CALL TAPLAC(K,JL,JU,TABS,NTABS,DI) # Subroutine that places
  # the TABS at the interfaces. DI is the infamous density index
  # which is 1 if the medium between the first two TABS is
  # interblob and 2 if blob.

  #
  # Sum the lengths in the segment running through density region.
  # Since the medium alternates between soup and blob every time
  # a TAB is crossed the sum will alternate between adding to
  # LGTH(NLIN,1) and LGTH(NLIN,2). This is accomplished by
  # applying an incredibly elegant formula that changes 1 to 2
  # and vice-versa.
  #
  #
  #
  #
  LOOP DO I= 1,NTABS-1
    LGTH(NLIN,DI)= LGTH(NLIN,DI) + TABS(I+1) - TABS(I)
    DI= (3 - (-1)**DI)/2
  CLOOP
CLOOP
RETURN
END

```

SUBROUTINE BLOPLAC

```

#
# Ranks blobs according to distance from some starting point. The
# rank is determined by the position of the blob's index number
# in the PLACE array. Eg. if blob no. 34 is the third blob along
# some line or ray then PLACE(3)= 34. The subroutine also handles
# the case of two or more blobs overlapping.

INCLUDE 'DISK:[DRAO]STNDRD.DEF'
INCLUDE 'BLOBVAR.INC'

INTEGER TMP,J,K
LOGICAL*1 FLAG

# Initialize variables and start loop that ranks the blobs according
# to size of DISTH(J,1)

FLAG= .TRUE.
J= NBAY
LOOP WHILE FLAG
  IF DISTH(PLACE(J),1) < DISTH(PLACE(J-1),1)
    TMP= PLACE(J-1)
    PLACE(J-1)= PLACE(J)
    PLACE(J)= TMP
  ELSE
    FLAG= .FALSE.
  CIF
  J= J-1
  IF (J==1) FLAG= .FALSE.
CLOOP

# Now start the loop that checks to see if any blobs overlap. If this
# is the case then "compound" the blobs by removing the second blob's
# index from the PLACE array.

K=1
LOOP WHILE K<= NBAY-1
  IF DISTH(PLACE(K),2) >= DISTH(PLACE(K+1),1)
    NBAY= NBAY-1 # If overlap exists decrease no. of effective
                # blobs by one.
    IF DISTH(PLACE(K+1),2) > DISTH(PLACE(K),2) # If the far intersection
      DISTH(PLACE(K),2)= DISTH(PLACE(K+1),2) # pt. of the second blob is
      CIF # further than that of the first blob (usually the case) then
      # set the far intersection pt. of the first blob to be that of the
      # second blob. Now start the loop that effectively removes the
      # second blob from the PLACE array and moves all further blobs
      # closer to first place in the PLACE array.
      LOOP DO J= K+1,NBAY
        PLACE(J)= PLACE(J+1)
      CLOOP
    ELSE
      K= K+1
    CIF
CLOOP
RETURN
END

```

SUBROUTINE TAPLAC(K,JL,JU,TABS,NTABS,DI)

```
#
Records positions of blob-interblob interfaces within a line segment.

INCLUDE 'DISK:[DRAO]STNDRD.DEF'
INCLUDE 'BLOBVAR.INC'
INCLUDE 'LSEG.INC'

REAL TABS(25)
INTEGER K,NTABS,DI,DT,J,JI,JL,JU,FLAG

DI= 1 # Density index for medium between first two TABS.
J= JL # Represents position of last blob within previous
      # line segment. Provides starting place for search
      # of the interfaces.
JI= J # JI is used so that the index of PLACE never exceeds
IF (JI>NBWAY) JI=NBWAY # the value NBWAY. These two lines
# are repeated two more times in this subroutine.
FLAG= 0 # FLAGS when routine goes through inner loop.
LOOP WHILE (J<=NBWAY) & (DISTH(PLACE(JI),DI)<HIBOUN(K))
  DT= DI # DT is density index for inner loop.
  # Now loop while there are interfaces between the segment
  # endpoints - LOBOUN and HIBOUN.
  LOOP WHILE (DISTH(PLACE(JI),DT)>LOBOUN(K)) & (DISTH(PLACE(JI),DT)~
    <HIBOUN(K)) & (J<=NBWAY)
    FLAG= 1 # Set to one since now in inner loop.
    JU= J # JU represents position of last blob within this line
          # segment and provides starting place for next segment.
    TABS(NTABS+1)= HIBOUN(K)
    TABS(NTABS)= DISTH(PLACE(J),DT) # "TAB" the interface
    NTABS= NTABS+1
    J= J+DT-1 # Change to next density region. Both of
    DT= (3-(-1)**DT)/2 # these are abundantly intelligent formulae.
    JI= J # Both of these explained
    IF (JI>NBWAY) JI= NBWAY # above.
  CLOOP
  XLOOP WHEN FLAG==1 # If inner loop entered exit outer loop because
  J= J+DI-1 # all required TABS found.
  JI= J # Explained
  IF (JI>NBWAY) JI= NBWAY # above.
  DI= (3-(-1)**DI)/2 # If the inner loop has not been
  # entered (i.e. no interface yet found in segment) change to
  # opposite density index using wonderfully bright formula. DI is
  # suppose to represent the density index at the "entrance" to
  # the inner loop.
CLOOP
RETURN
END
```

APPENDIX D: CONVOLUTION COMPENSATION FUNCTION

The compensating function described in Section 3.3 is derived by assuming that the unconvolved source has a Gaussian intensity distribution, i. e.

$$I(x, y) = I(0, 0) \exp[-(x/\theta_x)^2 - (y/\theta_y)^2] \quad D. 1)$$

where the y axis is north-south, the x axis east-west, θ_x, θ_y , are the 1/e half-widths in the x and y directions respectively and where $I(0, 0)$ is the intensity at the centre of the source. The observed intensity distribution $i(x, y)$ is given by

$$i(x, y) = I(x, y) * b(x, y) \quad D. 2)$$

where * denotes convolution and $b(x, y)$ is the beam pattern

$$b(x, y) = (1/(\pi ab)) \exp[-(x^2/a^2) - (y^2/b^2)] \quad D. 3).$$

Substituting D. 3) and D. 1) into D. 2) yields

$$i(x, y) = (1/(\pi ab)) I(0, 0) \int_{-\infty}^{\infty} dx' \exp[-x'^2/\theta_x^2] \exp[-(x-x')^2/a^2] \times \\ \times \int_{-\infty}^{\infty} dy' \exp[-y'^2/\theta_y^2] \exp[-(y-y')^2/b^2]$$

which, after some reduction, becomes

$$i(x, y) = (\theta_x/\theta_a)(\theta_y/\theta_b) I(0, 0) \exp[-(x/\theta_a)^2 - (y/\theta_b)^2] \quad D. 4)$$

$$\text{where} \quad \theta_a^2 = \theta_x^2 + a^2 \quad D. 5a)$$

$$\theta_b^2 = \theta_y^2 + b^2 \quad D. 5b).$$

Let $i_1(x)$ represent a slice of the two dimensional $i(x, y)$ in the x direction. Similarly $b_1(x)$ is the one dimensional analog of $b(x, y)$ given by

$$b_1(x) = (1/a\pi^{0.5}) \exp[-(x^2/a^2)] \quad D. 6).$$

which is normalized in the x direction only. It follows that

$$i_1(x) = I(x, 0) * b_1(x) \\ = (1/a\pi^{0.5}) I(0, 0) \int_{-\infty}^{\infty} dx' \exp[-(x'/\theta_x)^2] \exp[-(x-x')^2/a^2]$$

resulting in

$$i_1(x) = (\theta_x/\theta_a) I(0, 0) \exp(-x^2/\theta_a^2) \quad D. 7).$$

The convolved output of HIIBLOB3 would be represented by D. 7). The equivalent slice from a correct two dimensional treatment would give

$$i(x, 0) = (\theta_x / \theta_a)(\theta_y / \theta_b) I(0, 0) \exp(-x^2 / \theta_a^2) \quad \text{D. 8) .}$$

Therefore the compensating function is

$$i(x, 0) / i_1(x) = (\theta_y / \theta_b) \quad \text{D. 9)}$$

for an east-west slice. Similarly for a north-south slice we would have

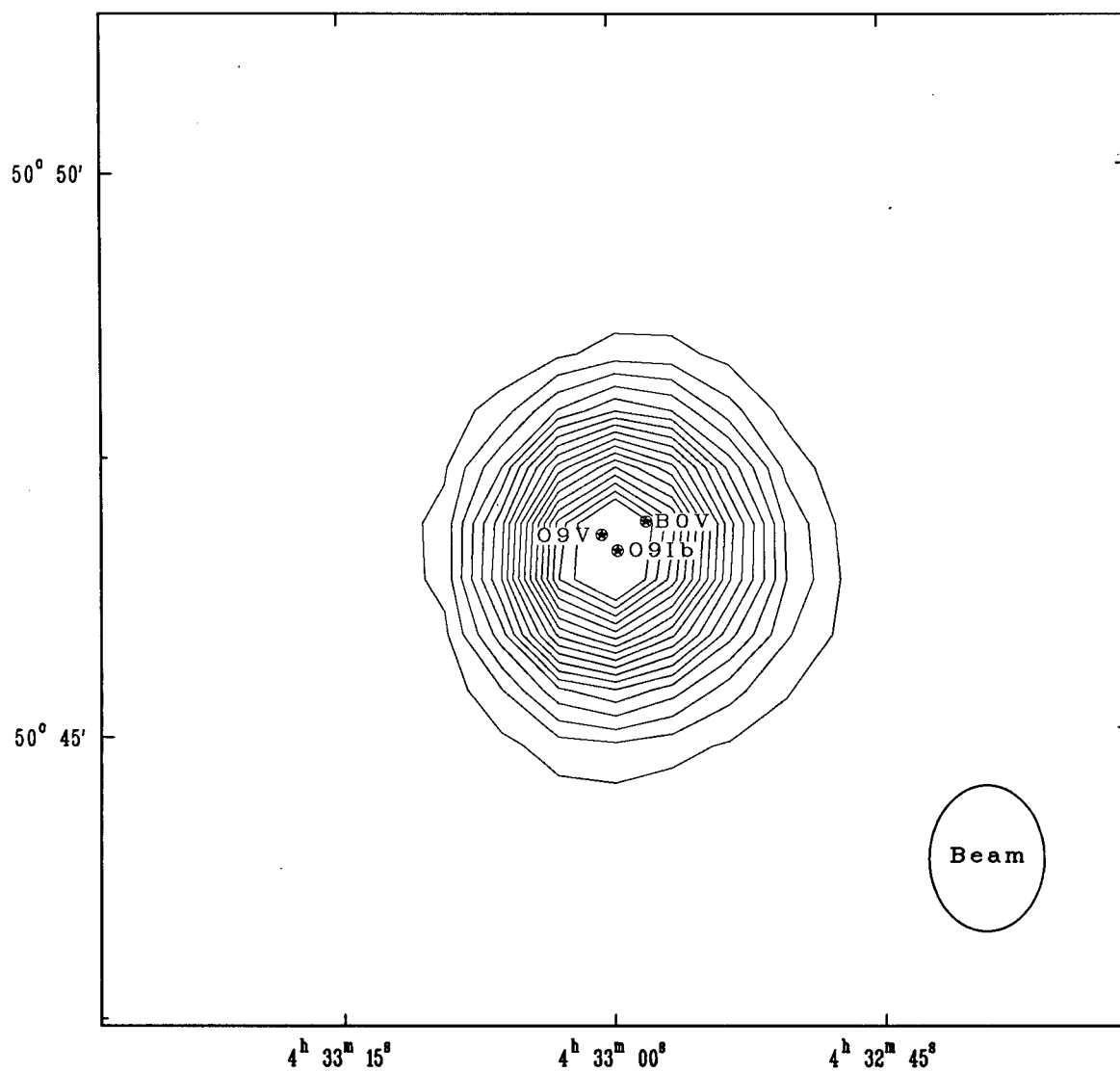
$$i(0, y) / i_1(y) = (\theta_x / \theta_a) \quad \text{D. 10)}$$

where $i_1(y)$ is the north-south analog of $i_1(x)$.

APPENDIX E: S211 HI MAPS AND SPECTRA

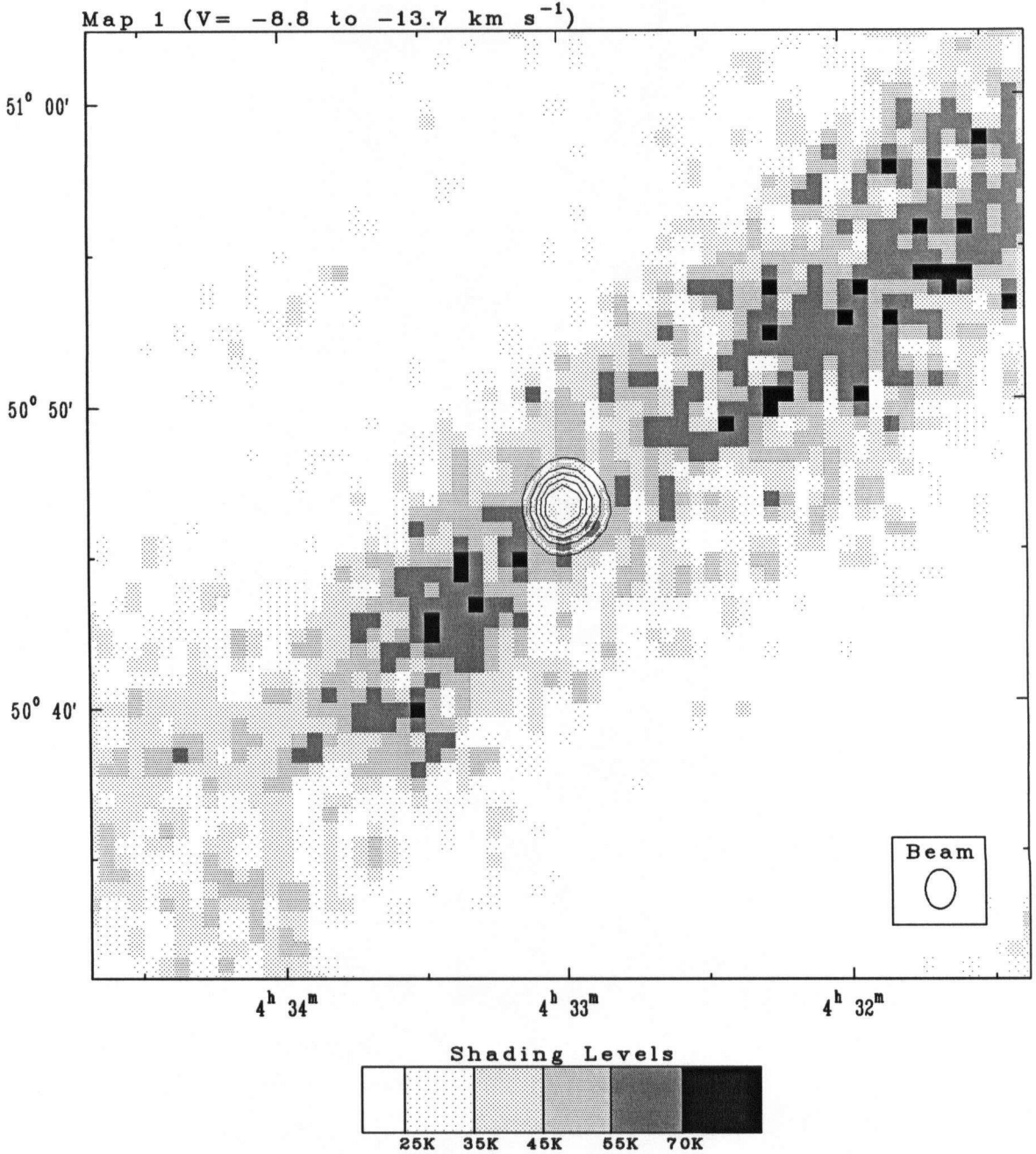
This appendix contains a continuum map of S211 depicting the positions of its ionizing stars (p127), 32' x 32' HI maps centred on S211 (pp128 to 138), HI velocity maps ($v-\alpha$, $\delta-v$) corresponding to the 32' x 32' area centred on S211 (p140), HI spectra averaged in blocks (pp142 to 143) and averaged in rings (pp145 and 146). The map of S211 and its ionizing stars labels the stars with their spectral classes according to Chini & Wink (1984). The S211 HI maps are the spectrum subtracted (SS) maps averaged in 5 km s^{-1} velocity ranges, except at those velocities where certain features are found near S211 (i.e. map 7), over the entire CC Survey bandwidth. As a result the noise in all maps, except map 7, is estimated to be about 5K rms; in map 7 this is 3K rms. A contour map of S211 is overlaying the HI maps for comparison. The HI velocity maps and spectra are discussed on pages 139, 141, 144.

S211 and Ionizing Stars



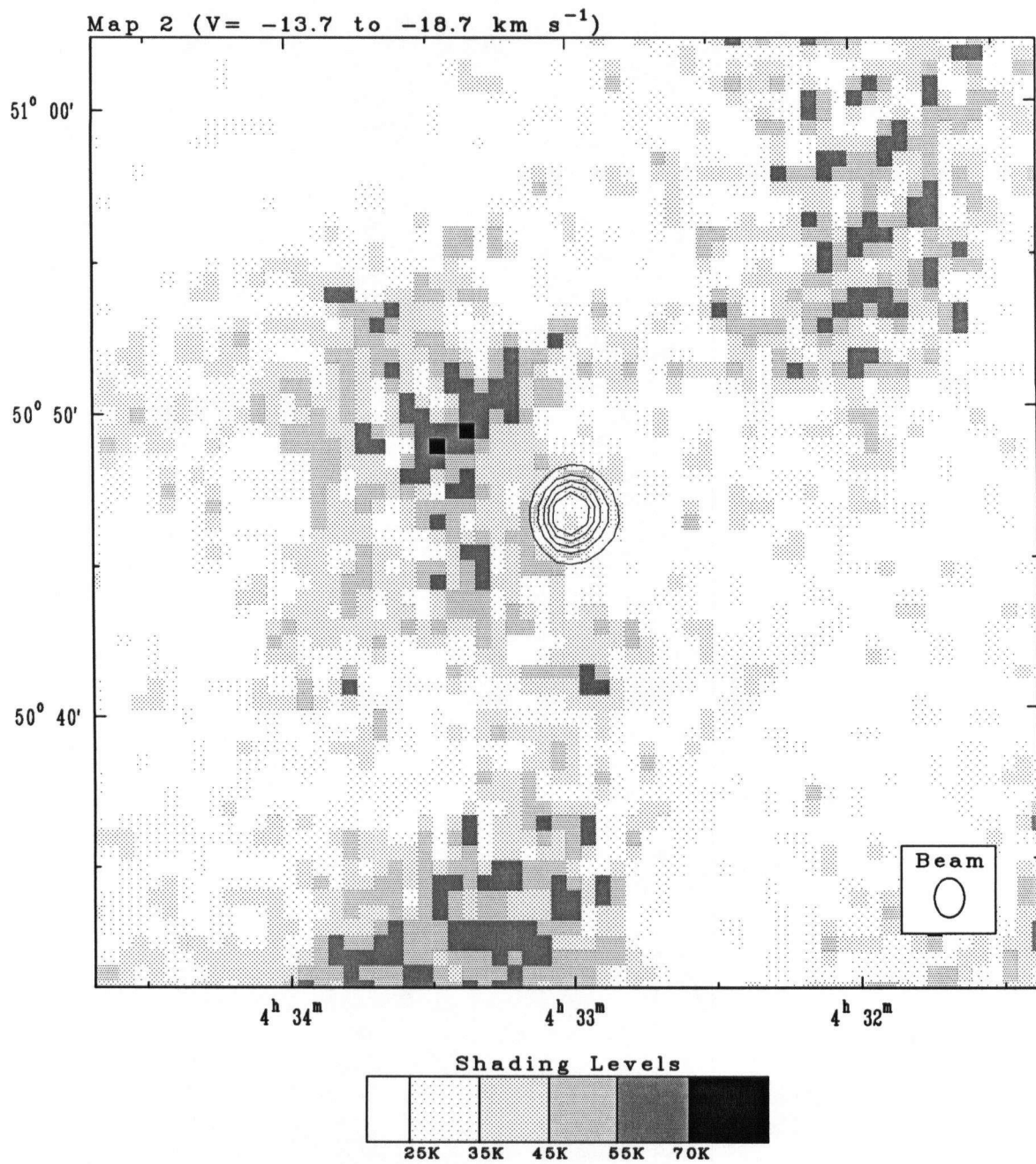
Contours: Multiples of 2K from 2K to 36K.
(Brightness Temperature Units)

S211 HI Maps



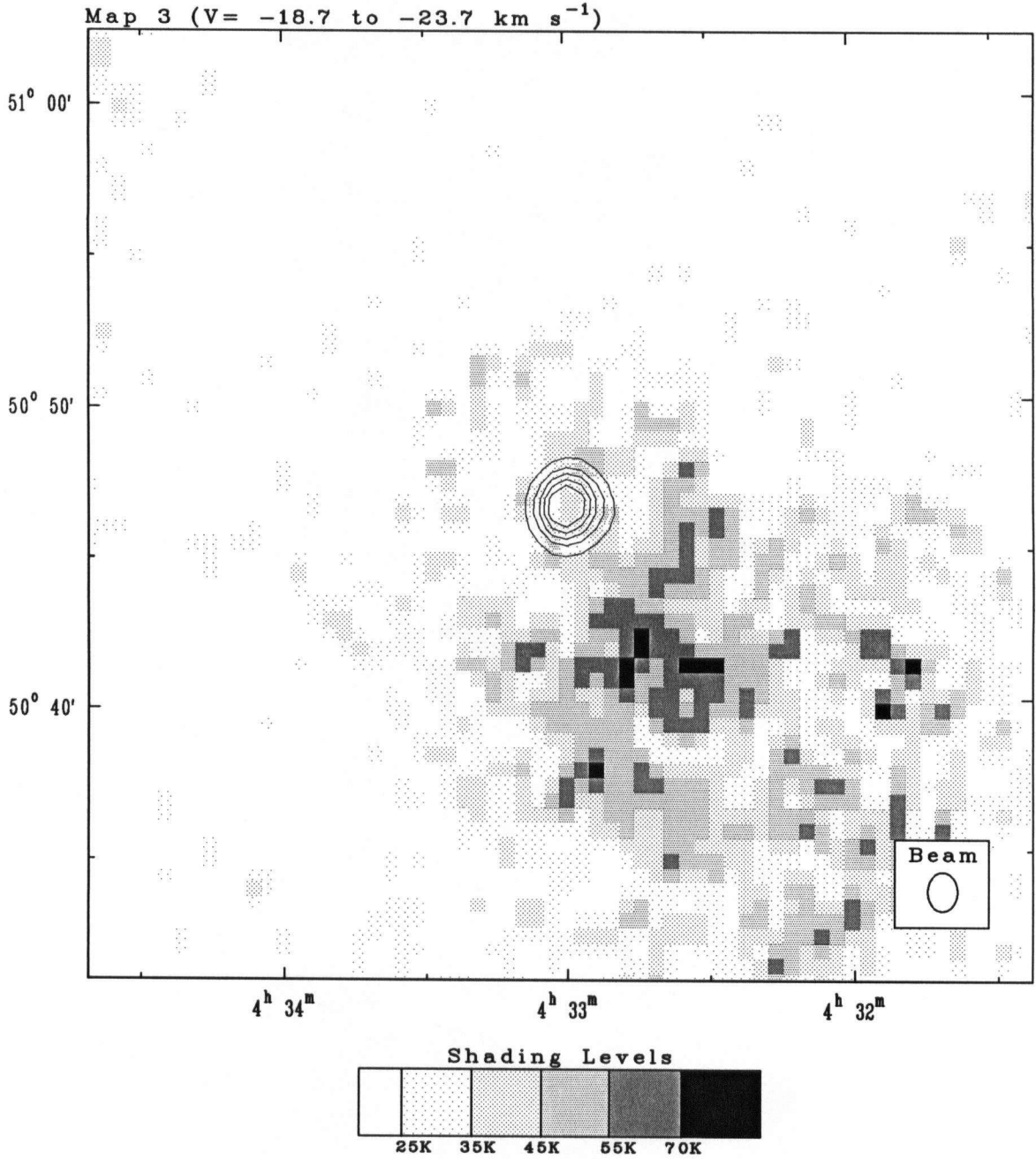
Contours: (6, 12, 18, 24, 30) K Brightness Temperature

S211 HI Maps



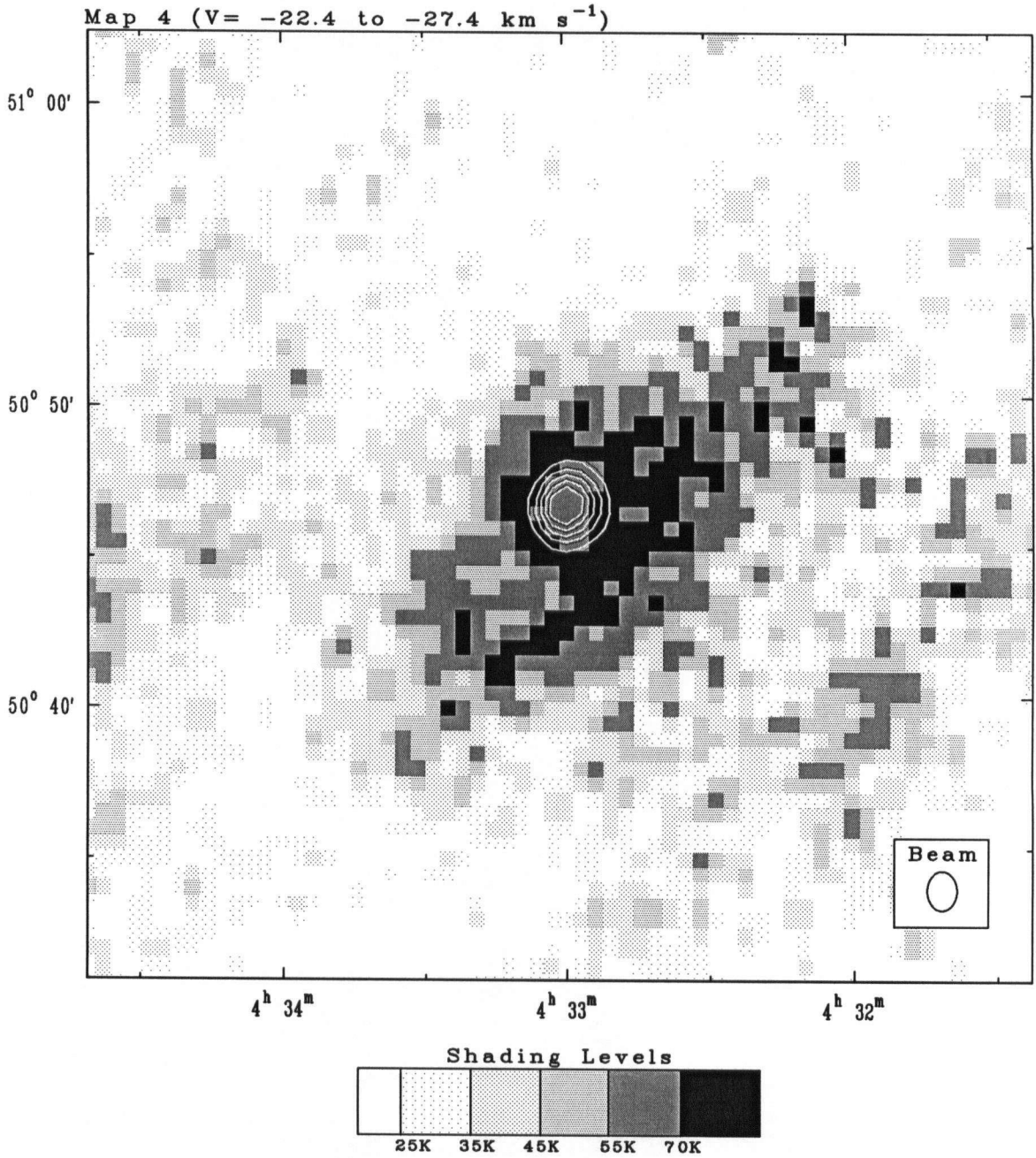
Contours: (6, 12, 18, 24, 30) K Brightness Temperature

S211 HI Maps



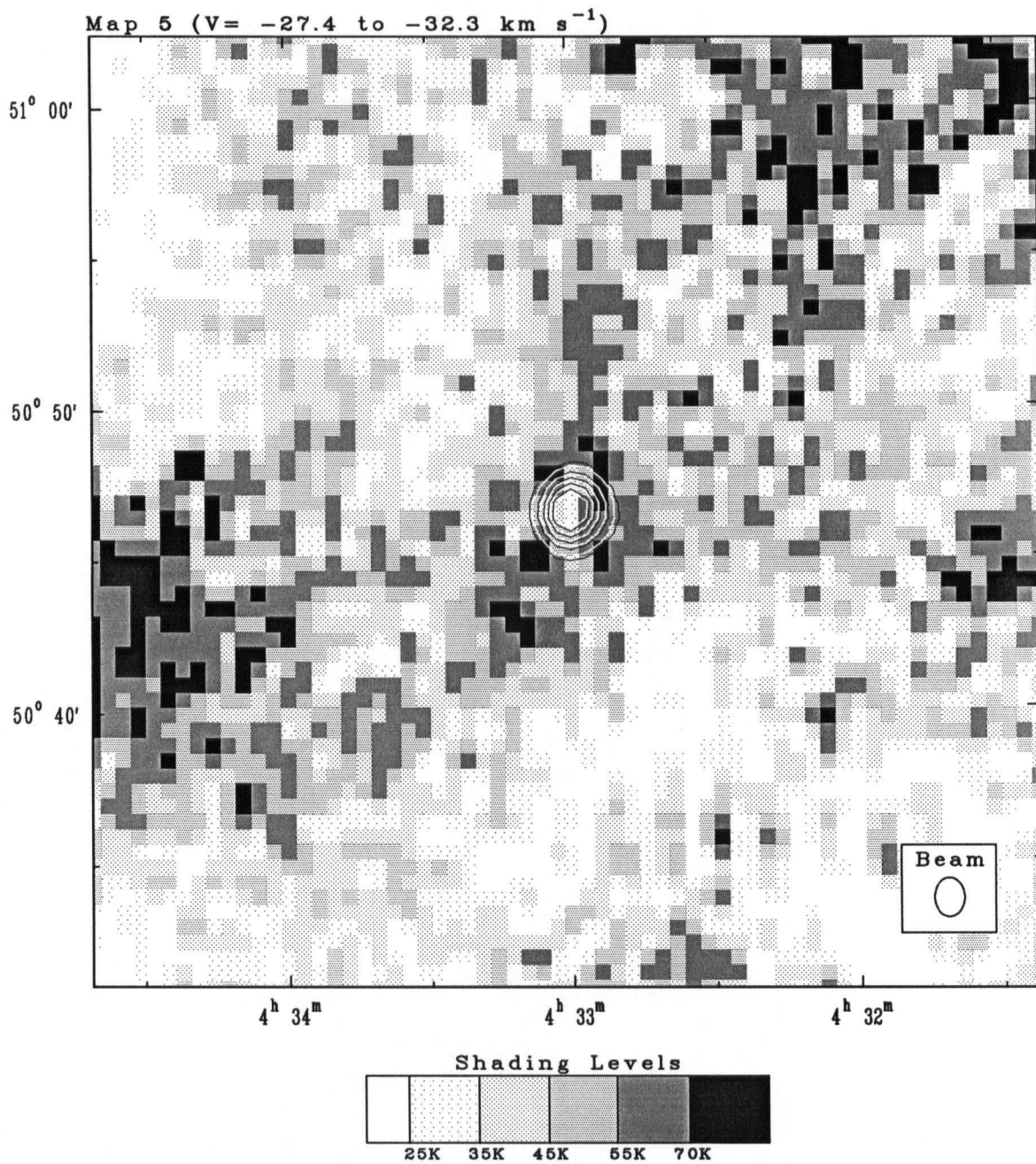
Contours: (6, 12, 18, 24, 30) K Brightness Temperature

S211 HI Maps



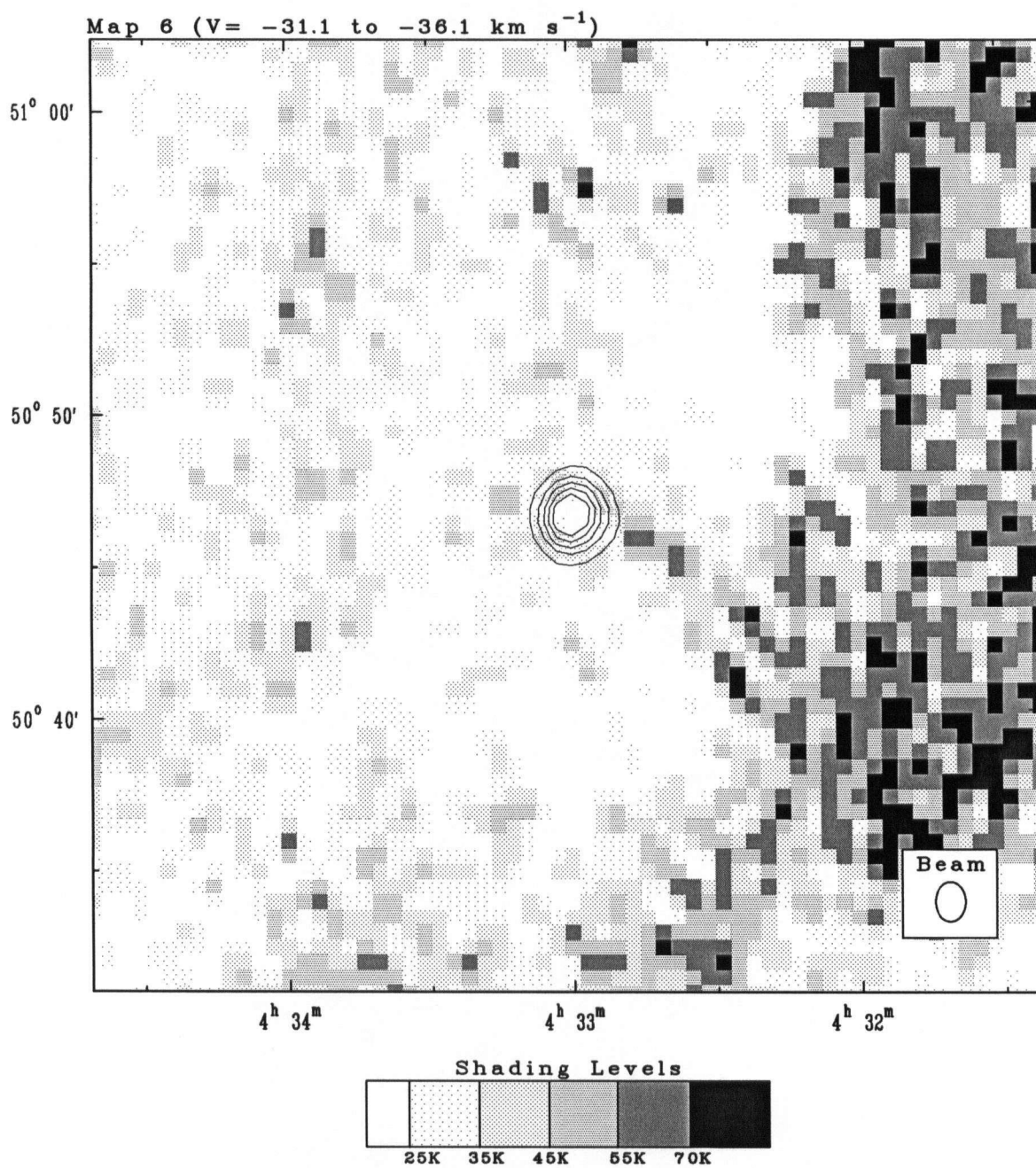
Contours: (6, 12, 18, 24, 30) K Brightness Temperature

S211 HI Maps



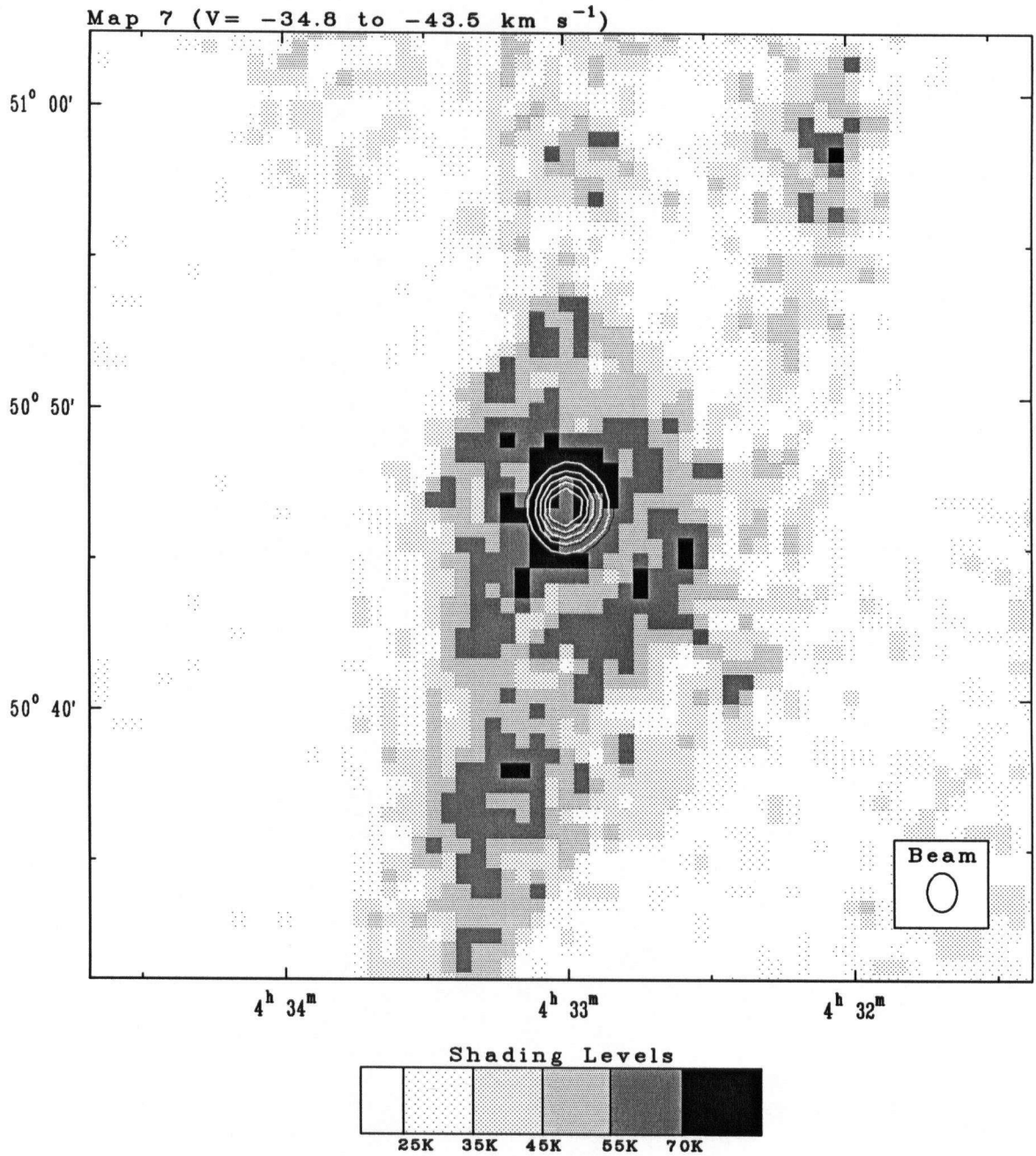
Contours: (6, 12, 18, 24, 30) K Brightness Temperature

S211 HI Maps



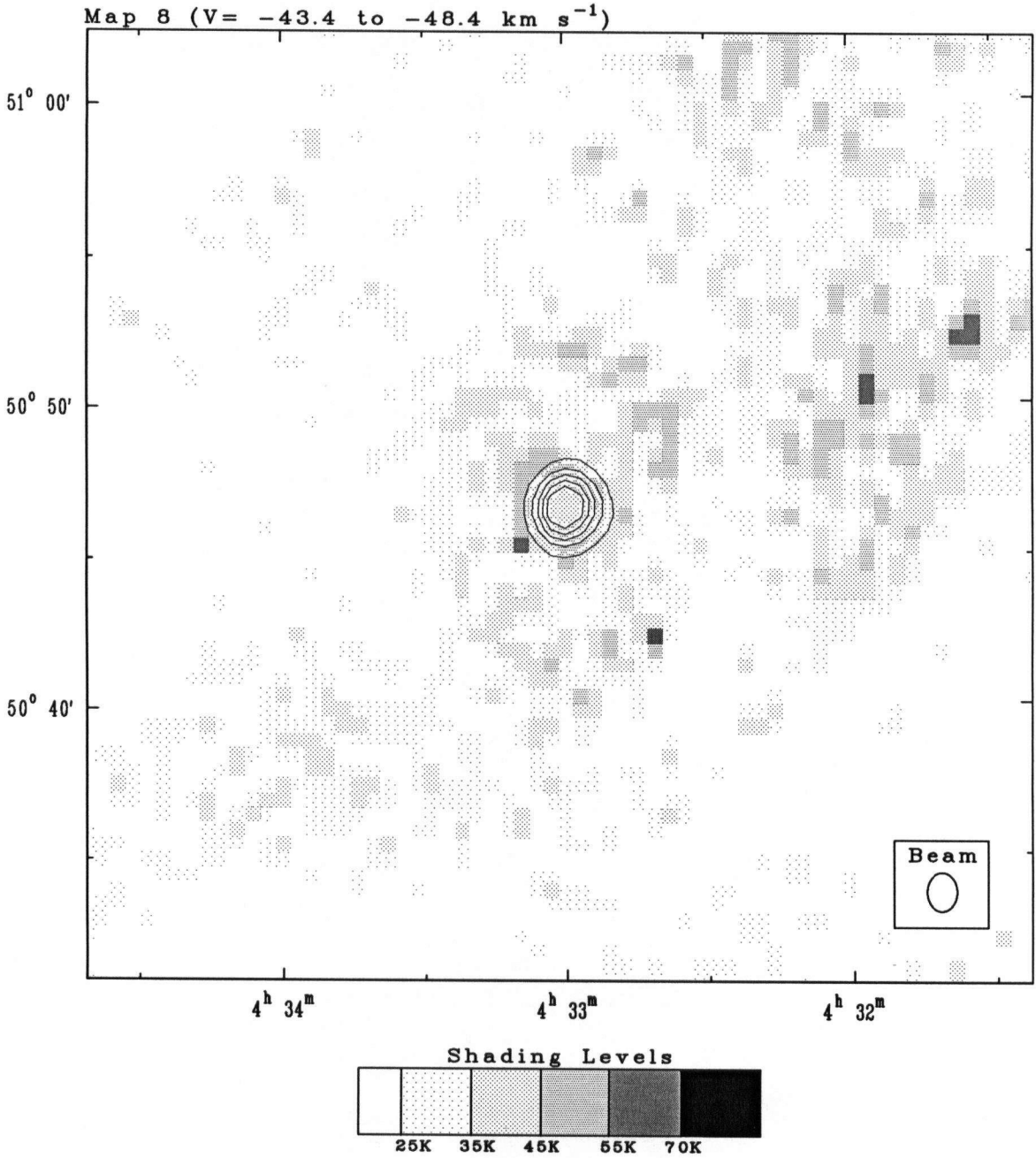
Contours: (6, 12, 18, 24, 30) K Brightness Temperature

S211 HI Maps



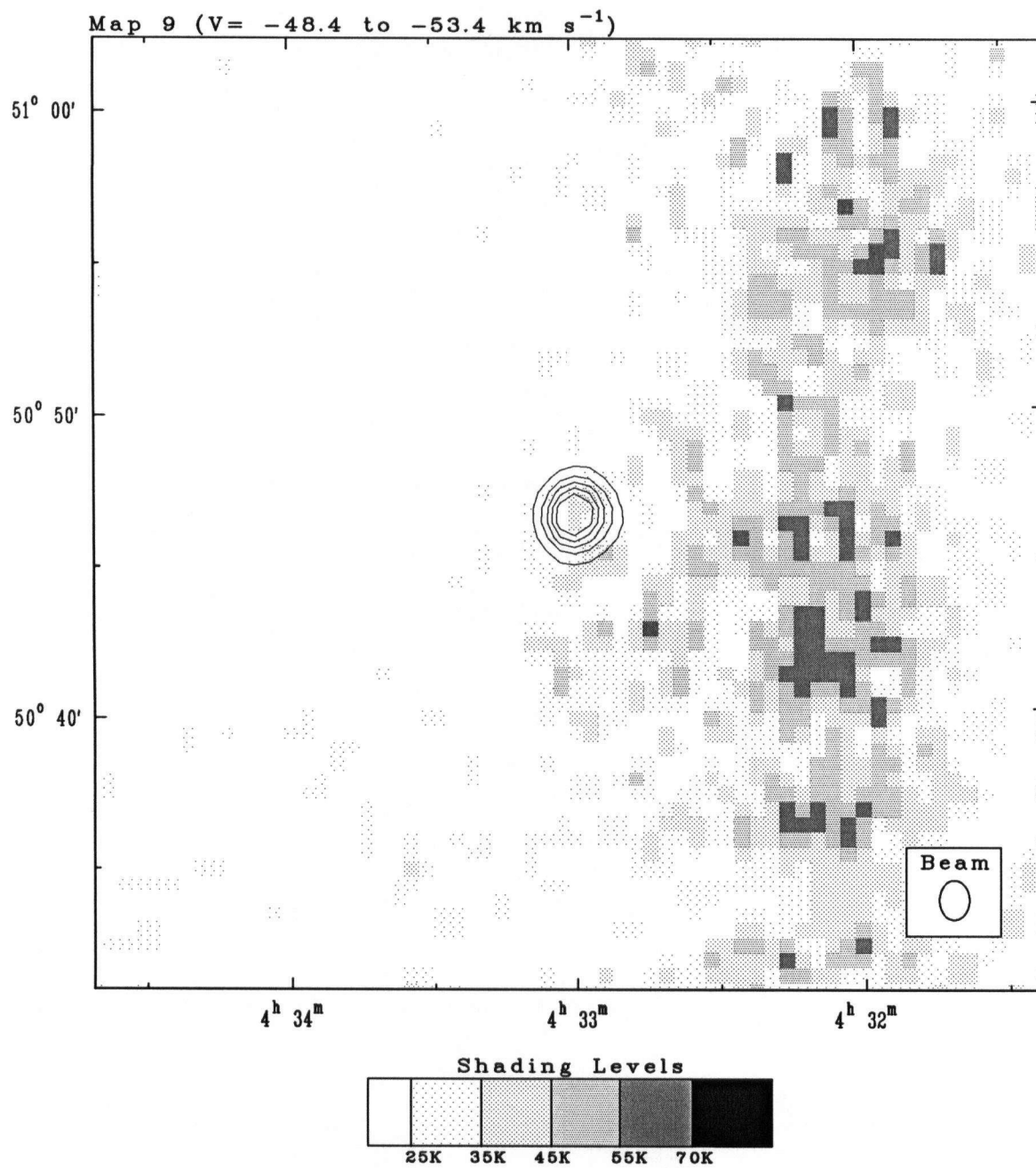
Contours: (6, 12, 18, 24, 30) K Brightness Temperature

S211 HI Maps



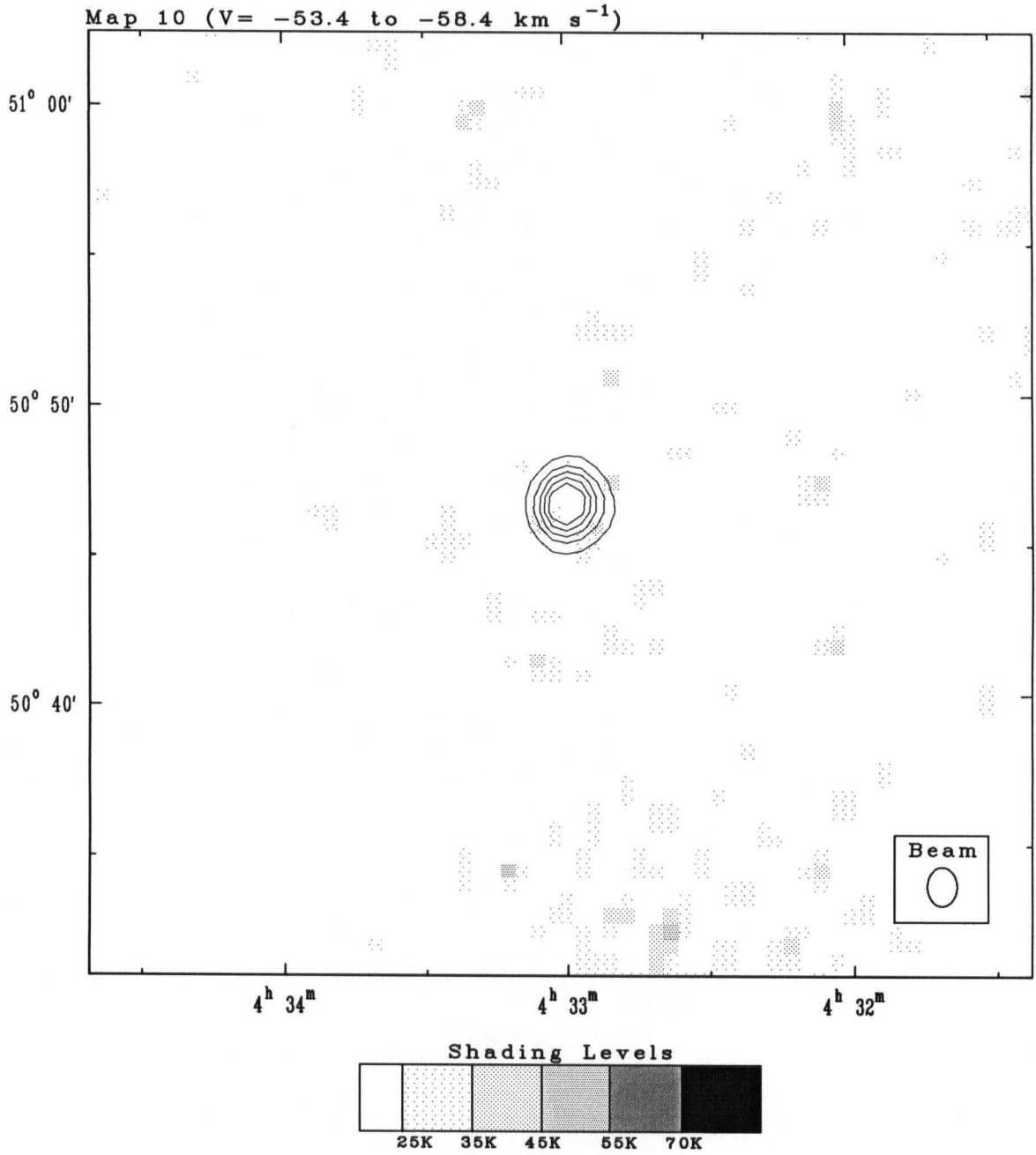
Contours: (6, 12, 18, 24, 30) K Brightness Temperature

S211 HI Maps



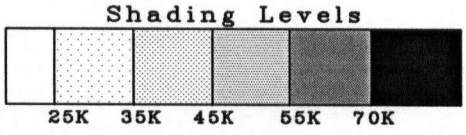
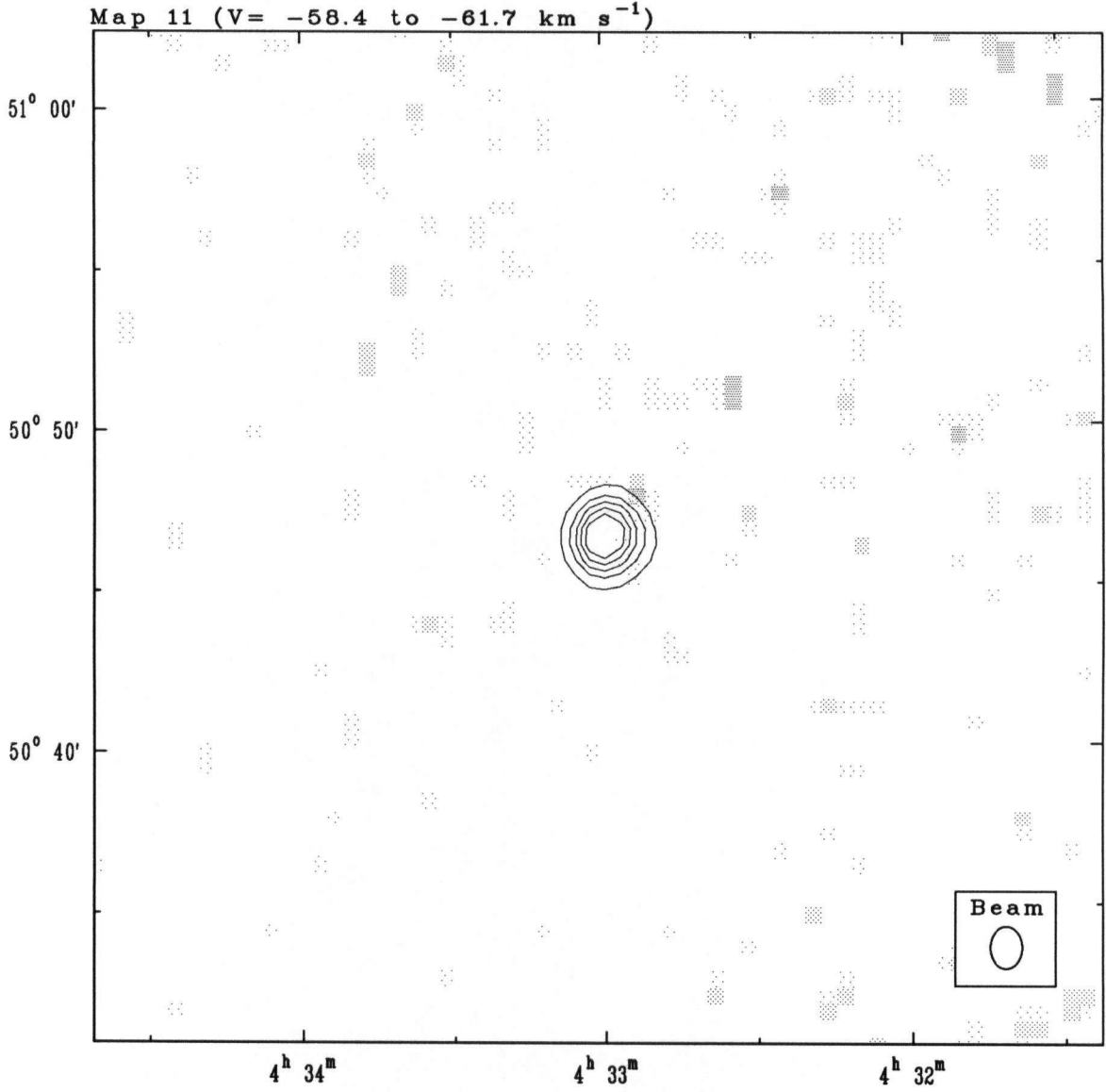
Contours: (6, 12, 18, 24, 30) K Brightness Temperature

S211 HI Maps



Contours: (6, 12, 18, 24, 30) K Brightness Temperature

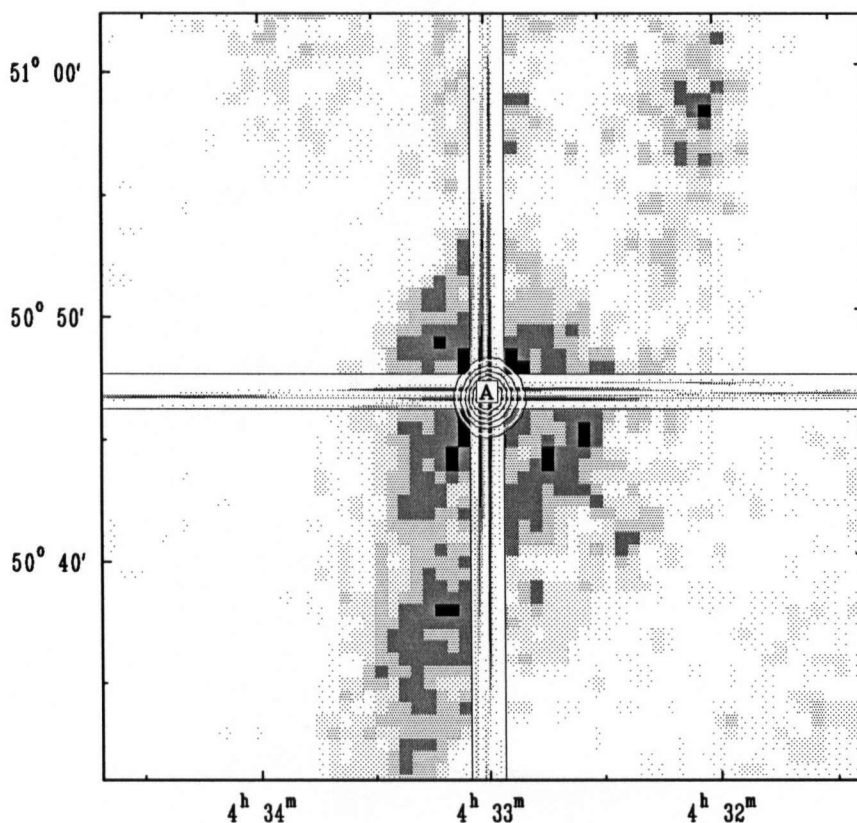
S211 HI Maps



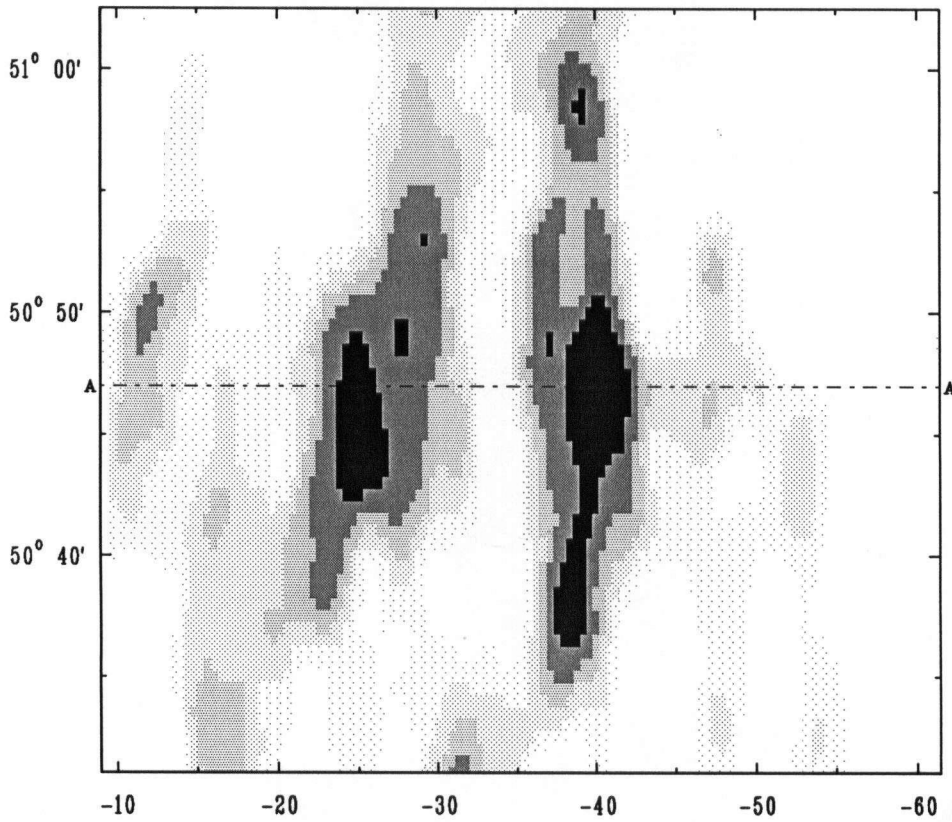
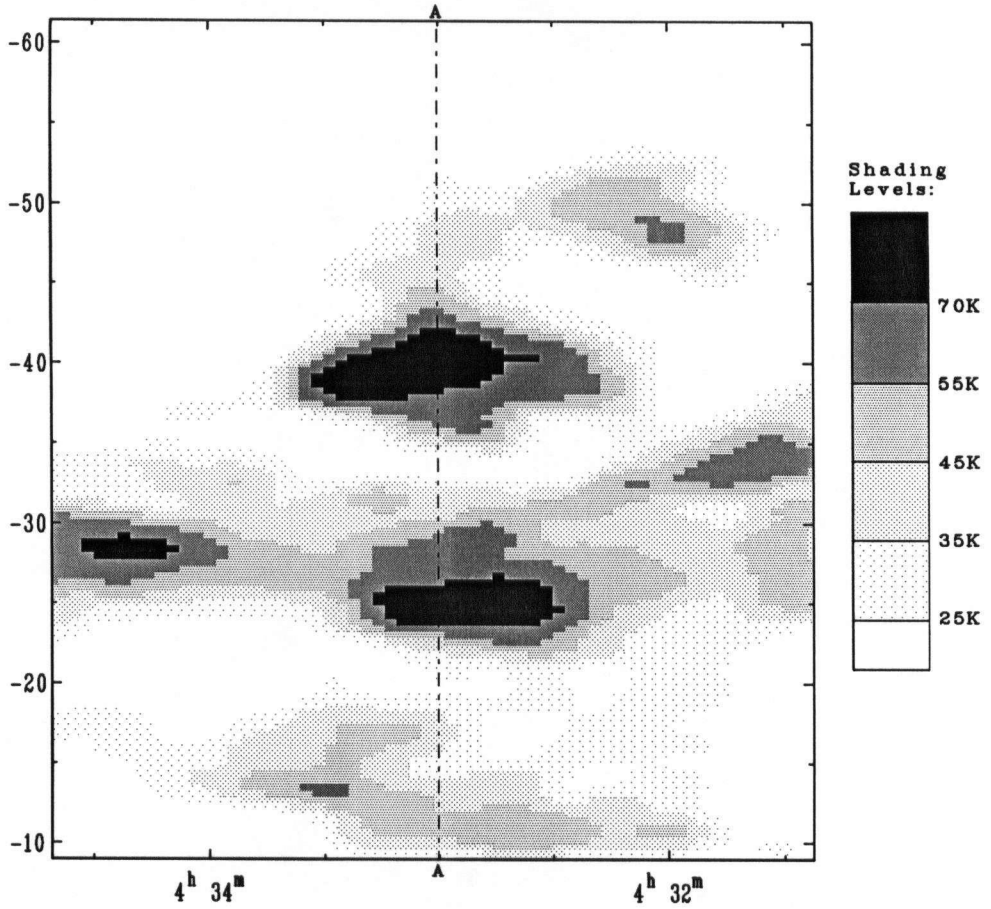
Contours: (6, 12, 18, 24, 30) K Brightness Temperature

S211 HI Velocity Maps

The following page shows a velocity-right ascension map (top) and declination-velocity map (bottom) which were taken at the positions of the horizontal and vertical bars shown in the map below. The position of the intersection marked "A" is represented by a dashed line in the velocity maps. Each bar contains a foreshortened version of its corresponding velocity map and has a 3 pixel (1'.5) thickness because each velocity map is a 3 pixel average in the spatial dimension indicated by the bar thickness; i.e. the $v-\alpha$ map has been averaged by 3 pixels in the δ direction and the $\delta-v$ map has been averaged by 3 pixels in the α direction. In addition, each map has been smoothed to 1.7 km s^{-1} resolution in the velocity direction and to $3'$ in the spatial direction (α or δ). The noise is estimated to be about 1 to 2K rms. The velocity axes are in km s^{-1} with respect to the local standard of rest.

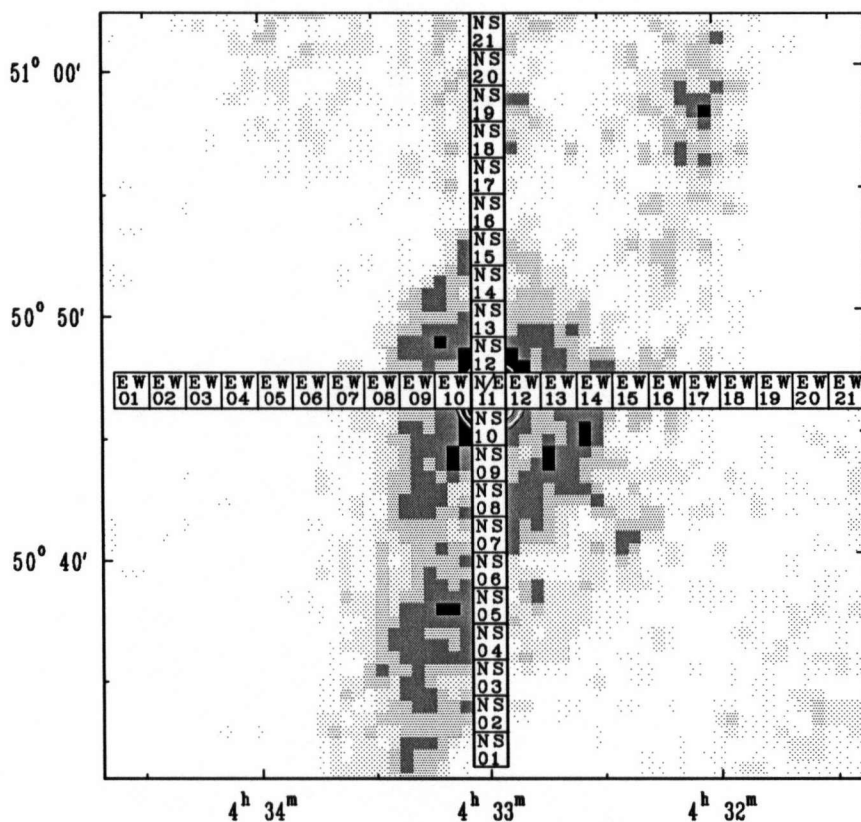


S211 HI Velocity Maps

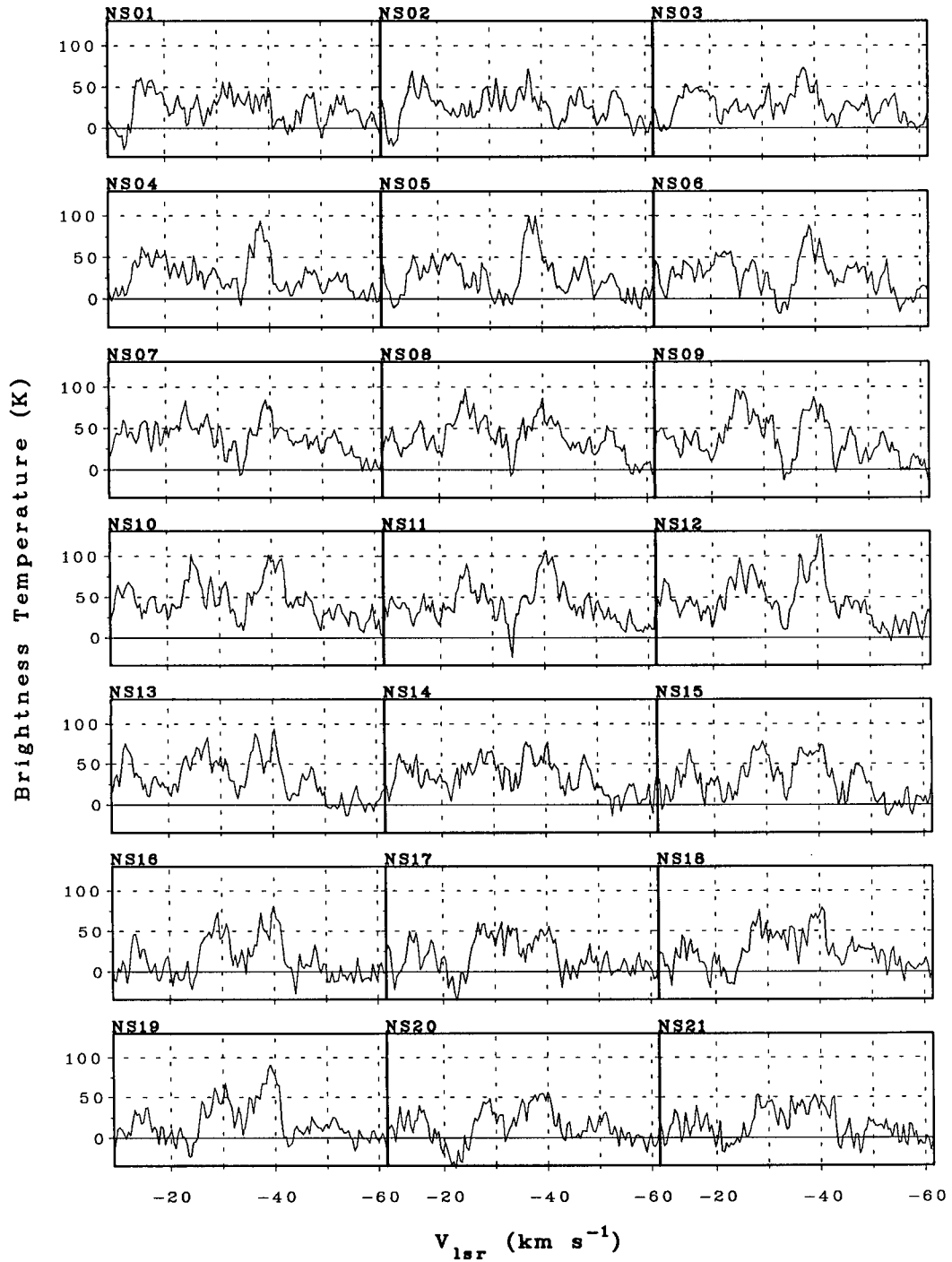


S211 HI Spectra (Block)

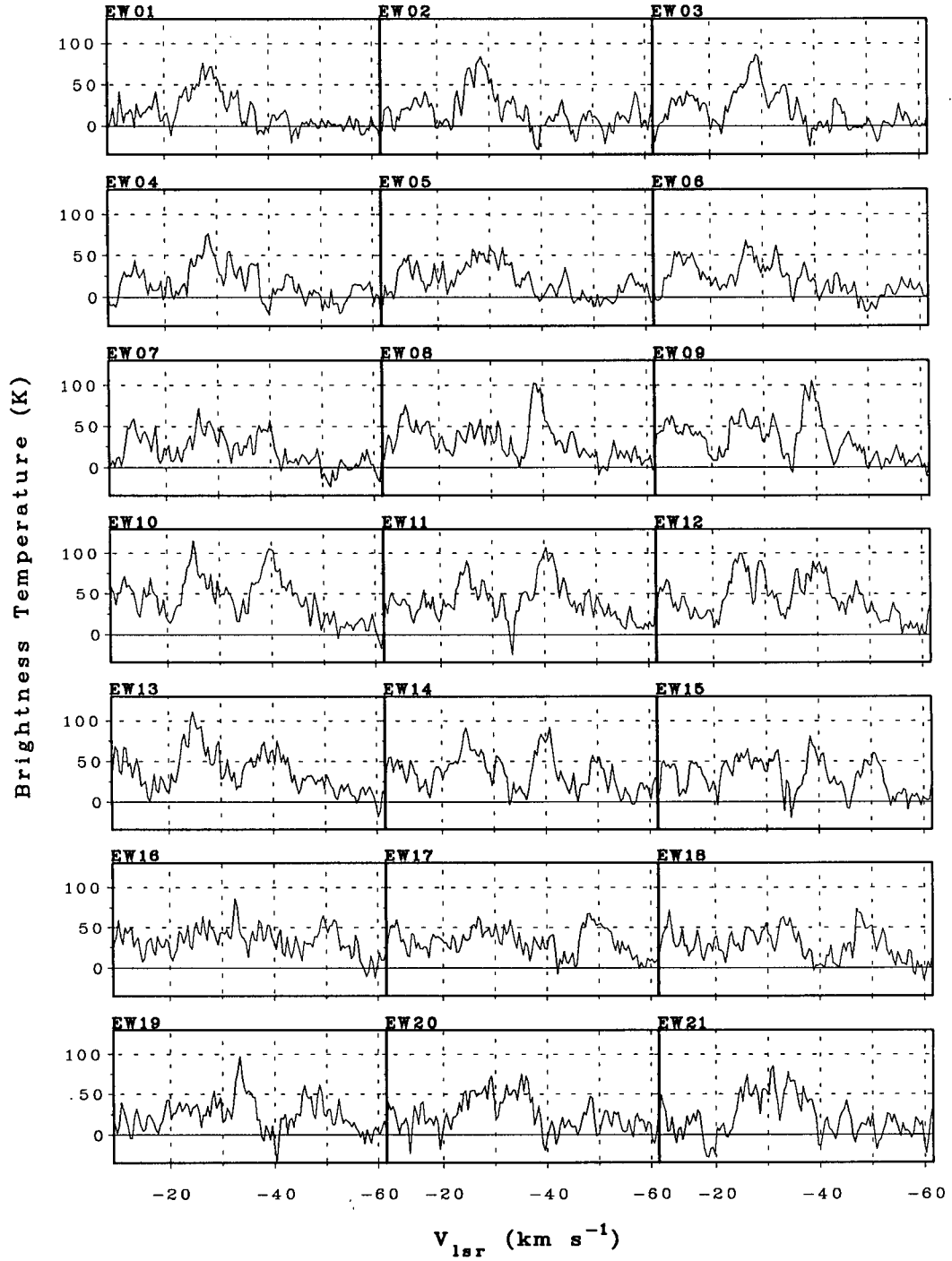
The spectra on the following two pages are spatial averages of 3 pixel by 3 pixel blocks at the positions shown in the map below. The spectra of the north-south blocks are denoted by NS and those of the east-west are denoted by EW. Notice that NS11 and EW11 are the same spectrum. The noise in each spectrum is estimated to be between 5 to 7K rms.



S211 HI Spectra (Block)

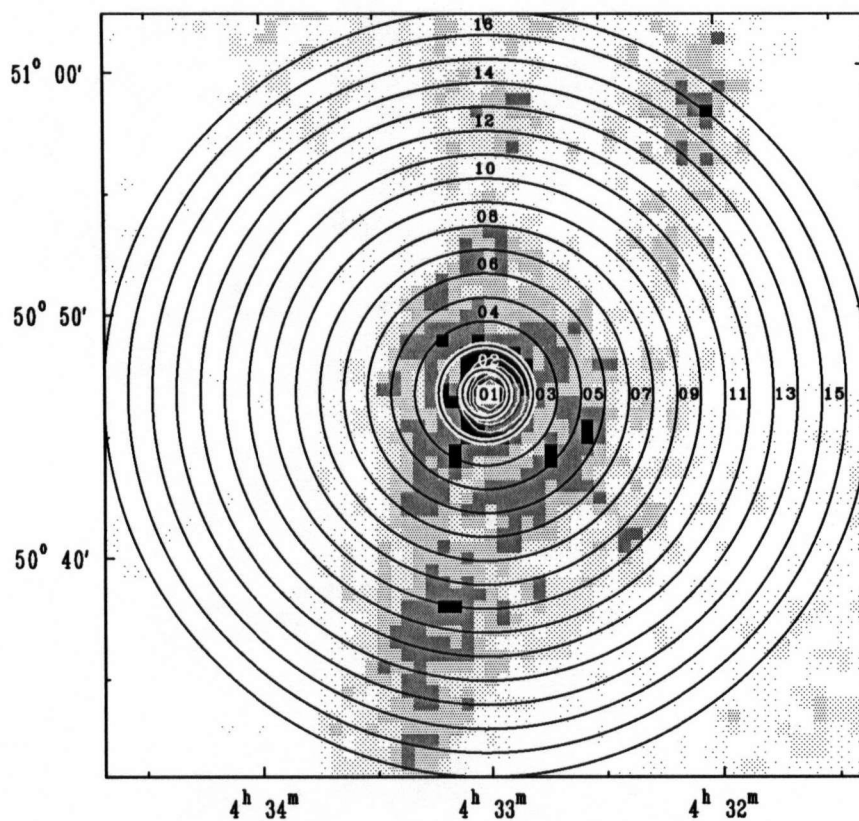


S211 HI Spectra (Block)

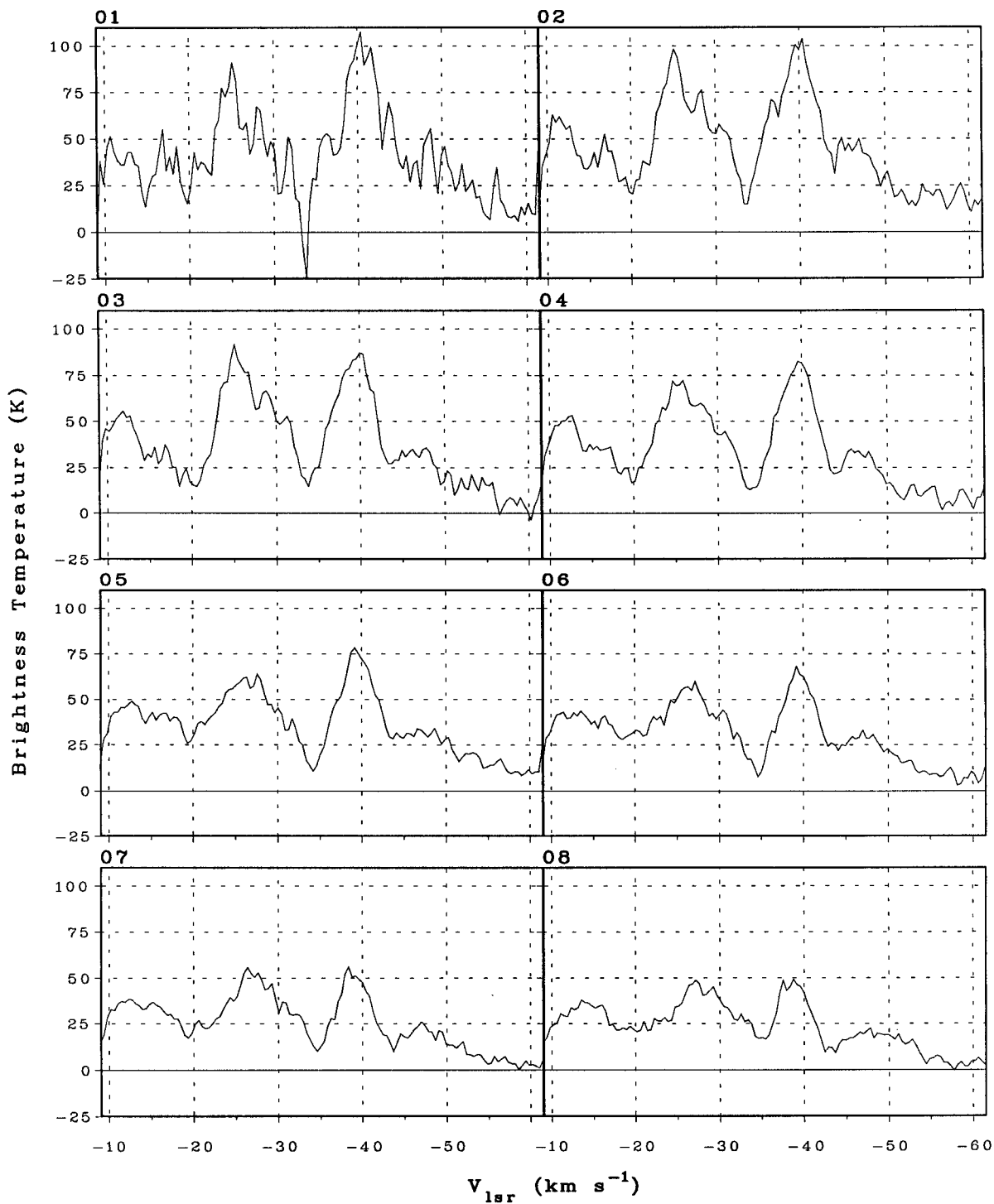


S211 HI Spectra (Ring)

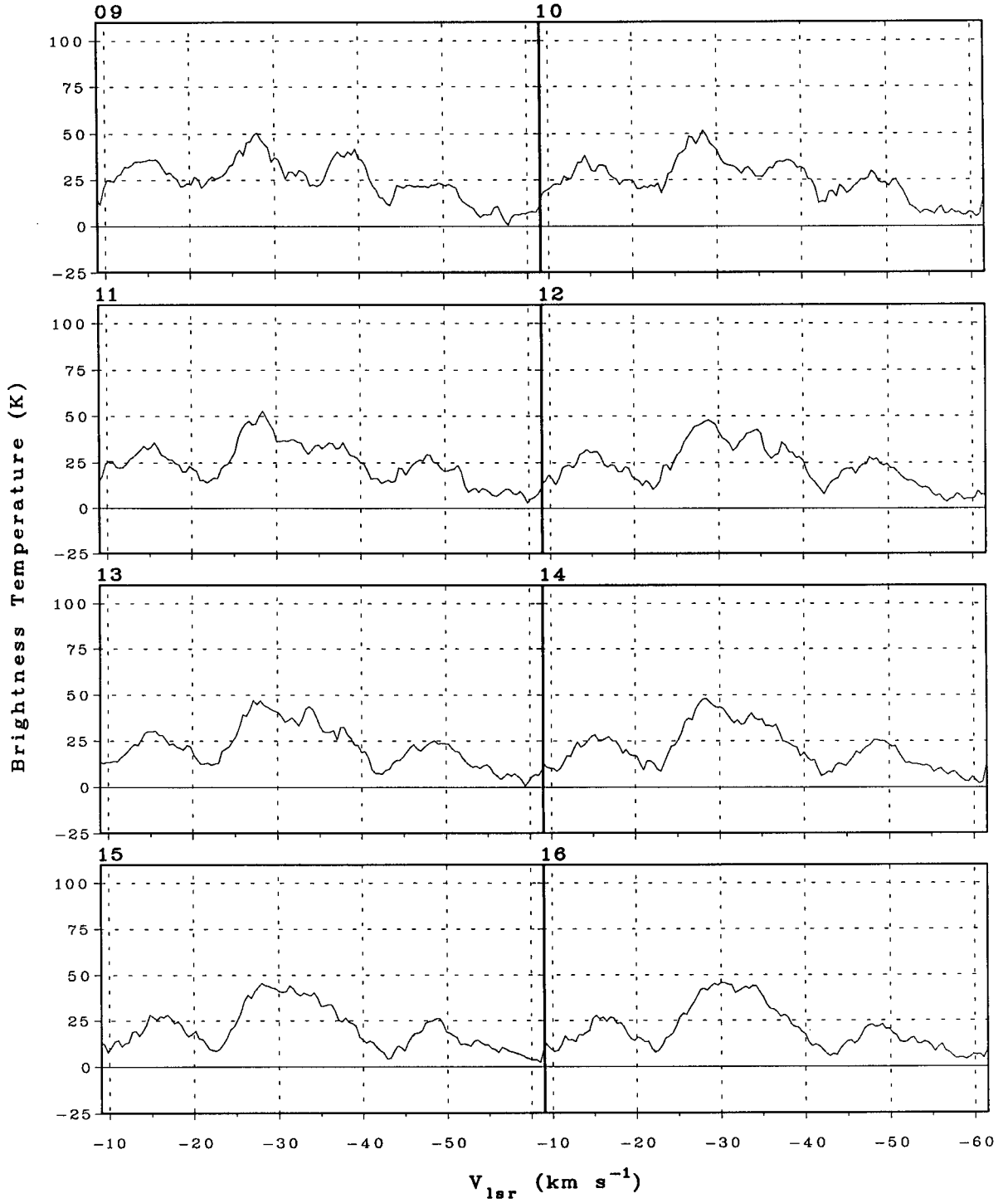
The spectra on the following two pages are spatially averaged in rings of 2 pixels (1') in thickness as shown in the map below. The number assigned to each of the spectra corresponds to a ring number below. The noise of the ring 1 spectrum is about 7K rms. The noise of the spectrum in ring number RN can be estimated from $\sigma_0(\text{RN})^{-0.5}$ where σ_0 is 5 to 7K. Because of quantization effects the spatial area for each spectrum is not exactly annular. The morphology of the spatial averaging is still adequately represented by the map below.



S211 HI Spectra (Ring)



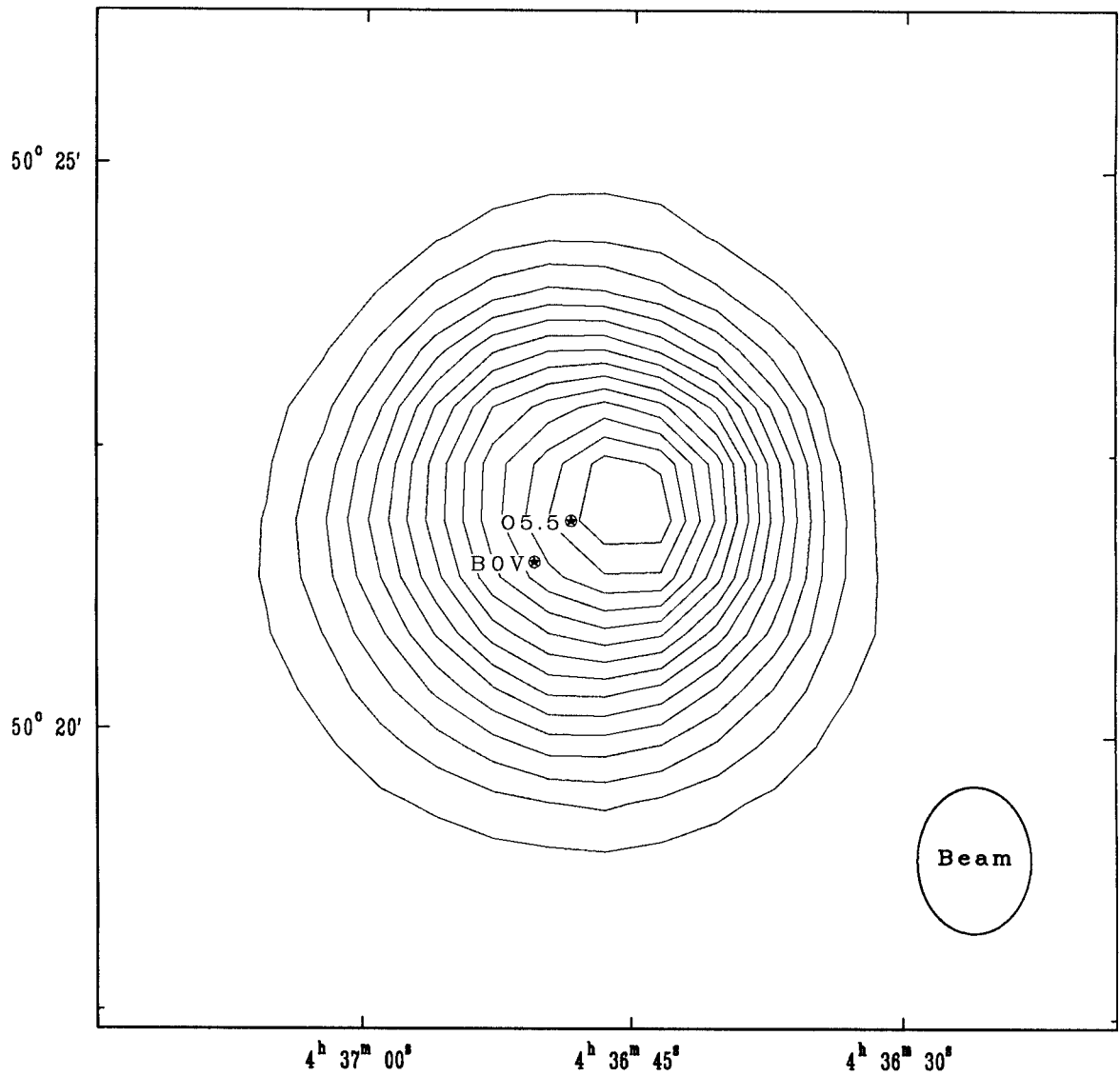
S211 HI Spectra (Ring)



APPENDIX F: S212 HI MAPS AND SPECTRA

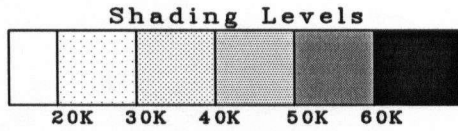
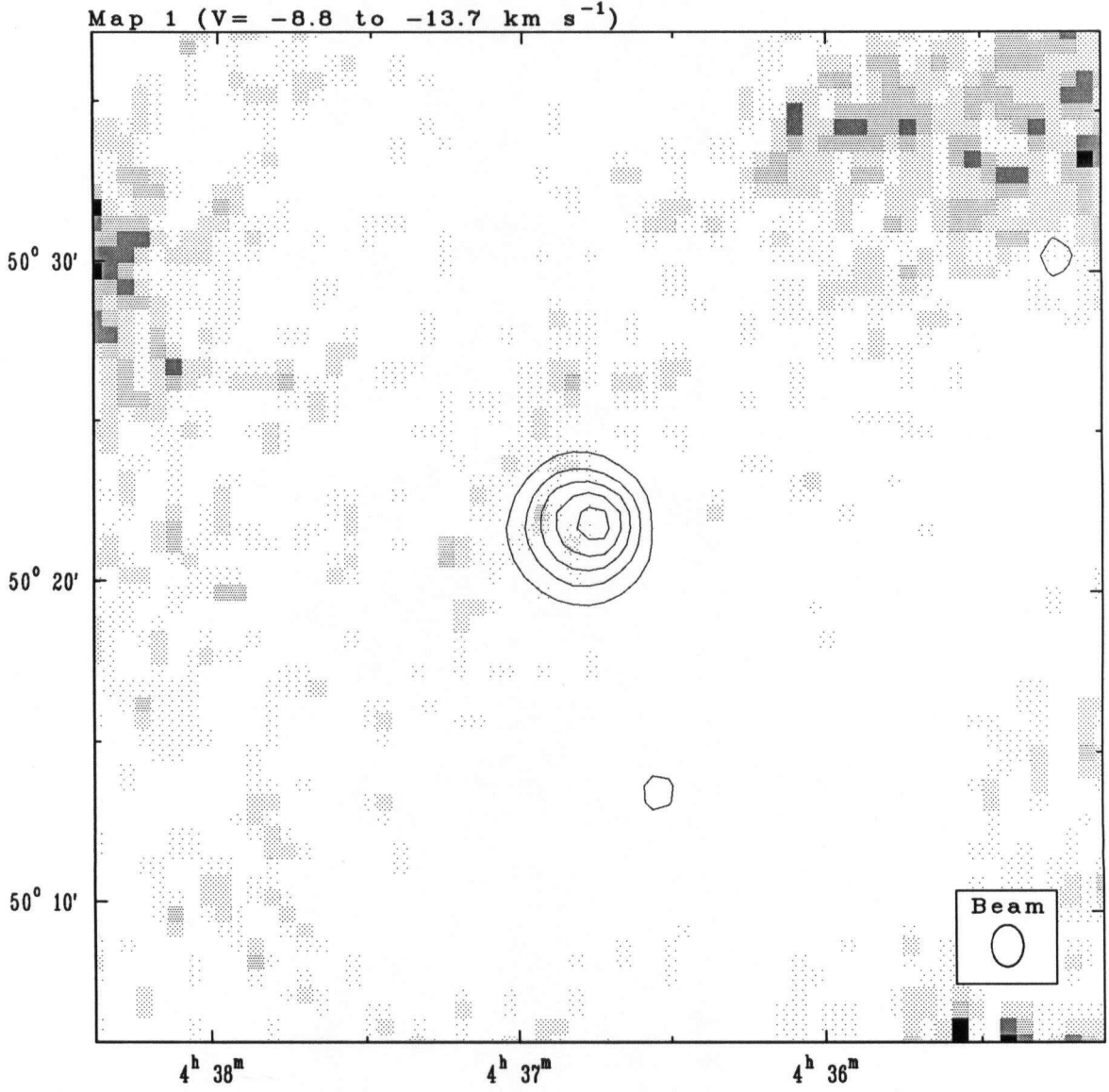
This appendix contains a continuum map of S212 depicting the positions of its ionizing stars (p148), 32' x 32' HI maps centred on S212 (pp149 to 156), HI velocity maps ($v-\alpha$, $\delta-v$) corresponding to the 32' x 32' area centred on S212 (p158), HI spectra averaged in quarter-rings east and west (pp160 to 161) and north and south (pp163 and 164). The map of S212 and its ionizing stars labels the stars with their spectral classes according to Moffat et. al. (1979). The S212 HI maps are the spectrum subtracted (SS) maps averaged in differing velocity ranges, depending on the contents of the field, over the entire CC Survey bandwidth. The noise in maps 1 to 3 and 5 is estimated to be about 5K rms; in map 4 this is about 7K rms; in maps 6 and 7 it is about 4K rms; for map 8 this is approximately 3K rms. A contour map of S212 is overlaying the HI maps for comparison. The HI velocity maps and spectra are discussed on pages 157, 159, 162.

S212 and Ionizing Stars



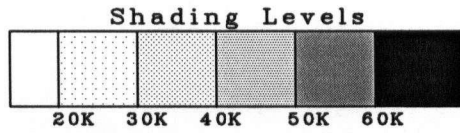
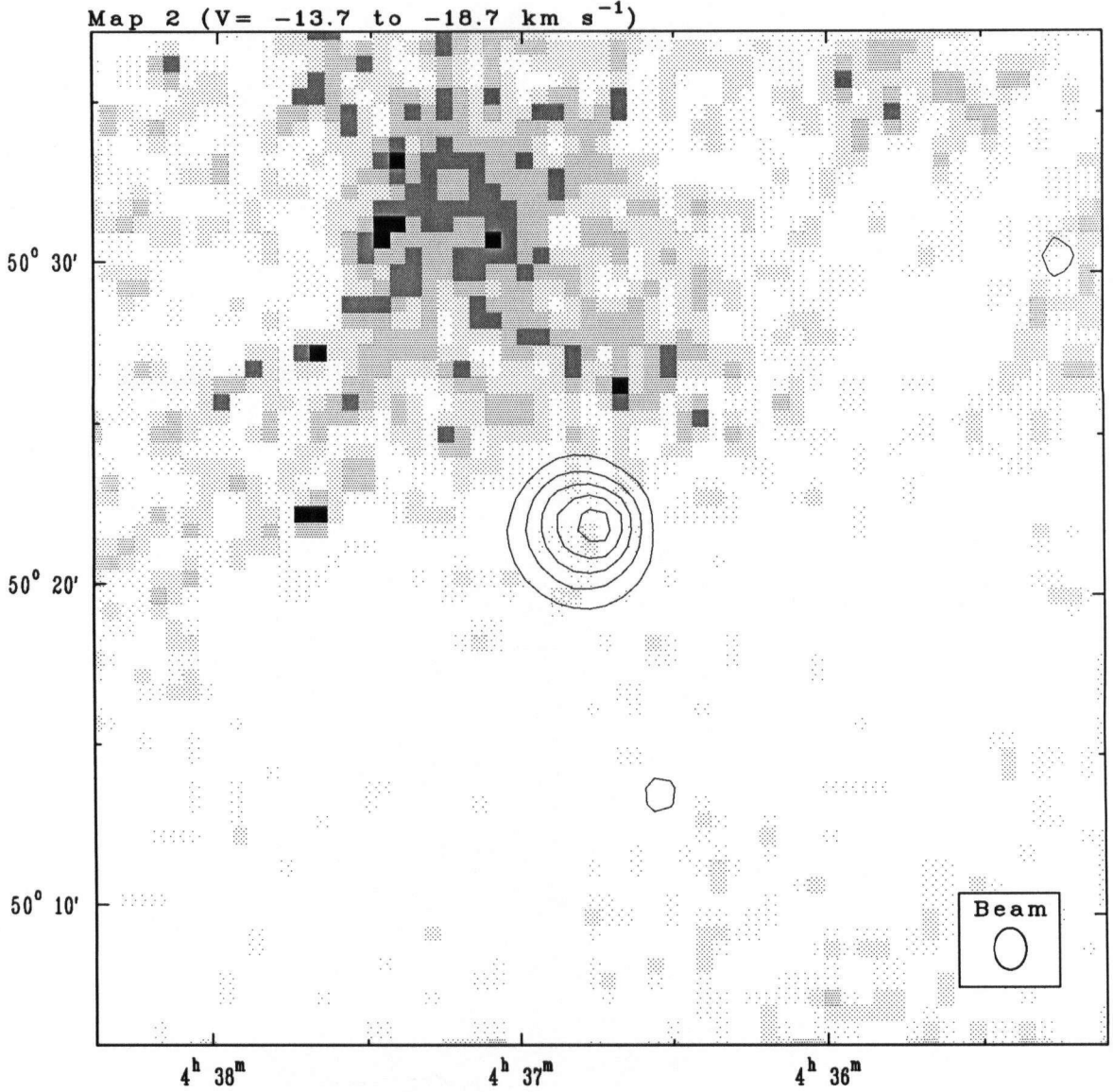
Contours: Multiples of 2K from 2K to 36K.
(Brightness Temperature Units)

S212 HI Maps



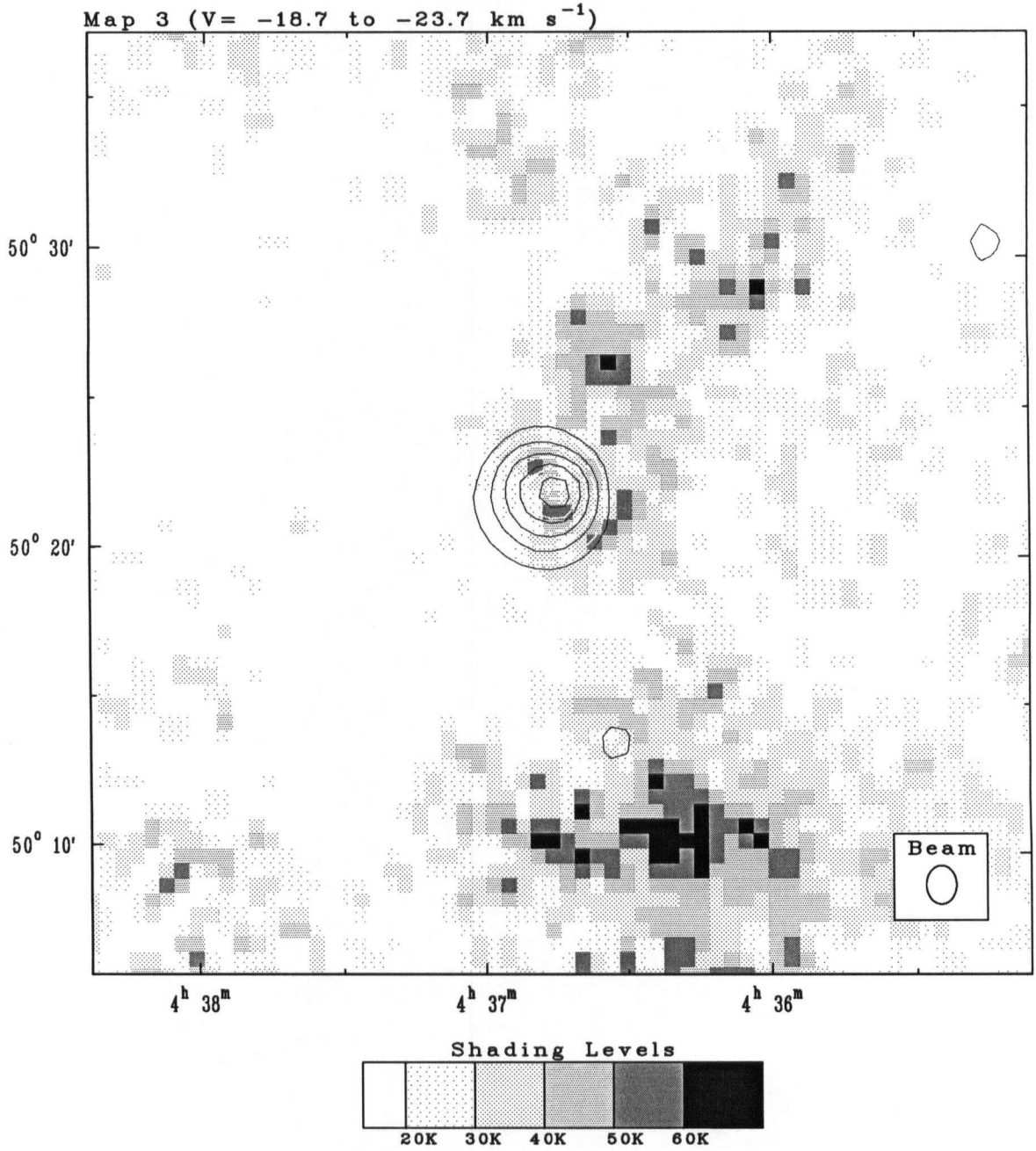
Contours: (6, 12, 18, 24, 30) K Brightness Temperature

S212 HI Maps



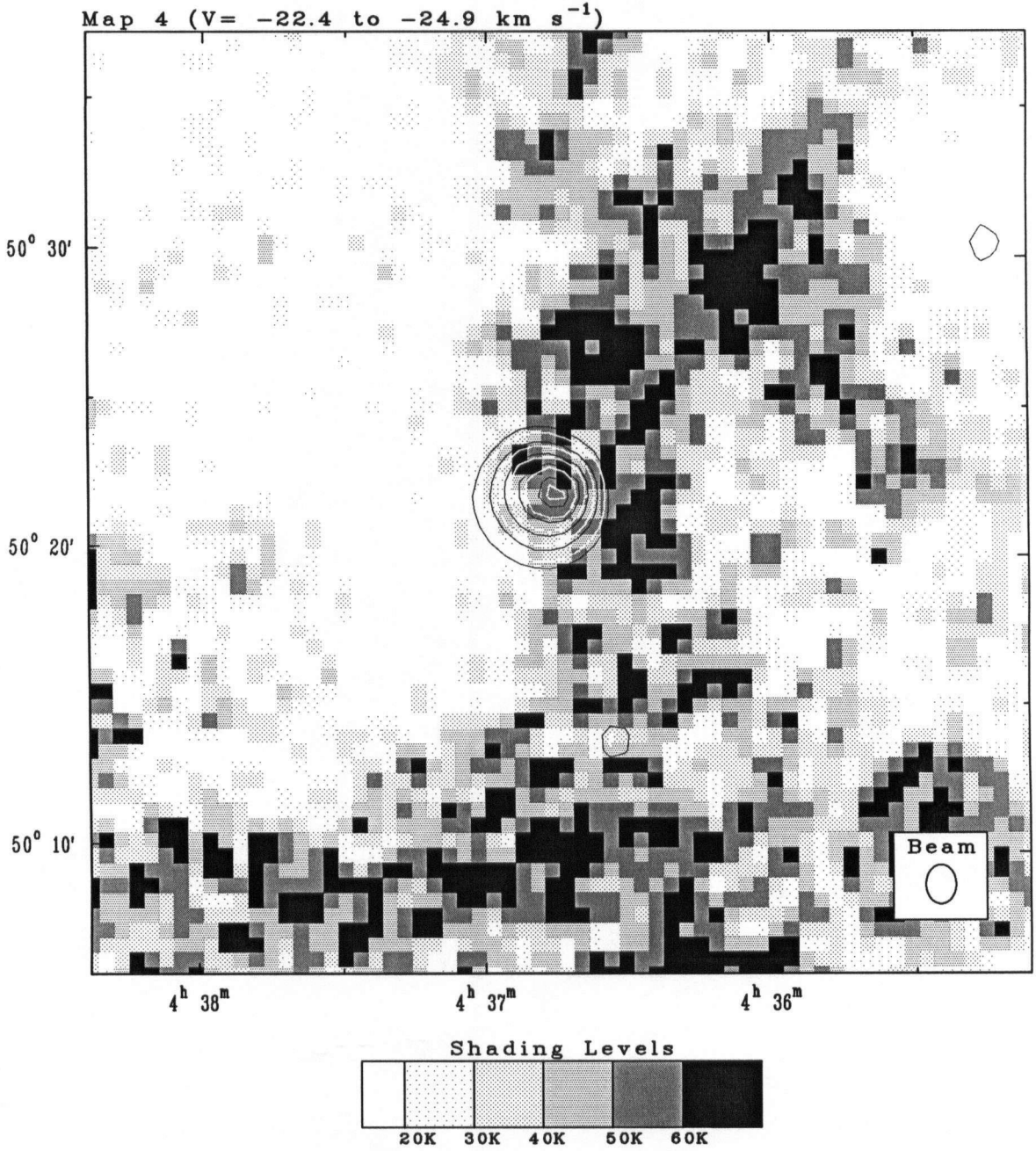
Contours: (6, 12, 18, 24, 30) K Brightness Temperature

S212 HI Maps



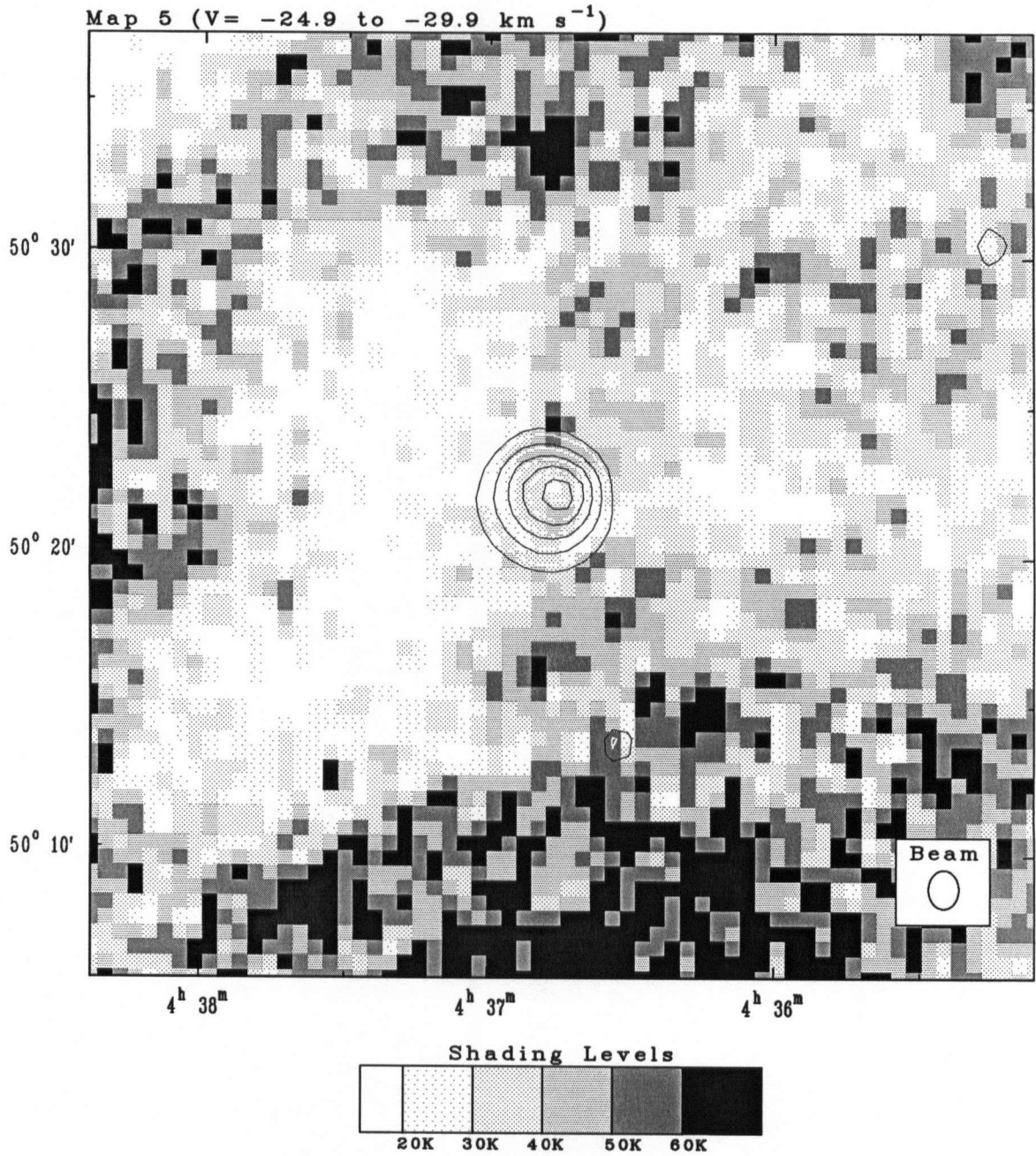
Contours: (6, 12, 18, 24, 30) K Brightness Temperature

S212 HI Maps



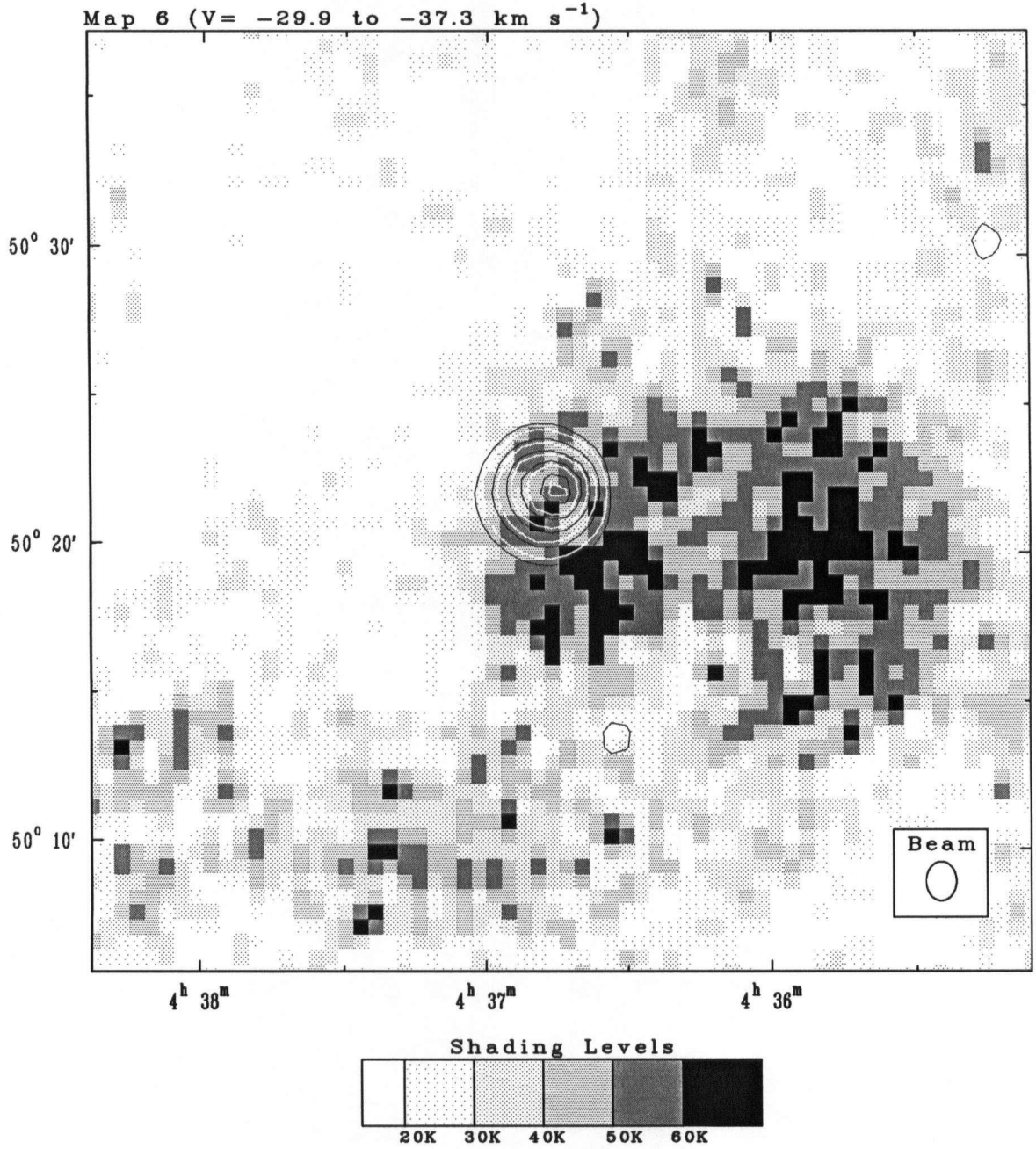
Contours: (6, 12, 18, 24, 30) K Brightness Temperature

S212 HI Maps



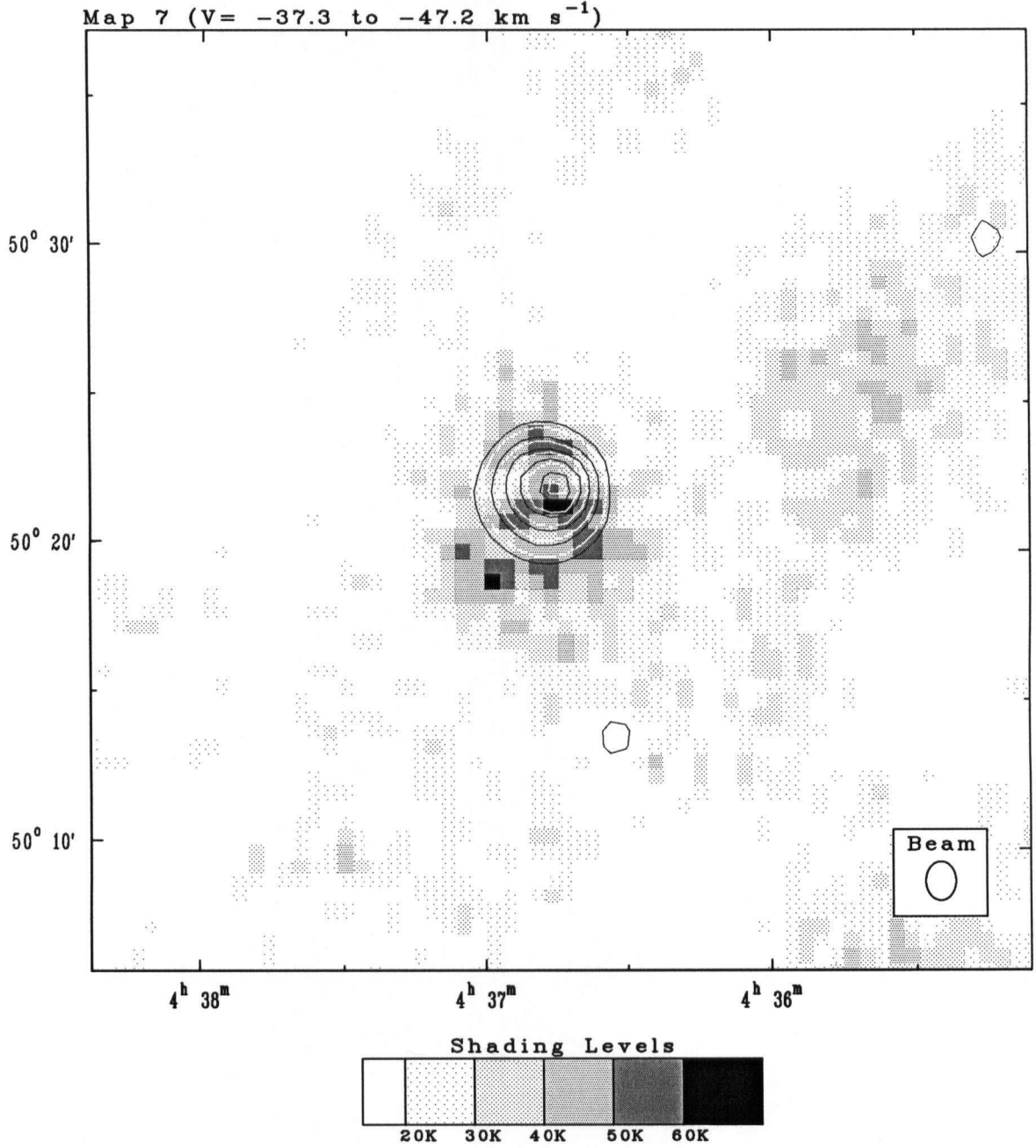
Contours: (6, 12, 18, 24, 30) K Brightness Temperature

S212 HI Maps



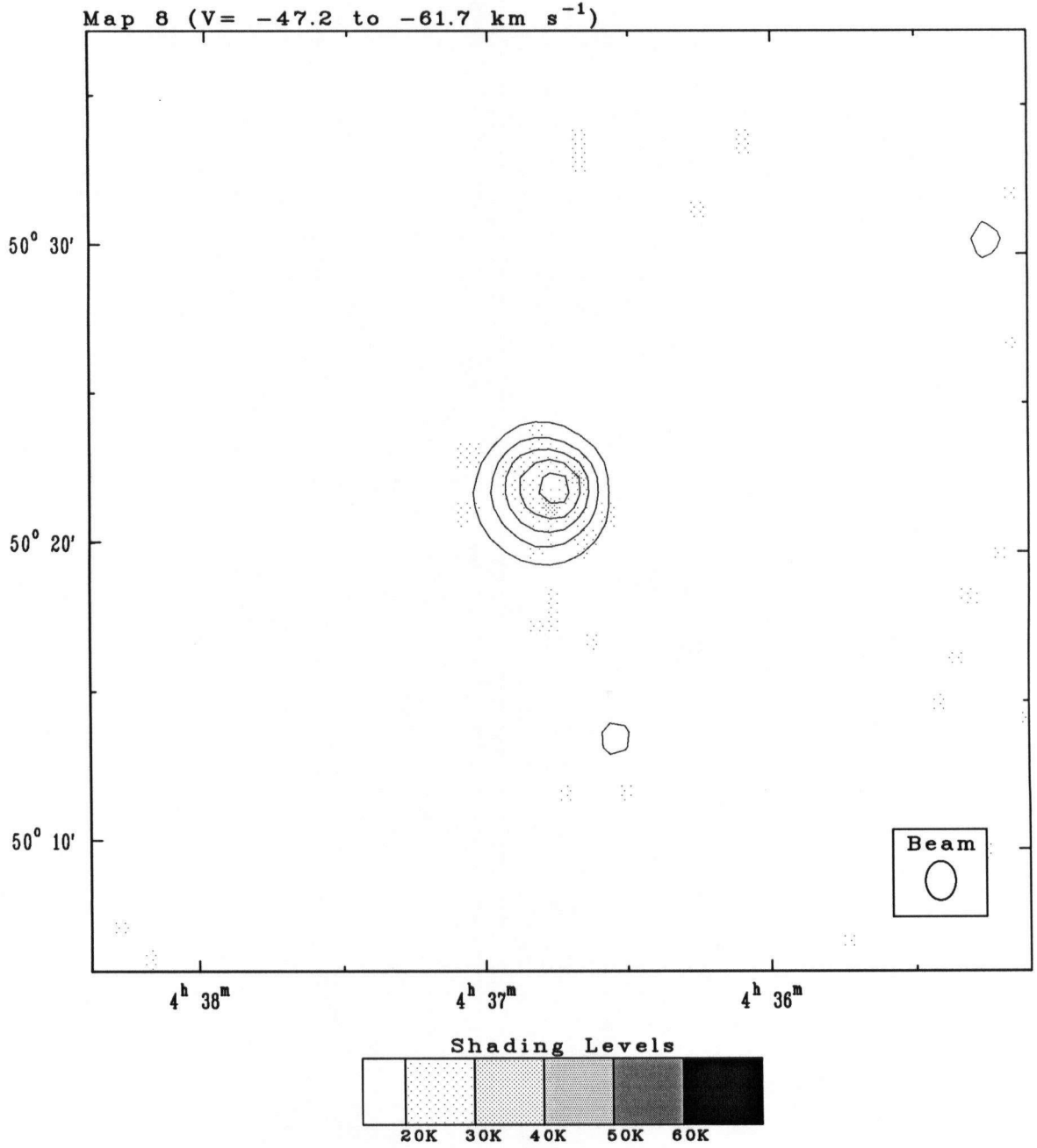
Contours: (6, 12, 18, 24, 30) K Brightness Temperature

S212 HI Maps



Contours: (6, 12, 18, 24, 30) K Brightness Temperature

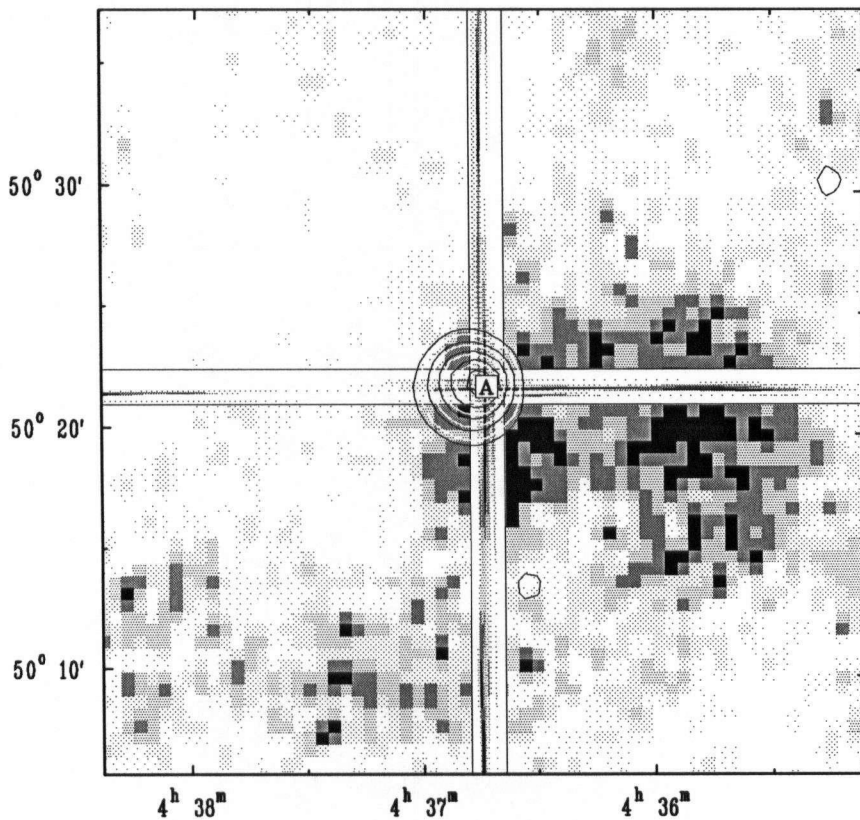
S212 HI Maps



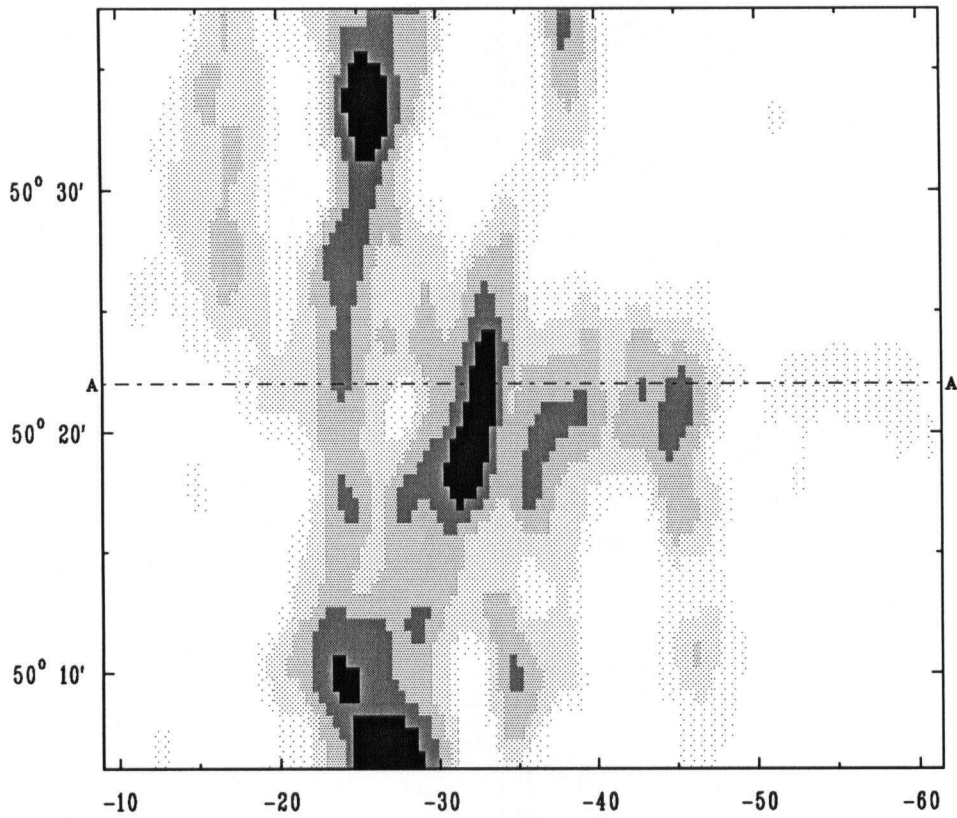
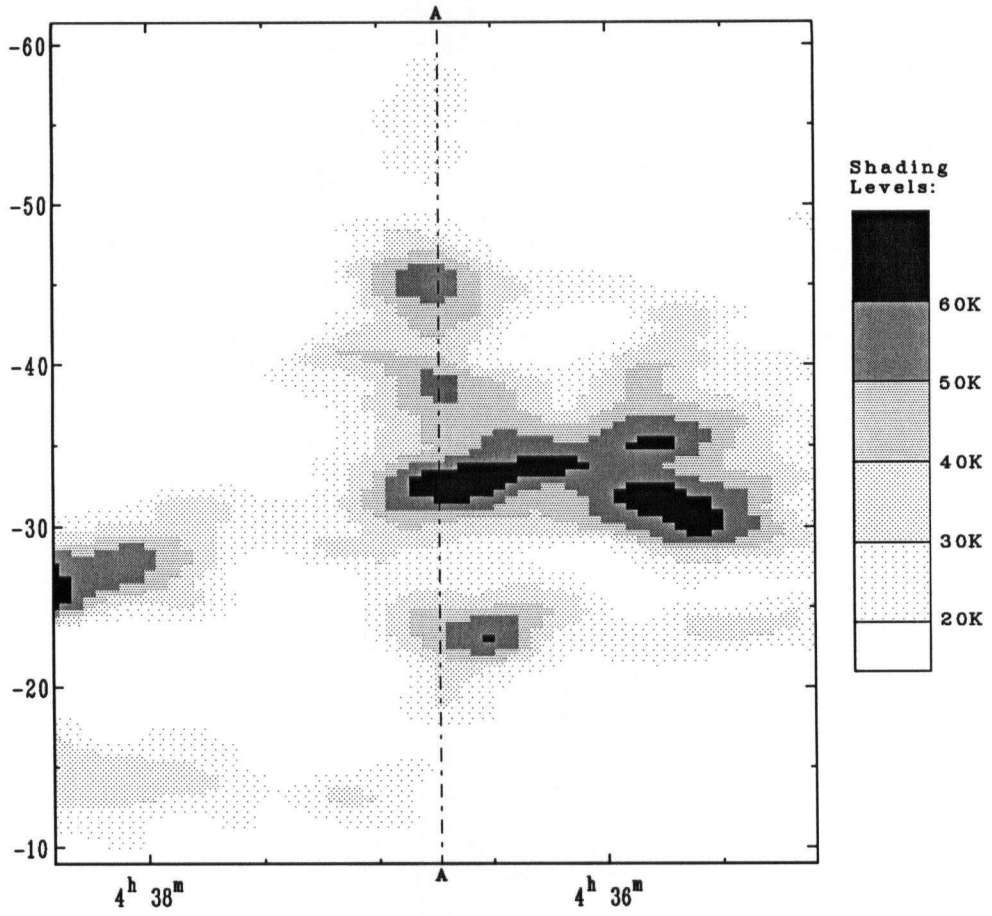
Contours: (6, 12, 18, 24, 30) K Brightness Temperature

S212 HI Velocity Maps

The following page shows a velocity-right ascension map (top) and declination-velocity map (bottom) which were taken at the positions of the horizontal and vertical bars shown in the map below. The position of the intersection marked "A" is represented by a dashed line in the velocity maps. Each bar contains a foreshortened version of its corresponding velocity map and has a 3 pixel (1'.5) thickness because each velocity map is a 3 pixel average in the spatial dimension indicated by the bar thickness; i.e. the $v-\alpha$ map has been averaged by 3 pixels in the δ direction and the $\delta-v$ map has been averaged by 3 pixels in the α direction. In addition, each map has been smoothed to 1.7 km s^{-1} resolution in the velocity direction and to 3' in the spatial direction (α or δ). The noise is estimated to be about 1 to 2K rms. The velocity axes are in km s^{-1} with respect to the local standard of rest.

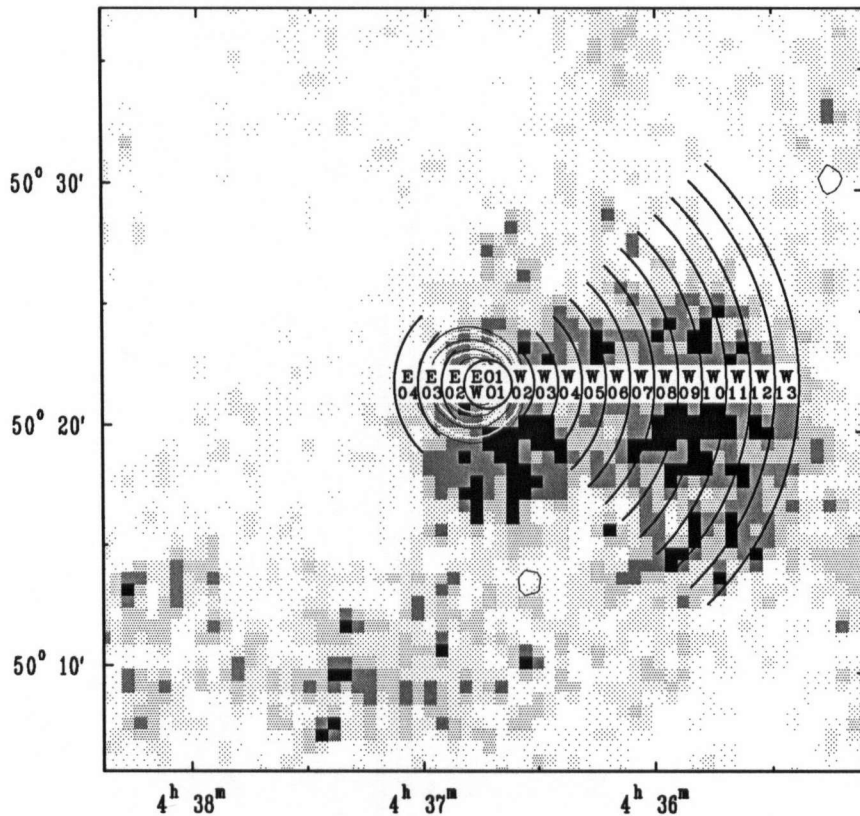


S212 HI Velocity Maps

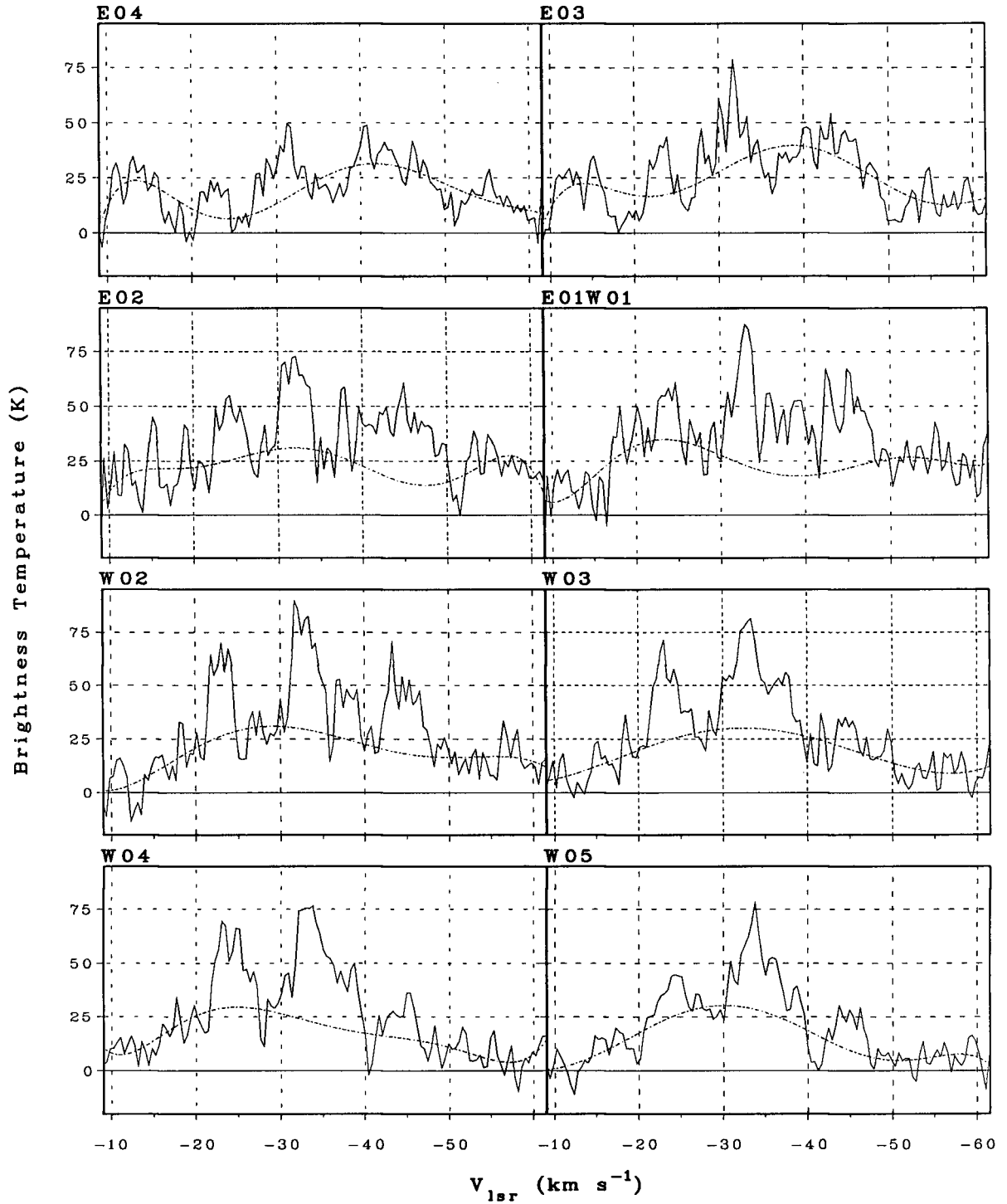


S212 HI Spectra (East-West)

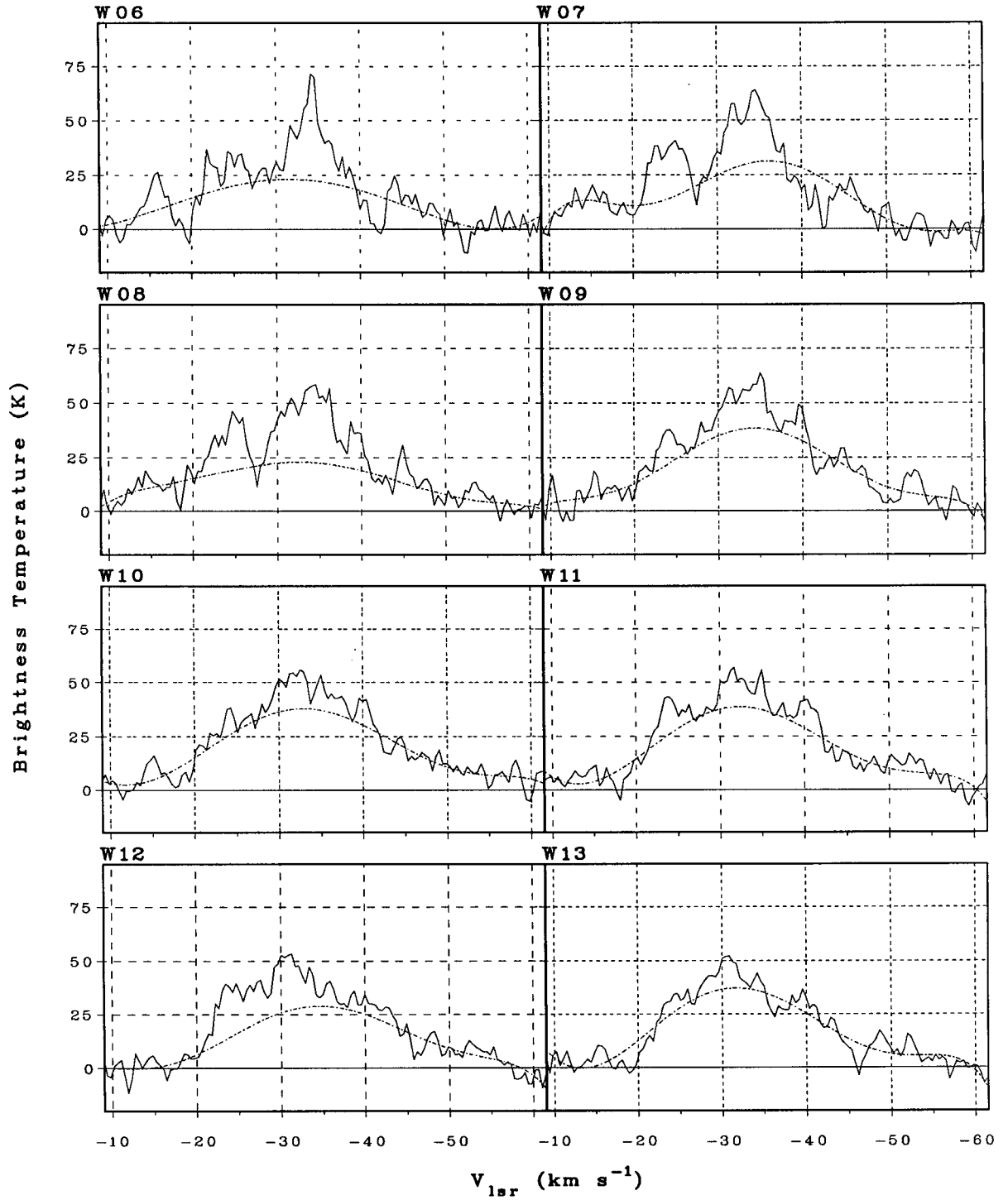
The spectra on the following two pages are spatially averaged in quarter-rings oriented east and west as shown in the map below. The quarter-rings are 2 pixels or 1' in thickness. The number assigned to each of the spectra corresponds to a ring number below. Notice that ring 1 is a full circle whose spectrum is the same for the spectra averaged in quarter-rings in each of the four cardinal directions (see page 162). The noise of the ring 1 spectrum is about 7K rms. The noise of the spectrum in ring number RN can be estimated from $\sigma_0(RN)^{-0.5}$ where σ_0 is 10 to 11K. Because of quantization effects the spatial area for each spectrum is not exactly annular. The morphology of the spatial averaging is still adequately represented by the map below. The dashed line accompanying each spectrum is a polynomial representing the baseline for the spectrum.



S212 HI Spectra (East-West)

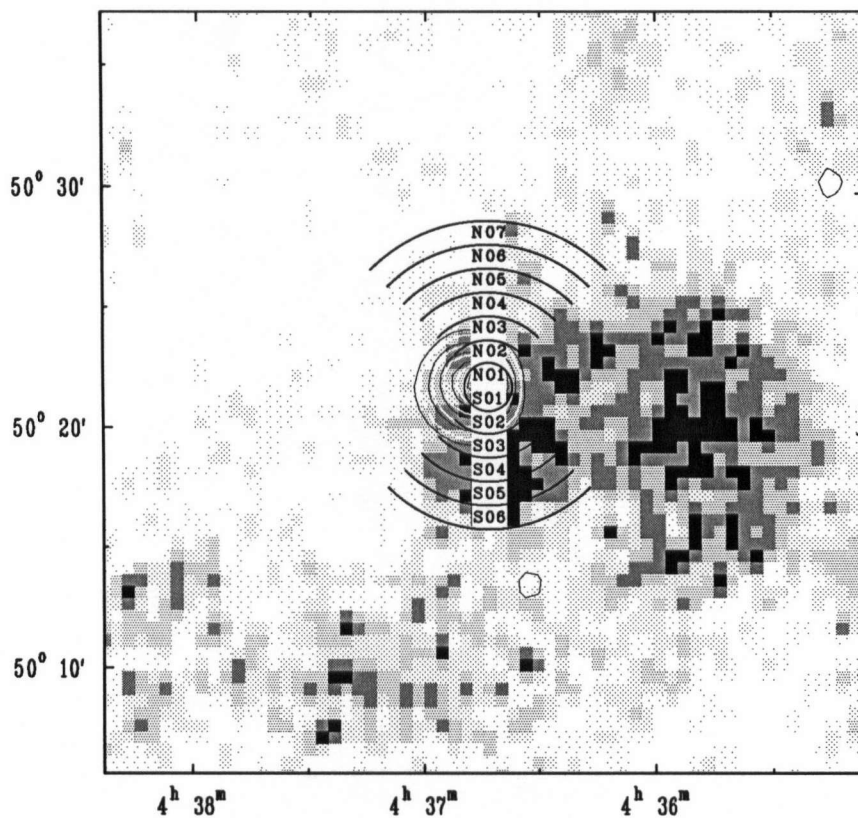


S212 HI Spectra (East-West)

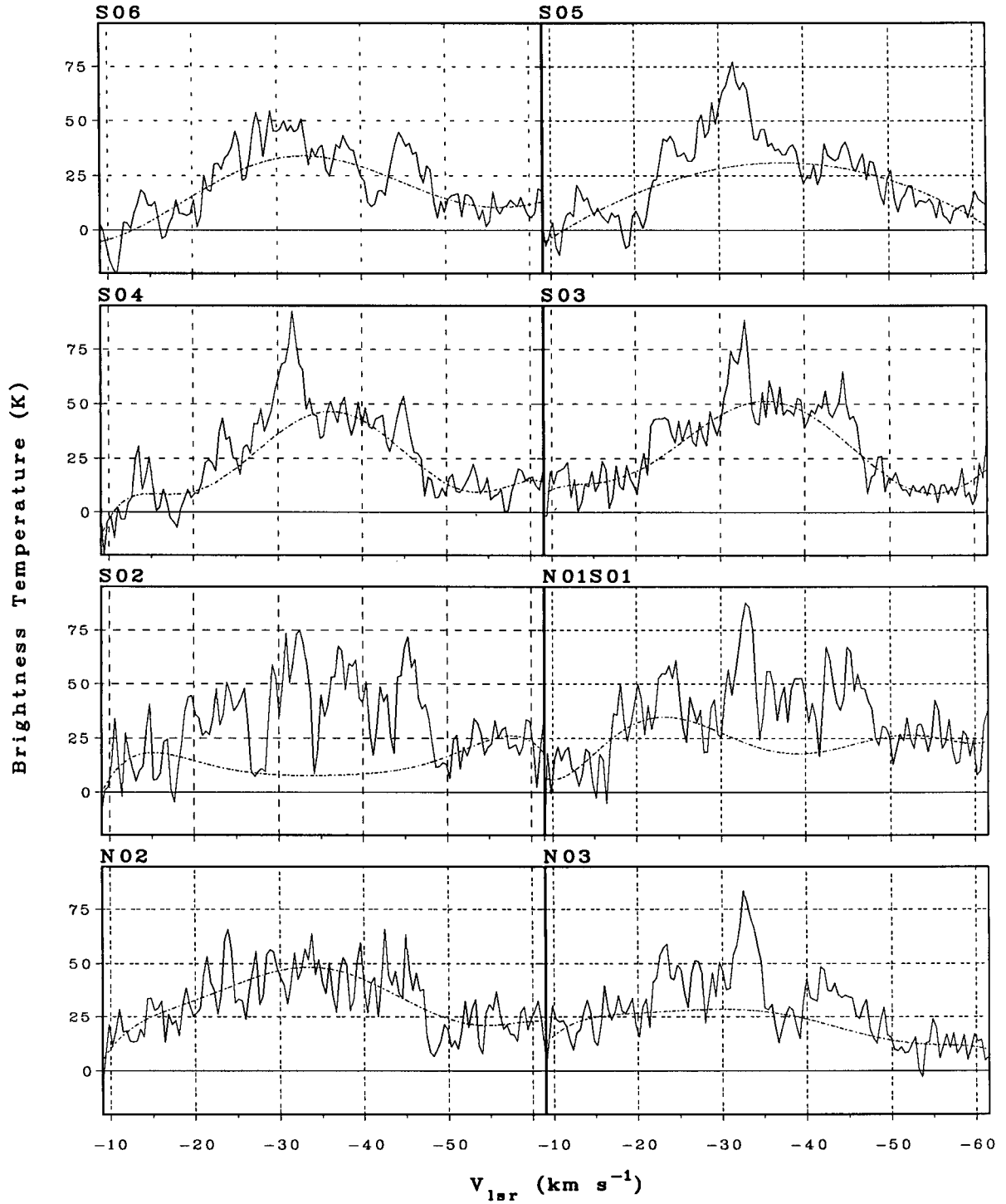


S212 HI Spectra (North-South)

The spectra on the following two pages are spatially averaged in quarter-rings oriented north and south as shown in the map below. The quarter-rings are 2 pixels or 1' in thickness. The number assigned to each of the spectra corresponds to a ring number below. Notice that ring 1 is a full circle whose spectrum is the same for the spectra averaged in quarter-rings in each of the four cardinal directions (see page 159). The noise of the ring 1 spectrum is about 7K rms. The noise of the spectrum in ring number RN can be estimated from $\sigma_0(RN)^{-0.5}$ where σ_0 is 10 to 11K. Because of quantization effects the spatial area for each spectrum is not exactly annular. The morphology of the spatial averaging is still adequately represented by the map below. The dashed line accompanying each spectrum is a polynomial representing the baseline for the spectrum.



S212 HI Spectra (North-South)



S212 HI Spectra (North-South)

